

# University of Southampton Research Repository ePrints Soton

Copyright © and Moral Rights for this thesis are retained by the author and/or other copyright owners. A copy can be downloaded for personal non-commercial research or study, without prior permission or charge. This thesis cannot be reproduced or quoted extensively from without first obtaining permission in writing from the copyright holder/s. The content must not be changed in any way or sold commercially in any format or medium without the formal permission of the copyright holders.

When referring to this work, full bibliographic details including the author, title, awarding institution and date of the thesis must be given e.g.

AUTHOR (year of submission) "Full thesis title", University of Southampton, name of the University School or Department, PhD Thesis, pagination

#### UNIVERSITY OF SOUTHAMPTON

## METAL DEPOSITION ON TiO<sub>2</sub>(110) VIA THERMAL EVAPORATION, PHOTOLYSIS AND THERMOLYSIS: A COMBINED FT-RAIRS AND XPS STUDY

#### **ALEXANDROS ANASTASOPOULOS**

## THESIS SUBMITTED FOR THE DEGREE OF DOCTOR OF PHILOSOPHY

#### SCHOOL OF CHEMISTRY

FACULTY OF ENGINEERING, SCIENCE AND MATHEMATICS

OCTOBER 2008 UNIVERSITY OF SOUTHAMPTON

#### ABSTRACT

#### FACULTY OF ENGINEERING, SCIENCE AND MATHEMATICS

#### SCHOOL OF CHEMISTRY

#### **Doctor of Philosophy**

#### METAL DEPOSITION ON TiO<sub>2</sub>(110) VIA THERMAL EVAPORATION, PHOTOLYSIS AND THERMOLYSIS: A COMBINED FT-RAIRS AND XPS STUDY

#### by Alexandros Anastasopoulos

Model systems combined with surface science techniques provide a powerful tool for the study of oxide supported metal overlayers. This thesis describes the synthesis and characterisation of Cu, Mo and Au overlayers on TiO<sub>2</sub>(110) deposited using a number of methods.

Cu overlayers were deposited on the TiO<sub>2</sub>(110) surface via Physical Vapour Deposition (PVD) at 295 K. Using CO as a probe adsorbate molecule, FT-RAIRS revealed that Cu islands with sizes less than ca. 3.5 nm exhibited predominantly high Miller Index surfaces, whereas larger islands exhibited (110), (100) and (111) facets. By comparing XPS and FT-RAIRS results collected before and after annealing, a complex growth mode is proposed which resembles a combination of Volmer-Weber and Stranski-Krastanov types. The reactivity between O<sub>2</sub> and pre-adsorbed CO appeared highest for the particles exhibiting the high Miller Index facets. Finally, FT-RAIRS allowed for the identification of a threshold Cu coverage, 4.48 MLE, above which the influence of the oxide support to the local dielectric field seized, and metallic behaviour was exhibited.

The photolysis of Mo(CO)<sub>6</sub> adsorbed on the TiO<sub>2</sub>(110) surface at 130 K was studied as an alternative to PVD deposition of Mo. Photo-dissociation of 1.53 L of exposed Mo(CO)<sub>6</sub> resulted in a single photoproduct, Mo(CO)<sub>3</sub>, which adopted a geometry perpendicular to the surface. The tricarbonyl was the main photoproduct following the dissociation of 2.73 L of exposed Mo(CO)<sub>6</sub>, although higher carbonyls were also observed with FT-RAIRS. Photolysis of adsorbed multilayers resulted in the production of Mo(CO)<sub>5</sub> and traces of Mo(CO)<sub>4</sub>. The dependence between the initial coverage of the Mo(CO)<sub>6</sub> and the photoproducts provides direct evidence of a substrate mediated decomposition path on TiO<sub>2</sub>(110).

The deposition of (CH<sub>3</sub>)<sub>2</sub>Au(acac) on TiO<sub>2</sub>(110) at different temperatures was examined to establish its potential application as an OrganoMetallic Chemical Vapour Deposition (OMCVD) precursor of highly dispersed Au particles. At 130 K, oxidised Au overlayers were prepared, whereas at 295 K a mixture of metallic and oxidised gold overlayers were observed, indicating the formation of an intermediate decomposition product of the precursor. In both cases, annealing above 700 K resulted in metallic Au. Deposition at 550 K resulted directly in the formation of metallic gold overlayers, but with some contamination by residual graphitic carbon.

## **Table of Contents**

Declaration of Authorship	vi
Acknowledgments	vii
Table of Abbreviations	viii
Chapter 1	
Introduction	1
1.1 Metal Overlayers Supported on Oxide Substrates	1
1.2 TiO <sub>2</sub> (110)	3
1.2.1 The Stoichiometric TiO <sub>2</sub> (110)-(1x1) Surface	3
1.2.2 Defects on the TiO <sub>2</sub> (110)-(1x1) Surface	5
1.2.3 TiO <sub>2</sub> (110) as Support for Metal Overlayers	7
1.3 Physical Concepts	8
1.3.1 Growth and Nucleation of Thin Films	8
1.3.2 Adsorption on Surfaces	9
1.3.3 Reaction Mechanisms	11
Chapter 2	
Instrumentation and Experimental Techniques	13
2.1 The UHV System	13
2.2 Sample Mounting and Preparation of an Atomically Clean TiO <sub>2</sub> (110) Surface	14
2.3 Fourier Transform Reflection Absorption InfraRed Spectroscopy (FR-RAIRS)	17
2.3.1 Theory	17
2.3.1.1 Metal Support	18
2.3.1.2 Semiconducting or Oxide Supports	21
2.3.2 Experimental Considerations	23
2.4 X-ray Photoelectron Spectroscopy (XPS)	26
2.4.1 Theory	26
2.4.2 Quantification of Spectra	29
2.5 Low Energy Electron Diffraction (LEED)	31
2.6 Physical Vapour Deposition (PVD)	34
2.7 Organometallic Chemical Vapour Deposition (OMCVD)	35

## Chapter 3

TiO <sub>2</sub> (110) Supported Cu Particles and Films	38
3.1 Introduction	38
3.1.1 PVD of TiO <sub>2</sub> (110) Supported Cu Particles and Films	38
3.1.2 Growth and Properties of Cu Supported on Various Metal Oxides	40
3.1.3 Catalytic Properties of Cu Supported on Various Metal Oxides	41
3.2 Experimental	43
3.3 Results and Discussion	46
3.3.1 CO Adsorption	46
3.3.1.1 Low Coverage	47
3.3.1.2 Medium Coverage	53
3.3.1.3 Continuous Film	59
3.3.2 Structural Changes During Growth	65
3.3.3 Interaction with O <sub>2</sub>	73
3.4 Conclusions	77
Chapter 4	
The Photolysis of MoCO <sub>6</sub> on TiO <sub>2</sub> (110)	80
4.1 Introduction	80
4.1.1 Photolysis of Mo(CO) <sub>6</sub> in Different Phases: Gas, Matrix Isolation and So	lution. 81
4.1.2 Adsorption and Photodecomposition of Mo(CO) <sub>6</sub> on Si and Metals	83
4.1.3 Adsorption of Mo(CO) <sub>6</sub> on Metal Oxide Surfaces	85
4.1.4 Infrared Assignment	86
4.2 Experimental	87
4.3 Results and Discussion	91
4.3.1 Deposition of Mo(CO) <sub>6</sub>	91
4.3.2 Photodecomposition of 1.53 L of Mo(CO) <sub>6</sub>	96
4.3.3 Photodecomposition of 2.73 L of Mo(CO) <sub>6</sub>	106
4.3.4 Photodecomposition of 20.2 L of Mo(CO) <sub>6</sub>	114
4.3.5 Temperature Effects- Formation of Carbon Free Particles	
4.3.6 Photodecomposition with Optical Filter	128
4.4 Conclusions	

## Chapter 5

The deposition of (CH <sub>3</sub> ) <sub>2</sub> Au(acac) on TiO <sub>2</sub> (110)	131
5.1 Introduction	131
5.1.1 Growth Mode of Au on TiO <sub>2</sub> (110) and TiO <sub>x</sub>	131
5.1.2 Catalytically Active Au Nanoparticles	133
5.1.3 Deposition of Au from (CH <sub>3</sub> ) <sub>2</sub> Au(acac)	136
5.2 Experimental	137
5.3 Results and discussion	139
5.3.1 Adsorption of (CH <sub>3</sub> ) <sub>2</sub> Au(acac) on the TiO <sub>2</sub> (110) Surface at 130 K	139
5.3.2 Annealing Behaviour of Adsorbed (CH <sub>3</sub> ) <sub>2</sub> Au(acac)	142
5.3.3 Room Temperature Deposition of (CH <sub>3</sub> ) <sub>2</sub> Au(acac)	146
5.3.4 Deposition of (CH <sub>3</sub> ) <sub>2</sub> Au(acac) at 550 K	149
5.3.5 FT-RAIRS Investigation of (CH <sub>3</sub> ) <sub>2</sub> Au(acac) Adsorption at 130 K	157
5.4 Conclusions	163
Chapter 6	
General Conclusions	164
6.1 TiO <sub>2</sub> (110) Supported Cu Particles and Films	164
6.2 The Photolysis of MoCO <sub>6</sub> on TiO <sub>2</sub> (110)	165
6.3 The Deposition of (CH <sub>3</sub> ) <sub>2</sub> Au(acac) on TiO <sub>2</sub> (110)	166
Appendix A	168
References	178

## **Declaration of Authorship**

I, Alexandros Anastasopoulos,

declare that the thesis entitled:

METAL DEPOSITION ON  $TiO_2(110)$  VIA THERMAL EVAPORATION, PHOTOLYSIS AND THERMOLYSIS: A COMBINED FT-RAIRS AND XPS STUDY and the work presented in the thesis are both my own, and have been generated by me as the result of my own original research. I confirm that:

- This work was done wholly while in candidature for a research degree at this University
- Where I have consulted the published work of others, this is always clearly attributed
- Where I have quoted from the work of others, the source is always given. With the exception of such quotations, this thesis is entirely my own work.
- I have acknowledged all main sources of help
- None of this work has been published before submission

Signed:		
Date:		

#### **Acknowledgments**

I owe a very special thanks to my supervisor Prof. Brian Hayden, for his guidance throughout my PhD, his generous funding and lessons on how to use UHV equipment, but above all for his magical ability to encourage me to continue with the research even when nothing seemed to work properly.

A big thank you to all members of the surface science laboratory, past and present: Mike R., Rafael C-M., Oliver S., Scott B., Tim N., Peter S., Laura W., Claire M., Chris L., Ben W., Naruo Y., Samuel G., Chris G., Rob N., Faisal A., Mehdi M., all helping me one way or another to finish this huge task.

I am grateful to the people from the mechanical workshop for never letting me down whenever equipment needed repairing. Rob, John, Dave (especially for welding my manipulator twice and with no leaks) and Alan thank you very much.

My friends here in Southampton for spending all these years together, supporting each other during the bad and the good days: Nota P., Giannis V., Clelia M., Phil N., Periklis P., Charis V., Elena P., Sofia P., Maria N., Peter S., Claire M., My friends in Athens: Giannis G., Alexandros D., Thanos L., Fragiskos S., Melpo G., Eirini K., Kostas V., Simos K., Harris G., Michalis Z., helping by just being friends.

A special thank you to Elias Maraziotis and his family for helping me during my fourth year.

To Nefeli for everything, 'αν δεν είχα και σένα τι θα ήμουν στην Γή'.

To my parents, Giannis and Dimitra. This work is dedicated to you. Ευχαριστώ για Όλα.

## **Table of Abbreviations**

2D	Two dimensional	
3D	Three dimensional	
AES	Auger Electron Spectroscopy	
AFM	Atomic Force Microscopy	
СНА	Concentric Hemispherical Analyser	
CVD	Chemical Vapour Deposition	
DFT	Density Functional Theory	
DRIFTS	Diffuse Reflectance Infrared Fourier Transform	
EELS	Electron Energy Loss Spectroscopy	
ESCA	Electron Spectroscopy for Chemical Analysis	
EXAFS	Extended X-ray Fine Structure	
FM growth mode	Frank-Van der Merwe	
FT-RAIRS	Fourier Transform Reflection Absorption Infrared Spectroscopy	
FWHM	Full Width Half Maximum	
Hg-Xe	Mercury Xenon	
HREELS	High Resolution Electron Energy Loss Spectroscopy	
HRTEM	High Resolution Transmission Electron Microscopy	
IMFP	Inelastic Mean Free Path	
InSb	Indium Antimonide	
IPS	Inverse Photoemission Spectroscopy	
IR	Infrared	
L	Langmuir	
LEED	Low Energy Electron Diffraction	
LEIS	Low Energy Ion Scattering	
LN	Liquid Nitrogen	

MCT	Mercury Cadmium Telluride		
ML	Monolayer		
MLE	Monolayer Equivalent		
OMCVD	OrganoMetallic Chemical Vapour Deposition		
PES	Photoelectron Spectroscopy		
PVD	Physical Vapour Deposition		
REMI	Resonance Enhanced Multiphoton Ionisation		
SK growth mode	Stranski-Krastanov		
SMSI	Strong Metal Support Interaction		
STM	Scanning Tunnelling Microscopy		
STS	Scanning Tunnelling Spectroscopy		
SXRD	Surface X-ray Diffraction		
TEM	Transmission Electron Microscopy		
TPD	Temperature Program Desorption		
TRIS	Time Resolved Infrared Spectroscopy		
TSP	Titanium Sublimation Pump		
UHV	Ultra High Vacuum		
UPS	Ultraviolet Photoelectron Spectroscopy		
UV	Ultraviolet		
VW growth mode	Volmer Weber		
XANES	X-ray Absorption Near Edge Structure		
XPS	X-ray Photoelectron Spectroscopy		

### Chapter 1

#### Introduction

Metal overlayers deposited on oxide supports have attracted interest from the scientific community as they find applications in different fields such as heterogeneous catalysis, microelectronics, gas sensing and magnetic applications for information storage. Complete understanding though of their properties has not yet been achieved. A way forward is to employ surface science techniques and tools to gain an insight into the fundamental behaviour of these systems.<sup>2</sup> Working though with oxides, induces a serious hurdle as most of them are insulating hence measurements with techniques that utilise electrons or ions are experimentally difficult.<sup>3</sup> As a result, there are currently two trends for studying these metal/oxide systems. In the first, the metal is deposited on a bulk single crystal oxide support, whilst in the second one deposition takes place on thin oxide films grown on a metallic substrate. With the second one the problem of conductivity can be overcome, although bulk single crystals of reducable oxides like TiO<sub>2</sub> can be used with all surface science techniques.<sup>5</sup> In the following section some general comments regarding the interaction of metals with oxide surfaces are going to be presented, followed by specific information regarding TiO<sub>2</sub>(110) as a support. At the end a section is devoted to physical concepts used throughout this work such as physical and chemical adsorption, growth mechanisms of thin films and reaction pathways.

#### 1.1 Metal Overlayers Supported on Oxide Substrates

One of the most significant observations for these systems lies with the fact that their properties depend on both overlayer and support. For example it has been shown that the catalytic activity towards CO oxidation of Au nanoparticles supported on TiO<sub>2</sub> is higher than Au supported on SiO<sub>2</sub>.<sup>6</sup> Another example is the deposition of Ag. On Mg(100) layer by layer growth is observed whereas on TiO<sub>2</sub>(110) three dimensional (3D) islands

are formed.<sup>7</sup> On the other hand, Cu forms 3D islands when deposited on Mg(100) and Ag 2D.<sup>7</sup> The chemical interactions between support and overlayer control the above behaviour, hence these are explained in the following paragraph.

In a recent review by Fu and Wagner, the chemical interactions taking place between metal overlayer and oxide support have been grouped into four categories.<sup>4</sup> The first involves a redox reaction where oxidation of the metal and reduction of the substrate takes place. According to Campbell such a reaction can take place when the heat of formation of the oxide of the metal,  $\Delta H_f^o$ , is more negative than that of the metal oxide support. For example the  $\Delta H_f^o$  for Nb is more negative than Ti, hence an oxidation should occurred when the latter is deposited on TiO2, and indeed this has been observed experimentally.9 These authors observed using High Resolution Transmission Electron Microscopy (HRTEM) the formation of a structurally distorted layer at the interface, which upon examination with Electron Energy Loss Spectroscopy (EELS) was found to contain oxidised Nb and reduced TiO2. The second interaction involves the formation of an alloy between the metal of the overlayer and the metal of the oxide. For example after reducing a 5 % Pt/CeTbO<sub>x</sub> catalyst at 1173 K, the formation of LnPt<sub>5</sub> (Ln=Ce or Tb) was observed. 10 The third interaction relates with encapsulation, upon which the metal particles are covered by a thin layer of reduced oxide support. Usually noble metals like Pt, Pd, and Rh exhibit this behaviour, for example in a review by Chen and Goodman, encapsulation of Pt was reported when the latter was deposited on TiO<sub>2</sub> and Al<sub>2</sub>O<sub>3</sub> thin oxide films. <sup>7</sup> This is usually attributed to the Strong Metal Support Interaction (SMSI), phenomenon according to which the adsorption behaviour of a catalyst is modified upon increasing its reduction temperature. 11 Finally, the fourth interaction taking place correlates to interdiffusion, where material from the metal diffuses into the support and vise versa. As a result interdiffusion zones can be observed at the interfaces. Since the oxide support used in this thesis was a rutile  $TiO_2(110)$  single crystal, the next section contains a short review of the (110)-(1x1) surface along with some information regarding the deposition of various metals on  $TiO_2(110)$ .

#### $1.2 \text{ TiO}_2(110)$

#### 1.2.1 The Stoichiometric TiO<sub>2</sub>(110)-(1x1) Surface

Bulk rutile TiO<sub>2</sub> exhibits a tetragonal unit cell with a=b=4.584 Å and c=2.953 Å.<sup>5</sup> The cell is comprised of two TiO<sub>2</sub> units with Ti occupying the corners and body-centre positions, while each Ti is coordinated to six neighboring O atoms situated at the vertices of a distorted octahedron. Each O atom is coordinated to three Ti atoms. A schematic of this unit cell can be observed in Figure 1-1a. The bulk rutile TiO<sub>2</sub> can terminate in different surface structures, which are produced by the various truncations of the octahedra. Ramamoorthy *et al.* have performed ab initio calculations on stoichiometric (1x1) surfaces to establish the most energetically favourable termination. According to their findings, amongst (110), (100), (011) and (001) the first one is the surface of lowest energy. Indeed this has also been observed experimentally. Hence the majority of experimental work has been performed on a (110) surface. Since TiO<sub>2</sub> single crystals used in this study were also of the (110) termination, the following discussion is going to be focused on the properties of this surface.

The stoichiometric TiO<sub>2</sub>(110)-(1x1) surface consists of a plane of alternating Ti and O rows along the [001] direction, while an extra row of bridging oxygen atoms exists every other Ti row.<sup>13</sup> The O atoms of these rows are twofold coordinated while the rest O atoms are threefold. The Ti atoms situated below the protruding row are sixfold coordinated, whilst the rest fivefold.<sup>5</sup> A ball and stick model of the surface along with a 2D representation can be observed in Figures 1-1b and 1-1c respectively. This description has been confirmed by Scanning Tunneling Microscopy (STM) and Atomic Force Microscopy (AFM) investigations. In STM the appearance of the surface is mainly characterized by alternating bright and dark rows along the [001], with the former being attributed to the Ti rows as electronic rather than geometric effects dominate the imaging.<sup>13</sup> On the other hand AFM images collected in the non contact mode represent the protruding O rows as bright features, consistent with the topographic orientation.<sup>14</sup> Nevertheless, the inverse picture has been recently obtained in non contact AFM,

indicating that electronic effects can be present in AFM due to charging of the tip. <sup>15</sup> Surface X-Ray Diffraction (SXRD) measurements have also shown that surface atoms near the bulk exhibit the smallest relaxation, whilst atoms further away from the bulk, hence bridging O, exhibit the larger relaxation. <sup>16</sup> Furthermore sixfold Ti atoms move away from the surface and fivefold Ti towards it. For bridging O atoms it was observed that they relax towards the surface. However, a recent LEED-IV study performed by the same group revealed that the bridging O atoms move away from the surface, while the relaxation of the in plane O atoms was found higher than before. <sup>17</sup> These discrepancies were attributed to improved methodology towards surface preparation. It is worth mentioning though, that the latest data were reproduced by *ab initio* DFT calculations to a very good agreement. <sup>18</sup>

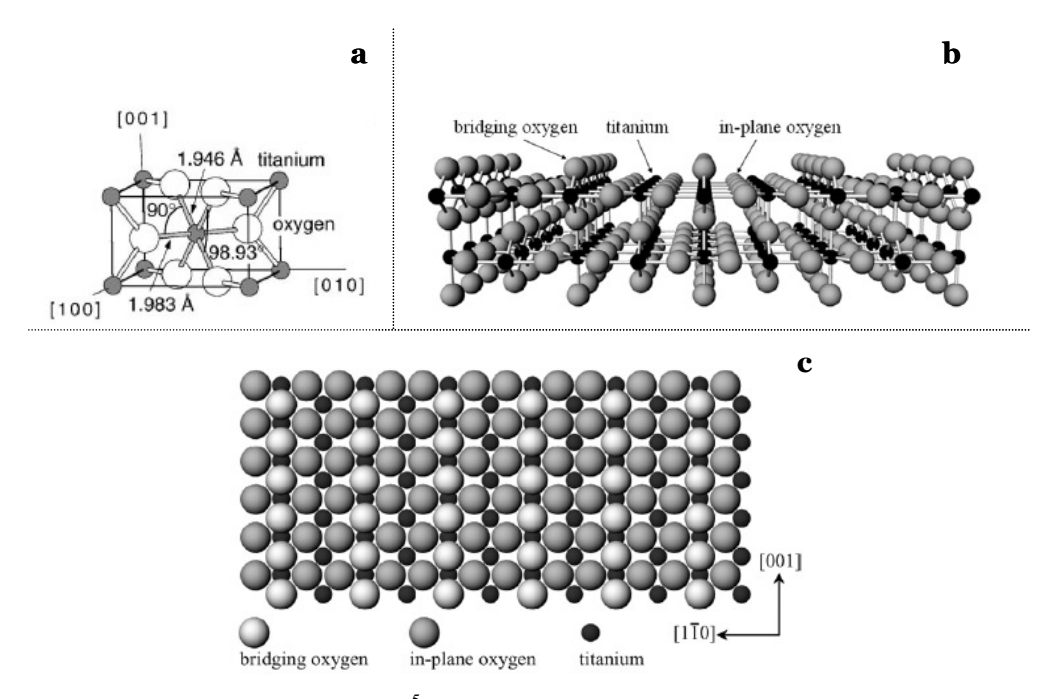


**Figure 1-1** (a) Unit cell of bulk  $TiO_2(110)$ , (b) ball and stick model of the  $TiO_2(110)$ -(1x1) surface and (c) its two dimensional representation. <sup>13</sup>

The aforementioned representation of the  $TiO_2(110)$ -(1x1) experimentally is difficult to be obtained as the existence of point defects is almost always unavoidable.<sup>5</sup> Nonetheless, it is the presence of those defects that make TiO<sub>2</sub>(110) attractive for many applications, as its surface chemistry is strongly related with them. 19, 20 These defects are usually created after annealing sputtered surfaces,<sup>21</sup> whilst they are imaged in STM as bright spots situated on top of dark rows.<sup>22</sup> Furthermore, Diebold et al. observed that upon exposure to O<sub>2</sub> their population decreased as a function of O<sub>2</sub> exposure.<sup>20</sup> This observation along with the fact that oxygen vacancies are known to be healed with O<sub>2</sub> led those authors to conclude that the observed defects were due to oxygen vacancies on the rows of bridge bonded O. Indeed, additional STM investigations have confirmed this allocation of oxygen vacancies, 19, 23, 24 although the interaction of those vacancies with O2 was found to be more complicated. For example Schaub et al. proposed that upon adsorption of O<sub>2</sub> on the vacancy, the molecule dissociated with one atom filling the vacancy while the other formed O2 with an O atom from a neighboring row, thus creating a new vacancy. 19 Du et al. observed three different locations for the second dissociated O atom near the oxygen filled vacancy.<sup>23</sup> The diffusion was not attributed to thermal effects but rather due to transient mobility due to dissociation. A transient mechanism has been proposed for the diffusion of O<sub>2</sub> molecules on the TiO<sub>2</sub>(110) surface at 240 K.<sup>22</sup> According to these authors, electron transfer from donor states of the surface resulted in the formation of charged O<sub>2</sub>. The diffusion of O<sub>2</sub> was attributed to its discharge, while the existence of donor states was allocated to the presence of oxygen vacancies.

Oxygen vacancies are related with another point defect, which is H adatoms. These are thought to originate from  $H_2O^i$  dissociation at oxygen vacancies.<sup>25-27</sup> The proposed mechanism for this dissociation involves first the occupation of one O vacancy by the OH fragment, and secondly the adsorption of H by a bridging oxygen atom of an adjacent row.<sup>25, 27</sup> The two OH pairs formed upon dissociation of  $H_2O$  are believed to be immobile on the surface, but could readily diffuse upon interaction with another  $H_2O$ 

\_

<sup>&</sup>lt;sup>1</sup> H<sub>2</sub>O is always present even in minimal quantities as residual in UHV chambers

molecule.<sup>28</sup> The H adatoms exhibit similar characteristics to oxygen vacancies when imaged with STM, hence their discrimination is often subtle.<sup>29</sup> Suzuki *et al.* identified them by collecting STM images before and after Electron Stimulated Desorption (ESD) tuned for H.<sup>29</sup> Recently, Bikondoa *et al.* managed to differentiate between H adatoms and O vacancies by monitoring their population after H desorption and after H<sub>2</sub>O exposure using STM.<sup>27</sup> They observed that the population of defects allocated to H adatoms increased upon adsorption of H<sub>2</sub>O, indicative of correctly allocating them to H adatoms. To conclude oxygen vacancies, individual OH and OH pairs are expected to be present on the TiO<sub>2</sub>(110) surface.<sup>15</sup>

Another important point defect on the TiO<sub>2</sub>(110) surface is Ti interstitials. These can exist on the surface after sputtering, and during annealing they will diffuse in the bulk to restore the stoichiometry, contrary to O vacancies which stay on the surface. 30 Ab initio calculations have also shown that Ti interstitials are the major diffusing species since their migration barriers are lower compared to the ones for oxygen vacancies.<sup>31</sup> Subsurface Ti interstitials are believed to play an important role in the electronic structure of the surface.<sup>24</sup> Wendt et al. based on STM and PES measurements proposed that these interstitials were responsible for the defect Ti3d state of TiO<sub>2</sub>(110) surface.<sup>24</sup> In addition, they observed that interaction with adsorbed O2 molecules brought the Ti atoms to the surface. A similar phenomenon was observed by Li et al. following the high temperature (500 to 710 K) oxidation of the TiO<sub>2</sub>(110) surface.<sup>32</sup> The Ti interstitials can also be driven to the surface collectively during the reoxidation procedure, thus forming extra rows of Ti on the (110) surface.<sup>33</sup> This phenomenon has serious implications as it can lead to the reconstruction of the surface from (1x1) to (1x2).<sup>34</sup> One model of reconstruction has been proposed by Pang et al. and involves the formation of added rows along the [001] direction the edges of which are terminated by O.35 Another proposed model comprised of the introduction of an added row of Ti<sub>2</sub>O<sub>3</sub> stoichiometry.<sup>36</sup> Bennett et al. observed both structures, albeit modifying the first one.<sup>34</sup>

#### 1.2.3 TiO<sub>2</sub>(110) as Support for Metal Overlayers

Single crystal  $TiO_2(110)$  has been extensively used as a support for metal overlayers as these systems find application in different fields as microelectronics and heterogeneous catalysis. In addition, as evident from the discussion of Sections 1.2.1 and 1.2.2 its surface is well characterised, hence it offers a very good starting point for every research.<sup>5</sup> Furthermore as it is reducable, all the surface science techniques can be employed without charging problems.<sup>2</sup> Over 24 different metals have been deposited on  $TiO_2(110)$ ,<sup>5</sup> and this interest is also reflected in the number of review papers devoting at least a section to the metal/ $TiO_2(110)$  system.<sup>1, 3-5, 7</sup>

Following discussion in Section 1.1 regarding the interaction of metals with metal oxide supports, the interaction of a metal with TiO<sub>2</sub>(110) can be classified by comparing the heat of formation of the deposited metal with that of Ti. But since TiO<sub>2</sub> can be reduced to Ti<sub>2</sub>O<sub>3</sub> or TiO, one should compare these ΔH<sub>f</sub><sup>o</sup> values against the one for the metal. By performing this Diebold has proposed that metals situated on the left hand side of a line that connects Co and Re in the periodic table, should react with TiO<sub>2</sub>(110) and form oxides.<sup>5</sup> Fu and Wagner have proposed another way of categorising the interaction between metals and  $TiO_2(110)$  according to the change of the surface work function,  $\Delta \varphi$ , and this is described below.  $^4$  The change of  $\Delta \varphi$  reflects the position of Fermi levels for metal and oxide before contact, which are indicative of electron flow after contact. The first category involves Cs, K, Na, Ca and Ba, the work function of which is less than 3.0 eV, much smaller that TiO<sub>2</sub>(110) ca 5.2 eV. As a result these are the highest reactive metals with the oxide surface, and upon deposition oxidised layers are expected to form. For example, Grant and Campbell reported the formation of ionic Cs up to ca 0.6 ML coverage,<sup>37</sup> whilst for Ba deposition Li et al. observed that up to 1 ML all Ba was in oxidised form while metallic Ba appeared after 1ML.<sup>38</sup> Recent theoretical calculations of K deposition on thin TiO<sub>2</sub> films have also predicted the formation of K ions upon adsorption.<sup>39</sup> As discussed in Section 1.3.1, this strong interaction between metal and support leads to the formation of layers (2D growth) of the former, as observed for Cs<sup>37</sup> and Ca. 40 The second category contains metals with work function values between 3.75

and 5 eV as Mo, Fe, Cr, V, Ti, Nb, Hf and Al. Redox reactions are expected as well to take place between metal and oxide but not to the extent observed for alkali metals. For example (Section 1.1) Nb forms a thin oxidised layer when deposited on  $TiO_2(110)$ , while See and Bartynski have reported the existence of oxidised phases of FeO and  $Fe_2O_3$  at the interface of  $Fe/TiO_2(110)$ . The third group contains three metals Au, Ag and Cu, whose work function is comparable to  $TiO_2(110)$ , 4.6 eV< $\varphi$ <5.4 eV. As explained in Chapters 3 and 5 little or no interaction takes place between Au or Cu and the  $TiO_2$  surface. Finally the last category includes metals with work function values above 5.4 eV. These are noble metals Pt, Pd, Rh, Ir and Ni. For these metals the opposite electron transfer is observed, from  $TiO_2(110)$  to the metal overlayer. The latter promotes the outward diffusion of Ti interstitials which lead to encapsulation of the overlayer. Indeed encapsulation of Pt,  $^{42}$  Rh,  $^{43}$  and Pd<sup>44</sup> has been observed experimentally when the latter are deposited on  $TiO_2(110)$ .

#### 1.3 Physical Concepts

#### 1.3.1 Growth and Nucleation of Thin Films

As discussed in the previous Section, the growth of metals on metal oxide supports can follow different modes, while this is a general result for the deposition of thin films on any substrate. It is now established that the growth of thin films on various substrates can proceed via three different types of growth. In the first type, Frank-Van der Merwe, the deposition proceeds layer by layer as the deposited atoms are bound stronger to the support that to themselves. The second one, Volmer-Weber, is characterised by the formation of islands of the deposited material, as these atoms bind stronger between one another. Finally, an intermediate type exists, Stranski-Krastanov, where upon completion of the first monolayer, the growth proceeds by forming islands. The latter appears when the Frank-Van der Merwe type is disrupted upon completion of one monolayer due to one or several factors, as for example the inability of the second layer to follow the lattice parameter of the first. Schematically these three growth modes are presented in figure 1-3. Thermodynamically the appearance of each mode can be

understood by taking into consideration the surface free energies of the substrate  $(\gamma_s)$ , the deposited material  $(\gamma_d)$  and the interfacial free energy between them  $(\gamma^*)$ . <sup>47</sup> When  $\gamma_d + \gamma^* \leq \gamma_s$  then the growth follows the Frank-Van der Merwe type, while when  $\gamma_d + \gamma^* \geq \gamma_s$  the Volmer-Weber type is followed. For the third type, Stranski-Krastanov,  $\gamma_d + \gamma^* \leq \gamma_s$  ceases to exist after the first layer is formed.

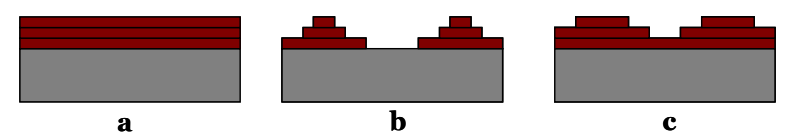


**Figure 1-2** The three different types of growth: (a) layer by layer or Frank-Van der Merwe, (b) island or Volmer-Weber and (c) layer-plus-island or Stranski-Krastanov.

The above approach though is only valid for a perfectly flat surface and it does not take into consideration kinetic processes during growth. For example surface diffusion, binding of atoms, re evaporation, overcoming steps. As a result several models have been developed to explain the procedure as a whole. Procedure as a whole at the initial stages of Cu growth on ZnO(000T), which is against the thermodynamically favoured 3D growth. According to this model when an atom lands on a 2D island, it feels the strong attraction towards the edge which along with the small energy barriers for downstepping, force it to nucleate at the edge. An atom landing on a clean ZnO(000T) site will diffuse until it encounters an island. Then upstepping is kinetically limited as the activation energy for the latter is larger than the thermal energies. These kinetic barriers can be overcome upon annealing, and 3D islands are formed.

#### 1.3.2 Adsorption on Surfaces

Adsorption of a molecule on a solid surface can be classified according to the nature of the bond formed between the two. Consequently, two adsorption forms exist: physical adsorption (physisorption) and chemical adsorption (chemisorption).<sup>48</sup> In the first case, the molecule is attracted to the surface via van der Waals forces, which are weak and

long range. In other words no real chemical bond exists between surface and molecule,  $^{49}$  and the bonding is characterized by a redistribution of electron densities.  $^{50}$  The total interaction potential ( $V_z$ ) as a function of the distance z from the surface, can be described by the following equation:  $^{49}$ 

$$V_{z} = Kn(r) - \frac{C_{v}}{|z - z_{v}|^{3}}$$
 (1-1)

where K is an experimentally derived constant, n(r) the ground state charge density of the surface,  $C_v$  is a constant related with the ability of the surface and molecule to polarise one another and  $z_v$  is a term that defines from where to measure the van der Waals interaction. Figure 1-3 represents calculated physisorption potentials for He adsorption on different surfaces. It is evident that a minimum exists a few Angstroms from the surface.

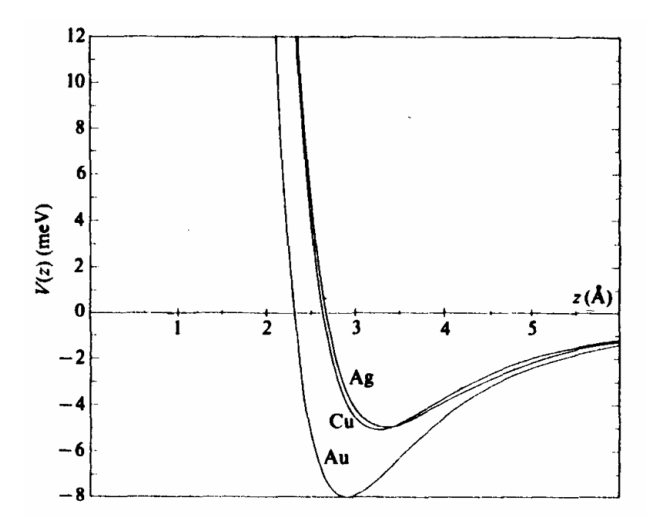


**Figure 1-3** Physical adsorption potential as a function of distance (z) calculated for He near jelium surfaces with noble metal electron densities.<sup>49</sup>

In the second case, chemisorption, a true chemical bond exists between adsorbate and surface. This bond is usually covalent, and much stronger that the van der Waals interaction of physisorption. This is reflected in the enthalpy of adsorption values, as for chemisorption typical values are near 200 kJ per mol whereas for physisorption around 20 kJ per mol. For chemisorption, two separate conditions exist. The first involves the dissociation of the molecule on the surface and the second the associate adsorption. For example,  $O_2$  adsorbs dissociatively, while CO in molecular form. A Lennard-Jones

potential can describe the energy of adsorbate-surface system as a function of their distance, and a schematic of this for the dissociative adsorption of a diatomic molecule (AB) can be found in Figure 1-4. The solid line represents the potential of the system while the dashed lines the potential of the individual atoms and the physisorption potential respectively. It can be observed that as the molecule approaches the surface, the energy of the system lowers and the molecule becomes physically adsorbed, potential well I. This is considered to be a precursor state.<sup>48</sup> Then by overcoming  $E_{\gamma}$  it can chemisorb by dissociation, potential well II. The potential of Figure 1-4 represents a case known as non-activated chemisorption. For an activated chemisorption to occur, the intersection of the two lines must be situated above  $0.^{48}$ 

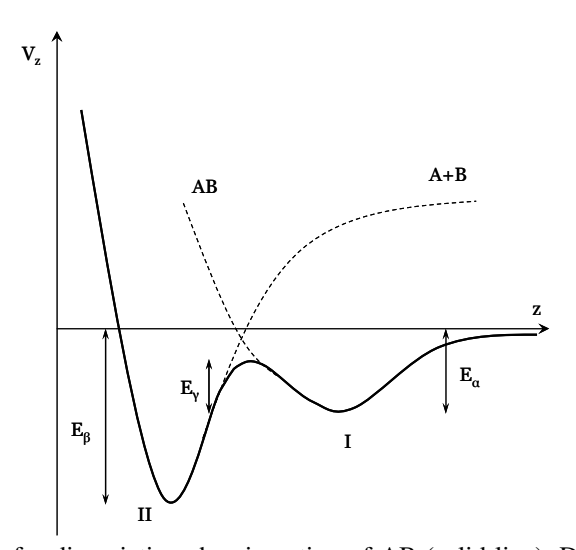


**Figure 1-4** Potential energy for dissociative chemisorption of AB (solid line). Dashed curves represent the potential for physisorption (AB) and individual atoms (A+B). The energy for chemisorption is depicted as  $E_{\beta}$ , whilst for physisorption  $E_{\alpha}$ . Schematic adapted from <sup>49</sup>

#### 1.3.3 Reaction Mechanisms

When a surface acts as a catalyst for any given reaction, then the mechanism of this reaction would follow either one of the following two types. In the simple case of two reactants A and B, the first type involves the reaction of the surface adsorbed reactant A with reactant B which is in the gas phase and is not adsorbed on the surface. This mechanism is called Eley-Rideal, and the reaction rate is proportional of the surface

coverage of A and of the partial pressure of B.<sup>48</sup> The second mechanism involves the reaction of A and B, with both being adsorbed on the surface. This type of mechanism is called Langmuir-Hinshelwood, and the reaction rate is proportional of the surface coverage of A and the surface coverage of B.<sup>48</sup> A schematic of both mechanisms is given in Figure 1-5, obtained from DFT calculations of the CO oxidation catalysed by Au nanoparticles supported in magnesia.<sup>51</sup> In the Eley-Rideal type (a), O<sub>2</sub> preadsorbed on a Au cluster reacts with an incoming CO to form CO<sub>2</sub>. In the Langmuir-Hinshelwood type (b), both molecules are adsorbed on the Au cluster, and react upon encounter to CO<sub>2</sub>. Finally it should be noted that both types should be treated more correctly as the two limits of possible mechanisms.<sup>49</sup>

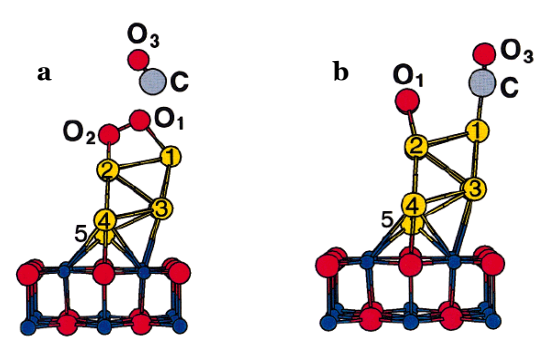


**Figure 1-5** Eley-Rideal (a) and Langmuir-Hinshelwood (b) mechanisms proposed for the CO oxidation catalysed by magnesia supported Au nanoparticles.<sup>51</sup>

### Chapter 2

## **Instrumentation and Experimental Techniques**

#### 2.1 The UHV System

All the experiments presented in this thesis were conducted in a UHV chamber with a base pressure of  $5x10^{-10}$  mbar. Pumping was provided via a Liebold turbo molecular pump (pumping rate 1000 l/s) supported by Edwards E2M12 rotary pump. Additional pumping was also supplied by a Titanium Sublimation Pump (Vacuum Generators) to improve the vacuum and minimise water contamination. The pressure was monitored using an ion gauge from AML. Three surface sensitive techniques were available to use with the chamber: Fourier Transform-Reflection Absorption Infrared Spectroscopy (FT-RAIRS), X-ray Photoelectron Spectroscopy (XPS) and Low Energy Electron Diffraction (LEED). The Fourier transform infrared spectrometer was a 1760x model from Perkin Elmer situated on one side of the chamber. The infrared beam travelled into the chamber and was collected on the opposite side (grazing angle geometry) with the aid of either an Indium Antimonide (InSb) or a Mercury Cadmium Telluride (MCT) detector, coupled to the spectrometer. Both entrance and exit windows were made from KBr. The XPS equipment comprised of an X-ray gun and an analyser. The XPS analyser (Concentric Hemispherical analyser, CHA) and gun (twin Al-Mg anode) were manufactured by Vacuum Generators. The angle between the analyser and the sample was at 15°. Finally the LEED equipment was supplied from Vacuum Science Instruments. Residual gas analysis and leak detection were performed using a quadropole mass spectrometer by Vacuum Generators. An ion gun (Ar<sup>+</sup>) from Ion Tech was also available, used for sample cleaning via the sputtering procedure. The simultaneous or individual dosing of various gases (maximum of three) was achieved using three Varian leak valves attached to a gas manifold. For the deposition of the materials two separate doser configurations were employed, which are presented in detail in the experimental section of relevant chapters. The sample was placed at the tip of a hollow stainless steel tube which was attached on the top of the chamber. Figure 2-1 represents a schematic of the UHV system described above.

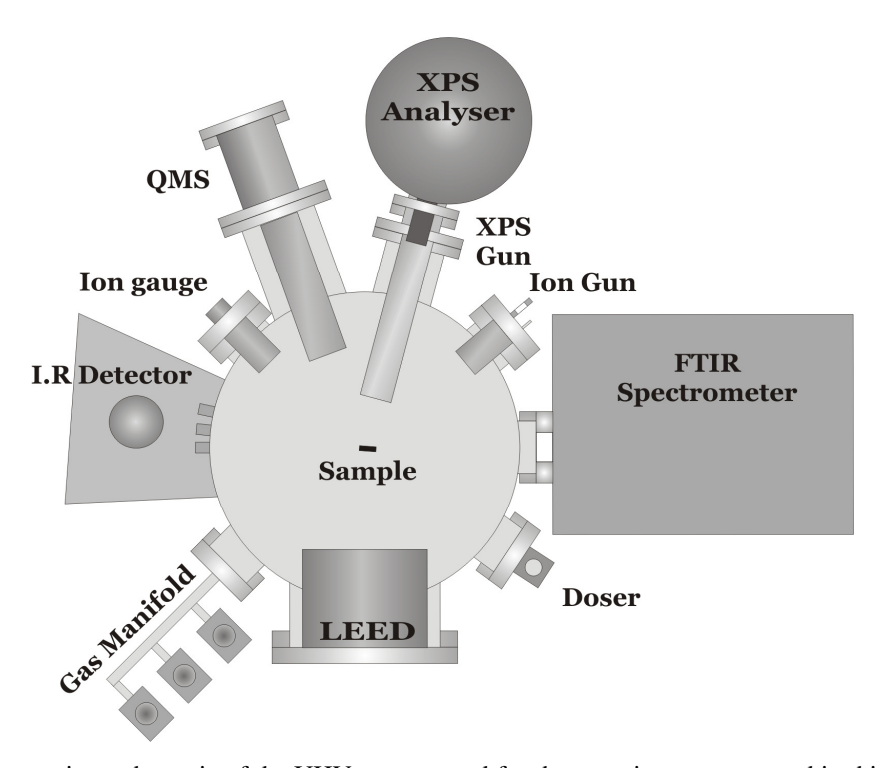


**Figure 2-1** A top view schematic of the UHV system used for the experiments presented in this study. Items not in scale.

#### 2.2 Sample Mounting and Preparation of an Atomically Clean TiO<sub>2</sub>(110) Surface

The TiO<sub>2</sub>(110) single crystal (PI-KEM ltd) was mounted on a homemade housing made from Ta foil. The latter was attached to a Cu block to allow for good thermal conductivity. Resistive heating of the sample was achieved by two W wires (0.25 mm in thickness) directly in contact with the Ta foil, that were spot welded on two Ta bars connected to the Cu block. A schematic of this arrangement can be observed in Figure 2-2. The Cu block was placed at the tip of a hollow stainless steel tube attached to a normal xyz manipulator, able to rotate around the z axis. Cooling of the sample down to 130 K was achieved by filling the hollow tube with Liquid Nitrogen (LN). In order to monitor the temperature of the sample, a K-type thermocouple was spot welded at the side of the Ta

boat. It should be mentioned that placing the thermocouple directly below the crystal was avoided because when once attempted it resulted in cracking of the crystal.

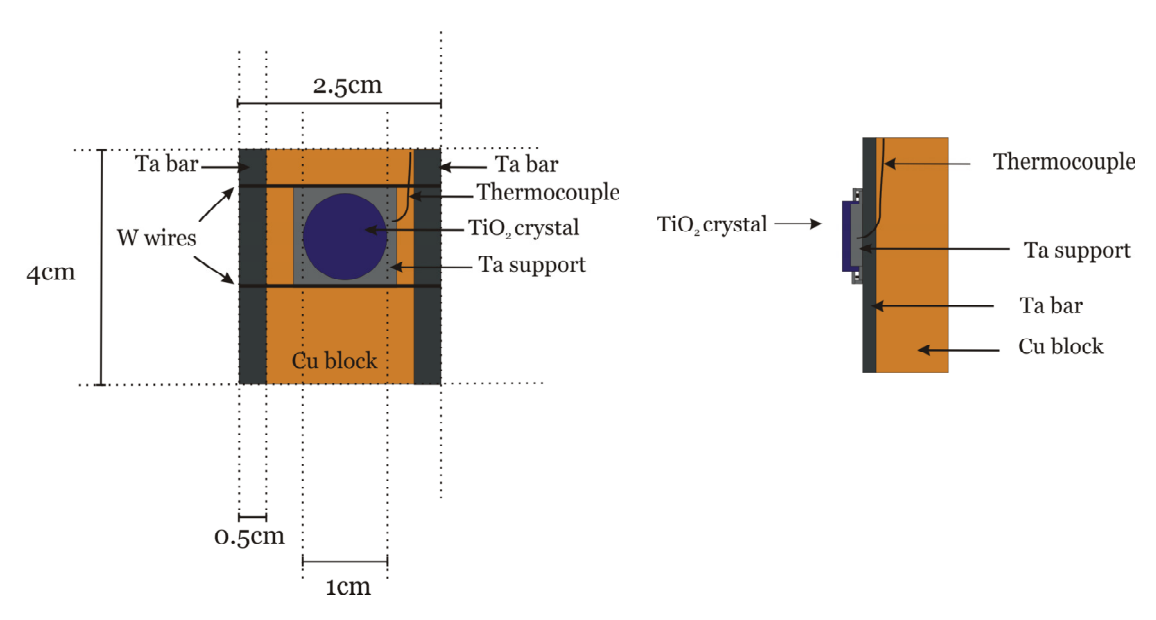


**Figure 2-2** A schematic of the Cu block used for the mounting of the TiO<sub>2</sub> crystal. Notice on the side view that the crystal's surface was above any other part of the holder. This was done to prevent any interference with the infrared beam.

In order to prepare an atomically clean TiO<sub>2</sub>(110) surface, the sample was subjected to repeated cycles of Ar<sup>+</sup> bombardment (2.4 kV, 0.6 mA, 20 min, at grazing angle) followed by thermal annealing at 900 K for 30 min. After the final cycle, oxygen treatment was employed for 5 min at 700 K. At the end of the cleaning procedure an atomically clean TiO<sub>2</sub>(110) surface was achieved. This was verified both by XPS and LEED. Figure 2-3 represents an XPS spectrum of the Ti(2p) energy region immediately after treatment. Both the characteristic Ti(2p<sub>3/2</sub>) and Ti(2p<sub>1/2</sub>) peaks were observable at 458.7 eV and 464.5 eV respectively. Their positions and energy difference of 5.8 eV were in very good agreement with literature values.<sup>52</sup> Spectra collected from the C(1s) region did not reveal any C contamination of the surface. Figure 2-4 represents a picture of the LEED fluorescent screen collected immediately after cleaning the surface. A clear (110)-(1x1) pattern was observable, indicating the presence of long range order.<sup>53</sup> Finally, recent

studies have indicated that annealing the  $TiO_2(110)$  surface in oxygen can cause the appearance of rosette structures which comprise of partially incomplete  $TiO_2$  layers.<sup>5, 21</sup> Hence, the possibility of such structures being present on our surface cannot be excluded. However, their existence can only be monitored using STM, a technique not available in this work.

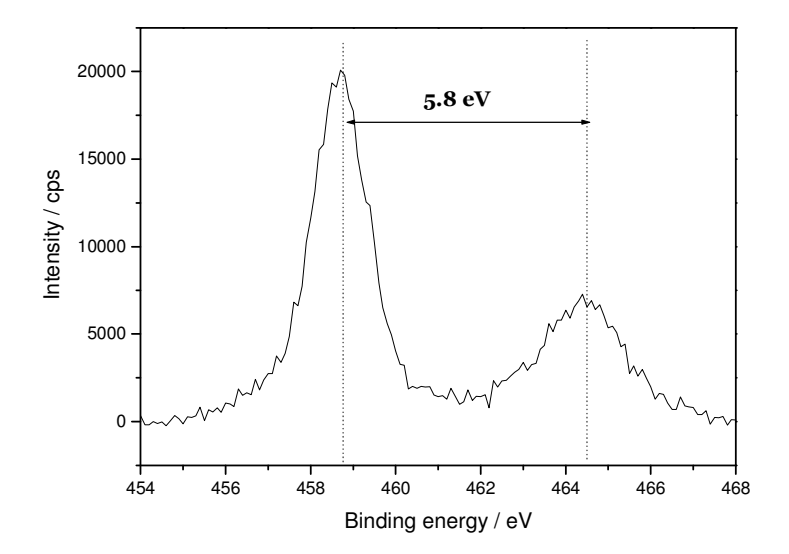


**Figure 2-3** Ti(2p) energy spectrum collected immediately after cleaning treatment. Both  $Ti(2p_{3/2})$  and  $Ti(2p_{1/2})$  peaks were present.

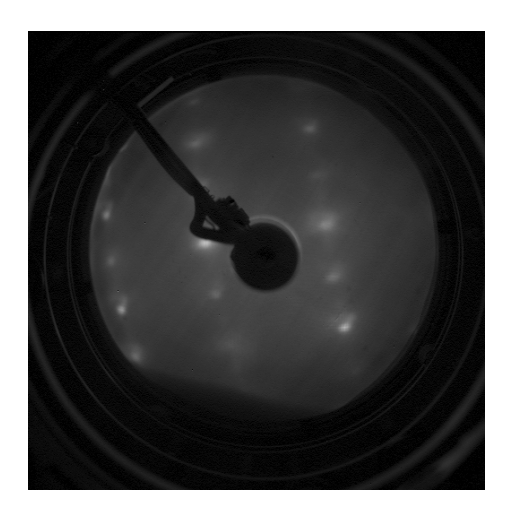


Figure 2-4 LEED picture collected immediately after cleaning treatment. A (110)-(1x1) pattern can be observed due to presence of long range order on the  $TiO_2(110)$  surface.

#### 2.3 Fourier Transform Reflection Absorption InfraRed Spectroscopy (FR-RAIRS)

Over the last 30 years, the FT-RAIRS technique has proven to be a valuable tool for studying surfaces and the molecular processes that take place on them. By examining a FT-RAIRS spectrum, a wealth of information can be obtained that spans from the identification of adsorbates and determination of their chemical environment and molecular symmetry, to the characterisation of the structure and reactivity of a surface. In the following section the theoretical aspects of this technique are going to be discussed with an emphasis shown on oxide and semiconductor supports as these are the relevant ones to this thesis.

#### 2.3.1 Theory

As with every variation of infrared spectroscopy, FT-RAIRS utilises the absorption of radiation that takes place when the electromagnetic field of an infrared beam excites the vibrational modes of a molecule, which in this case is adsorbed on the surface. But rather than collecting the transmitted beam as routinely done in an I.R spectroscopy measurement, the beam reflected off the surface is collected and analysed. A typical geometry of this can be found in Figure 2-5, where one should note that both components of the I.R beam, p and s, can potentially excite the vibrational modes of the adsorbates. In reality though, this strongly depends on the properties of the substrate, i.e. metal, semiconductor or oxide. Finally the quantity that is normally used in FT-RAIRS is that of  $\Delta R/R$  which is defined from equation (2-1) as:

$$\Delta R / R_o = \frac{R_o - R}{R_o} \tag{2-1}$$

where  $R_o$  is the reflectivity of the clean surface and R the reflectivity of the adsorbate covered surface.

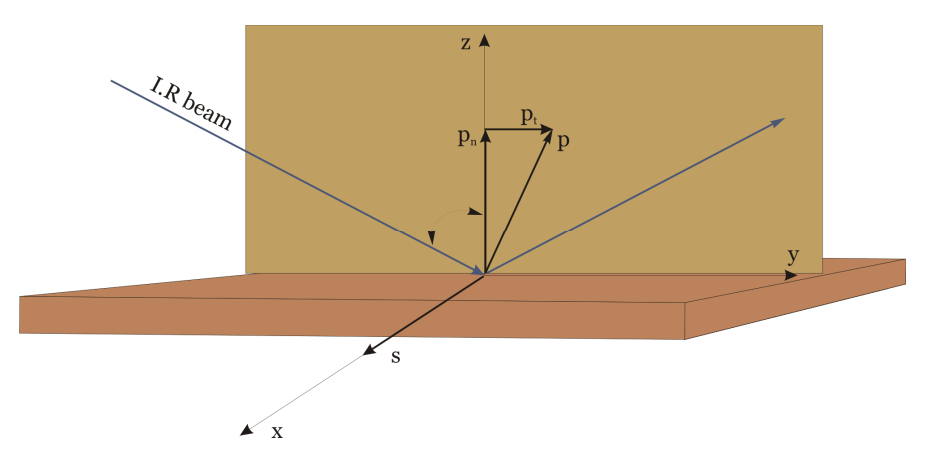


**Figure 2-5** Reflection of infrared light at a surface. Depending on the surface, all components can potentially be infrared active.

#### 2.3.1.1 Metal Support

Historically the RAIRS technique has been developed on well defined metal surfaces. S4-56 The theoretical treatment of these systems has long been established and a short description is going to be presented here, to serve as a basis for the discussion on oxide surfaces. The vibrational dipole of molecules adsorbed on a metallic surface will induce and equal and opposite dipole on the latter, due to the presence of free electrons. As a result the net electric field is going to be zero for vibrations oriented parallel to the surface, and non-zero for vibrations perpendicular to it. Thus the actual surface poses a strict selection rule, which is called the surface selection rule, according to which only light polarised perpendicular to the surface can excite vibrations. More precisely only the p<sub>n</sub> component can be involved in infrared active excitations, as shown in Figure 2.5. Furthermore it has been established that the angle of incidence of the light has to be near 90° (grazing) as this will lead to a greater interaction with the adsorbate. The reason for this is not only the fact that the length travelled by the light is greater but also  $|\vec{p}_n| \cong |\vec{p}|$ . S7

All the above considerations can also be expressed mathematically by using the three layer model, developed by McIntyre and Aspnes.<sup>58</sup> In this model, Figure 2-6, the optical properties of adsorbate film, metal substrate, and vacuum are taken into consideration.<sup>54</sup> More precisely the quantity used is the dielectric constant  $\varepsilon$ , which

expresses the macroscopic response of a solid to electromagnetic radiation.<sup>59</sup> This function is generally complex and can be written as:

$$\mathcal{E}_i = \mathcal{E}_i^{\text{Y}} + i\mathcal{E}_i^{\text{Y}} \tag{2-2}$$

with i=1, 2 and 3 for the substrate, adsorbate layer and vacuum respectively, and  $\epsilon$  and  $\epsilon$  the refractive index and absorption coefficient.

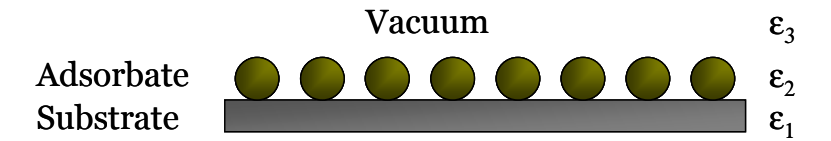


**Figure 2-6** The three layer model: vacuum  $\varepsilon_3$ , adsorbate  $\varepsilon_2$  and substrate  $\varepsilon_1$ 

With the above in mind one can express the change in reflectivity for both p and s components as:

$$\frac{\Delta R_s}{R_s} = \frac{8\pi d}{\lambda} \cos \varphi \operatorname{Im}\left[\frac{\varepsilon_2 - \varepsilon_1}{1 - \varepsilon_1}\right] \tag{2-3}$$

$$\frac{\Delta R_p}{R_p} = \frac{8\pi d}{\lambda} \cos \varphi \operatorname{Im}\left[\frac{\varepsilon_2 - \varepsilon_1}{1 - \varepsilon_1} \frac{1 - (1/\varepsilon_2 \varepsilon_3)(\varepsilon_2 + \varepsilon_3)\sin^2 \vartheta}{1 - (1/\varepsilon_2)(1 + \varepsilon_2)\sin^2 \vartheta}\right] \text{ with } \varepsilon_3 = 1 \qquad (2-4)$$

where d is the thickness of the adsorbate layer,  $\phi$  is the angle of incidence and  $\lambda$  the wavelength of the radiation.

Using Equations (2-3) and (2-4) a simulation has been performed in the literature where the dependence of  $\Delta R/R$  from the angle of incidence can be obtained.<sup>60</sup> These findings are presented in Figure 2-7.

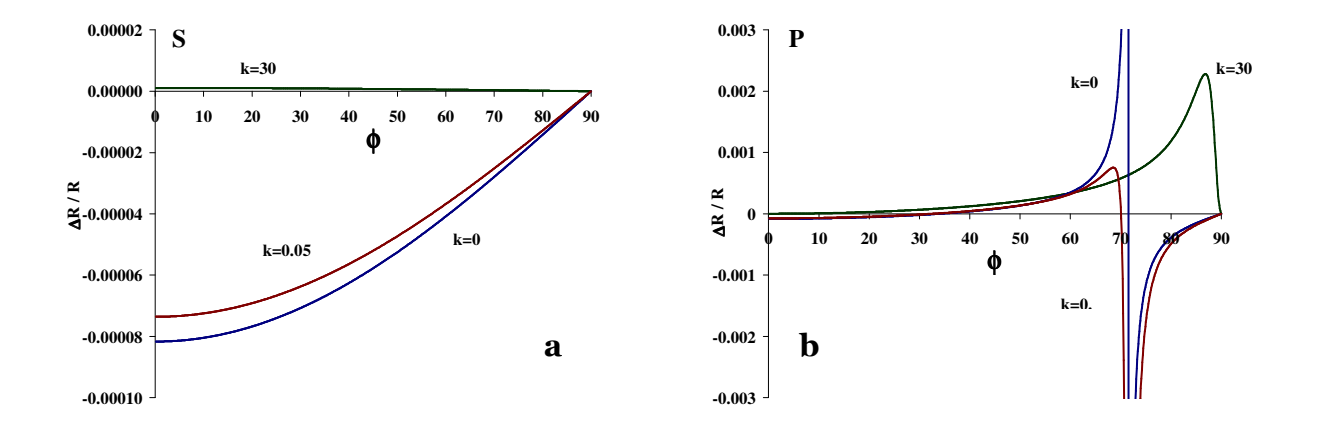


**Figure 2-7**  $\Delta$ R/R as a function of angle of incidence for the s (figure a) and the p (figure b) component of infrared light. With k=30 representing the behaviour of a metal, k=0.05 of an oxide and k=0 of a semiconductor.<sup>60</sup>

It becomes obvious that the change in reflectivity for the s component is almost zero for all the values of  $\phi$ , agreeing with the qualitative approach of the image dipole. As far as the p component is concerned, maximum values appear near 90° highlighting the need for performing RAIRS at grazing angles of incidence. By changing the values for  $\epsilon_1$  similar information can be extracted for an oxide or semiconducting surface, Figure 2-7. For the p component of the radiation, maximum absolute values of  $\Delta R/R$  appear at angles around 70°, which is the Brewster angle  $\phi_B$ . It is noteworthy that depending on which side of  $\phi_B$  the incident angle lays, either a transmission or an absorption band is going to be present on the spectrum<sup>ii</sup>. For the s component a transmission band is predicted, as image dipoles cannot be formed near the surface of these supports. Nevertheless, such an approach does not take into consideration the fact that the p-component of the radiation is actually comprised of two vectors,  $p_n$  and  $p_s$ . For metals this is not important as  $p_s$  will not excite any vibrations as it is parallel to the surface. But for an oxide surface this vector is infrared active, along of course with the s component. Thus a new model has to be used which is going to be presented in the following section.

-

ii Since  $\Delta R = R_{clean surface} - R_{adsorbate covered}$ ,  $\Delta R < 0$  will result in a transmission band and  $\Delta R > 0$  in an absorption band.

#### 2.3.1.2 Semiconducting or Oxide Supports

In order for a model to be able to fully characterise the I.R behaviour of the three layer arrangement, Figure 2-6, it has to include the microscopic characteristics of the adsorbate layer. This has been done by Chabal by separating the x, y and z components of the electric field at the vacuum-substrate interface and assuming a Lorentz oscillator to model the microscopic properties of the adsorbate layer.<sup>59</sup> If it is assumed that for a semiconductor  $\varepsilon_1$  is real and isotropic, the change in reflectivity for each component of the infrared light can be written as:

$$\frac{\Delta R_s}{R_s} = \frac{2\pi v}{\cos \varphi} I_y(\mathcal{E}_y^{\nu} d_y) \tag{2-5}$$

$$\frac{\Delta R_p}{R_p} = \frac{2\pi v}{\cos \varphi} [I_x(\varepsilon_x^{"}d_x + I_z \frac{\varepsilon_1^2}{\varepsilon_z^2 + \varepsilon_z^{"}} (\varepsilon_z^{"}d_z)]$$
 (2-6)

where  $I_{x,y,z}$  are the intensities of the field, as expressed by:

$$I_{x} = \frac{4\cos^{2}\varphi}{1-\varepsilon_{1}} \frac{\left[\left(1/\varepsilon_{1}\right)\sin^{2}\varphi - 1\right]}{\left[\left(\left(1+\varepsilon_{1}\right)/\varepsilon_{1}\right)\sin^{2}\varphi - 1\right]}$$
(2-7)

$$I_{y} = \frac{4\cos^{2}\varphi}{1-\varepsilon_{1}} \tag{2-8}$$

$$I_z = \frac{4\cos^2\varphi}{1 - \varepsilon_1} \frac{(1/\varepsilon_1)\sin^2\varphi}{[((1 + \varepsilon_1)/\varepsilon_1)\sin^2\varphi - 1]}$$
(2-9)

In addition to the above equations, the three components  $(\varepsilon_x, \varepsilon_y, \varepsilon_z)$  of the anisotropic dielectric function of the adsorbate layer have to be expressed in terms of meaningful microscopic quantities. This can be performed by employing a Lorentzian oscillator parameterisation of the adsorbate layer, and then the dielectric function for any vibrational mode will be:

$$\widetilde{\varepsilon}(\omega) = \varepsilon_{\infty} + \frac{\widetilde{\omega}_{p}^{2}}{\widetilde{\omega}_{0}^{2} - \widetilde{\omega}^{2} - i\gamma\widetilde{\omega}}$$
(2-10)

with  $\varepsilon_{\infty}$  the electronic part of the dielectric function,  $\omega_p$  the plasma frequency associated with the adsorbate layer and  $\gamma$  the natural line width of the oscillator.

Thus by employing all of the above a model calculation of  $\Delta R/R$  as a function of wavenumber has been made by Hayden<sup>60</sup> and the results for an angle of incidence of 80° are presented in Figure 2-8.

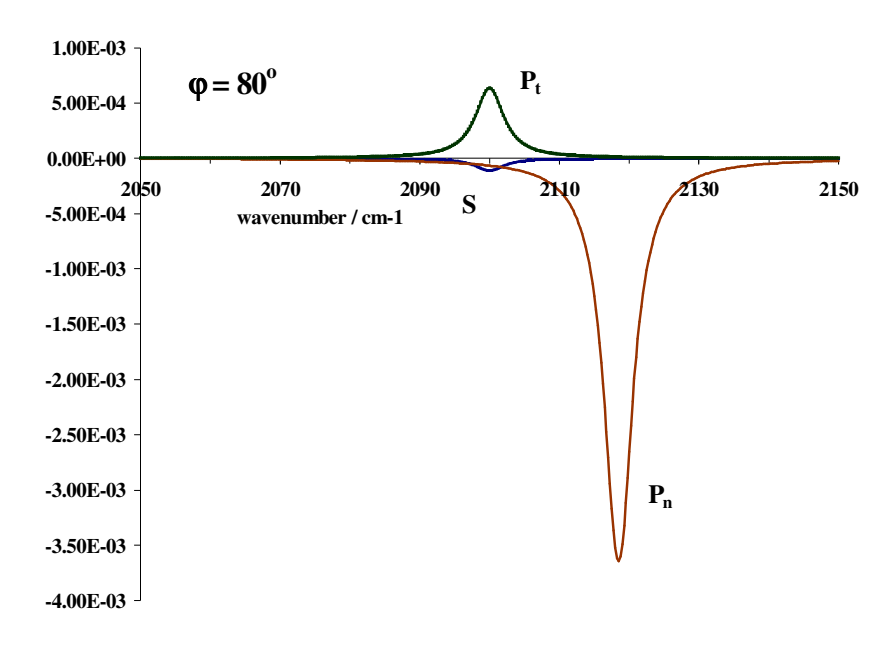


Figure 2-8 Model calculation of  $\Delta R/R$  as a function of wavenumber for all components i.e.  $p_t$ ,  $p_n$  and s. Angle of incidence at  $80^{\circ}$ .

According to this plot, all components of the radiation are infrared active and coupling to them will result in either absorption or transmission bands. More precisely coupling to the  $p_s$  vector (parallel to the surface plane) will lead to an absorption band whereas coupling to the  $p_n$  vector (perpendicular) will lead to a transmission band. The latter is also shifted away form the singleton frequency as a result of dipole coupling along the z direction. Finally a small transmission band is predicted for coupling to the s component of the radiation. Thus contrary to a metal substrate where only perpendicular aligned modes can be studied, conducting RAIRS on a metal oxide or semiconducting support can provide an insight for all the available orientations. This can be extremely

useful in the adsorption studies of both isotropic and oriented molecules as information regarding the adsorption geometry of these systems can be acquired from the RAIRS spectra. 61, 62 Moreover when combined with an azimuthal dependence, the molecular orientation of the adsorbates can be determined. 63-65

#### 2.3.2 Experimental Considerations

Conducting FT-RAIRS on a metal oxide support is extremely difficult as both reflectivity and sensitivity are low. Furthermore the collected spectra can be complex in interpretation as all available modes can be infrared active. In real experimental conditions the correct angle of incidence has to be found that will result in maximum signal. In addition one has to be certain that the infrared beam is only reflected from the metal oxide surface and not from some other part of the manipulator. Thus, in order to calibrate our experimental set up, experiments were undertaken at the beginning of this study where rhodium carbonyl chloride [Rh(CO)<sub>2</sub>Cl]<sub>2</sub> was deposited on the TiO<sub>2</sub>(110) single crystal surface. The behaviour of this system has already been examined and FT-RAIRS spectra of the organometallic molecule adsorbed on the oxide surface are well documented.<sup>61</sup>

[Rh(CO)<sub>2</sub>Cl]<sub>2</sub> (Sigma Aldrich, 97 %) was placed inside a glass vial, attached to a leak valve. The latter was connected to the UHV chamber at the doser position, Figure 2-1. The organometallic was introduced into the chamber through a thin stainless steel tube, its open end situated approximately 15 mm from the sample. During deposition the sample was kept at 130 K. All FT-RAIRS spectra were collected using: a Mercury Cadmium Telluride (MCT) detector; a p polarised light; a spectral resolution of 4 cm<sup>-1</sup>, 200 scans, in the spectral region from 2200 to 1900 cm<sup>-1</sup>.

Figure 2-9 represents the spectra collected from the deposition of [Rh(CO)<sub>2</sub>Cl]<sub>2</sub> as a function of exposure. Following the initial two exposures, up to 4.78 L, no bands were observable on FT-RAIRS spectra. Nevertheless after 8.2 L features started to emerge around 2100 and 2050 cm<sup>-1</sup>. These grew into well distinguished infrared peaks after 11.62

L of [Rh(CO)<sub>2</sub>Cl]<sub>2</sub>. More precisely three transmission bands were observable at 2108, 2094 and 2048 cm<sup>-1</sup> respectively whereas an absorption band was evident at 2087 cm<sup>-1</sup>. The intensity of bands grew upon further exposure of the molecule but their position remained unchanged. Upon comparing these results with previously published data by Evans *et al.*,<sup>61</sup> a very good agreement was observed. This comparison, along with the identification of the bands, can be found in Table 2-1. Finally it is noteworthy that both transmission and absorption bands were observable as predicted by the theory.

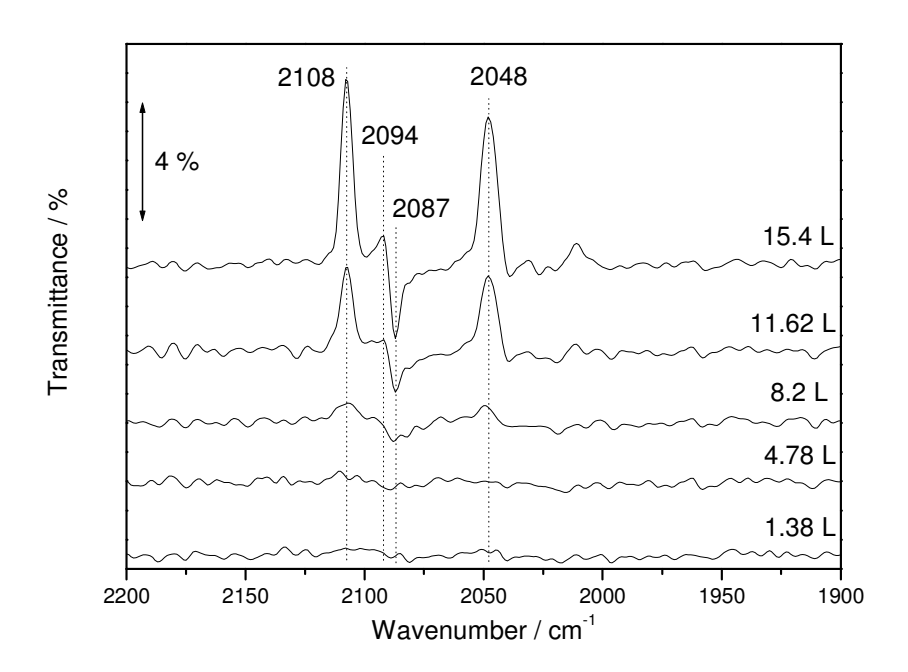


**Figure 2-9** FT-RAIRS spectra of the  $TiO_2(110)$  surface as a function of  $[Rh(CO)_2Cl]_2$  exposure in Langmuir (L).

**Table 2-1** Assignment of the observable bands, along with a comparison with previously published results.

Vibrational mode	This study / (cm <sup>-1</sup> )	Observed by Evans <i>et al.</i> / (cm <sup>-1</sup> )
A1	2108	2108
B1	2094	2094
B1	2086	2087
B2	2048	2050

Approximately at the midpoint of this study some important repairs had to be conducted on the manipulator which supported the TiO<sub>2</sub> single crystal. As a result the optimum position for conducting FT-RAIRS had to be obtained once again. Bearing in mind that one part of this study would involve the investigation of Cu particles and films deposited on the metal oxide crystal, it was chosen to use a Cu (110) single crystal in order to regain the optimum position.

Prior to loading the Cu(110) single crystal on the manipulator, the latter was polished with alumina paste of varying size (5 , 1 and 0.05 μm particles respectively). Once inside the UHV chamber the crystal was cleaned by repeated cycles of sputtering (5 min, 1.8 kV, 0.6 mA) and annealing (25 min at 673 K).<sup>66</sup> In order to test the alignment of the FT-RAIRS set up, CO adsorption studies were performed at 130K on Cu(110) surface. FT-RAIRS spectra were collected using: an Indium Antimony (InSb) detector, a p polarised light; a spectral resolution of 4 cm<sup>-1</sup>, 100 scans, in the spectral region from 2200 to 1900 cm<sup>-1</sup>.

Figure 2-10 represents spectra collected after exposing the Cu(110) crystal to 3 L of CO. The spectrum collected from the bare surface is also shown as a reference. A sharp single peak situated at 2094 cm<sup>-1</sup> was observable which can be attributed to the v(C-O) mode, in accordance with Pritchard *et al.* <sup>67</sup> It should also be noted that only absorption peaks were observable which is in agreement with the theory presented in the previous section. Some studies were also performed where prior to any CO dosing, the Cu(110) surface was exposed to 15L of O<sub>2</sub> at 400 K. On the inset of Figure 2.10 the FT-RAIRS spectrum of v(C-O) is presented for O<sub>2</sub> covered surface. The presence of O<sub>2</sub> altered the appearance of the spectrum, with two bands emerging at 2106 and 2070 cm<sup>-1</sup>, probably due to CO adsorbing on two different sites. <sup>68</sup>

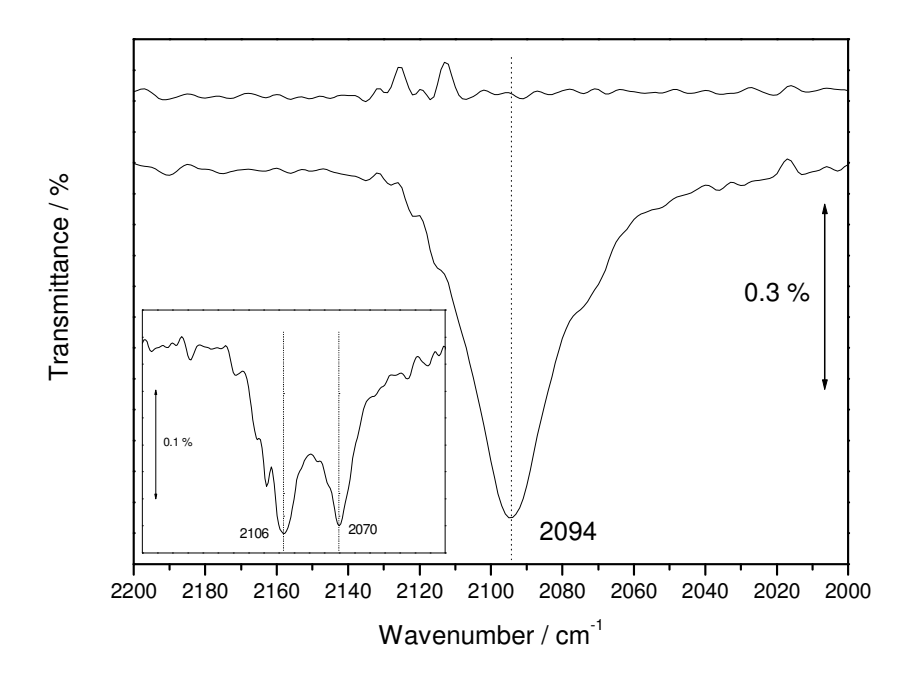


**Figure 2-10** FT-RAIRS spectra collected before (top) and after (bottom) the Cu(110) single crystal was exposed to 3L of CO. Inset: FT-RAIRS spectrum after exposing the O<sub>2</sub> covered surface to 3L of CO.

#### 2.4 X-ray Photoelectron Spectroscopy (XPS)

#### 2.4.1 Theory

X-ray Photoelectron Spectroscopy has been routinely used since its development in the early 60s by Siegbahn, to study the elemental composition and chemical state of surfaces. As a consequence it is also know as Electron Spectroscopy for Chemical Analysis, a term not commonly used nowadays due to the existence of a variety of techniques with the same objective.<sup>69</sup> The fundamental principal behind XPS lies with the photoelectron effect as explained by Albert Einstein (Nobel prize in Physics, 1921). According to the photoelectron effect, photons of suitable energy can excite electrons of occupied states of a solid and as a result escape the material with a certain kinetic energy. A simple mathematical expression describes this phenomenon:<sup>50</sup>

$$h\nu = E_{kin} + E_b + \Phi \tag{2-11}$$

where hv is the energy of incoming photons,  $E_{kin}$  the kinetic energy of photoelectrons,  $E_b$  the binding energy of photoelectrons and  $\Phi$  the work function of the material. A schematic representation of the process can be found in Figure 2-11.

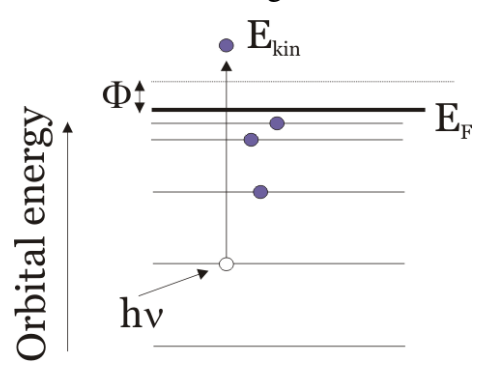


Figure 2-11 The photoelectric phenomenon

According to Equation (2-11) if hv,  $E_{kin}$  and  $\Phi$  are known quantities then the binding energy of the photoelectrons, thus the electronic configuration of the material, can be obtained. In an XPS experimental set up the energy of incoming photons is known as they are produced from a soft x-ray source which is usually either Al- $K_a$  (hv=1486.6 eV) or Mg- $K_a$  (hv=1253.6 eV). The kinetic energy of the photoelectrons can be measured using an electrostatic deflection analyser, which can selectively allow electrons of only certain energy to pass through it by applying an electrostatic field. Thus by knowing also  $\Phi$ , the binding energy of the excited photoelectrons can be calculated. Because of the energy value of the x-rays used, the information acquired from an XPS spectrum is related with the core electrons of the material. As the energy configuration of these is unique for each element, an elemental analysis can be performed. Of course information regarding the valence band can also be obtained but this energy region near the Fermi level is better studied using Ultraviolet Photoelectron Spectroscopy.

Although in theory Equation (2-11) contains all the required information in order to understand a XPS spectrum, in reality some of the features present in a spectrum cannot be explained by it. The reason for this is the fact that Equation (2-11) is only an approximation. This approximation follows Koopmans theorem according to which: 'for a closed shell molecule the ionisation energy of an electron in a particular orbital is approximately equal to the negative of the orbital energy calculated by a self consistent

field method'. According to the above the excitation of a photoelectron does not affect the electronic state of its environment and hence the binding energy measured should be equal to the real binding energy of the electron. In reality this is not true because as soon as a hole is created by the photoelectron some of the electrons are going to relax to lower energy state in order to screen it. Consequently, the energy of the outgoing photoelectron is going to be affected by this process and will appear shifted from the expected one. These shifts are known as final state effects since they originate from the photoelectric excitation. On the other hand, shifts that originate from a change of the chemical environment are known as initial state effects or 'true' chemical shifts. <sup>69,71</sup> Due to these an identification of different chemical states, i.e. oxidised or reduced species can be made.

To conclude, it is important to explain why XPS is a surface sensitive technique. When photoelectrons or electrons in general, travel through a material they can lose their energy due to various phenomena such as plasmon scattering, single particle electron excitations involving valence electrons and ionisation of core levels of the atoms. Seah and Dench have presented a collection of both theoretical and experimental findings upon which the distance covered by an electron before losing its energy is calculated for various materials. This distance is known as the Inelastic Mean Free Path (IMFP) and its value as a function of the energy (above the Fermi level) of the electrons can be found in Figure 2-12.

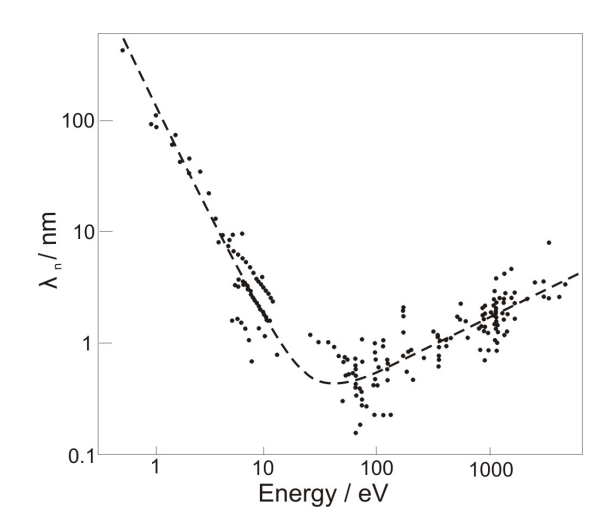


Figure 2-12 The IMFP in nanometres as a function of electron energy for a wide selection of elements, redrawn from  $^{72}$ 

A minimum in the IMFP at around 0.5 to 1 nm, is observed in the energy region between 50 and 1000 eV. Thus as photoelectrons produced by soft x-rays typical have values in this range, XPS is a strictly surface sensitive technique. Seah and Dench have also presented an equation that best describes the trend observed in Figure 2-12:

$$\lambda_m = \frac{538}{E^2} + 0.41(aE)^{1/2} \tag{2-12}$$

where  $\lambda_m$  is the IMFP in monolayers, E is the energy of the electrons above the Fermi level in electronvolts and a is the monolayer thickness in nanometres which can be defined as:

$$a = \sqrt[3]{\frac{A}{\rho nN} \times 10^{24}}$$
 (2-13)

where A is the atomic or molecular weight, n is the number of atoms in the molecule, N is the Avogadro's number and  $\rho$  is the bulk density in kg per m<sup>3</sup>.

#### 2.4.2 Quantification of Spectra

Although the main objective of XPS is to provide an insight in the elemental composition and chemical state of surfaces, quantified information can also be extracted from a photoelectron spectrum. Seah has provided a way of calculating either the fractional monolayer coverage of an adsorbate on a surface or the thickness of an overlayer adsorbed on the surface. This method is widely used in the literature and it is the one used throughout this thesis for the calculation of coverage values. When a substrate B is covered by a fractional monolayer  $\phi_A$  of A, the detected signal of B,  $I_B$ , is constituted by two parts. One is due to the covered area (attenuated signal) and one due to the adsorbate free surface (unattenuated signal). This leads to the expression:

$$I_B = I_B^{\infty} [1 - \varphi_A + \varphi_A \exp(-\frac{a_A}{\lambda_A \cos \vartheta})]$$
 (2-14)

where  $a_A$  is defined in equation (2-13),  $\lambda_A = 0.41 a_A^{1.5} E_A^{0.5}$  (an approximation of Equation (2-12) with  $\lambda$  in nanometres),  $\theta$  is the angle of emission, and  $I_B^{\infty}$  is the signal from pure B. Values of  $I_X^{\infty}$  in general are used to calibrate the measured intensity  $I_X$  and they are also known as Atomic Sensitivity Factors.

The intensity of the signal due to the adsorbate can be defined as:

$$I_{A} = \varphi_{A} I_{A}^{\infty} [1 - \exp(-\frac{a_{A}}{\lambda_{A} \cos \vartheta})]$$
 (2-15)

By combining Equations (2-14) and (2-15) and assuming high electron energies and small coverage values,  $\phi_A$  can be written as

$$\varphi_{A} = \frac{\lambda_{A} \cos \vartheta}{a_{A}} \cdot \frac{I_{A}/I_{A}^{\infty}}{I_{B}/I_{B}^{\infty}}$$
 (2-16)

This equation is used for the calculation of submonolayer coverages. For coverages above 1 ML this equation is not accurate and the following has to be used.

The intensity of an adsorbate covered substrate B can be defined as:

$$I_B = I_B^{\infty} \exp\left[-\frac{d_A}{\lambda_A \cos \vartheta}\right] \tag{2-17}$$

where  $d_A$  is the thickness in nm of the adsorbate layer. The intensity of the latter can be expressed as:

$$I_A = I_A^{\infty} [1 - \exp(-\frac{d_A}{\lambda_A \cos \vartheta})]$$
 (2-18)

By combining equations (2-17) and (2-18) and solving for d<sub>A</sub> the following is produced:

$$d_A = -\lambda_A \cos \vartheta \ln(\frac{I_A^{\infty} \cdot I_B}{I_A I_B^{\infty} + I_A^{\infty} I_B})$$
 (2-19)

With equation (2-19) the thickness of the film can be calculated. The coverage in ML can then be calculated by dividing by the atom size.

It should be noted that application of these equations typically provides results with errors of the order of 15-20 %.<sup>74</sup> This is because they are based on the measurement of the intensity of the peaks, (or areas)<sup>74</sup> which can be difficult to estimate. Furthermore the use of the atomic sensitivity factors contributes towards the error as they also contain some degree of uncertainty.

### 2.5 Low Energy Electron Diffraction (LEED)

Information regarding the structure of surfaces and their adsorbates is extremely valuable, as the physical properties of these systems can be better understood. Low Energy Electron Diffraction is a surface science technique that can readily provide such structural information. Historically the first experiments demonstrating this technique were conducted by Davisson and Germer (1927), with which they famously proven the wave nature of electrons.<sup>75</sup> It started to be routinely used throughout in the early 60s as a consequence of the development of UHV technology. A description of the basic principles of LEED is given below.

At 1924 de Broglie discovered the wave nature of electrons, which as mentioned before was confirmed experimentally by Davisson and Germer. According to de Broglie the wavelength ( $\lambda$ ) of a moving electron, or of a beam of monoenergetic electrons, can be defined from the following equation:

$$\lambda = \frac{h}{p} = \frac{h}{\sqrt{2mE}} \tag{2-20}$$

where h is Planck's constant and p, m, and E the momentum, mass and energy of the electron. With the correct use of units, equation (2-20) can be rewritten as:

$$\lambda = \sqrt{\frac{150}{E}} \tag{2-21}$$

where E is in electronvolts (eV) and  $\lambda$  in Angstroms (Å).

According to Equation (2-21), the wavelength value of electrons with energies between 10 to 500 eV will vary between 3.9 to 0.64Å, respectively. These values are smaller or equal to the interatomic distances of most crystalline materials. As a result, the atoms of the materials can act as diffraction centres for the electrons, in the same manner that diffraction gratings act for light. In LEED the surface under study is bombarded with a monoenergetic beam of low energy electrons, Figure 2-13. When these reach the surface, they are scattered from surface atoms. But only elastically scattered electrons interfere constructively and produce diffraction patterns. These are formed on a fluorescent screen situated in front of the sample, in a geometry that allows only elastically backscattered electrons to be collected. Of course not all electrons are elastically backscattered, and in order to prevent inelastic electrons from reaching the screen a set of grids are placed in front of the latter and set at a potential that filters these electrons out. The diffraction pattern formed on the fluorescent screen is a representation of the reciprocal lattice of the material, which is directly related to the real space crystal lattice.

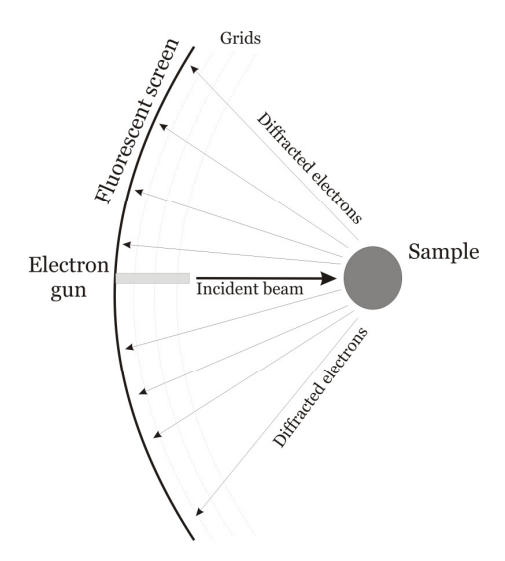


**Figure 2-13** A schematic of LEED experimental set up. The incident beam of electrons is diffracted back by the surface of the sample, and the diffracted electrons form the LEED pattern on the fluorescent screen. In front of the latter, a set of grids is placed to filter out inelastically scattered electrons.

The diffraction of electrons from crystalline solids and their surfaces follows the same rules as x-ray diffraction. In order to describe it, it is useful to introduce Figure 2-14 where we assume that a beam of X-rays is scattered from two lattice points A and B. These are connected with a translation vector of the real lattice  $\vec{R} = n_1 \vec{a} + n_2 \vec{b} + n_3 \vec{c}$ . The incident beam's direction is  $\hat{n}$ , while its wavelength is  $\lambda$  and its wavenumber vector is  $\vec{k} = \frac{2\pi}{\lambda} \hat{n}$ . A necessary condition for the diffraction to take place is that x-rays (or electrons) have to be elastically scattered from the surface. As a result the scattered beam will have the same wavelength but the wavenumber vector  $\vec{k}$  is going to lie in a different direction  $\hat{n}$ , such that  $\vec{k}' = \frac{2\pi}{\lambda} \hat{n}'$ .

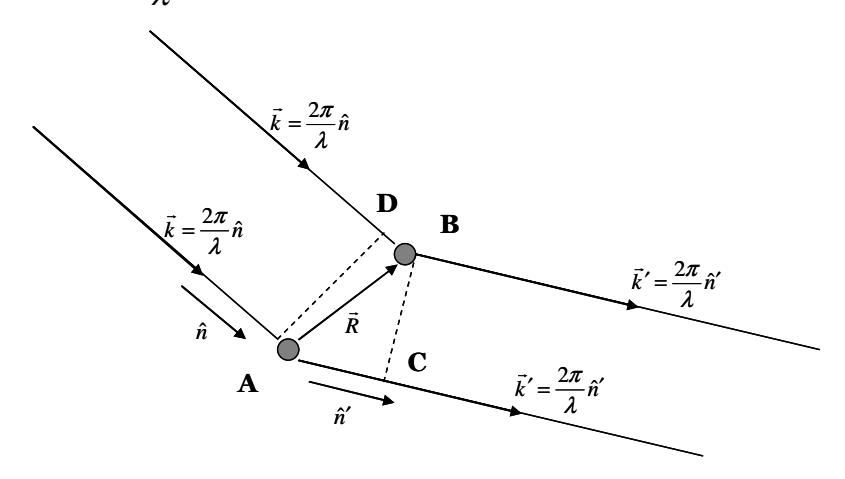


Figure 2-14 A simple geometrical model to explain the diffraction of x-rays from a crystal.

From Figure 2-14 one can determine that the difference ( $\Delta$ ) in the path length covered by the incident and scattered beams will be:

$$\Delta = AC - BD = \vec{R} \cdot \hat{n}' - \vec{R} \cdot \hat{n} = \vec{R} \cdot (\hat{n}' - \hat{n})$$
 (2-22)

The latter has to be an integer number or wavelengths, thus

$$\vec{R} \cdot (\hat{n}' - \hat{n}) = n\lambda \tag{2-23}$$

Using the definitions of  $\vec{k}'$  and  $\vec{k}$ , equation (23) can be rewritten as

$$\frac{\lambda}{2\pi}\vec{R}(\vec{k}' - \vec{k}) = n\lambda \Leftrightarrow$$

$$\vec{R}(\vec{k}' - \vec{k}) = 2\pi n$$
(2-24)

The latter can also be expressed as

$$e^{i\vec{R}(\vec{k}'-\vec{k})} = 1 \tag{2-25}$$

But according to the definition of the reciprocal lattice

$$e^{i\vec{G}\vec{R}} = 1 \tag{2-26}$$

where  $\vec{G} = h\vec{a}' + k\vec{b}' + l\vec{c}'$  the translational vector of the reciprocal lattice.

By equating equations (2-25) and (2-26), the definition of x-ray (or electrons) diffraction from a solid as given by Laue can be reached which is *that in order for constructive* interference to take place between the scattered beams the change of the wavenumber vector should be equal to a vector of the reciprocal lattice, or

$$\Delta \vec{k} = \vec{k}' - \vec{k} = \vec{G} \tag{2-27}$$

According to Equation (2-27), the direction of the scattered beams is determined by the vector of the reciprocal lattice. As these directions intersect the fluorescent LEED screen they give rise to diffraction spots. Thus these diffraction spots are a direct representation of the reciprocal lattice of the surface.<sup>78</sup>

#### 2.6 Physical Vapour Deposition (PVD)

The term Physical Vapour Deposition (PVD) is used to describe a variety of techniques that result in the formation of nanoparticles or films on various substrates. The main physical process behind any PVD technique lies with the vaporisation of any given material. As the latter is vaporised in the form of atoms or molecules, its vapours travel towards the substrate where they condense and form the film. The two main factors that differentiate the various techniques are the environment in which the deposition takes place, i.e. vacuum or low pressure gas or plasma, and the method of vaporisation of the material. As a result three main categories exist: vacuum deposition or evaporation, sputter deposition and ion planting.<sup>79</sup> Vacuum evaporation was the PVD technique used in this thesis, and consequently is described in more detail.

In vacuum evaporation the vapour atoms do not undergo any collisions with any residual gas prior to condensing on the sample. As a result these depositions have to take

place under UHV conditions. More importantly though, the transition from liquid (evaporation) or solid (sublimation) phase to vapour<sup>iii</sup> is thermally activated.<sup>79</sup> Consequently the important factor controlling the deposition is the temperature of the source that contains the material. As it can be seen in Figure 2-15, the vapour pressure of any given element strongly depends on temperature. Good deposition rates can be achieved with vapour pressure values above 10<sup>-4</sup> Torr. Thus for most materials this involves temperatures well above room temperature. In order for these temperatures to be reached, the source is heated using various methods that span from electron and laser beams to resistively heated configurations.<sup>80</sup> Such a configuration was also used in this study, and its details are presented in Chapter 3.

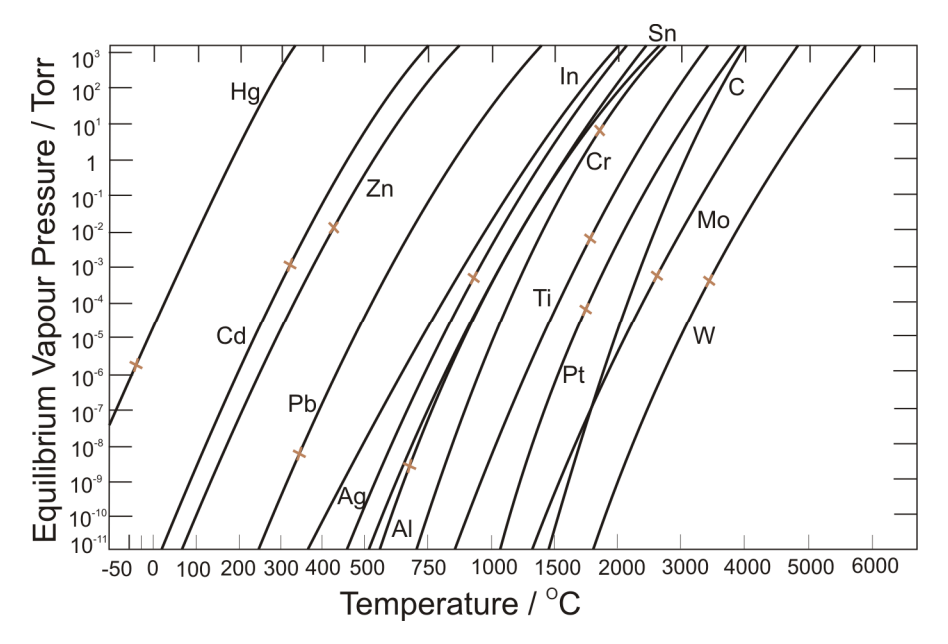


**Figure 2-15** The vapour pressure of different elements as a function of temperature, redrawn from  $^{79}$  The symbol x marks the melting point value.

## 2.7 Organometallic Chemical Vapour Deposition (OMCVD)

Chemical Vapour Deposition (CVD) is an alternative process to PVD for preparing thin solid films, coatings and nanoparticles. These are formed from the gaseous

 $<sup>^{\</sup>rm iii}$  process which will eventually lead to the formation of a film.

phase by a chemical reaction or dissociation.<sup>81</sup> In most cases these gaseous reactants are first activated by heat, light or plasma followed by the formation of a stable solid product.<sup>82</sup> These processes can be either homogeneous or heterogeneous, while a simple schematic of them can be found in Figure 2-16. Depending on the source that provides the energy for the reaction or dissociation of the precursors, CVD processes can be categorised into: thermal, plasma enhanced, photo assisted, laser induced, electron beam assisted, ion beam assisted and scanning tunnelling microscopy CVD.<sup>83</sup>

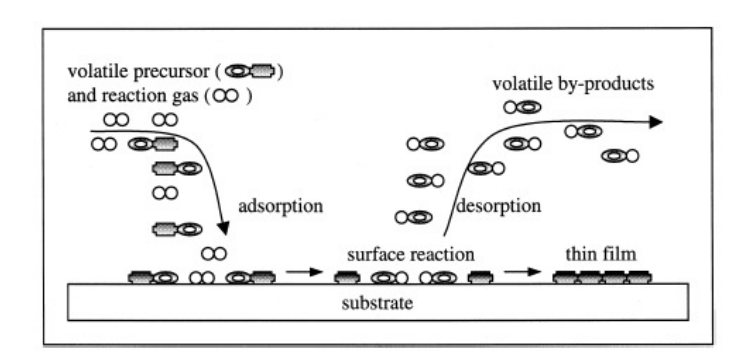


**Figure 2-16** The formation of a thin film using CVD. The precursors can either decompose on the surface or in the gas phase. The by-products of the reactions have to be volatile in order to be removed from the film.<sup>83</sup>

CVD processes can also be distinguished with respect to the precursors used. When the latter is an organometallic compound the process is called Organometallic Chemical Vapour Deposition (OMCVD)<sup>iv</sup>. <sup>82</sup> A variety of materials can be synthesised using this method such as semiconductors, metallic and dielectric films in crystalline or amorphous phase. These find applications in many technological areas such as solar cells, optical memory and information recording systems and optical communications to name but a few from a long list. <sup>84</sup>

An important property of the organometallic compounds used in OMCVD is their volatility. This property defines how easy they can vaporise, and subsequently transported, in the gas phase, to the substrate. The vapour pressure of organometallic compounds is related with temperature according to the following expression<sup>83</sup>:

-

<sup>&</sup>lt;sup>iv</sup> This technique is historically known as Metalorganic Chemical Vapour Deposition (MOCVD) but in accordance with the exact definition of the precursors used, the term currently used is OMCVD.

$$\log(p) = \frac{B - A}{RT}$$

where p is the pressure in Torr, A and B are pressure constants, R is the gas constant and T is the temperature in K.

As a result certain compounds need to be at elevated temperatures during deposition, although this was not the case with the organometallics used in this study except for [Rh(CO)<sub>2</sub>Cl]<sub>2</sub> in section 2.3.2.

OMCVD has recently found a new application, the deposition of ultra-thin films or nanoparticles on to various substrates. During such a process the chemical and physical properties of the surface play an important role in the adsorption and nucleation of the organometallic as shown for Mo(CO)<sub>6</sub> on alumina, [Rh(CO)<sub>2</sub>Cl]<sub>2</sub> on alumina or titania or [PtMe<sub>2</sub>(COD)] on HOPG.<sup>85</sup> To conclude, it should be noted that all the studies performed during this work both for Mo(CO)<sub>6</sub> and (CH<sub>3</sub>)<sub>2</sub>Au(acac) were investigated with this application in mind.

## **Chapter 3**

# TiO<sub>2</sub>(110) Supported Cu Particles and Films

#### 3.1 Introduction

#### 3.1.1 PVD of TiO<sub>2</sub>(110) Supported Cu Particles and Films

The growth mode of Cu on the  $TiO_2(110)$  surface has been the subject of several investigations, with contradicting results. According to the studies of Møller and Wu, the growth of Cu overlayers follows a Stranski-Krastanov (SK) mode.<sup>53</sup> This conclusion was drawn from a combination of LEED and Auger Electron Spectroscopy (AES) measurements. Nakajima et. al. agreed with the above, assigning a break in the evolution of the Cu(3d) photoemission intensity as a function of coverage to the formation of the first monolayer.<sup>86</sup> On the contrary, Low Energy Ion Scattering (LEIS) experiments have indicated that the growth of Cu on the oxide surface proceeds via a Volmer-Weber (VW) mode.<sup>87</sup> It should be noted that LEIS is sensitive to the top most layer of the surface, thus probably more reliable in elucidating growth modes. Characteristics of 3-D growth were also observed in TEM studies.<sup>88</sup> In addition, the presence of 3D islands was evident in Scanning Tunnelling Microscopy (STM) measurements performed during growth. 89 2-D islands were also observed, but these were quickly transformed in 3D before covering the surface. An indication as to which mode is adopted could lie with the interaction between metal and support. For example Cr ( and Fe to a lesser extent) which interacts strongly with the support, has been found to completely wet the surface. 90, 91 On the other hand, the interaction of Cu with TiO2 is weak as indicated by atomically abrupt interfaces imaged in TEM, 92 and by UPS and Inverse Photoemission Spectroscopy (IPS) measurements which did not reveal any Cu oxidation.<sup>41</sup>

Another interesting topic is the location of Cu nucleation sites on the  $TiO_2$  surface. Surface X-ray Diffraction (SXRD) measurements of Cu overlayers on  $TiO_2(110)$  have revealed that at the interface O atoms of the surface were displaced up to 0.06 nm

while no change was observed for the Ti ones.<sup>93</sup> This result clearly suggested the formation of a Cu-O bond. The same conclusion was reached following Density Functional Theory (DFT) calculations, with Cu bonding preferentially on top of bridging oxygen sites, 94 along the [001] direction. 95 Indeed Cu atoms of the first layer have been found to form between the characteristic protruding O rows, located along [001] direction, of the TiO<sub>2</sub> surface. 96 In addition along this direction an incommensurate growth was observed, whilst along the [170] direction commensurate growth predominated. 97 On the other hand, recent STM studies following the initial stages of growth, less than 0.5 ML of Cu, have revealed that more that 70 % of Cu islands resided in step edges. 89 Another interesting feature originating from this investigation was the appearance of a self limiting growth mode. At these low coverages, only the density of Cu islands appeared to increase and not their size. Two possible explanations were given, a rejection mechanism due to strain fields developing around Cu clusters, or preferential nucleation into new islands rather than on existing ones. For higher coverage values, above 7ML, it has been found that Cu clusters exhibited surface characteristics of the Cu(111) plane but with minority sites resembling Cu(110).98 Cu films have been found to exhibit fcc(111) patterns,99 while an epitaxial relation was observed to exist with TiO<sub>2</sub>.88

Upon annealing Cu overlayers to temperatures higher than ca. 570 K, the general trend observed is in accordance with the coalescence of smaller particles into larger ones. 41, 87 Further details are going to be given regarding these processes in the results section. The effect of higher temperatures has also been examined during growth. Wagner *et al.* reported that the deposition of Cu on TiO<sub>2</sub>(110) at 473 K resulted in the formation of large (40 nm in width) (111) faceted islands. 100 Deposition at temperatures higher than 773 K resulted in the formation of CuO and Cu<sub>2</sub>O at the metal/oxide interface. 101 This oxidation was attributed to the high mobility of lattice oxygen at these temperatures. At the other extreme, deposition at 160 K was found to resemble structures observed at room temperature indicating the high mobility of Cu atoms on the TiO<sub>2</sub>(110) surface. 87 In concluding this section it is worth mentioning an interesting effect observed by Zhou *et al.* for particles observed at 1 ML coverage. Upon exposure to oxygen gas at RT, these 3D islands were converted to 2D islands. 102 They attributed this effect to a

weakening of the metal-metal bond due to the adsorption of O, as the Cu-O bond is stronger than the Cu-Cu bond. This transition was not observed for higher coverage overlayers. <sup>103</sup>

## 3.1.2 Growth and Properties of Cu Supported on Various Metal Oxides.

Besides TiO<sub>2</sub>, the structural properties and growth behaviour of supported Cu overlayers deposited via PVD has been investigated on other metal oxides such as ZnO, SiO<sub>2</sub> and Al<sub>2</sub>O<sub>3</sub>. Ernst et al. have studied the growth mode of Cu on ZnO(0001)-O single crystals, during deposition at 130 K.<sup>104</sup> Using a combination of XPS, LEIS and LEED, they observed a Stranski-Krastanov (SK) type of mode. At low coverages, Cu atoms formed 2D structures without though wetting the surface completely. At a critical coverage, covering approximately 50 % of the surface, 3D islands started to form, which grew into larger clusters upon further Cu evaporation. It should also be mentioned that Cu particles exhibited metallic character even from the first stages of growth. Annealing the 2D structures up to 850 K resulted in their 3D transformation, as the latter are the thermodynamically favoured structures. In separate communications, they have also reported that as deposited overlayers exhibited (110) like structures, that where transformed upon annealing into (111) like ones. 105, 106 These conclusions were derived by comparing TPD experiments of adsorbed H<sub>2</sub>O<sup>105</sup> and CO<sup>106</sup> to previously published data on Cu(110) and Cu(111). Cu deposited on ZnO single crystals at 300 K was also found to follow a Stranski-Krastanov mode. 107 An epitaxial relation was also observed between the overlayer and the support. Furthermore in this study, three different crystal orientations were investigated in an effort to mimic the behaviour of high surface area catalysts. It was concluded that the (0001) and (1010) surfaces adsorbed CO with the same affinity as pure Cu, while the (000ī) surface much weaker due to stronger bonding of Cu on the latter.

On a  $SiO_2$  thin film prepared on a Mo(110) substrate Cu has been observed to adopt again the Stranski-Krastanov growth mode at 100 K.<sup>108</sup> According to FT-RAIRS spectra, as-deposited Cu overlayers of different coverages exhibited surface structures

resembling the (111) and high index crystal planes. Upon annealing to 900 K several new features emerged in the FT-RAIRS spectra which were attributed to the structural transformation of Cu surfaces. A variety of structures was observed as (110), (111), (211) and (311). In addition, the two dimensional structures were transformed into three dimensional ones. Finally, it should be noted that less than 0.1 ML of Cu was found to be oxidised, as indicated by a second Cu TPD peak situated around 1000 K.<sup>109</sup> A bond between the metal and surface O was also observed at the initial stages of growth of Cu on an α-Al<sub>2</sub>O<sub>3</sub>(0001) single crystal, as confirmed by AES.<sup>110</sup> The formation of Cu(I) species during the first stages of growth (less than 0.4 ML) was reported during the deposition of Cu on a thin alumina oxide.<sup>111</sup> These researchers also observed the formation of 3D islands above ca 2ML. For smaller coverages, Rainer *et al.* suggested that 2D islands were present on the surface, thus the deposition of Cu on Al<sub>2</sub>O<sub>3</sub> should follow the Stranski-Krastanov mode.<sup>112</sup> Using FT-RAIRS they also observed the same plethora of surface structures, especially upon annealing, previously noticed for the Cu/SiO<sub>2</sub> system.

#### 3.1.3 Catalytic Properties of Cu Supported on Various Metal Oxides.

The catalytic properties of Cu/metal oxide systems have been explored for a variety of reactions. On planar oxides and in particular Al<sub>2</sub>O<sub>3</sub>, Wu and Goodman studied the reaction of <sup>15</sup>NO+CO with Cu particles less than 100 nm in size, in the temperature range between 150 and 250 K. <sup>113</sup> They observed that in addition to <sup>15</sup>N<sub>2</sub> and <sup>15</sup>N<sub>2</sub>O generated due the dissociation of <sup>15</sup>NO, some CO<sub>2</sub> was also produced by the reaction of adsorbed CO and O. Recently the reaction of methanol with metallic and oxygen covered Cu particles supported on TiO<sub>2</sub>(110) was also investigated. <sup>114</sup> Methanol was adsorbed at 100 K while TPD spectra were recorded up to 950 K. It was found that this process mainly produced formaldehyde, CO<sub>2</sub>, H<sub>2</sub>O and H<sub>2</sub> both for the metallic and the oxygen covered Cu. The reactivity though of the oxidised particles was severely enhanced as the presence of oxygen facilitated the scission of O-H bond. On the other hand no particle size effects were observed. The same research group has also reported the decomposition of Dimethyl Methylphosphonate (DMMP) on TiO<sub>2</sub>(110) supported Cu particles. <sup>115</sup> Again particle size

effects were not observed, but different decomposed products were found for thin Cu films, as TiO<sub>2</sub> can also induce decomposition of DMMP.

The room temperature oxidation of CO on high surface area Cu/TiO<sub>2</sub> and Cu/ZnO catalysts has been reported by Boccuzzi and Chiorino. 116 Following the characterization of the process with FTIR spectroscopy, they proposed that the oxidation proceeded via two separate paths. In the first one direct oxidation of gas phase O<sub>2</sub> with Cu adsorbed CO resulted in the production of CO2. According to the second scheme proposed, formation of carbonate like species took place following the interaction of adsorbed CO and surface lattice oxygen. This process was promoted or activated by gas phase O<sub>2</sub>. The hydrogenation of CO on various high surface area Cu/metal oxide systems was studied and compared by Chen et al. 117 Maximal rates were observed for p-type supports such as ZrO<sub>2</sub>, while n-type oxides, as Al<sub>2</sub>O<sub>3</sub>, exhibited similar rates to bulk Cu. Nevertheless for TiO<sub>2</sub> and MgO, n-type, almost no activity was detected. These results were interpreted taking into consideration electronic effects between the support and Cu. On the other hand Cu/TiO<sub>2</sub> catalysts were found to demonstrate the highest TOF for the methanol synthesis from CO<sub>2</sub> hydrogenation between Cu/SiO<sub>2</sub> and Cu/Al<sub>2</sub>O<sub>3</sub>. The rate limiting step for this reaction was the creation of formate species on the surface of every catalyst. The authors argued that a synergistic effect between Cu and TiO<sub>2</sub>, not present for the other two catalysts, enhanced the activation of H<sub>2</sub>, thus promoting the hydrogenation of intermediate formate species. Cu/TiO<sub>2</sub> catalysts have also been found to promote the production of H<sub>2</sub> via the water gas shift reaction (WGSR), although they were not as active as Au/TiO2. 119 Recently Nian et al. reported that calcined CuO loaded TiO2 nanotubes catalysed the selective reduction of NO with NH<sub>3</sub> with higher activity that TiO<sub>2</sub> nanoparticles. 120 They attributed this increase due to formation of Cu<sub>x</sub>Ti<sub>1-x</sub>O<sub>2</sub> solid solutions produced by the calcination process. These solid solutions were identified by XRD, XANES and EXAFS. Finally Cu nanoparticles, less than 10 nm, dispersed on three different oxide supports, were found to be highly active towards the partial oxidation of cyclohexane. 121 This activity remained after the first experiment for two of the supports, TiO<sub>2</sub> and γ-Al<sub>2</sub>O<sub>3</sub>, while Fe<sub>2</sub>O<sub>3</sub> became inactive. This deactivation was attributed to

particle size effects, as larger Cu particles were formed on Fe<sub>2</sub>O<sub>3</sub> after the first cycle, as observed on TEM images.

#### 3.2 Experimental

The experiments described in the following sections were performed in the UHV chamber described in Section 2.1. The surface of the  $TiO_2(110)$  single crystal was cleaned through repeated cycles of sputtering and annealing, followed at the end by  $O_2$  treatment. As previously discussed in Section 2.2 this procedure resulted in a well ordered surface, free of C contamination.

For the deposition of Cu the PVD technique was utilised. The homemade PVD source consisted of a Ta tube, 2.5 cm in length and 0.25 cm wide, resistively heated by two W wires spot welded on either side of the source. A K-type thermocouple spot welded in the middle of the tube was used to monitor the temperature. Current was supplied to the source by spot welding the W wires onto two feedthroughs of a four feedthrough flange. The other two were used to connect the thermocouple wire. At the end of each power feedthrough one thick, 0.5 nm, Ni rod was attached to prevent evaporation of stainless steel due to the high temperatures produced at the contact point between the W wire and the rod. A Ta sheet was spot welded at the end of each Ni rod to stop any evaporating material from contaminating other parts of the chamber. Cu in the form of a thin wire (99.999% Goodfellows) was placed in the Ta tube, without any treatment. Once inside the chamber, the PVD source was approximately 10 cm away from the sample. Under ultra high vacuum, the source was outgassed for one to two hours at 650 °C. A schematic of the arrangement can be found in Figure 3-1.

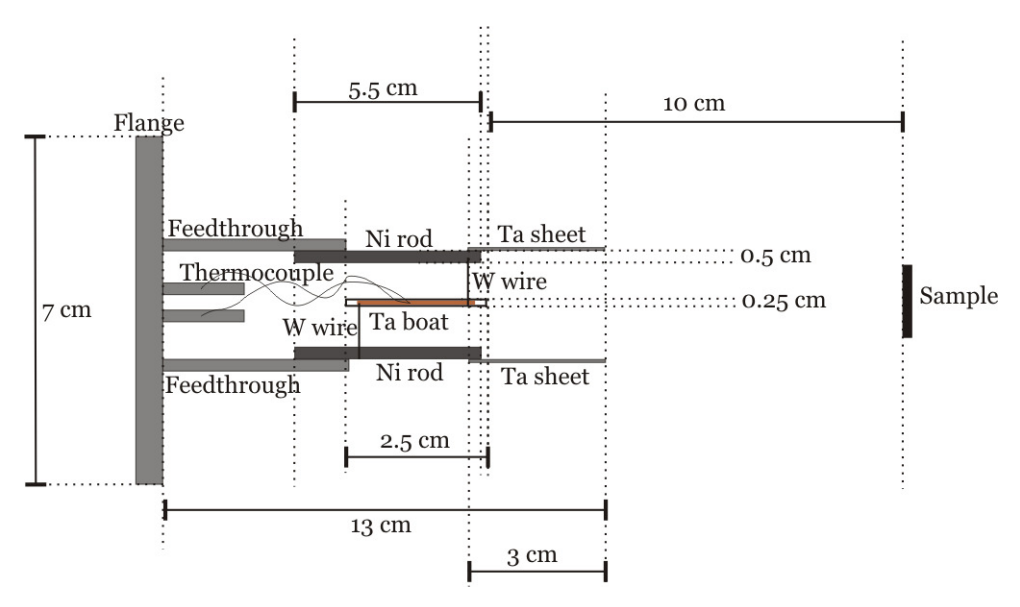
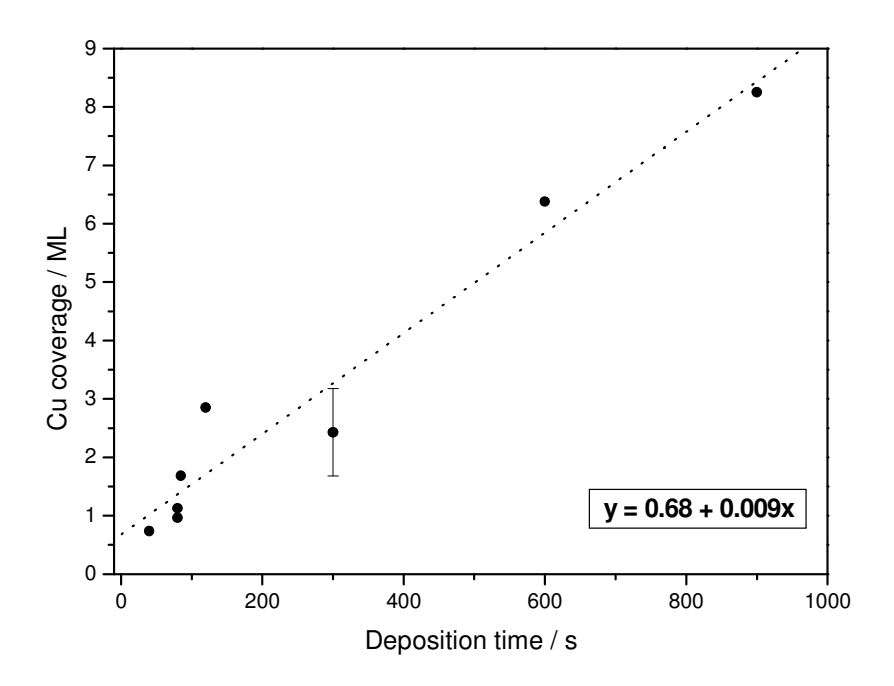


Figure 3-1 A schematic (side view) of the PVD source. Items not in scale.

As discussed in Section 2.6, the evaporation rate of each material strongly depends on the temperature of the source. In addition, other factors can affect the deposition such as the geometry of the source and its position from the sample. In order to establish the appropriate conditions for our source, several trial depositions were performed. In these trials, the temperature of the source was varied while the deposition time was kept constant. The amount present on the surface was confirmed via XPS. It was found that deposition temperatures above 1000 °C resulted in the formation of Cu films quite fast, while deposition temperatures below 1000 °C had very slow deposition rates. Consequently, 1000 °C was selected as an adequate deposition temperature for the deposition of both particles and films. Figure 3-2 represents different Cu coverage values achieved using 1000 °C, as a function of deposition time. Employing a linear regression fit of these data, a deposition rate of 0.009 ML/s was calculated. While the PVD source was heated to the required temperature, the sample was kept facing towards the opposite direction as evaporation occurred even below 1000 °C. At 1000 °C the sample was turned to face the source and the deposition commenced. XPS spectra collected from C(1s) region after deposition, indicated no C contamination on the surface. All depositions reported in this chapter took place with the TiO<sub>2</sub>(110) crystal at 295 K.



**Figure 3-2** Cu coverage as a function of deposition time. From the linear fit of these data, an average deposition rate of 0.009ML / s was estimated. The equation used for the fit can be found as an inset in the figure. Cu coverage values were calculated from XPS using equations 2-16 for the fractional coverage and 2-19 for films above 1 ML.

All FT-RAIRS spectra were collected via the InSb detector and 1760-x Perkin Elmer spectrometer. Each spectrum was recorded (collection time of 60 s) using a p-polarised light, 100 scans and resolution of 4 cm<sup>-1</sup> in the spectral region from 2200 cm<sup>-1</sup> to 1900 cm<sup>-1</sup>. XPS spectra were collected using the Mg anode (1253.6 eV), while for each scan the energy regions of C(1s), Ti(2p), O(1s) and Cu(2p) were measured. The spectra were collected using a 0.1 eV step, duel time of 1 s and averaged over 3 scans. Analysis of the XPS data was performed using the WSPECTRA software, which estimates the area, intensity and position of the peaks by fitting the raw spectra with a Gaussian-Lorentzian function. Prior to any analysis a Shirley background<sup>122</sup> was subtracted from the raw data. The coverage values were estimated using Equations 2-16 and 2-19 of Section 2.4.2. As mentioned in that Section, an error of the order of 15-20 % can be expected from these calculations. The LEED diffraction patterns were collected with an electron beam of 100 eV. CO adsorption studies were performed with the sample at 130 K. CO (99.999% purity,

Messer) was introduced into the chamber via a variable leak valve. All exposure values quoted here are in Lanqmuirs (1L is defined as an exposure of  $10^{-6}$  Torr for 1 s). Spectra recorded during the 130 K exposure of the clean  $TiO_2(110)$  to CO did not reveal any features.

The experimental protocol followed for the experiments described in this chapter had as follows. Initially, the surface was cleaned through repeated cycles of sputtering and annealing. Subsequently Cu was deposited at 295 K. While the sample was cooling down to 130 K, XPS and LEED measurements were undertaken to establish the coverage and structure of Cu overlayers. Once at 130 K CO adsorption studies took place, with FT-RAIRS data recorded after each CO exposure. Additional XPS spectra were collected following annealing of the Cu covered surface.

#### 3.3 Results and Discussion

#### 3.3.1 CO Adsorption

It would be useful before presenting the results of this study to mention some information regarding the particle size of the Cu overlayers prepared within this investigation. The combination of XPS, FT-RAIRS and LEED used here cannot reveal direct information of the size of Cu particles. But by comparing findings of different researchers with our XPS measurements, an estimation of these sizes can be made. As mentioned in chapter 2, section 2.3.2, the thickness of an overlayer supported on a substrate can be calculated using the area values of XPS peaks. *Yang et al.* have presented a study where the average size of Cu particles deposited on the BCB polymer was calculated using XPS data. As part of their investigation they correlated this average particle size with the thickness of the Cu overlayer, verifying their findings using AFM and TEM. In addition, Diebold *et al.* while studying the growth mode of Cu on TiO<sub>2</sub> have reported a model with which the average size of the Cu particles could be calculated using XPS data. Again a correlation between this size and the thickness of the Cu overlayer was made. In both models Cu particles were treated as having hemispherical shape.

Comparing these findings with thickness values calculated from our XPS data an estimation of the size of Cu particles was made. This comparison is presented in Table 3-1.

**Table 3-1** An estimation of the average Cu cluster sizes obtained by comparing thickness values calculated from XPS data with previously published results.

Coverage / MLE (this study)	Thickness / nm (this study)	Cluster Size / A (from <sup>123</sup> )	Cluster Size / A (from <sup>87</sup> )
0.73 ( in ML)	0.15	20 to 22	21 to 23
1.36	0.3	31 to 33	25 to 27
1.68	0.38	32 to 34	26 to 28
2.85	0.64	40 to 42	31 to 33
4.48	1.01	45 to 47	36 to 38
6.04	1.37	49 t0 51	41 to 43
6.37	1.44	51 to 53	42 to 44
8.25	1.87	55 to 57	47 to 49

#### 3.3.1.1 Low Coverage

FT-RAIRS spectra of CO adsorbed on 0.73 ML of Cu deposited on the TiO<sub>2</sub> single crystal as a function of exposure are presented in Figure 3-3. From the first stages of exposure, 0.5 L, features were observable in the spectrum. These comprised of two bands: a dominant one at 2017 cm<sup>-1</sup> and a shoulder situated at 2100 cm<sup>-1</sup>. Upon increasing the exposure to 3L, the former saturated and the latter grew into a full peak. At 6 L, the spectrum was composed of one main transmission band at 2100 cm<sup>-1</sup> along with a small shoulder at 2107 cm<sup>-1</sup>. Following 9 L of exposure the system reached saturation.

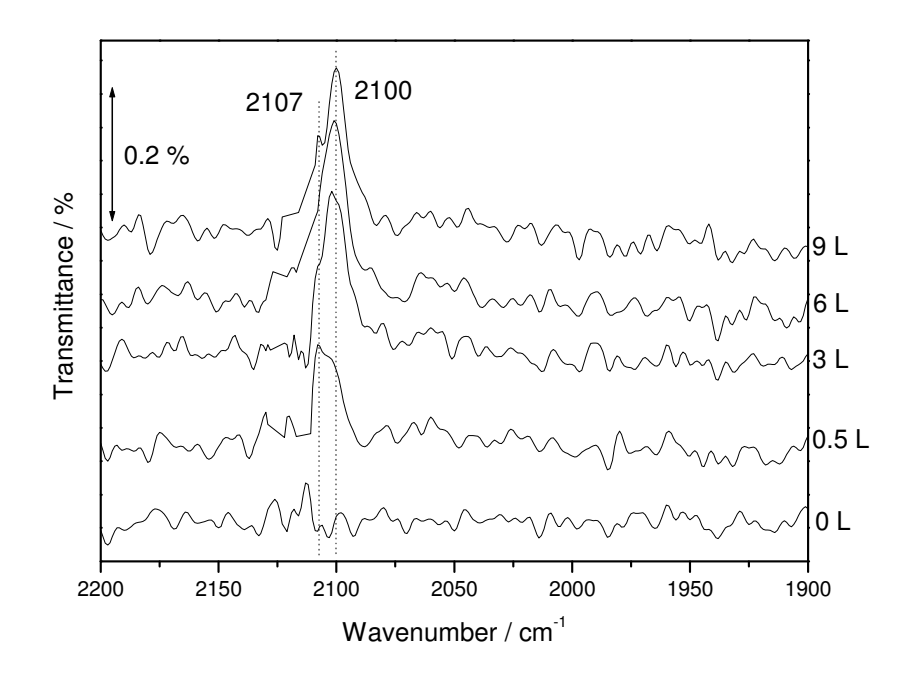


**Figure 3-3** FT-RAIRS spectra of CO adsorbed at 130 K on a 0.73 ML overlayer of Cu on  $TiO_2(110)$ . CO exposures are shown on the right hand side of the plot.

The presence of only transmission bands in the spectra of Figure 3-3 indicated that at 0.73 ML of Cu, the size of the deposited islands was indeed very small, as it was not enough to transform the character of the local dielectric field into metallic. The appearance of two separate transmission bands in FT-RAIRS spectra hinted the presence of two differently bound CO molecules. This difference might have risen from CO adsorbed on two different Cu surfaces. As it has been shown by Pritchard *et al.*,<sup>67</sup> the position of v(C-O) bands due to CO adsorption on Cu single crystals is strongly dependent on the crystal structure. For example CO adsorbed on Cu(111) exhibits a band at 2071 cm<sup>-1</sup> whereas on Cu(110) it is at 2093 cm<sup>-1</sup>. Bands at higher wavenumbers (similar to Figure 3-3) are attributed to CO bound on high index planes. It is very hard to recognise the exact Cu surface structure on to which CO molecules were adsorbed, but based on the available literature, the (211), (311) and (755) are the main candidates. At coverage of 0.73 ML, Cu has already formed islands on the oxide surface, <sup>87, 89</sup> thus it would be fair to assume that these islands exhibited relatively high index plane facets. As a reference

hereafter, Table 3-2 summarises the bands attributed to CO adsorbed on different Cu facets, as reported by Pritchard *et al*.

**Table 3-2** The positions of infrared absorption bands for CO adsorbed on various single crystal Cu faces at saturation coverage, by Pritchard *et al.* <sup>67</sup>

Cu single crystal face	Wavenumber / cm <sup>-1</sup>	
(100)	2085	
(111)	2076	
(110)	2093	
(211)	2100	
(311)	2102	
(755)	2098	

Islands formed at Cu coverage near to a monolayer exhibited similar behaviour. Figure 3-4 represents FT-RAIRS spectra collected after CO adsorption at 1.68 MLE of Cu as a function of CO exposure. Again at the early stages of dose a broad feature was observable around 2100 cm<sup>-1</sup>. As the exposure increased the position of this feature remained the same whereas its intensity value changed dramatically after 1L of CO. At this value the feature was comprised of two peaks similar to the ones observed in Figure 3-3, i.e. one at 2107 cm<sup>-1</sup> and another at 2102 cm<sup>-1</sup>. Upon further increase in exposure, the spectra were characterised only by one transmission band situated at 2100 cm<sup>-1</sup> which can be attributed to CO bound on Cu islands with structures similar to the high index facets. Hence, unlike the sub-monolayer islands, Figure 3-3, these larger clusters appeared to accommodate only one formation since a single infrared band was observed.

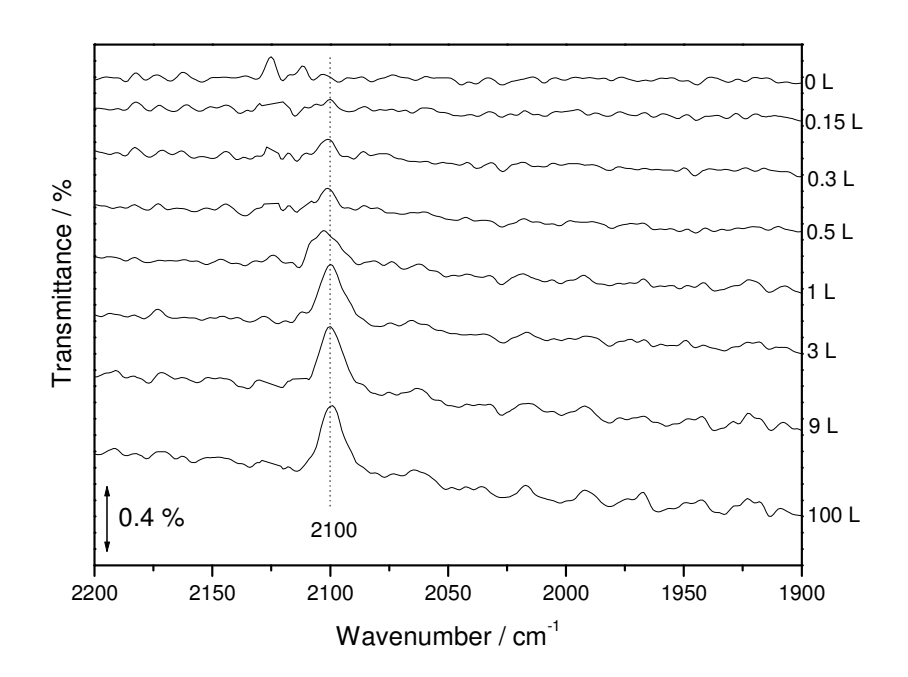
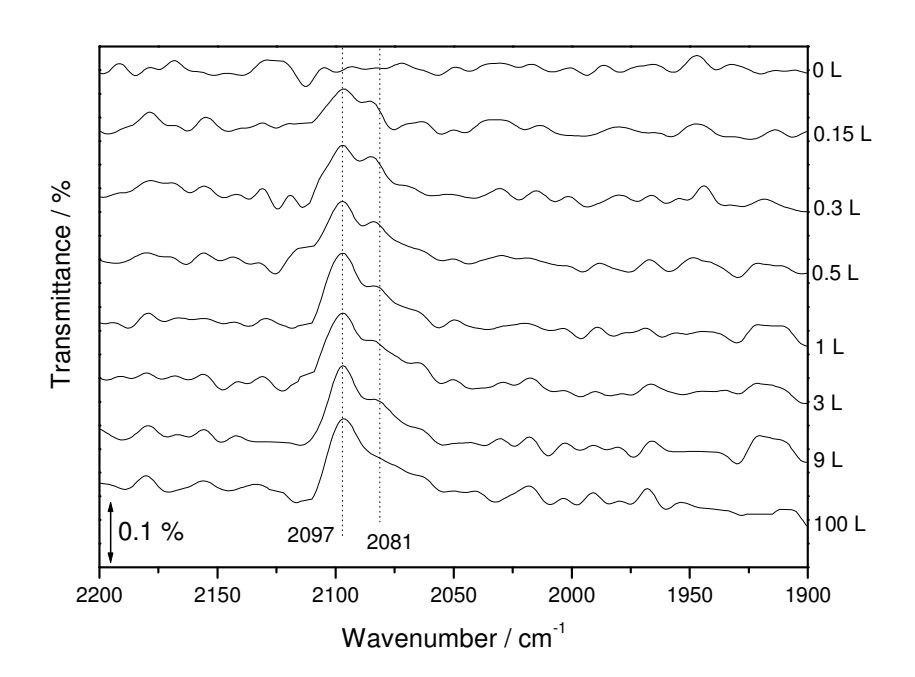


Figure 3-4 FT-RAIRS spectra of CO adsorbed at 130 K on a 1.68 MLE overlayer of Cu on  $TiO_2(110)$ . CO exposures are shown on the right hand side of the plot.

Annealing the 1.68MLE particles to 650 K introduced two main changes in the CO adsorption spectra, as it can be observed in Figure 3-5. Firstly the main peak red shifted to 2097 cm<sup>-1</sup> and secondly a new feature emerged at around 2081 cm<sup>-1</sup>, in the form of a broad shoulder even from very low exposure values, 0.1 L. The two features grew in intensity upon increasing exposure, with the one at 2097 cm<sup>-1</sup> remaining the dominant band. The newly observed feature at 2081 cm<sup>-1</sup> could be attributed to CO bound on low Miller index faces, such as (100) and (111). Generally during annealing, clusters on the surface become extremely mobile and as a result several processes take place. One of them is the formation of larger clusters.<sup>87</sup> An important consequence of this process is that a section of the substrate previously covered by Cu is now exposed. This effect was evident in XPS spectra collected from the Ti(2p) region, where the XPS signal of the support increased due to the annealing, Figure 3-6. XPS spectra collected in Cu(2p) region, Figure 3-7, revealed a decrease in the Cu (2p<sub>3/2</sub>) peak signal. This was due to the fact that metal atoms located at the centre of these clusters could no longer contribute to the XPS signal. Another important process taking place during annealing is the reorganisation of metal

particles into thermodynamically favoured structures which in this case manifested itself with the appearance of the v(C-O) band at 2081 cm<sup>-1</sup>. Finally encapsulation of some particles could occur, a phenomenon that has not been observed though for Cu islands on  $TiO_2$ .



**Figure 3-5** FT-RAIRS spectra of CO adsorbed at 130 K on a 1.68 MLE overlayer of Cu on  $TiO_2(110)$ , after the latter were annealed at 650 K. CO exposures are shown on the right hand side of the plot.

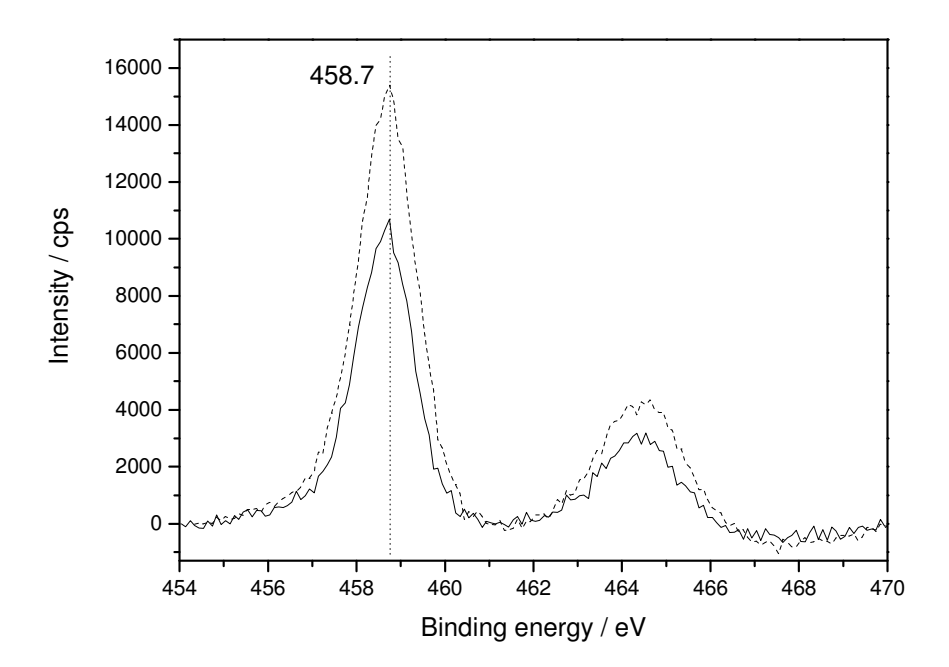


**Figure 3-6** Ti(2p) energy region measured after 300 K deposition of 1.68 MLE Cu (solid line) and after annealing the surface at 650 K (dotted line).

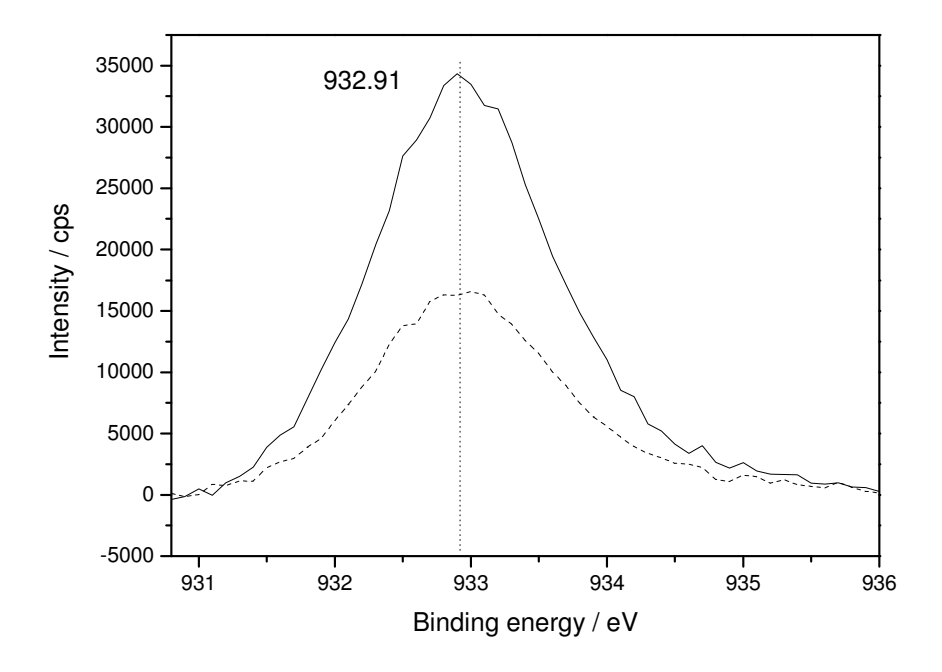


**Figure 3-7**  $Cu(2p_{3/2})$  energy region measured after 300 K deposition of 1.68 MLE Cu (solid line) and after annealing the surface at 650 K (dotted line).

## 3.3.1.2 Medium Coverage

Upon increasing the size of the metallic islands, the appearance of infrared spectra also changed, as it can be observed in Figure 3-8. This Figure represents FT-RAIRS spectra of CO adsorption on 6.04 MLE Cu islands as a function of exposure.

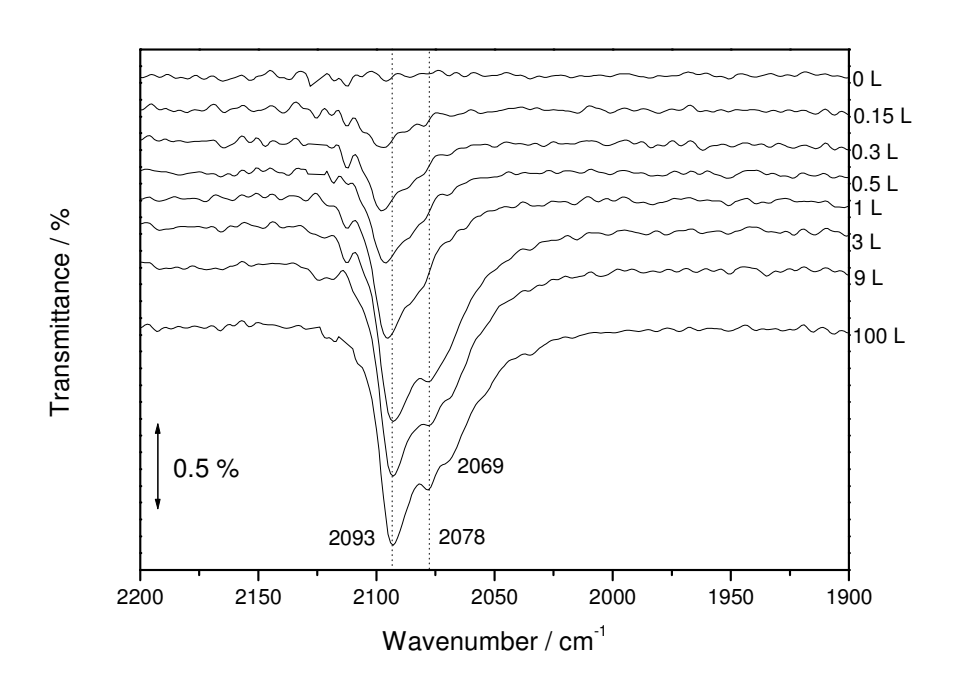


Figure 3-8 FT-RAIRS spectra of CO adsorbed at 130 K on a 6.04 MLE overlayer of Cu on  $TiO_2(110)$ . CO exposures are shown on the right hand side of the plot.

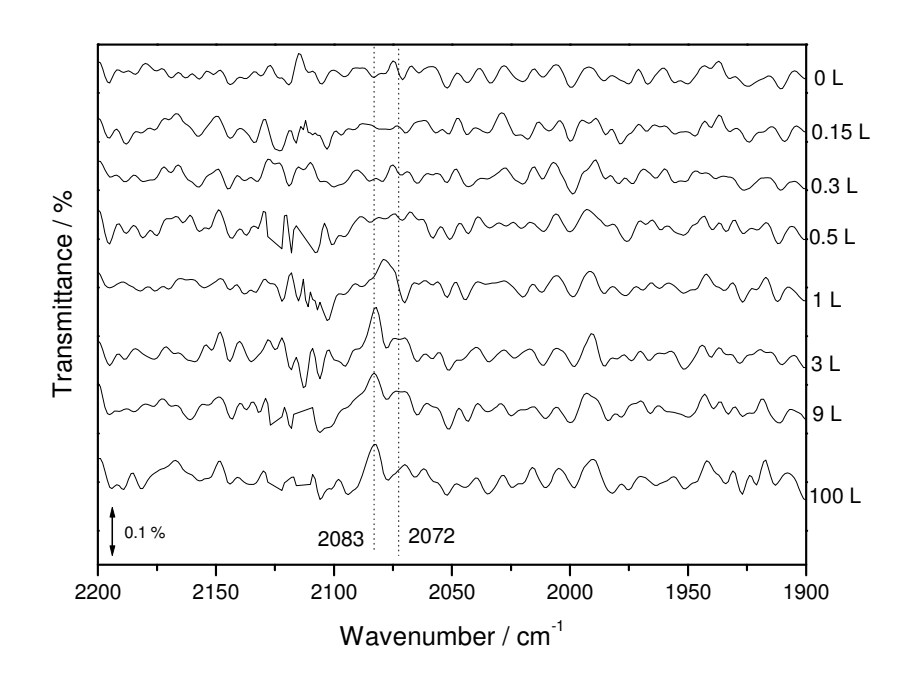
After 0.15 L of CO an absorption band was distinguishable at 2098 cm<sup>-1</sup>. As the exposure increased this band red shifted to 2093 cm<sup>-1</sup> and reached saturation after 3 L of CO. Following 1 L of exposure to CO, a broad shoulder was also evident, situated next to the absorption peak. This shoulder grew into a peak at 2078 cm<sup>-1</sup> after 3 L of exposure, while a new shoulder emerged at 2069 cm<sup>-1</sup>. At exposure values above 9 L no alteration took place indicating that all features reached saturation. According to Table 3-2, the peak at 2093 cm<sup>-1</sup> can be attributed to CO bound on (110) facets whereas the peak at 2078 cm<sup>-1</sup> to CO bound on (100) facets. The small shoulder at 2069 cm<sup>-1</sup> can be correlated with the (111) facet. Thus, it can be assumed that by increasing Cu particle size, the surface no

longer accommodated high index facets but instead low Miller index structures were formed. Cu particles grown on thin films of  $SiO_2$  are also known to exhibit the same behaviour.  $^{108,\,124}$ 

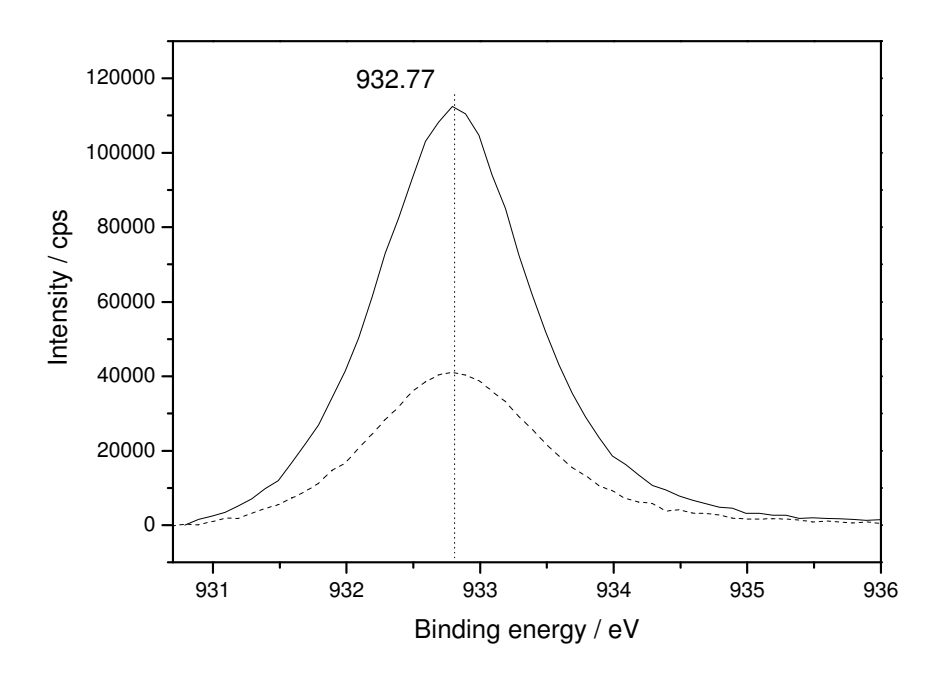
Comparing the spectra of Figures 3-3 (Cu coverage 1.68 MLE) and 3-8 another important difference can also be observed: the switching of the v(C-O) modes from transmission to absorption. This change is an important consequence of conducting FT-RAIRS experiments on oxide single crystals. As mentioned in Chapter 2, Section 2.2.1, depending on the character of the local dielectric field, either transmission, absorption or both bands will appear in FT-RAIRS spectra. When the field is dominated by the oxide character of the support then transmission bands will emerge. On the other hand, when the character is metallic absorption bands will be present. There is also an intermediate state when the local dielectric field is in transition, hence bands in both directions are observed. As already mentioned, at 1.68 MLE coverage the size of Cu overlayer (ca. 3.5 nm) is not sufficient to transform the character of the local field to metallic. As a result, transmission bands appeared in the FT-RAIRS spectra of Figure 3-3. On the other hand, at 6.04 MLE coverage the size of the deposited Cu islands (ca. 5.2 nm) was sufficient to transform the character of the dielectric field to metallic, thus absorption bands were observable on the FT-RAIRS spectra. This conversion of FT-RAIRS bands is consistent with previous studies during which the PVD of metals on  $TiO_2(110)$  was examined. <sup>61, 63, 125, 126</sup> According to those investigations, the adsorption of CO on low coverage Rh <sup>61, 126</sup> or Pd <sup>63,</sup> resulted in the appearance of transmission bands, whereas CO adsorption on higher coverage overlayers resulted in absorption bands. For all systems, Rh, Pd and here Cu, the transformation of the local dielectric field occurred over a narrow region of overlayer size, and as discussed in the following Section, 3.3.2, a consistency appears to exist between size and transformation.

Figure 3-9 represents FT-RAIRS spectra of CO adsorbed on 6.04 MLE of Cu/TiO<sub>2</sub> as a function of CO exposure, collected after annealing at 650 K. During the first stages of CO exposure no infrared bands were observable on the spectra. It was only after exposing the surface to 1 L of CO that a peak appeared at 2079 cm<sup>-1</sup>, which as the

exposure increased grew in intensity and blue-sifted to 2083 cm<sup>-1</sup>. In addition, after 3L a small band was also introduced in the spectra, at 2072 cm<sup>-1</sup>. By comparing the spectra pre and post annealing, the first observation that can be made is the disappearance of the 2093 cm<sup>-1</sup> feature. A possible explanation for this would be that as part of the reorganisation taking place during annealing, the structures of Cu clusters changed to the most thermodynamically favourable. The second observation that can be made is the expression of v(C-O) modes of Figure 3-9 as transmission rather than absorption peaks. Following the discussion of the previous paragraph, this transformation would indicate that the annealed Cu particles were not large enough to retain the metallic character of the local dielectric field exhibited by the as deposited Cu overlayer. At first instance, this result contradicts XPS results collected before and after annealing. Figures 3-10 and 3-11 represent spectra of Cu(2p<sub>3/2</sub>) and Ti(2p) energy regions respectively collected after the 300 K deposition and after the 650 K annealing. The reduction of Cu(2p<sub>3/2</sub>) peak intensity along with the increase of the Ti(2p<sub>3/2</sub>) peak intensity, are consistent with agglomeration of Cu into larger particles, similar to the one described for the 1.68 MLE overlayer. Nevertheless the FT-RAIRS spectra of Figure 3-9 indicate the formation of smaller islands upon annealing. The results from both techniques can be reconciled by adopting the following deposition model. During the RT deposition the growth mode followed by Cu is a mixture of Volmer-Weber (VW, 3D islands) and Stranski-Krastanov (SK, 2D followed by 3D) type. More precisely, the Cu first layers form 2D structures without though wetting the entire oxide surface. Subsequently, 3D islands are formed on top of the flat islands. Upon annealing these complex structures are transformed into 3D islands, which exhibit a high dispersion on the TiO<sub>2</sub>(110) surface. Assuming this complex growth mode would not be unreasonable, bearing in mind first the differences observed in the literature regarding the growth mode of Cu on TiO<sub>2</sub>(110) and secondly the fact that Au which belongs to the same periodic group as Cu, exhibits a similar type of growth on TiO<sub>2</sub>(110). 128, 129



**Figure 3-9** FT-RAIRS spectra of CO adsorbed at 130 K on a 6.04 MLE overlayer of Cu on  $TiO_2(110)$ , after the latter were annealed at 650 K. CO exposures are shown on the right hand side of the plot.



**Figure 3-10**  $\text{Cu}(2p_{3/2})$  energy region measured after 300 K deposition (solid line) of 6.04 MLE Cu and after annealing the surface at 650 K (dotted line).

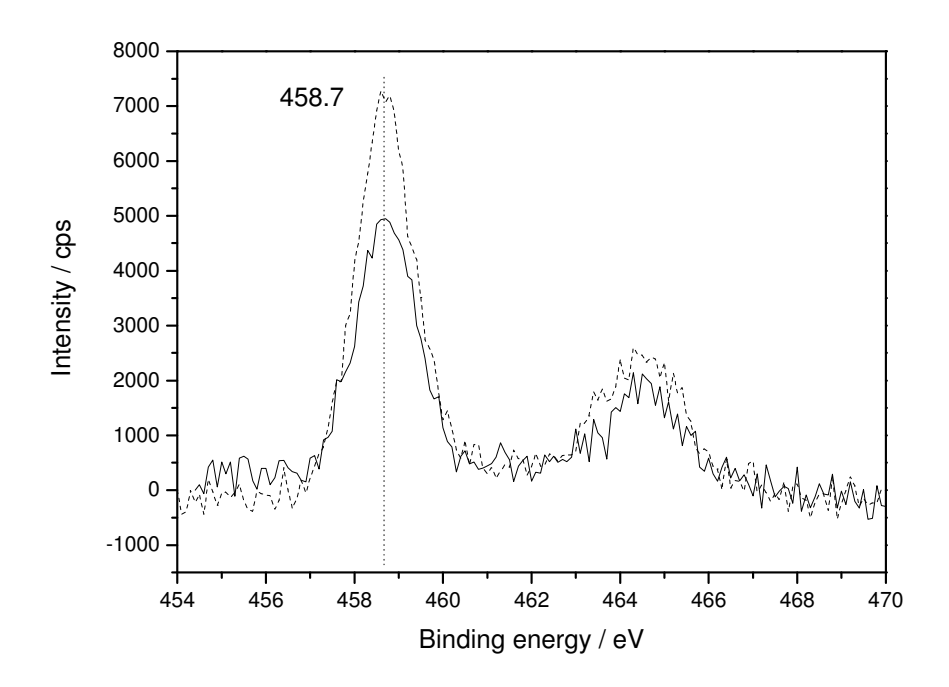


**Figure 3-11** Ti(2p) energy region measured after 300 K deposition (solid line) of 6.04 MLE Cu and after annealing the surface at 650 K (dotted line).

Further increase in Cu coverage, 8.25 MLE, resulted again in variation on the CO adsorption spectra, Figure 3-12. One single peak was observed after 0.1 L of exposure situated at 2089 cm<sup>-1</sup>. Upon increasing the exposure, the peak increased also in intensity and sifted to 2083 cm<sup>-1</sup>. After 3 L of CO, new features emerged on: one band at 2071 cm<sup>-1</sup> along with a small shoulder at 2093 cm<sup>-1</sup>. As with the spectra of 6.04 MLE, these were also dominated by the same three distinctive features attributed to CO bound to structures that resemble the (110), (100) and (111) facets respectively. Contrary to the smaller clusters, the first band to appear on the spectra was the one allocated to the (100) site. As this peak saturated the other absorption features emerged as well.

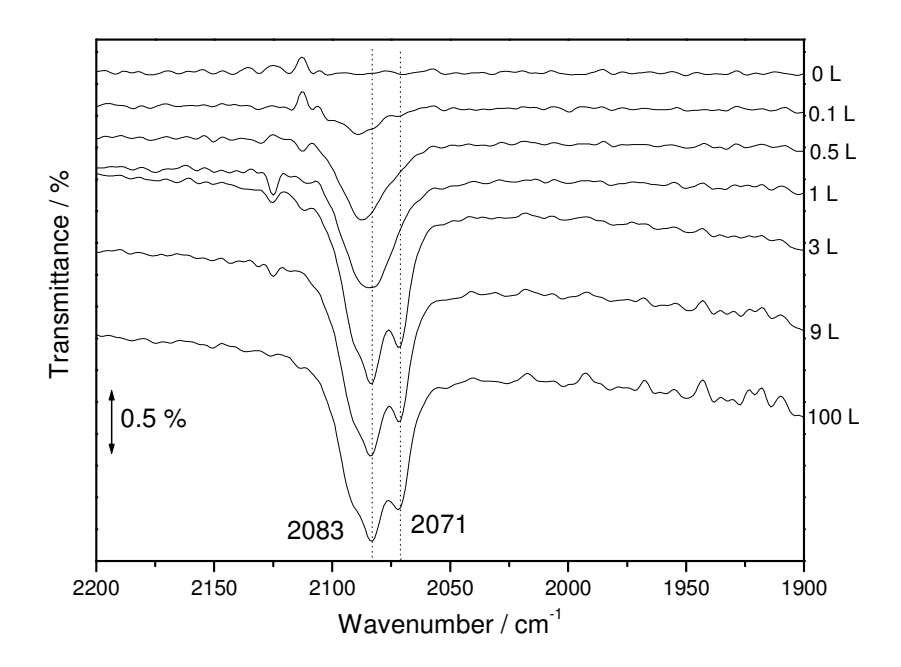


Figure 3-12 FT-RAIRS spectra of CO adsorbed at 130 K on a 8.25 MLE overlayer of Cu on  $TiO_2(110)$ . CO exposures are shown on the right hand side of the plot.

Upon annealing the surface, only the 2085 cm<sup>-1</sup> and 2073 cm<sup>-1</sup> features were present in the recorded FT-RAIRS spectra, Figure 3-13. Again the direction of the bands was inverted indicating the formation of highly dispersed Cu islands. Furthermore the dominant band was the one attributed to CO adsorbed on the (111) surface indicating that the majority of clusters formed structures with (111) facets. This was the highest measured coverage, as further increase in deposition time resulted in the disappearance of the XPS substrate signal. In order though to gain some information regarding the coverage of the continuous films, the equation of the linear regression presented in Figure 3-2 was used to extrapolate the coverage values.

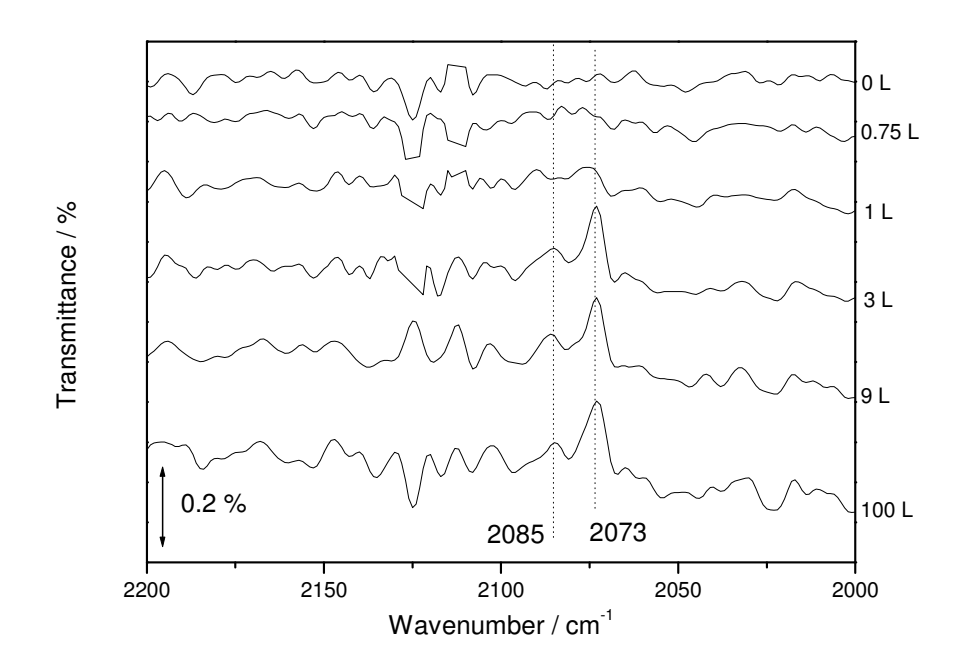
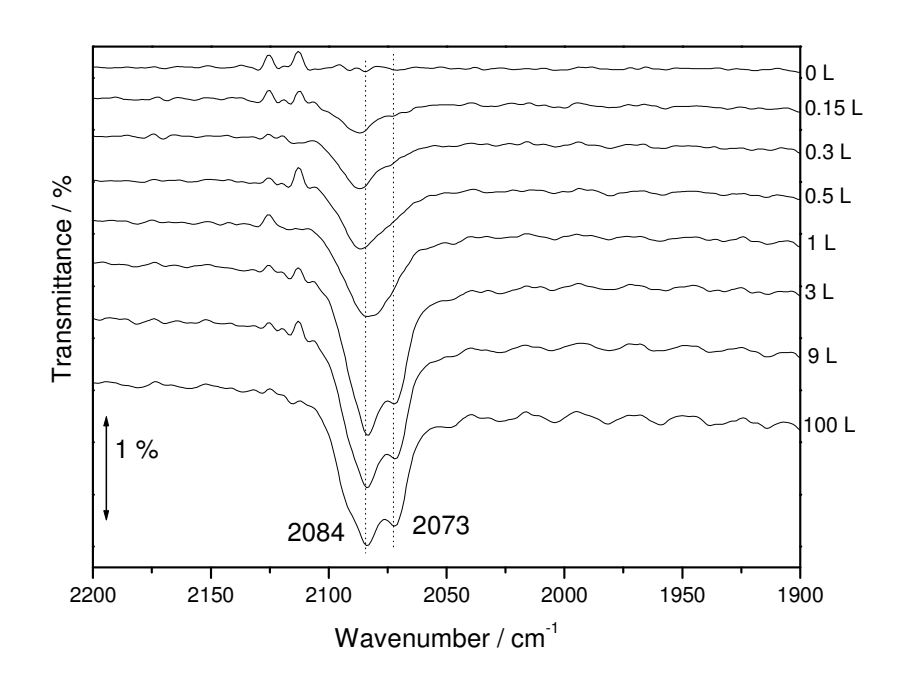


Figure 3-13 FT-RAIRS spectra of CO adsorbed at 130 K on a 8.25 ML overlayer of Cu on  $TiO_2(110)$ , after the latter were annealed at 650 K. CO exposures are shown on the right hand side of the plot.

#### 3.3.1.3 Continuous Film

The third part of this study was to investigate the behaviour of adsorbed CO on TiO<sub>2</sub> supported Cu films. FT-RAIRS spectra of CO bound on a Cu thin film, 8.95 MLE, are presented in Figure 3-14 as a function of CO exposure. No noticeable differences were observed between the response of the Cu film and the 8.25 ML Cu clusters. Again the spectra were initially dominated by a peak at 2084 cm<sup>-1</sup> and following further increase in exposure the two other features at 2071 cm<sup>-1</sup> and 2093 cm<sup>-1</sup> emerged.



**Figure 3-14** FT-RAIRS spectra of CO adsorbed at 130 K on a thin Cu film on TiO<sub>2</sub>(110). CO exposures are shown on the right hand side of the plot.

On the contrary important changes were observed to FT-RAIRS spectra collected after annealing the surface to 650 K, Figure 3-15. These were dominated by the presence of a single absorption band situated at 2073 cm<sup>-1</sup>, although a small shoulder at 2083 cm<sup>-1</sup> was also evident. The first appeared on a higher wavenumber value at the early stages of dose, but as the exposure increased it red-sifted to the saturation value. The shoulder at 2083 cm<sup>-1</sup> emerged after 1 L of CO. Although these same features were also observed for the 8.25 ML clusters the main difference can be found in the direction of the band. The intense absorption peak observed here is a strong indication that the local dielectric field of the film was no longer dominated by the substrate, but it retained its metallic character even after annealing. Consequently the annealed particles were large enough to exhibit metallic character. Annealing the 8.95 MLE Cu film transformed most of the (110) and (100) sites to the (111) one as indicated by the strong absorption at 2073 cm<sup>-1</sup> and by the LEED patterned observed after anneal. This pattern, which can be observed in Figure 3-16, revealed the existence of two formations on the surface. One due to the (110) structure of the TiO<sub>2</sub> support expressed as well defined small spots, and one

due to the (111) structure of the annealed Cu film expressed as blurred large spots. In addition this mixed pattern revealed an epitaxial relation between Cu overlayer and  $TiO_2(110)$  substrate with  $Cu(111)//TiO_2(110)$ , in accordance with previously published studies of this system, <sup>88</sup> and of PVD of Pd on  $TiO_2(110)$ . <sup>127</sup>

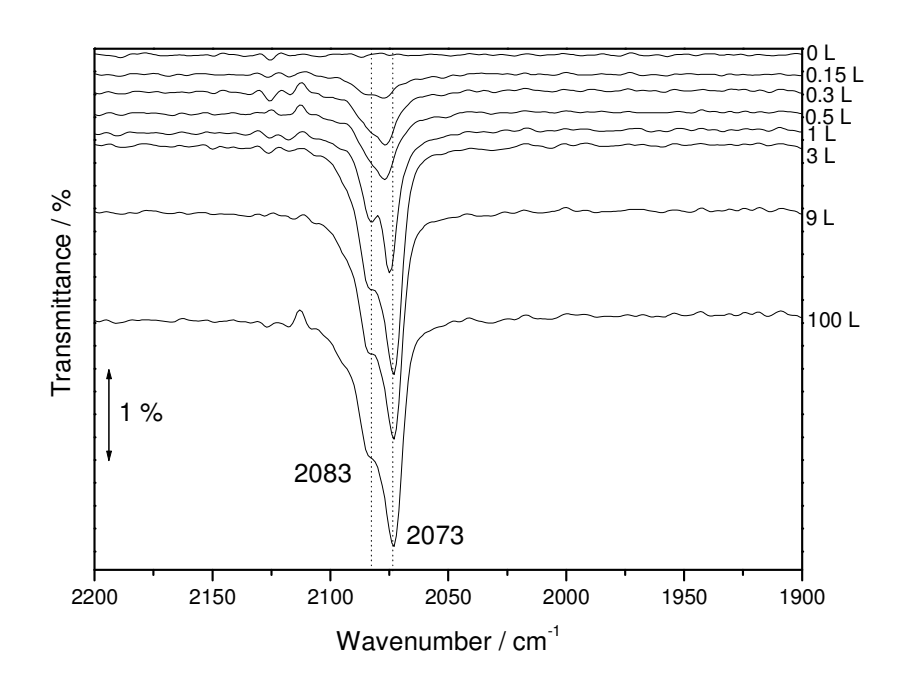
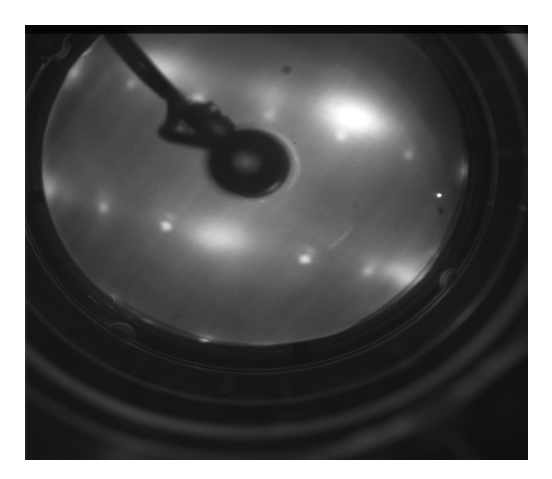


Figure 3-15 FT-RAIRS spectra of CO adsorbed at 130 K on thin Cu film, 8.95 MLE, on  $TiO_2(110)$ , after the latter were annealed at 650 K. CO exposures are shown on the right hand side of the plot.



**Figure 3-16** LEED picture collected after annealing the  $TiO_2$  supported thin Cu film at 650 K. Both (110) and (111) patterns can be observed; the latter being attributed to the Cu film (larger spots) and the former to the oxide support (smaller sports).

An interesting comment regarding the influence of the local dielectric field in the appearance of FT-RAIRS spectra can be made by comparing spectra collected from the annealed 8.25 and 8.95 MLE Cu overlayers (Figures 3-13 and 3-15). Although the two Cu structures differ by 0.7 MLE, an approximate ten-fold increase can be observed in the intensity values of the main infrared peaks. This substantial difference can be explained by taking into consideration the character of the local dielectric field for both coverages. For the highly dispersed islands, the latter is non-metallic in nature hence the small intensity values. On the other hand, the metallic nature exhibited for thin film results in high intensity values. Analogous trends have also been observed during the growth of Pd and Rh particles on TiO<sub>2</sub>(110).

Finally the CO adsorption was studied on a thicker film of Cu deposited on TiO<sub>2</sub>. The coverage of this film was estimated at 15.17 MLE. The FT-RAIRS CO adsorption spectra as a function of exposure can be found in Figure 3-17. Similar to the medium coverage and the 8.95 MLE film results, the spectra of Figure 3-17 were characterised by the three absorption features: one peak at 2071 cm<sup>-1</sup>; a second one at 2083 cm<sup>-1</sup> and one shoulder at 2093 cm<sup>-1</sup>. Thus this film, 15.17 MLE, was also characterised by the three structures that were encountered before, with the majority of the sites following the (100) and (111) formations.

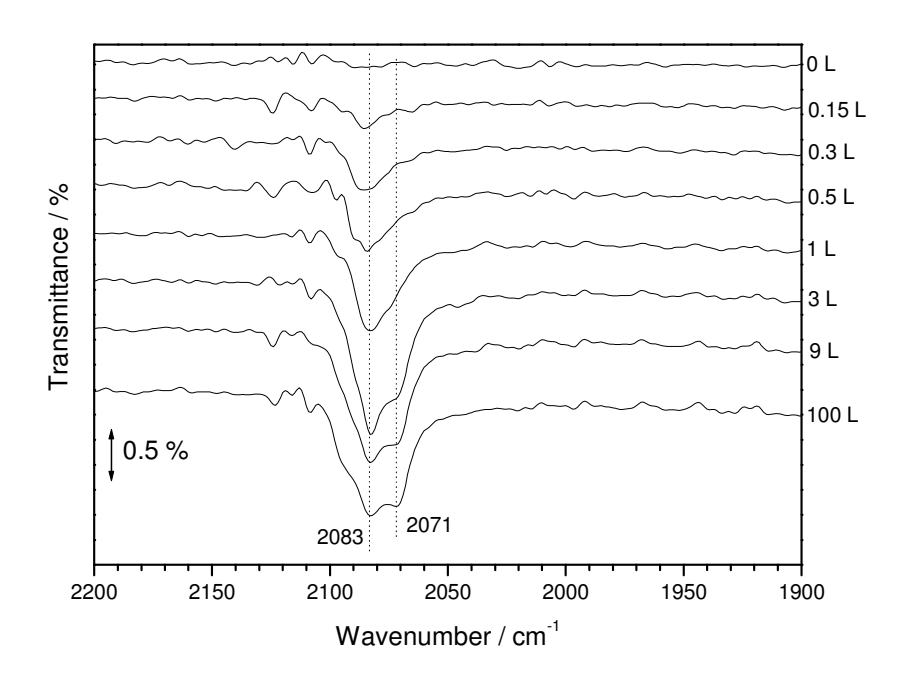


**Figure 3-17** FT-RAIRS spectra of CO adsorbed at 130 K on a 15.17 MLE Cu film on  $TiO_2$  (110). CO exposures are shown on the right hand side of the plot.

Annealing the 15.17 MLE Cu film at 650 K, resulted in the transformation of the two other structures into the (111) formation. The strong absorption feature present on the FT-RAIRS spectra at 2072 cm<sup>-1</sup> was indicative of this, as it can be observed in Figure 3-18. Furthermore the LEED pattern collected after annealing revealed only one structure present on the surface. The formation appearing in Figure 3-19 is characteristic of Cu(111). Unlike the LEED pattern of Figure 3-16 no signal due to the TiO<sub>2</sub>(110) support was present.

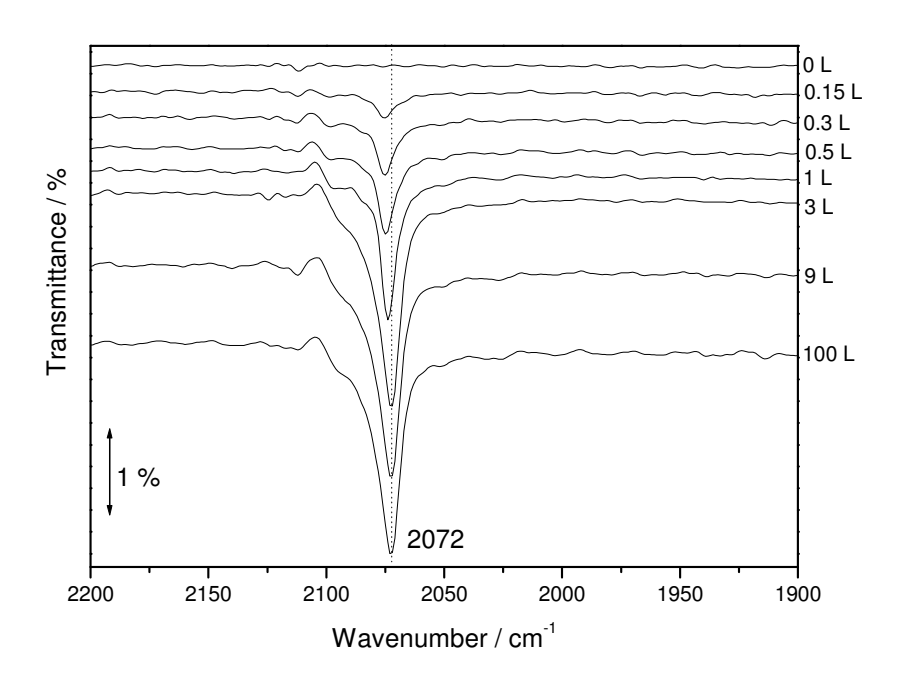


**Figure 3-18** FT-RAIRS spectra of CO adsorbed at 130 K on Cu film on  $TiO_2(110)$ , after the latter was annealed at 650 K. CO exposures are shown on the right hand side of the plot.



**Figure 3-19** LEED picture collected after annealing the TiO<sub>2</sub> supported Cu film at 650 K. Only the (111) pattern was observed which is attributed to the Cu film.

## 3.3.2 Structural Changes During Growth

According to data presented in the previous Section, the adsorption of CO on various Cu coverages resulted in different FT-RAIRS spectra. In this section these coverage dependent changes, from sub monolayer islands up to thin films, are going to be discussed in detail.

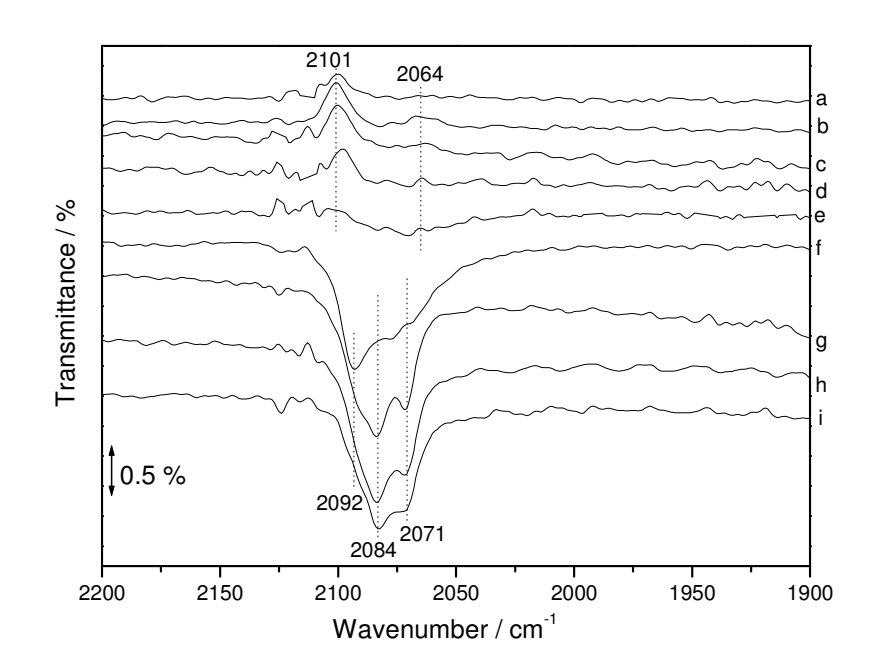


**Figure 3-20** FT-RAIRS spectra of CO adsorbed on  $TiO_2$  supported Cu as a function of the overlayer's coverage: a) 0.78 ML, b) 1.36 MLE, c) 1.68 MLE, d) 2.85 MLE, e) 4.48 MLE, f) 6.37 MLE, g) 8.25 MLE, h) 8.95 MLE, i) 15.17 MLE. Spectra collected at CO saturation coverage.

Figure 3-20 represents FT-RAIRS spectra collected at CO saturation coverage as a function of Cu coverage. Up to 2.85 MLE spectra were characterised by a transmission band around 2101 cm<sup>-1</sup>. As mentioned earlier this wavenumber value is in very close proximity to the values observed for CO bound on a variety of Cu terminations such as (211); (311) and (755) facets. Hence it can be assumed that these Cu islands could accommodate structures with high Miller index faces. The origin of this phenomenon though is difficult to determine. A possible explanation could involve the nature of TiO<sub>2</sub>

sites where nucleation took place. As mentioned in the Introduction, STM studies performed during the RT deposition of Cu on a  $TiO_2(110)$  single crystal revealed that at the early stages of nucleation most clusters were located at step edges of the substrate.<sup>89</sup> Although in this case the Cu coverage of the surface reached higher values, still one would expect the majority of the islands to be at these step sites. This preferential nucleation could affect the formation of specific structures on the Cu clusters leading to the characteristic CO adsorption bands observed here. The existence of the transmission band for coverages up to 2.85 ML would indicate that Cu clusters of these sizes were not capable of transforming the character of the local dielectric field into metallic. According to Table 3-1 the sizes corresponded to  $3.7 \pm 0.6$  nm, for 2.85 MLE Cu. Finally for all the above coverages the LEED pattern observed was that of  $TiO_2(110)$ .

A special note has to be made regarding plot e of Figure 3-20, which represents the FT-RAIRS spectrum collected at 4.48 MLE Cu coverage after saturation with CO. Indeed, the appearance of the spectrum was complex as both transmission and absorption bands were recorded. The absorption band was manifested as a broad peak centred around 2070 cm<sup>-1</sup>, while the transmission band appeared as a less intense peak situated at 2100 cm<sup>-1</sup>. This result hints at a transition of the local dielectric field, with its character changing from reflecting the semiconducting support to that of the metallic overlayer. This coverage value appeared to be a threshold, after which no transmission bands were observable in FT-RAIRS spectra. According to Table 3-1 this should correspond to Cu clusters with an average size of  $4.2 \pm 0.6$  nm. Upon comparing this behaviour with FT-RAIRS spectra collected from other TiO<sub>2</sub>(110) supported metals, an interesting observation can be made. For Pd supported clusters the switching of infrared modes from transmission to absorption occurred for clusters with sizes above 5 nm, 127 while for Rh supported overlayers the threshold coverage was estimated at ca. 15 MLE, 126 which corresponds to an approximate thickness of 4 nm, assuming a nearest neighbour distance of 2.67 Å for close packed fcc Rh. Hence, for all three TiO<sub>2</sub>(110) supported overlayers the transformation of the local dielectric field occurred over a narrow size region, ca 1 nm. Since the dielectric function of the oxide support remains constant, the transformation of the local dielectric field could be associated with a change in the dielectric function of the

metal clusters. In the optical region such phenomena have been observed as in the case of Au nanoparticles embedded in Al<sub>2</sub>O<sub>3</sub> matrix.<sup>131</sup> These authors observed a significant change in the dielectric function of the Au nanoparticles, when the size of the latter decreased below 3.5 nm. Significant differences in the optical response as a function of particle size have also been reported by Bigot *et al.* upon studying Cu and Ag nanoparticles embedded in transparent matrixes.<sup>132</sup>

FT-RAIRS spectra collected after the deposition of 6.37 MLE Cu were characterised by bands attributed to Cu(111), Cu(110) and Cu(100) adsorption sites. As mentioned in Section 3.3.1.2, the size of the as-deposited Cu overlayers was sufficiently large to induce a metallic character to the local dielectric field. Consequently, only absorption peaks were observed in FT-RAIRS spectra. In spectrum f of Figure 3-20, the main absorption peak corresponded to CO molecules adsorbed on Cu(110) facets. This would indicate that the major formation adopted by the Cu overlayer was that of Cu(110), although the intensity of the other two bands, reduced only by ca. 20% relative to the 2092 cm<sup>-1</sup> one, hinted that Cu(100) and Cu(111) were not minor adsorption sites. Indeed by increasing the coverage to 8.25 MLE of Cu, the two absorption bands at 2084 and 2071 cm<sup>-1</sup> became the dominant features in the spectrum. Consequently at this coverage the major adsorption sites must have been Cu(100) and Cu(111). Nevertheless the presence of a shoulder at 2092 cm<sup>-1</sup> would be consistent with the existence of Cu(110) sites as well.

In general, all the above results highlight the presence on the TiO<sub>2</sub>(110) surface of multifaceted Cu overlayers. For the low coverage regime, overlayers were dominated by structures accommodating high Miller index facets. On the other hand upon increasing Cu coverage, these structures were transformed into the most thermodynamically favoured, which are the low Miller index (110), (100) and (111). The presence of different Cu facets has indeed been confirmed by TEM studies of this system, although much higher Cu thicknesses, above 20 nm, were examined. <sup>88, 92, 100</sup> For Cu(110) and Cu(111) Lu and Cosandey proposed an epitaxy parallel to TiO<sub>2</sub>[001] and TiO<sub>2</sub>(110) respectively, <sup>88</sup> while Wagner *et al.* proposed the growth of Cu(100) parallel to TiO<sub>2</sub>[1ī0] direction. <sup>92, 100</sup> A note has to be made regarding the interpretation of the intensity of bands of Figure 3-20.

It has been previously reported that bands at higher frequency tend to borrow intensity from bands with lower frequency values. 54-56, 98 Nevertheless, we believe that this is not the case here as due to the size of the Cu overlayers, the CO oscillators adsorbed on the different facets are separated, hence no intensity borrowing can take place. However, for the smaller particles described in Section 3.3.1.1 the issue of intensity borrowing cannot be excluded. Finally, there was not much difference between the FT-RAIRS spectra collected after CO adsorption on 8.25 ML of Cu and on Cu films, 8.95 and 15.17 MLE respectively. Two peaks at 2084 and 2071 cm<sup>-1</sup> were present in all of them indicating that the Cu overlayers accommodated structures similar to the (100) and (111) formations. Some (110) sites must have also been present giving rise to the small shoulder around 2091 cm<sup>-1</sup>.

As mentioned in the previous paragraph, FT-RAIRS spectra collected after the CO adsorption on 8.25 MLE of Cu bore many similarities with those from the thin films. On the other hand though, the data collected from XPS and LEED revealed interesting differences. Figure 3-21 represents the XPS spectra of the Ti(2p) energy region collected after Cu deposition of 8.25 MLE and of the thin films. Both Cu films blocked the Ti signal whereas for the 8.25 MLE overlayer a small feature due to Ti(2p<sub>3/2</sub>) was observable. No LEED pattern was observed for the Cu islands or the 8.95 MLE thin film whereas a faint hexagonal pattern was observed for the 15.17 MLE film. Hence combining the results from the two techniques several points could be made. The first is that after 8.25 MLE deposition some portion of the oxide surface still remained uncovered. It was substantial enough to contribute to the XPS spectrum but not enough to produce a pattern on the fluorescent LEED screen. The second is that the thickness of the 8.95 MLE film was large enough to block photoelectrons and diffracted electrons originating from the support. Finally, long range order of the Cu overlayer was present only on the 15.17 MLE film as a faint (111) LEED pattern was observed.

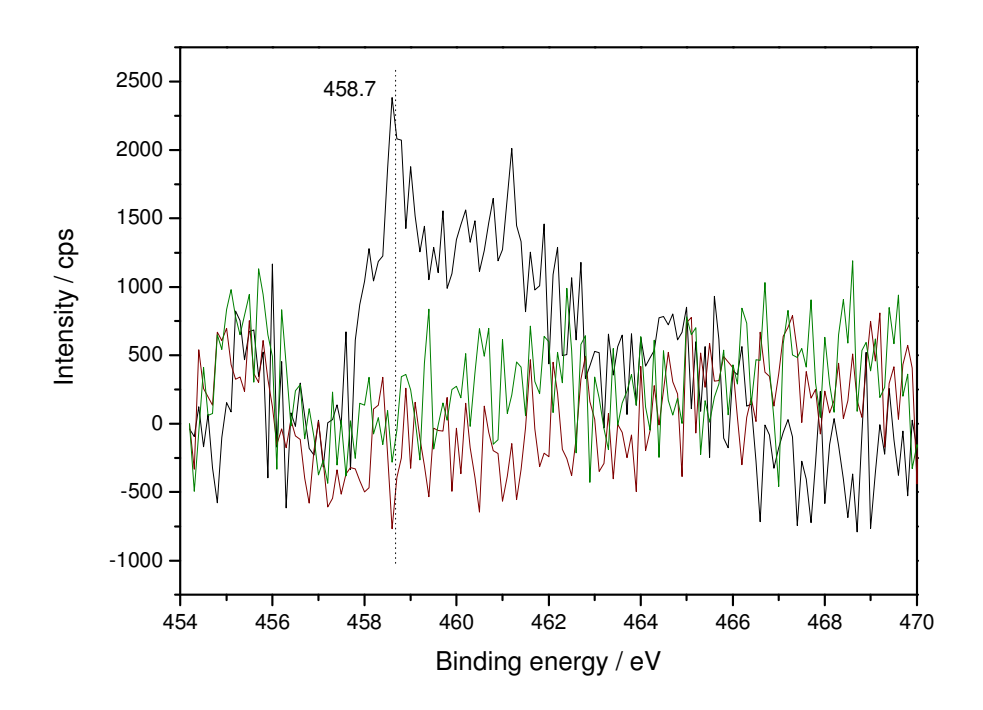


**Figure 3-21** Ti 2p energy region after three different depositions: a) 8.25 ML of Cu (black line), b) 8.95 MLE film (red line), c) 15.17 MLE film (green line).

A remark that has to be made at this stage correlates with the interpretation of the Ti(2p) signal of 8.25 MLE Cu, Figure 3-21. As argued previously, it belonged to some portion of the oxide support being left uncovered by the deposited material. An opposing argument to the latter would be that the overlayer had formed a film rather than islands, and that the signal of the Ti peak was due to photoelectrons escaping this metallic film. Thus in order to understand which of the previous arguments was valid, a calculation was made of the inelastic mean free path (IMFP) of these photoelectrons. Using Equation (2-12) provided by *Seah and Dench*, <sup>72</sup> Section 2.3.2, it was calculated that for electrons with kinetic energy of 794.9 eV (Ti(2p<sub>3/2</sub>) at 458.7 eV binding energy) the IMFP for Cu would be 5.508 MLE. Therefore if the 8.25 MLE overlayer had actually formed a film on the surface, no photoelectrons from the oxide support could have been detected.

Another interesting information extracted from XPS spectra relates with the position of  $\text{Cu}(2p_{3/2})$  peak. Figure 3-22 represents the binding energy value of  $\text{Cu}(2p_{3/2})$  peak as a function of Cu coverage. As it can be observed, increasing Cu coverage (or Cu

cluster size) resulted in a decrease of the Cu(2p<sub>3/2</sub>) peak position. Within experimental error,  $\pm 0.1$  eV, the value of bulk Cu(2p<sub>3/2</sub>) (at 932.7 eV)<sup>87</sup> was obtained for coverages above 4 MLE, or according to Table 3-1 for clusters with average size above 4 nm. The trend observed here is commonly observed for metal clusters supported on relatively inert substrates, 133 as for example for Au supported on different substrates (C, SiO2 and Al<sub>2</sub>O<sub>3</sub>), <sup>134</sup> Ag and Pd supported on amorphous C, <sup>135</sup> and Pd supported on TiO<sub>2</sub>(110). <sup>136</sup> This shift of the core level binding energy has been attributed to the inability of small clusters to neutralise effectively the hole left behind by the ejection of a photoelectron, <sup>133</sup>, <sup>137</sup> hence final state effects are responsible for the observed shift. Mason though has proposed that for certain substrates as C and SiO<sub>2</sub> changes in the initial-state electronic structure can account for the core level shifts. 134 Based on XPS spectra collected near the Fermi level, he has shown that the population of valence states of smaller clusters is quite different from larger ones, thus their initial state electronic structure will be quite different. For C supported Pd clusters, Kuhrt and Harsdorff have proposed that both initial and final state effects take place, with the latter contributing to the core level shift and the former to a narrowing of the valence band. Despite the different explanations though, the trend observed in Figure 3-22 for the Cu(2p<sub>3/2</sub>) peak position is consistent with previously published findings.

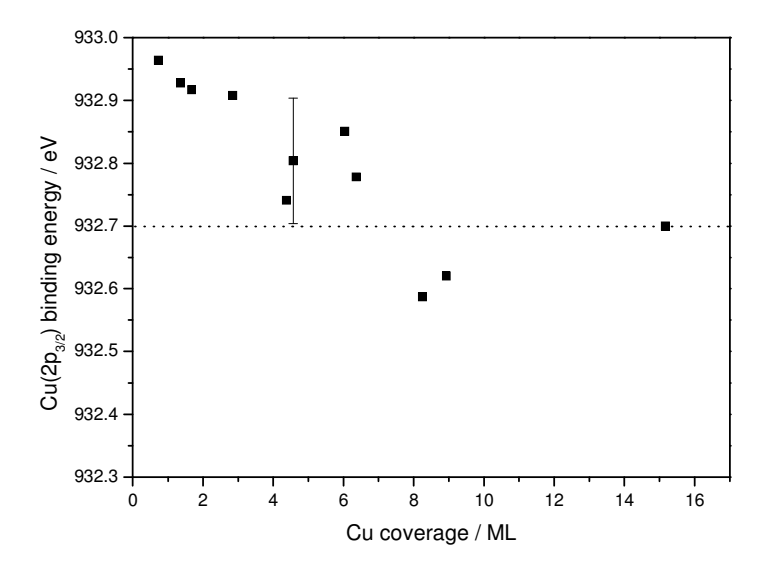


**Figure 3-22**  $Cu(2p_{3/2})$  binding energy value as a function of Cu coverage. The dotted vertical line represents the literature value of  $Cu(2p_{3/2})$  at 932.7 eV.<sup>87</sup>

Figure 3-23 represents the FT-RAIRS spectra collected after CO adsorption on the annealed Cu/TiO<sub>2</sub> system as a function of Cu coverage. As it can be observed, several changes were introduced in the spectra as a consequence of the annealing procedure. For example at the low coverage regime, a tendency was observed for peaks assigned to CO bound on high Miller index sites to shift towards lower wavenumber values. For higher coverages the transformation of absorption to transmission bands was observed. Finally for Cu thin films, a single absorption band attributed to Cu(111) adsorption sites was recorded.

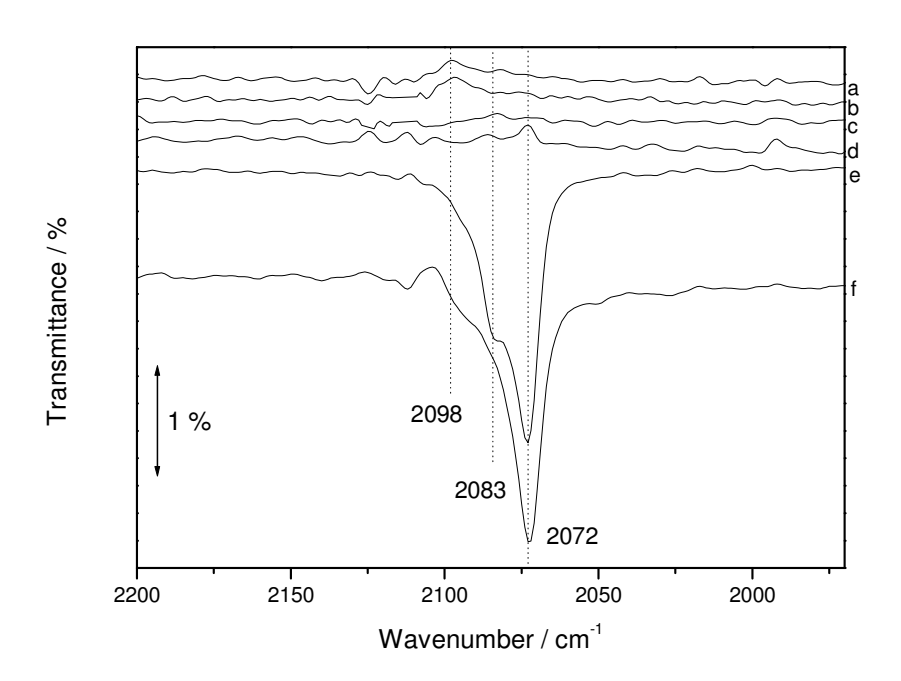


**Figure 3-23** FT-RAIRS spectra of CO adsorbed on TiO<sub>2</sub> supported Cu, after annealing at 650 K, as a function of the overlayer's coverage: a) 1.68 MLE, b) 2.85 MLE, c) 6.37 MLE, d) 8.25 MLE, e) 8.95 MLE film, f) 15.17 MLE film.

One of the main consequences of the annealing process is agglomeration of smaller clusters and formation of larger ones. The mechanism of this process, also know as Ostwald ripening,<sup>87</sup> has been described by Campbell *et al.* for Cu islands deposited on a ZnO substrate,<sup>104</sup> and has as follows. Upon annealing Cu atoms that are located on the first few layers of the island move upwards as the energy barriers, previously inaccessible, can

be overcome. In addition smaller Cu clusters with increased mobility attach themselves to the larger ones, providing in this way new atoms on the first layers, which later are going to move upwards. The end result of all these processes is first the formation of large particles, primarily in height, and secondly an increase in the surface area of the substrate. The XPS data collected in this study are in agreement with the previous findings. For all Cu coverages, spectra recorded at the Ti(2p) energy region after anneal exhibited an increase in the Ti(2p<sub>3/2</sub>) peak area when compared with the values obtained after 300 K deposition. On the other hand, Cu(2p<sub>3/2</sub>) peak area measured after annealing had a value lower than the one measured after the 295 K deposition. The reason being that as clusters grew bigger, fewer photoelectrons contributed to the spectra since the ones originating from the core of the clusters could not reach the detector. Similar behaviour has been observed for various oxide supported Cu systems such as Cu/WO<sub>x</sub>, <sup>138</sup> Cu/ZnO<sup>107</sup> and Cu/TiO<sub>2</sub>. <sup>41, 87, 101</sup> These results are summarised in Table 3-3, where a comparison is made between the area values of Cu(2p<sub>3/2</sub>) and Ti(2p<sub>3/2</sub>) peaks before and after annealing at 650 K.

**Table 3-3** A comparison of  $Cu(2p_{3/2})$  and  $Ti(2p_{3/2})$  peak areas calculated from XPS spectra collected after 300 K PVD and after annealing at 650 K, for different Cu coverages. Also shown is the  $Cu(2p_{3/2})$  peak area ratio between annealed and deposited surface. All ratios have values below 1 indicating that the  $Cu(2p_{3/2})$  signal of the as deposited islands was higher.

Coverage / MLE	Area after deposition		Area after anneal		Cu ratio
	Cu(2p <sub>3/2</sub> )	Ti(2p <sub>3/2</sub> )	Cu(2p <sub>3/2</sub> )	Ti(2p <sub>3/2</sub> )	
1.68	57170.18	17287.96	28872.35	25442.63	0.505025
2.85	78248.17	17011.29	29992.64	17594.05	0.383301
6.37	159582.8	8251.701	65874.78	12143.33	0.412794
8.25	286869.8	7932.151	50243.03	17469.18	0.175142
8.95	249380.6	0	152941.5	4009.406	0.613285
15.17	226294.4	0	136657.1	0	0.603891

As discussed in Section 3.3.1.2, FT-RAIRS results collected after annealing at 650 K, Figure 3-23, would appear to contradict the XPS findings. The reason for this discrepancy is that the transformation of FT-RAIRS modes from absorption to transmission observed for the medium coverage islands is indicative of formation of Cu

particles not sufficiently large to retain the metallic character of the local dielectric field. This difference though can be resolved by assuming that Cu grows on the  $TiO_2(110)$  surface by a complex type of mode. The latter is a mixture of the Volmer-Weber and Stranski-Krastanov types, resulting initially in 2D islands that do not wet the entire surface and upon which 3D structures are formed. Upon annealing these complex formations were transformed into 3D Cu particles, which exhibited a high dispersion on the  $TiO_2(110)$  surface.

The annealing process resulted also in the structural transformation of Cu islands and films. A tendency was observed for the formation of thermodynamically favoured structures. For the low coverage islands, the red shift of the v(CO) peak and the appearance of the broad feature around 2082 cm<sup>-1</sup> were indicative of a change from high to low Miller index like structures. For larger islands and films, annealing appeared to transform the majority of their sites into Cu(111). Especially for the metallic films, FT-RAIRS spectra were dominated by a sharp peak at 2072 cm<sup>-1</sup> and furthermore a (111) pattern was observed with LEED, Figures 3-16 and 3-19. This behaviour is in agreement with the one observed for ZnO(0001)-O supported Cu. More precisely, using TPD they observed that upon annealing both submonolayer and multilayer islands, CO desorbed at temperatures associated with adsorption on Cu (111) sites. On the contrary, as-deposited islands exhibited TPD peaks associated CO bound on Cu(110) sites.

### 3.3.3 Interaction with O<sub>2</sub>

In the previous sections a detailed investigation was presented regarding the structural properties of  $TiO_2$  supported Cu particles and films. This study would have been incomplete without any examination of the catalytic properties of this system. Hence, the interaction of  $O_2$  with CO adsorbed on various Cu coverages was examined, and these results are presented below.

Figure 3-24 represents spectra collected before and after O<sub>2</sub> exposure for a 2.85 MLE Cu coverage. Prior to the oxygen dose, the surface was saturated with 100 L of CO which resulted in the sharp peak at around 2099 cm<sup>-1</sup>. As mentioned earlier this band can be attributed to CO bound on sites with high Miller index facets. As evident from Figure 3-24, the introduction of O<sub>2</sub>, 137 L, resulted in the complete disappearance of the v(C-O) band from the spectrum. Two reasons could be responsible for this behaviour. The first relates to CO displacement due to oxygen molecules. The other one is consistent with a reaction taking place between adsorbed CO and O<sub>2</sub>. These two possibilities are going to be examined in more detail further on as such a discussion would be more inclusive after the results for higher Cu coverages are presented.

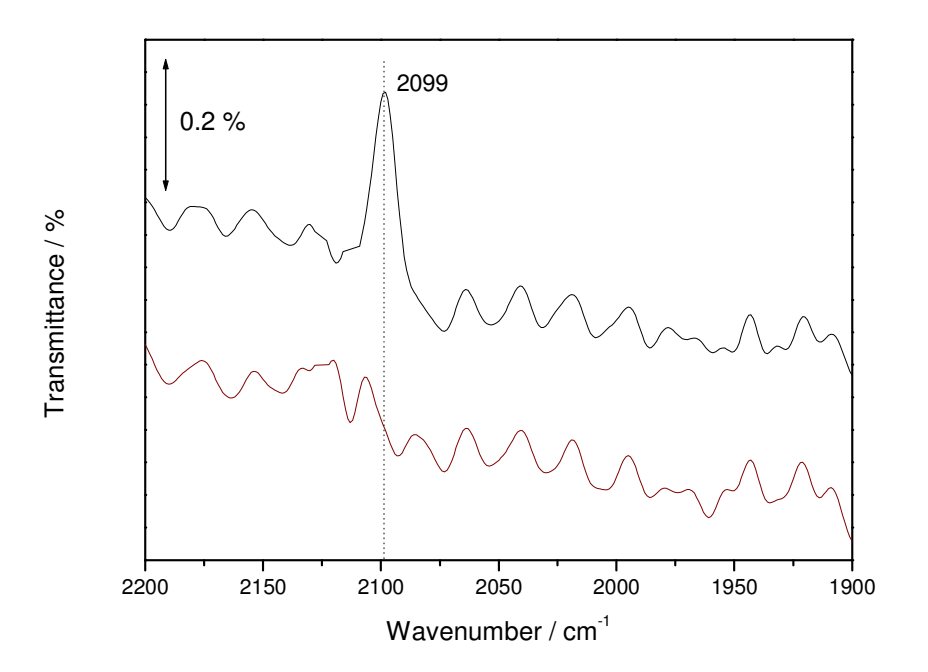


**Figure 3-24** FT-RAIRS spectra of the v(C-O) region recorded before (black line) and after 137 L of  $O_2$  exposure (red line). Before exposing to molecular oxygen the 2.85 MLE overlayer was saturated with 100 L of CO.

Thus Figure 3-25 represents the spectra collected pre and post  $O_2$  exposure for a Cu coverage of 6.37 MLE. It becomes apparent that a different behaviour was observed for this overlayer. Upon exposing the surface to  $O_2$  the FT-RAIRS spectrum of the adsorbed CO was transformed in three major ways. To begin with the intensity of the main absorption feature situated at 2092 cm<sup>-1</sup> was reduced. Secondly the small band at 2078 cm<sup>-1</sup>

 $^{1}$  disappeared completely, and finally a new feature appeared on the spectrum with the form of a small shoulder situated around 2108 cm $^{-1}$ . As with the thinner overlayer, some CO molecules were removed from the surface either through displacement or via reaction with  $O_2$  but contrary to the previous system, CO was left on the surface. In addition, the appearance of a new feature at higher wavenumbers would be in accordance with an interaction between the adsorbed CO and  $O_2$ . It would also be useful here to remember the spectrum of Figure 2-10, where similar behaviour was observed for CO adsorbed on a  $O_2$  covered Cu(110) crystal.

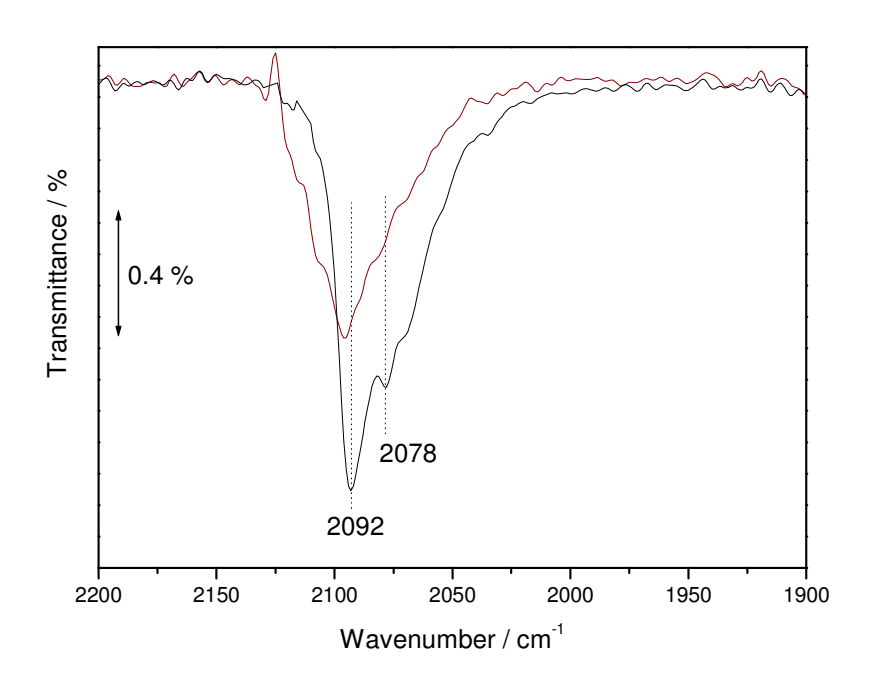


**Figure 3-25** FT-RAIRS spectra of the v(C-O) region recorded before (black line) and after 137 L of  $O_2$  exposure (red line). Before exposing to molecular oxygen the 6.37 MLE overlayer was saturated with 100 L of CO.

Finally the interaction of molecular oxygen with adsorbed CO was also studied for the thick Cu film, 15.17 MLE. Figure 3-26 represents the FT-RAIRS spectra collected before and after the introduction of O<sub>2</sub> inside the chamber for the annealed film. For this overlayer, the structure of which was dominated by the (111) formation, significant changes where not observed. Indeed only a small reduction in the intensity value of the 2072 cm<sup>-1</sup> peak was detected.

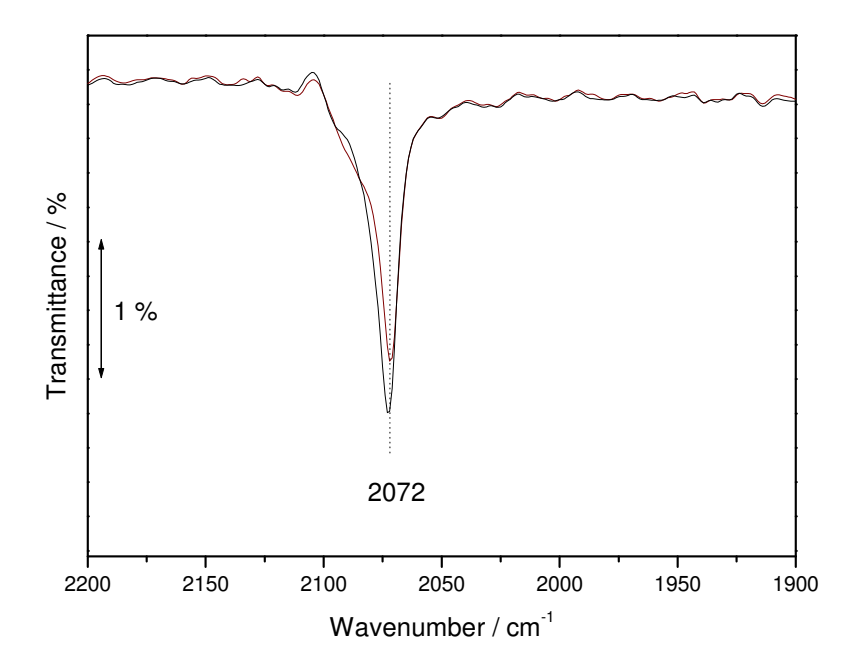


**Figure 3-26** FT-RAIRS spectra of the v(C-O) region recorded before (black line) and after 137 L of  $O_2$  exposure (red line). Before exposing to molecular oxygen the annealed (650 K) film was saturated with 100 L of CO.

According to the last three figures, the introduction of molecular oxygen induced different responses to FT-RAIRS spectra of various Cu coverages. The most noticeable changes were observed for the low and medium coverage overlayers, whereas little to no change was observed for the Cu film. A possible explanation for the observed differences could lie in the size of the Cu particles. Over the past few years it has been established that TiO<sub>2</sub> supported metal nanoparticles, Au in particular, exhibit enhanced catalytic activity towards CO oxidation when compared with that of bulk metals. <sup>139, 140</sup> For 4 and 5 nm size Cu particles (2.85 and 6.37 MLE respectively) an interaction appeared to have taken place between O<sub>2</sub> and CO. On the other hand little interaction was observed for the thin Cu film. The observed differences could alternatively be explained by taking into consideration the coverage dependent structural changes, described previously. As demonstrated in Section 3.3.2 small Cu particles exhibited structures with high miller index formations, whereas the structures of larger particles resembled the (110), (100) and (111) facets. Previous studies on Cu single crystals have shown that the crystal structure can affect the catalytic

activity. For example Fu and Somorjai have shown that the (311) surface of Cu is more active towards the CO oxidation than the Cu(110) one. <sup>141</sup> In addition Iwasawa *et al.* have demonstrated that the catalytic reactivity of oxygen atoms towards  $CO_2$  production is much higher on a Cu(110) than a Cu(111) surface. <sup>142</sup>

As stated earlier, the disappearance or alteration of CO bands from infrared spectra collected from the 2.85 and 6.37 MLE overlayers, cannot constitute a proof that a reaction took place. Another explanation could involve the displacement of the adsorbed species by the molecular oxygen as the latter binds stronger to Cu than CO. Nevertheless there are reports in the literature that a reaction can take place, despite the fact that CO is adsorbed first. For example, Crew and Madix observed that exposing a partially oxygen and CO covered, Cu(110) surface to oxygen at 150 K, resulted in CO oxidation.<sup>68</sup> They claimed that the partially oxidised surface was responsible for the catalytic activity. Of course in the experiments reported here there was no preadsorption of oxygen onto the Cu particles, but the presence of surface lattice O might have played a similar role. Boccuzzi and Chiorino have proposed two possible independent pathways for the oxidation of CO on Cu/TiO<sub>2</sub>. The first involves the production of CO<sub>2</sub> from the direct interaction of O<sub>2</sub> with CO adsorbed on the metallic particles. The second one involves the formation of carbonate species from the interaction of CO with oxygen from the surface lattice. They propose that the latter is enhanced by the O<sub>2</sub> of the gas phase.

### 3.4 Conclusions

The growth of Cu clusters and films on the  $TiO_2(110)$  surface has been investigated, using CO as a probe molecule. According to the results presented in this Chapter, a dependence has been found between the size of Cu overlayers and the structure that their surfaces accommodate. For the smallest clusters, up to ca 3 nm, high Miller index structures were indentified based on the vibrational properties of adsorbed CO. As Cu overlayers increased in size, these structures were transformed to the more

-

<sup>&</sup>lt;sup>v</sup> Experiments were actually performed with preadsorbed O<sub>2</sub> but no CO adsorption was detectable with FT-RAIRS for different overlayer coverages.

thermodynamically stable formations of (110), (100) and (111). XPS results revealed that even for the highest coverages, a portion of the TiO<sub>2</sub>(110) surface was still left uncovered. Thin Cu films exhibited the same structural characteristics as the 8.25 MLE clusters, although according to XPS results complete wetting of the oxide surface took place. A size dependence shift of the core level binding energy of Cu(2p<sub>3/2</sub>) was also observed, which was attributed to ineffective screening of core holes created during the photoelectron process. Upon annealing XPS provided evidence of coalescence for all coverages examined, although the transformation of FT-RAIRS bands from absorption to transmission for the 6.37 and 8.25 MLE overlayers hinted the formation of highly dispersed Cu particles. The accommodated surface structures were also affected by annealing at 650 K, with Cu(111) being the major post annealing formation. This effect was especially pronounced for Cu thin films, with a Cu(111) hexagonal pattern observable in LEED and the FT-RAIRS band attributed to CO adsorbed on Cu(111) sites dominating the spectra. From the LEED pattern collected after annealing the 8.95 MLE overlayer, an epitaxial relation between Cu and TiO<sub>2</sub>(110) was also found. Finally, the interaction of molecular oxygen with the already adsorbed CO was investigated. According to FT-RAIRS spectra, this interaction was pronounced for the low Cu coverage overlayers, whereas no interaction was observed for the annealed thin Cu film. A summary of FT-RAIRS, XPS and LEED findings is presented in Table 3-4 for characteristic Cu coverages.

**Table 3-4** A summary of results obtained from XPS, FT-RAIRS and LEED for 4 characteristic Cu coverages, for as deposited and annealed overlayers. Coverages are selected as limits after which important changes were recorded in the three techniques. The last row compares the results collected via FT-RAIRS following the interaction of the system with O<sub>2</sub>. Band positions are given in cm<sup>-1</sup>, while bold numbers represent the dominant peak.

Cu coverage >	2.85 / MLE	6.37 / MLE	8.95 / MLE	15.17 MLE		
Technique ▼						
	High Miller index facets	(110), (100), (111) facets	(110), (100), (111) facets	(110), (100), (111) facets		
FT-RAIRS	Transmission band (2100)	Absorption bands ( <b>2092</b> , 2084, 2071)	Absorption bands (2092, <b>2084</b> , 2071)	Absorption bands (2092, <b>2084, 2071</b> )		
XPS	Core level shift	Bulk value	Bulk value	Bulk value		
LEED	TiO <sub>2</sub> (110) pattern	No pattern	No pattern	Faint (111) Cu pattern		
	Annealing at 650 K					
	High Miller index and (111)	(100) and (111) facets	(111) major facet, (100) as	(111) facet		
	facets	Transmission bands (2083, <b>2072</b> )	well			
FT-RAIRS	Transmission bands (2098, 2072)		Absorption bands (2072, 2083)	Absorption band (2072)		
XPS	Evidence of coalescence	Evidence of coalescence	Evidence of coalescence	-		
LEED	TiO <sub>2</sub> (110) pattern	TiO <sub>2</sub> (110) pattern	Mixed (110) TiO <sub>2</sub> and (111) Cu pattern	(111) Cu pattern		
Interaction with O <sub>2</sub>						
FT-RAIRS	Strong	Little	-	None		

# **Chapter 4**

# The Photolysis of MoCO<sub>6</sub> on TiO<sub>2</sub>(110)

As an alternative to Physical Vapour Deposition, Mo particles can potentially be prepared via Organometallic Chemical Vapour Deposition using Molebnynum Hexacarbonyl, Mo(CO)<sub>6</sub>, as the organometallic precursor. Previous studies though have shown that common thermal decomposition is not adequate as the prepared Mo particles suffered from C contamination.<sup>62</sup> Consequently, in this Chapter the photolysis of adsorbed Mo(CO)<sub>6</sub> is examined as a different method of removing the CO ligands.

### 4.1 Introduction

Before presenting the various studies relevant to the photolysis of Mo(CO)<sub>6</sub> in the gas phase or in various media and supports, it is important to explain why this organometallic compound (and the other two transition metal hexacarbonyls of the same periodic group) undergoes such transformations when irradiated with UV light. The Mo(CO)<sub>6</sub> molecule is susceptible to photodecomposition under UV radiation, as according to its electronic spectrum several transitions take place in this energy region. These transitions are identified by the appearance in electronic spectra of absorptions due to ligand field transitions or metal to ligand and ligand to metal excited states.<sup>143</sup> The identification and assignment of these transitions was performed in the late 60s by Gray and Beach, and their findings are summarised in Table 4-1.<sup>144</sup>

**Table 4-1** Mo(CO)<sub>6</sub> transitions and their assignment by Gray and Beach. The equivalent energies are calculated here using E=hv.

Wavelength / nm	Wavenumber / cm <sup>-1</sup>	Energy / eV	Assignment
319	31350	3.89	$^{1}A_{1g} \rightarrow ^{1}T_{1g}$
286.7	34880	4.33	${}^{1}A_{1g} \rightarrow {}^{1}T_{1u}$
265.3	37680	4.68	$^{1}A_{1g} \rightarrow ^{1}T_{2g}$
228	43860	5.44	$^{1}A_{1g} \rightarrow ^{1}T_{1u}^{(2)}$
193	51810	6.43	$t_{2g}(\pi) \to t_{2g}(\pi^*)$

### 4.1.1 Photolysis of Mo(CO)<sub>6</sub> in Different Phases: Gas, Matrix Isolation and Solution.

The photolysis of  $Mo(CO)_6$  in the gas phase can proceed via two alternative paths. The first involves dissociation of the molecule due to single photon absorption whilst the second involves multi-photon excitations. Eventually each path leads to the formation of different photoproducts. According to different authors, the fluence of the light used for the photodecomposition determines which process will be adopted.

During the single photon excitation process, photon absorption by the initial molecule results to the ejection of one CO and the production of an unsaturated fragment in an excited state. The excess in energy leads to the ejection of another CO, with the process continuing in a similar manner until the retained energy stops being adequate for decomposition to continue. These can be summarised as:

$$Mo(CO)_{6} + h\nu \rightarrow Mo(CO)_{5}^{*} + CO$$

$$Mo(CO)_{5}^{*} \rightarrow Mo(CO)_{4}^{*} + CO$$

$$Mo(CO)_{4}^{*} \rightarrow Mo(CO)_{3}^{*} + CO$$

$$(4-1)$$

Both Ishikawa *et al.* and Ganske *et al.* using Time Resolved Infrared Spectroscopy (TRIS) independently found that the major photofragments due to the single photon absorption were Mo(CO)<sub>5</sub>, Mo(CO)<sub>4</sub> and Mo(CO)<sub>3</sub>. According to these studies the population of each photofragment depended on the laser energy used. Thus the

dominant features of the spectra for lower excitation energy were bands due to  $Mo(CO)_5$ , whereas higher energy photons resulted in the formation of mainly  $Mo(CO)_3$ . The photofragments also reacted either with the parent molecule to form more complicated molecules, for example  $Mo(CO)_6 + Mo(CO)_5 \rightarrow Mo_2(CO)_{11}$ , or with CO to recombine into the previous fragment, for example  $Mo(CO)_4 + CO \rightarrow Mo(CO)_5$ . The geometry adopted for the three photofragments had as follows:  $C_{4v}$  for  $Mo(CO)_5$ ,  $C_{2v}$  for  $Mo(CO)_4$  and finally  $C_{3v}$  for  $Mo(CO)_3$ . The above mechanism of sequential CO elimination was also adopted by Venkataraman *et al.* <sup>147</sup> Based on qualitative molecular orbital arguments they attributed the first step to a repulsive overlap of the  $5\sigma$  orbital of CO and a hybrid metal orbital. The following steps were explained as statistical like decompositions. This justification though was not confirmed by the experimental and theoretical treatment of Cavanagh *et al.*, although they did not propose an alternative one. <sup>155</sup>

Photofragments with lower number of CO, i.e. Mo(CO)<sub>2</sub>, Mo(CO) or even neutral or ionised Mo, can be produced via the multi-photon excitation path, which, as stated earlier, is accessible by increasing the fluence of the laser used for the photolysis. Tyndall and Jackson suggested that this process proceeds via a combination of phenomena which comprise of both sequential and direct dissociation channels. In their interpretation the latter involved the direct absorption of two or three photons by the parent molecule whilst the former involved the absorption of a second photon by one of the original photoproducts. These photoproducts were also observed by Chen *et al.* and Yu *et al.* by increasing the energy of the excitation light.

Photodissociation of the metal carbonyl in matrix isolation or in solution has been shown to yield results different from the ones for the gas phase. In one of the first studies performed, Perutz and Turner observed that the photolysis of M(CO)<sub>6</sub> (M=Mo,Cr,W) in a variety of matrices resulted in the generation of M(CO)<sub>5</sub>. A weak chemical bond was found to exist between the unsaturated carbonyl and the matrix gas. Similar results were found by later studies following the photolysis of these carbonyls in noble gas matrices where the formation of M(CO)<sub>5</sub>L (L=Ar, Kr and Xe) was observed. Is noble gas matrices where the formation of M(CO)<sub>5</sub>L (L=Ar, Kr and Xe) was observed. Is no solution, photolysis has been found to proceed in a analogous way. After its

production, the unsaturated pentacarbonyl forms a bond with the solution,  $Mo(CO)_5(Sol)$ . Further dissociation of the molecule is prevented due to the efficient energy relaxation imposed by the bond. Interestingly though, prolonged photolysis of  $Mo(CO)_6$  in a  $CH_4$  matrix at 20 K, resulted in the production of two secondary photofragments  $Mo(CO)_4$  and  $Mo(CO)_3$ . A possible explanation could involve the absorption of a second photon by  $Mo(CO)_5$ .

# 4.1.2 Adsorption and Photodecomposition of Mo(CO)<sub>6</sub> on Si and Metals

One of first single crystal materials chosen as a substrate for the adsorption and subsequent photodecomposition of Mo(CO)<sub>6</sub> was Si. This was primarily thanks to the potential application of Mo in microelectronic applications, when grown on semiconducting surfaces via photo assisted CVD. A brief summary of these studies is going to be presented in the following paragraph.

Mo(CO)<sub>6</sub> can adsorb on a Si single crystal surface at liquid nitrogen temperatures forming a physical bond,<sup>167</sup> with TDS studies revealing zeroth order desorption kinetics.<sup>165, 168</sup> Similar thermal desorption spectra have also shown that the molecule adsorbs on the surface without any dissociation.<sup>167</sup> Furthermore the O<sub>h</sub> symmetry exhibited in the gas phase is to a large extent also present in the Si supported carbonyls.<sup>169</sup> Illuminating the Mo(CO)<sub>6</sub> –Si system with UV light (either from a laser or from a continuous source) results in the photodecomposition of the adsorbed molecule, with the cleavage of the first CO bond being identified as the rate determining step.<sup>168</sup> By performing HREELS Gluck *et al.* proposed that the major photofragments included Mo(CO)<sub>5</sub>, Mo(CO)<sub>4</sub> and Mo(CO)<sub>5</sub>.<sup>167</sup> Richter *et al.* however, using FT-RAIRS could only confirm the presence of Mo(CO)<sub>5</sub>.<sup>170</sup> Unsaturated photofragments were also observed in TDS spectra.<sup>168</sup> Nevertheless Mo(CO)<sub>x</sub> (x=1,2) or Mo species have never been reported. This would indicate that quenching of highly excited states was favoured by adsorption on the Si surface. According to a proposed mechanism for the photolytic reaction, the adsorption of sequential photons first by the initial molecule and then by the

photofragments leads to their photodissociation.<sup>167</sup> Interestingly Resonance Enhanced Multiphoton Ionisation (REMPI) studies of the CO molecules produced from the photolysis revealed two different desorption channels.<sup>171</sup> The first involved CO molecules that underwent minimal interactions with either Si or the adlayer. The second one involved molecules that did interact with Si or the adlayer. Finally the photolysis of thick Mo(CO)<sub>6</sub> layers resulted in polymerisation, which was exhibited by the appearance of Mo<sub>2</sub>(CO)<sub>6+x</sub> species.<sup>169</sup>

Significant amount of work has also been perfored on the adsorption and photodecomposition of Mo(CO)<sub>6</sub> supported on various metal substrates. At low temperatures, ca 100 K, Mo(CO)<sub>6</sub> can adsorb either molecularly or via dissociation depending on the substrate. For example on Cu(111)<sup>172</sup>, Ag(111)<sup>173</sup> and Pt(111)<sup>174</sup> it has been found to physisorb as a molecule, whereas on Ru(001)<sup>175</sup> and Rh(100)<sup>176</sup> is adsorbed dissociatively. It has been proposed that the interaction of CO with each surface could account for this difference. 175 CO adsorbs weakly on Cu and as a result no strong interaction can take place that could result in dissociation. On the other hand Rh adsorbs CO strongly, with a temperature of desorption at 500 K compared to 150 K for Cu. The substrate contribution to the dissociative adsorption was also demonstrated from the fact that Mo(CO)<sub>6</sub> multilayers desorbed molecularly from both Rh(100) and Ru(001). 175, 176 Similar surface effects were also observed during the photolysis of adsorbed molecules. For Rh(100) it was found that the yield of Mo(CO)<sub>6</sub> photolysis increased by an order of magnitude when a layer of CO was preadsorbed on Rh(100). This increase was explained by means of less effective quenching of the exited states by the CO layer. 176 Photodecomposition of Mo(CO)<sub>6</sub> adsorbed on Pt resulted in the formation of Mo(CO)<sub>6-x</sub> species on the surface, which were bound stronger than the parent molecule. 174

 $Mo(CO)_6$  has also been employed as a precursor for the high temperature CVD of Mo films and clusters on metallic substrates. Hrbek *et al.* have reported the deposition of metallic Mo nanoclusters on Au(111)-(22x $\sqrt{3}$ ).<sup>177</sup> During deposition the sample was kept at 500 K in order to break the Mo-CO bonds. Further annealing to 600 K was needed to fully remove the CO from the surface. Nevertheless this method was only effective for

Mo coverages below 0.15 ML. For higher coverages the Mo clusters were contaminated with C and O.<sup>178</sup> High temperature CVD (700 K) of Mo(CO)<sub>6</sub> was also employed in the deposition of Mo films on Al substrate.<sup>179</sup> Although this process resulted in the appearance of MoC and Mo<sub>2</sub>C, C was later removed by annealing to 1200 K. This last step though produced the formation of MoAl alloy. NiMo alloy was also formed following a similar CVD procedure.<sup>180</sup>

# 4.1.3 Adsorption of Mo(CO)<sub>6</sub> on Metal Oxide Surfaces

The adsorption behaviour of Mo(CO)<sub>6</sub> on high surface area alumina, Al<sub>2</sub>O<sub>3</sub>, has been extensively studied in the past. 181 On a more recent study Reddy and Brown identified two Lewis acid adsorption sites for Mo(CO)<sub>6</sub>. <sup>182</sup> On a partially dehydroxylated surface the decarbonylation of the molecule proceeded via a Mo(CO)<sub>5</sub> intermediate, before terminating with the formation of Mo(CO)<sub>3</sub>. On a fully hydroxylated surface no Mo(CO)<sub>3</sub> formation was observed although the presence of a lower subcarbonyl was identified that resulted from the decarbonylation of Mo(CO)<sub>5</sub>(OH). On both surfaces these processes were found to be reversible at room temperature. On planar alumina relative few studies have been performed, mainly by the Tysoe group whose approach was to deposit a thin alumina film on a Mo(100) substrate. 183-187 Contrary to the high surface area supports no Mo(CO)<sub>6</sub> adsorption was observed at room temperature. The hexacarbonyl was found to adsorb as a molecule on the dehydroxylated surface at 190 K. Upon progressive heating up to 245 K, the latter decomposed to Mo(CO)<sub>5</sub> and Mo(CO)<sub>3</sub> as identified by FT-RAIRS. Further heating resulted to the formation of a strongly bound adsorbate which was identified as an oxalate species. 188 Similar results were observed for the hydroxylated and partially hydroxylated surface, and the degree of decarbonylation was found to depend on the extent of hydroxylation. High temperature deposition (700 K) on hydroxylated alumina resulted in the formation of MoC. Annealing to 1500 K resulted in the removal of carbon contamination by reacting with oxygen from the substrate. 184 Bao et al. recently observed the same behaviour. 189

There are not many studies in the literature investigating the adsorption and decomposition of Mo(CO)<sub>6</sub> on planar TiO<sub>2</sub> substrates. Evans et. al. using TiO<sub>2</sub>(110) reported the physisorption of the hexacarbonyl at 150 K.<sup>62</sup> By means of FT-RAIRS they were able to identify different bands attributed both to the monolayer and multilayer. This difference was explained as a dipole coupling effect taking place in the multilayers and not as different species produced by dissociation of the monolayer. Annealing resulted in the formation of weakly bound Mo(CO)<sub>5</sub> carbonyls that desorbed above 220 K. Deposition at 400 K resulted in the formation of Mo with a substantial amount of graphitic carbon present on the surface. Analogous results have recently been reported by Prunier et. al. although their investigation hinted that some dissociation of the molecule must have taken place during adsorption at 140 K. 190 Upon annealing all the adsorbed hexacarbonyl was decarbonylated producing submonolayer coverages of Mo. In order to increase this amount they first irradiated the system with a strong photon beam (30 to 350 eV). This resulted in the formation of stable Mo(CO)<sub>x</sub> species that when annealed to 420 K produced higher Mo coverages than before. An MoO<sub>2</sub> overlayer on TiO<sub>2</sub>(110) has also been produced by the adsorption of Mo(CO)<sub>6</sub> at 673 K in UHV environment, followed by 30 min thermal treatment in air at 853 K. 191 Photodecomposition of Mo(CO)<sub>6</sub> via UV irradiation has only been reported on high surface area TiO<sub>2</sub>. <sup>192</sup> According to this study, the photooxidation of the carbonyl does not proceed via direct absorption of the irradiation and subsequent breaking of the M-CO bond. The proposed mechanism involves enhanced decarbonylation of Mo(CO)<sub>6</sub> by photoinduced electron holes of the TiO<sub>2</sub>, which will lead to MoO<sub>3</sub>.

### 4.1.4 Infrared Assignment

As it can be observed from the previous discussion, many studies have utilised infrared spectroscopic techniques to characterise the photolysis process. As this greatly facilitated our FT-RAIRS study, Table 4-2 summarises previously observed assignments. In addition Figure 4-1 represents the geometries adopted by  $Mo(CO)_6$  and its photofragments.

**Table 4-2** Infrared bands (cm<sup>-1</sup>) of Mo(CO)<sub>6</sub> and its photofragments as observed by different authors in various media

Molecule	Assignment	Gas phase 152	Gas phase <sup>151</sup>	In CH <sub>4</sub> <sup>164</sup>
$Mo(CO)_6$	$T_{1u}$	2003		1993
Mo(CO) <sub>5</sub>	$A_1$			2093
	Е	1990	1983	1967
	$A_1$	1942	1940	1926
Mo(CO) <sub>4</sub>	$A_1$			2057
	$B_1$	1972	1914	1887
	$A_1$	1946		1927
	$\mathrm{B}_2$	1911	1970	1945
Mo(CO) <sub>3</sub>	$A_1$		1990	1981
	Е	1891	1888	1862

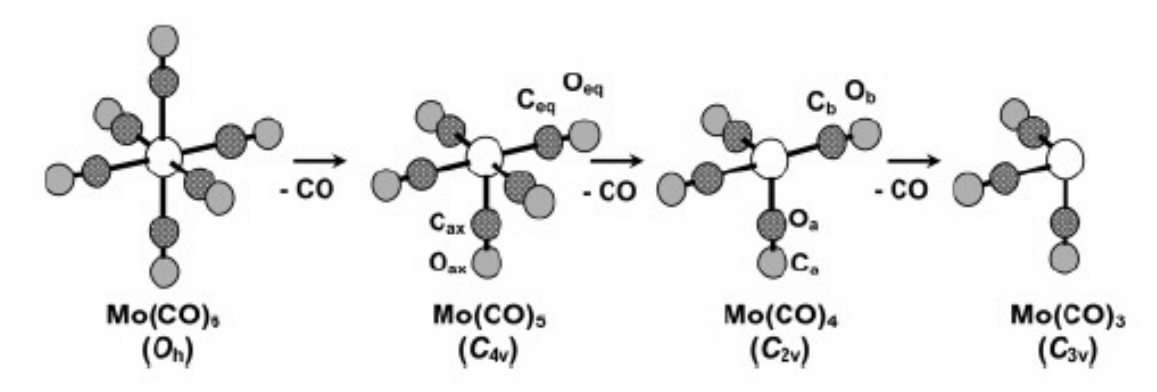


Figure 4-1 Geometries adopted by Mo(CO)<sub>6</sub> and its photofragments, in the gas phase <sup>154</sup>

## 4.2 Experimental

The experiments described in the following sections regarding the adsorption and subsequent photolysis of  $Mo(CO)_6$  on  $TiO_2(110)$ , were performed in the UHV chamber described in section 2.1. The surface of the  $TiO_2(110)$  crystal was cleaned through repeated cycles of sputtering and annealing, followed at the end by  $O_2$  treatment. As previously discussed in Section 2.2 this procedure resulted in a well ordered surface,

free of C contamination. The organometallic (Sigma-Aldrich, solid crystals, 99% pure) was placed inside a glass vial as acquired, i.e. without any further purification. The glass vial was covered with aluminium foil to prevent any photodecomposition, and attached to a leak valve already connected to the chamber. Subsequently, repeated freeze-pump-thaw cycles were performed to purify the hexacarbonyl. Before each deposition, further purification was employed as discussed later. The organometallic was introduced into the chamber through a thin stainless steel tube, the open end of which was situated approximately 15 mm from the front of the sample.

The photolysis experiments were performed using the light produced by an Hg-Xe lamp (185 W) acquired from Advanced Radiation Corporation, the energy spectrum of which can be found in Figure 4-2 as provided by the supplier. Emission peaks can be observed in the energy range, 190 to 320 nm (Table 4.1), required for the excitation of Mo(CO)<sub>6</sub> or the TiO<sub>2</sub> (rutile) band gap. The lamp was placed inside an Oriel housing that allowed for the focusing of the beam. The housing was powered by an Oriel controller, while all experiments were performed at a power of 140 W. As thermal decomposition due to the radiation had to be avoided, a water filter was placed in the beam between focusing optics and the UHV window. This comprised of a water filled cylinder which had both its bases made from quartz glass. The beam of light entered the chamber via a quartz UHV window and illuminated the sample. Some small portion of the manipulator was also illuminated during the experiments, despite all efforts to prevent it. For the experiments described in Section 4.3.6. an optical filter was used to cut-off specific wavelengths. This was placed in front of the quartz UHV window. The filter was supplied by UQG optics and its spectrum is provided in Figure 4-3, as supplied by the manufacturer. A schematic of the entire arrangement can be found in Figure 4-4.

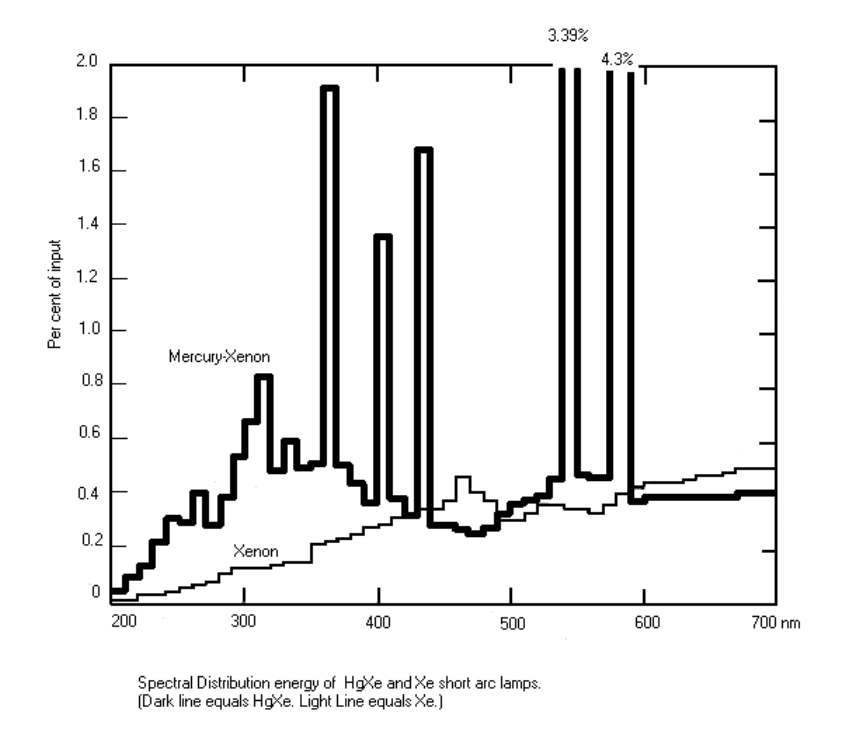


**Figure 4-2** Emission spectrum of Hg-Xe lamp as provided by the supplier. Clear emission peaks can be observed in the energy region of  $Mo(CO)_6$  transitions.

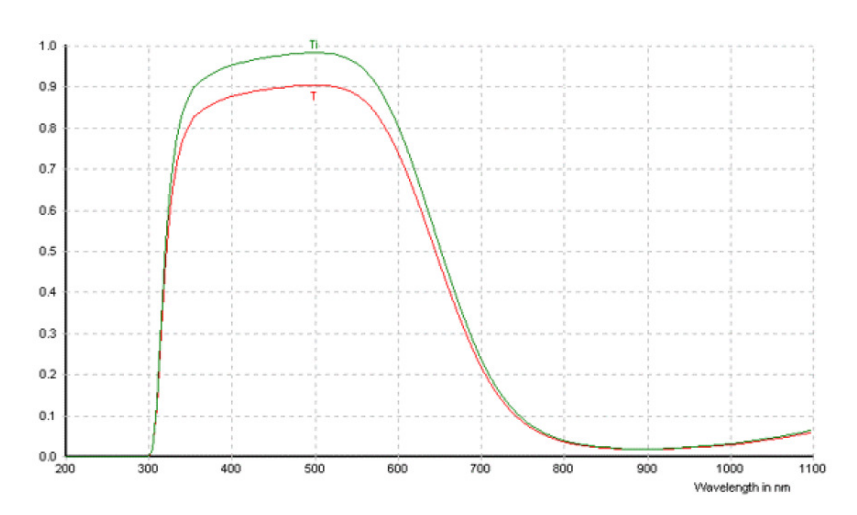


**Figure 4-3** Transmission spectrum of the optical filter used during the experiments of section 4.3.6, provided by the supplier, UQG optics.

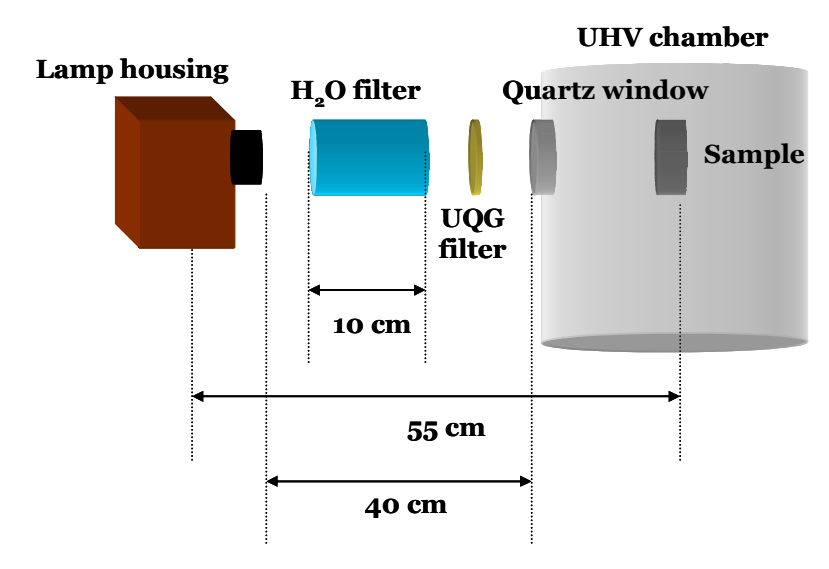


Figure 4-4 Schematic of the experimental arrangement used during photolysis.

All FT-RAIRS spectra were collected via the InSb detector and 1760-x Perkin Elmer spectrometer. Each spectrum was recorded (collection time of 60 s) using a p-polarised light, 100 scans and resolution of 4 cm<sup>-1</sup> in the spectral region from 2100 cm<sup>-1</sup> to 1900 cm<sup>-1</sup>. XPS spectra were collected using the Mg anode (1253.6 eV), while for each scan the energy regions of C(1s), Ti(2p), O(1s) and Mo(3d) were measured. The C(1s) and Mo(3d) spectra were collected using a 0.1 eV step, duel time of 1 s and averaging over 2 scans. The O(1s) spectra were collected using a 0.1 eV step, duel time 0.5 s and averaging over 2 scans while the Ti(2p) spectra using a 0.1 eV step, duel time 0.5 s and 1 scan. Employing these settings resulted in a collection time of less than 12 min. This was done to prevent any significant decomposition of the Mo(CO)<sub>6</sub> during the scan. The analysis of the XPS data was performed using the WSPECTRA software, which estimates the area, intensity and position of the peaks by fitting the raw spectra with a Gaussian-Lorentzian function. Prior to any analysis a Shirley background<sup>122</sup> was subtracted from the raw data. The coverage values were estimated using equation 2-16 of section 2.4.2. As mentioned in that Section, an error of the order of 15-20 % can be expected from these calculations.

The experimental protocol used for each experiment had as follows. Initially the glass vial containing the organometallic was outgassed for 10 min,  $P_{ch}=1\times10^{-7}$  mbar. During this procedure the sample was facing away from the doser. Upon completion the

TSP was operated for 60 s to help the system recover the base pressure. One or two cycles of sputtering and annealing were then employed to clean the surface from contaminants due to the outgassing. The surface was then checked with XPS, and if contamination was still present, further cycles of sputtering and annealing were performed. Subsequently, the sample was cooled down to 130 K and the experiments could commence. Both deposition and photolysis procedures took place at 130 K, whilst no temperature increase was observed when the sample was irradiated with the light beam. An FT-RAIRS spectrum was collected after each exposure of the surface to Mo(CO)<sub>6</sub>. The time of each photolysis was controlled using a manual shutter placed in front of the quartz UHV window, while after each illumination an FT-RAIRS spectrum was collected. During the XPS study of the photodecomposition process, a XPS spectrum was first collected prior to exposure to UV light. Subsequently each UV illumination was followed by an XPS scan. Finally it should be noted that all the exposure values quoted here are in Langmuirs (1L is defined as an exposure of 10<sup>-6</sup> Torr for 1 s).

#### 4.3 Results and Discussion

# 4.3.1 Deposition of Mo(CO)<sub>6</sub>

Before discussing the photolysis of Mo(CO)<sub>6</sub> on the oxide support, it is imperative to examine the adsorption properties of this molecule on the surface and subsequently the way its deposition proceeded. Figure 4-5 represents a FT-RAIRS spectrum collected after exposing the surface to 0.37 L of Mo(CO)<sub>6</sub>. Three features were observable, two of them as transmission bands at 2034 and 2008 cm<sup>-1</sup> and a single one as absorption band situated at 1963 cm<sup>-1</sup>. Upon increasing the exposure the appearance of these bands changed as it can be observed in Figure 4-6, where the FT-RAIRS spectra collected for increasing exposure values are presented. For 1.53 L of Mo(CO)<sub>6</sub> both transmission peaks blue shifted to 2039 and 2020 cm<sup>-1</sup> whereas the absorption band red shifted to 1954 cm<sup>-1</sup>. Upon further dosing, the 2017 cm<sup>-1</sup> band saturated in the form of a shoulder while the two other features continued to increase in intensity. Their positions on the other hand remained constant at 2041 and 1951 cm<sup>-1</sup> respectively. Further Mo(CO)<sub>6</sub> exposures (not shown) resulted only to an increase in the intensity of the two modes, with

their shape and position remaining the same. A spectrum collected for a multilayer of Mo(CO)<sub>6</sub> adsorbed on the TiO<sub>2</sub> surface can be found on the inset of Figure 4-6.

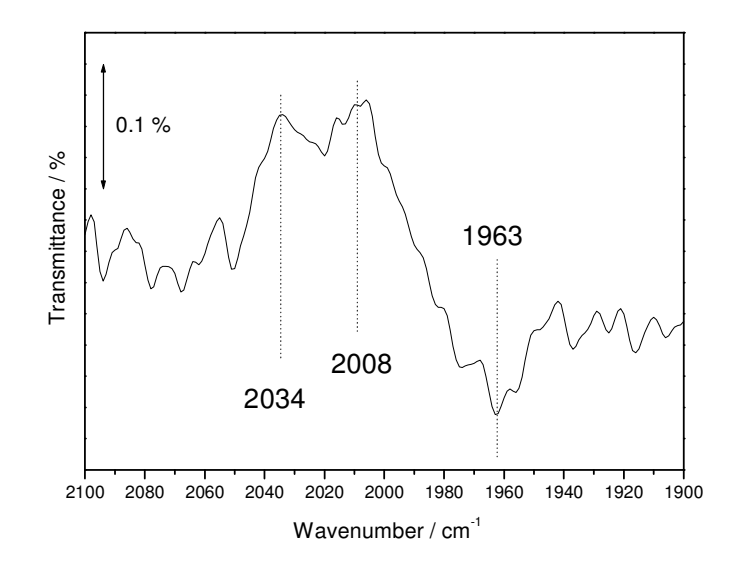
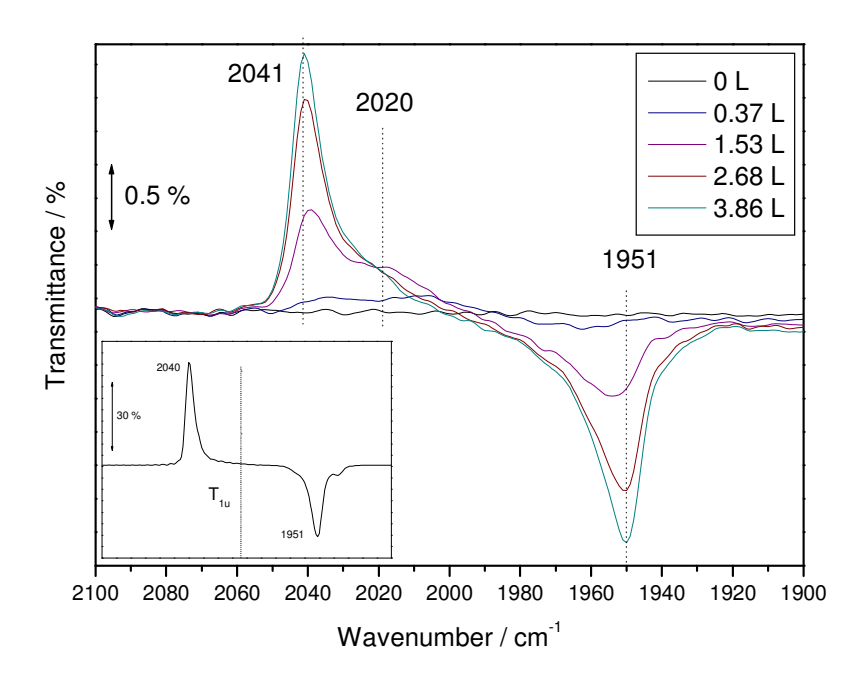


Figure 4-5 FT-RAIRS spectrum of  $Mo(CO)_6$  adsorbed on the  $TiO_2(110)$  surface, collected after 0.37 L exposure at 130 K.



**Figure 4-6** FT-RAIRS spectra of  $Mo(CO)_6$  adsorbed on the  $TiO_2(110)$  surface as a function of exposure. Inset: FT-RAIRS spectrum collected following the exposure of 7.33 L of  $Mo(CO)_6$ , vertical line represents the position of the triple degenerate v(C-O)  $T_{1u}$  mode at the gas phase.

On the spectral region recorded here, the Mo(CO)<sub>6</sub> molecule has one active IR mode with T<sub>1u</sub> symmetry, which in the gas phase manifests itself at 2003 cm<sup>-1</sup> (see also inset of Figure 4-6).<sup>193</sup> As a result, the bands observed in Figures 4-5 and 4-6 can be attributed to the three fold degenerate v(C-O) mode. As it was described in Section 2.2.1 one of the advantages of performing FT-RAIRS on an oxide surface is that both components of the p-polarised light become infrared active. Consequently the infrared radiation can excite modes that are parallel to the surface plane, which normally would have been inactive due to dipole screening. A demonstration of this phenomenon can be observed in previous spectra, Figure 4-6, where the transmission bands can be allocated to CO vibrations perpendicular to the surface, and the absorption band to modes parallel to the surface, as previously described by Evans *et al.* and Cavanagh *et al.*.<sup>62, 170</sup> The deviation from the gas phase value that was observed for both bands, 2014 and 1951 cm<sup>-1</sup> respectively, can be explained by taking into consideration the effect of dipole coupling. Coupling of dipoles aligned perpendicular to the surface gave rise to the blue shift, whereas coupling of dipoles aligned parallel to the surface gave rise to the red shift.<sup>60, 62</sup>

Another interesting point arising from the spectra of Figures 4-5 and 4-6 is the evolution of the bands. Figure 4-5 represents spectra collected at the very beginning of the deposition, thus it would be reasonable to assume that the features observed were due to adsorbates directly in contact with the support. Furthermore the transmission and absorption bands at 2034 and 1963 cm<sup>-1</sup> are suggestive that the coverage of the molecule on the surface was near the monolayer threshold, as suggested by previous studies. Further increase in exposure, Figure 4-6, resulted in the formation of multilayers on the titania surface, indicated again from the two characteristic peaks at 2041 and 1951 cm<sup>-1</sup>. Although the interpretation of these two modes is clear, there is some controversy in the literature regarding the nature of the 2008 cm<sup>-1</sup> mode as its frequency value is similar to the ones from Mo(CO)<sub>x</sub> fragments. Health As mentioned in section 4.1.3, Prunier *et. al.* have reported that some dissociation of Mo(CO)<sub>6</sub> must take place upon adsorption on the TiO<sub>2</sub> surface. Based on previous studies and our FT-RAIRS and XPS results (next paragraph) we believe that this is not the case. The nature of the 2008 cm<sup>-1</sup> mode can be

explained by taking into consideration the effect of dipole coupling. At the initial stages of growth the islands were isolated on the surface thus the dipole coupling should have been minimal. As a result only one mode should be observed at the gas phase value of 2003 cm<sup>-1</sup>. The 2008 cm<sup>-1</sup> peak observed here is very close to the gas phase frequency (at 2003 cm<sup>-1</sup>)<sup>152</sup> and it could originate from isolated molecules on the surface. Of course the presence of the other two bands at 2034 and 1963 cm<sup>-1</sup> would indicate that some clustering of the molecules must have taken place even at 0.37 L of exposure.

The deposition of the Mo(CO)<sub>6</sub> molecule on the oxide surface was also examined using XPS. Figures 4-7 to 4-9 represent spectra collected from Mo(3d), C(1s) and O(1s) energy regions for three different exposure values. In Figure 4-7 two peaks appeared even from 1.53 L of exposure at 228.7 and 232 eV that can be assigned to the Mo(3d<sub>5/2</sub>) and Mo(3d<sub>3/2</sub>) transitions of Mo respectively. Their energy spacing, 3.2 eV, is in agreement with the spin orbit splitting reported for molybdenum.<sup>73</sup> Upon further increase in exposure, the intensity of both peaks increased while no change was observed in their position. Similar behaviour was also observed for the C and O spectral features. For C(1s) region, Figure 4-8, a single peak at 287.8 eV was observable attributed to the CO ligands of the molecule. A second peak appearing for higher exposure values has been previously identified as a satellite peak. 194 The O(1s) region, Figure 4-9, was initially dominated by the O peak of the support situated at 530.5 eV, while O from the molecule contributed to the spectrum with the formation of a small peak at 534.3 eV. As multilayers, 20.2 L, were formed on the surface, the latter became the dominant feature in the spectrum. For all spectra an important observation is the fact that the position of the peaks attributed to Mo(CO)<sub>6</sub> did not change, indicating that no change in the chemical environment took place upon deposition. This observation would be in accord with the physisorption of the intact molecule on the surface. Finally by utilising the area under the  $Mo(3d_{5/2})$  peak and the area under the C(1s) peak, the coverage of both on the surface was calculated using Equation 2-16 of Chapter 2. The results of these calculations can be found in Table 4-3.

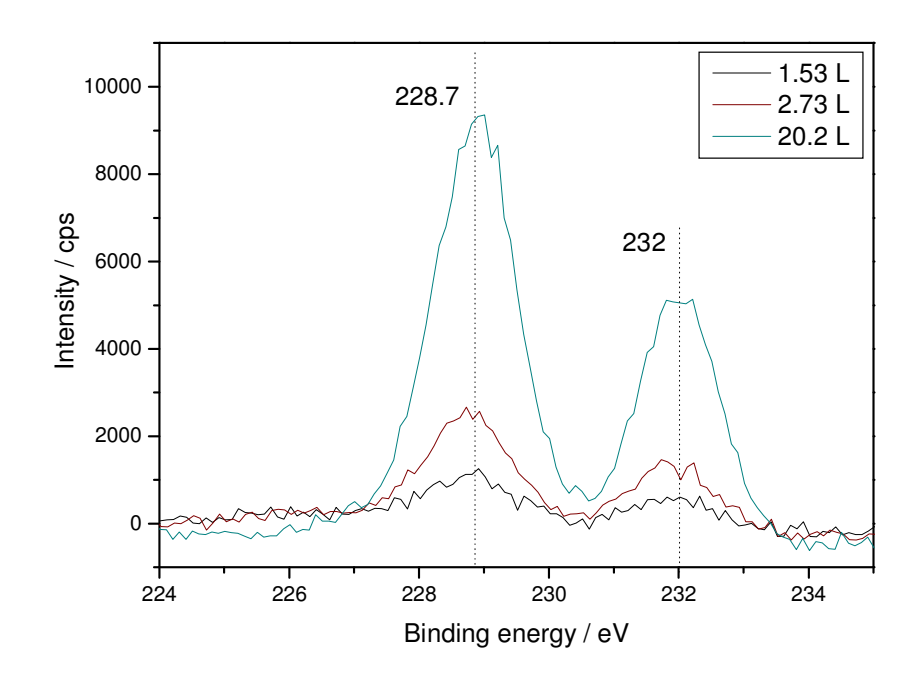


**Figure 4-7** XPS spectra of Mo(3d) region as a function of Mo(CO)<sub>6</sub> exposure.

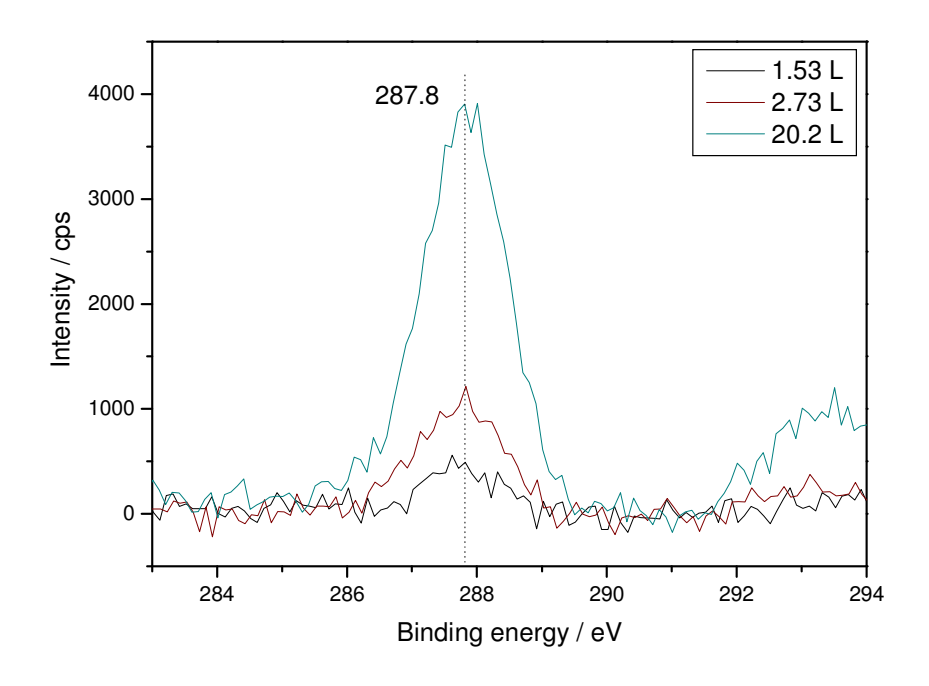


**Figure 4-8** XPS spectra of C(1s) region as a function of Mo(CO)<sub>6</sub> exposure.

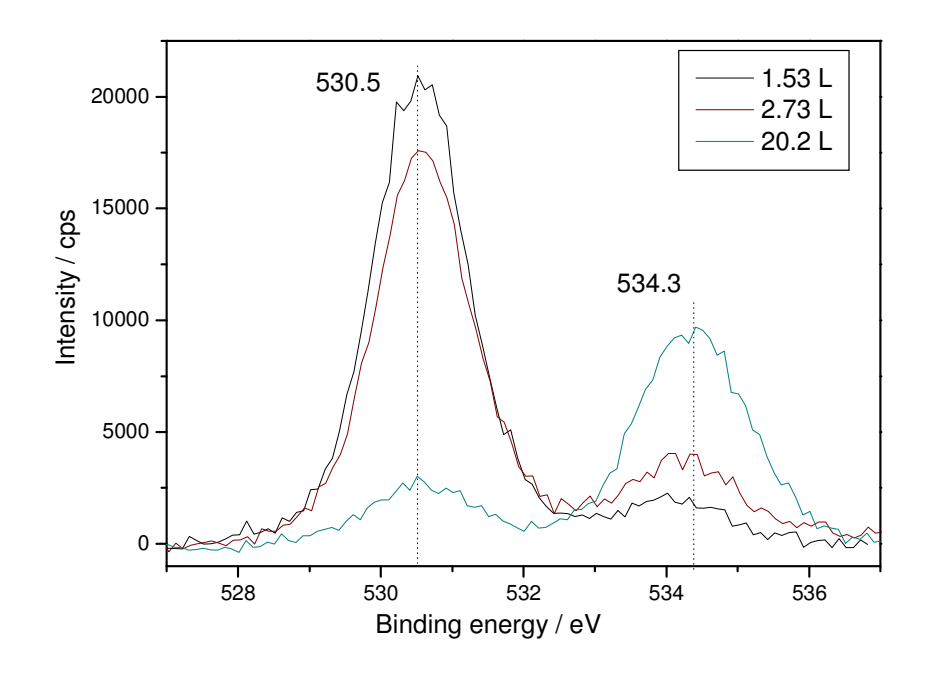


Figure 4-9 XPS spectra of O(1s) region as a function of Mo(CO)<sub>6</sub> exposure.

**Table 4-3** Mo and C coverage calculations for three different depositions.

Mo(CO) <sub>6</sub> exposure / L	Mo coverage / ML	C coverage / ML
1.53	0.34	0.81
2.73	0.7	1.78
20.2	14.95	37.92

## 4.3.2 Photodecomposition of 1.53 L of Mo(CO)<sub>6</sub>

The main objective of this study was the investigation of the photodecomposition of the physisorbed Mo(CO)<sub>6</sub> on the TiO<sub>2</sub> surface. Towards this goal, three different Mo coverage regimes were examined: 0.34 ML, 0.7 ML and 7.33 MLE. In this section the first one resulting from a 1.53 L deposition is presented. As it was mentioned previously this should result in the formation of multilayers on the surface but with a substantial proportion of the molecules being in contact with the support.

Figure 4-10 represents FT-RAIRS spectra collected from the Mo(CO)<sub>6</sub> covered surface (0.34 ML of Mo) as a function of irradiation time. The first spectrum (black line) was collected immediately after the 1.53 L deposition and before any exposure to UV radiation. The latter induced several transformations to the spectra. After 30 s irradiation the intensity of the two main bands at 2041 and 1954 cm<sup>-1</sup> was reduced by half whereas the shoulder around 2020 cm<sup>-1</sup> grew in intensity. Near the 2041 cm<sup>-1</sup> transmission band, an unresolved transmission peak was also observable at 2033 cm<sup>-1</sup>. A further 60 s irradiation (90 s in total) resulted in the appearance of a new transmission band at 2017 cm<sup>-1</sup>, while the two transmission and absorption bands of the multilayer continued to decrease in intensity. Similar behaviour was also observed for the 2033 cm<sup>-1</sup> peak. All three bands almost disappeared from the spectra after 150 s irradiation and at the same time the 2017 cm<sup>-1</sup> red shifted and a new transmission band started to emerge around 2006 cm<sup>-1</sup>. This was the dominant band in the spectrum collected after 270 s irradiation, whilst a further 120 s of irradiation resulted in the red shift of this band. The final spectrum was collected after total irradiation of 690 s. As it can be observed from the inset of Figure 4-10 it was composed of several unresolved transmission bands around 2000 cm<sup>-1</sup>. It is worth pointing out that two transmission bands at 1967 and 1943 cm<sup>-1</sup> must correspond to noise coming from the spectrometer or the detector rather than the actual adsorbates, as will be discussed in Section 4.3.5. To summarise, the spectra of Figure 4-10 can be divided into two regions. The first, up to 90s radiation, contains spectra that retained most of the characteristic vibrations of the parent molecule. The second, longer radiation times, all vibrational modes of the parent molecule disappeared and new vibrations were observed which are assigned below.

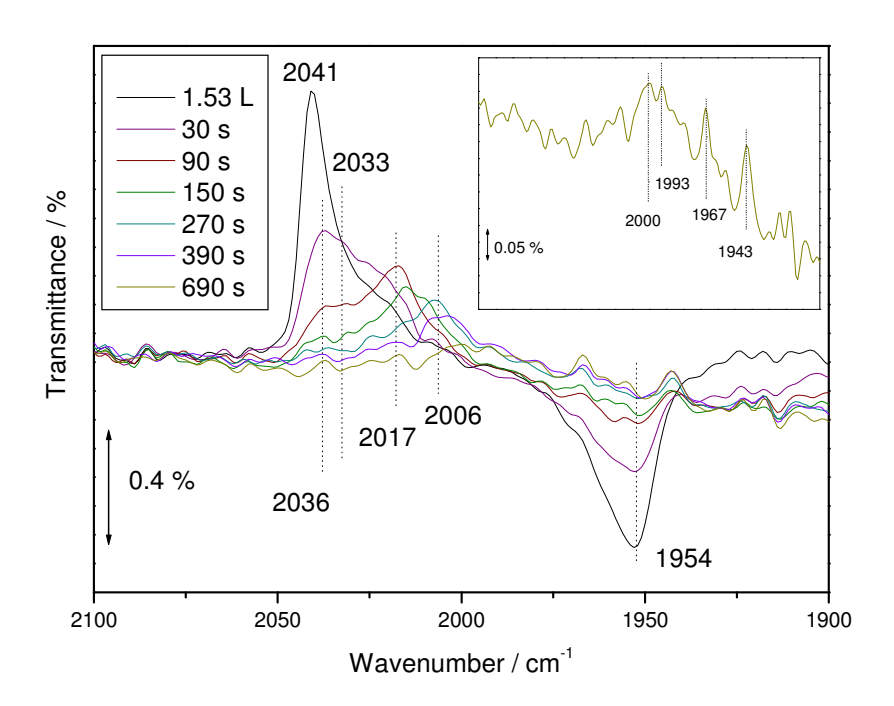


**Figure 4-10** FT-RAIRS spectra collected from the surface as a function of irradiation time. The first, black line, measured after 1.53 L of Mo(CO)<sub>6</sub>. Inset: spectrum collected after the final 690 s irradiation.

As mentioned in Section 4.1.1, the absorption of selected wavelength radiation from the Mo(CO)<sub>6</sub> molecule will lead to the photodecomposition of the latter by removal of CO ligands. FT-RAIRS spectra collected in this study, following the sequential irradiation of the adsorbed molecule were consistent with the aforementioned statement. After 30 s of irradiation, approximately half of Mo(CO)<sub>6</sub> molecules remained unaffected, as indicated by the ca. 50 % reduction in intensity of the two characteristic peaks at 2036 and 1954 cm<sup>-1</sup> respectively. Nevertheless, new species were also formed on the surface, hinted by the unresolved band at 2033 cm<sup>-1</sup>, and the growth of the broad shoulder around 2020 cm<sup>-1</sup>. The formation of those species can be attributed to the photodecomposition of Mo(CO)<sub>6</sub> molecules, hence their identity should be that of Mo(CO)<sub>x</sub>. Additional irradiation induced further changes to FT-RAIRS spectra, with the appearance for example of two distinct bands after 270 s of irradiation at 2017 and 2006 cm<sup>-1</sup> respectively. The three bands at 2033, 2017 and 2006 cm<sup>-1</sup> can be assigned to different photodecomposed species on the surface, labelled for the moment A, B and C respectively. The effect of progressive irradiation can be best described with the help of Figure 4-11. In this figure,

the intensity of four characteristic bands is plotted against irradiation time. These bands are: first the one due to the parent molecule at 2041 cm<sup>-1</sup>, second the one attributed to species A at 2033 cm<sup>-1</sup>, third the 2017 cm<sup>-1</sup> band allocated to species B and finally the one assigned to species C at 2006 cm<sup>-1</sup>.

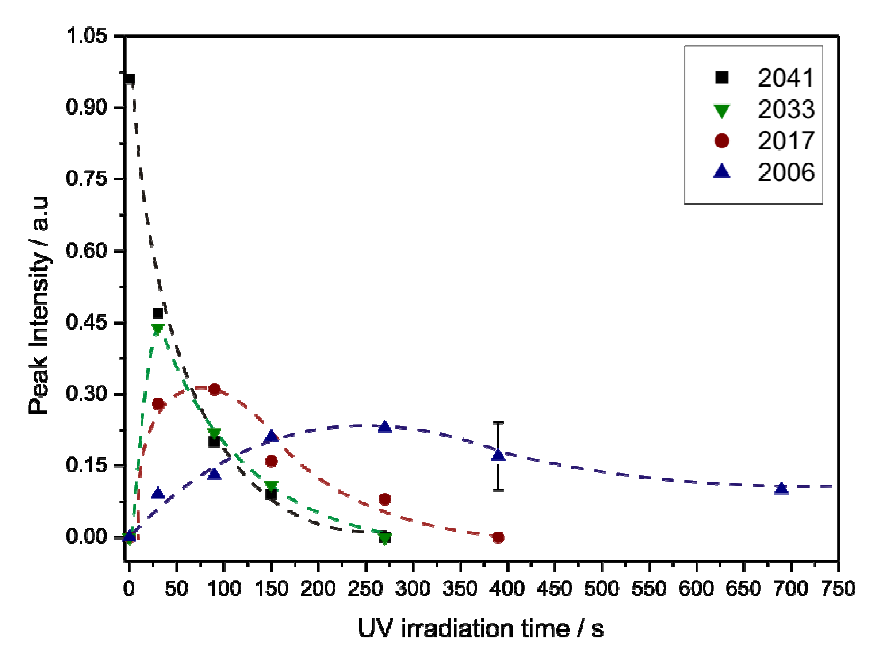


**Figure 4-11** Intensity of four characteristic FT-RAIRS bands of Figure 4-10, as a function of UV irradiation time. Black squares represent the intensity of the peak situated initially at 2041 cm<sup>-1</sup>, green triangles represent the intensity of the peak situated initially at 2033 cm<sup>-1</sup>, red circles represent the intensity of the peak situated initially at 2017 cm<sup>-1</sup> and blue triangles represent the intensity of the peak situated initially at 2006 cm<sup>-1</sup>. Lines are drawn as guide to the eye.

Following the data of Figure 4-11, after 270 s of irradiation no peak was recorded for the 2041 cm<sup>-1</sup> band (black squares), indicating that by 270 s all parent molecules had photodecomposed. The peak assigned to photoproduct A (green triangles) exhibited a maximum in intensity after 30 s of irradiation, followed by a non linear decrease as a function of irradiation time. Similar to the parent molecule, by 270 s photoproduct A was also removed from the surface. On the other hand the intensity of the band attributed to photoproduct B (red circles) exhibited a maximum in intensity after 90 s of irradiation, followed by a steady decrease. By 390 s of irradiation, species B was also removed from the surface, as indicated by the intensity value of the 2017 cm<sup>-1</sup> peak.

Finally the intensity of the peak attributed to photoproduct C (blue triangles), reached a maximum after 270 s of irradiation, while even after 690 s its value remained almost unchanged within experimental error. According to the above description, at the initial stage of irradiation, after 30 s, the main product of Mo(CO)<sub>6</sub> photolysis is species A although both B and C were also present on the surface to a lesser extent. After 90 s of irradiation, the opposite effect was observed, with species B being the major photofragment. Prolonged irradiation though, resulted in the disappearance of both peaks attributed to species A (after 270 s) and B (after 390 s) whereas the only remaining contribution in the FT-RAIRS spectra was from the band attributed to species C. Since the temperature of the sample remained the same for the whole period of irradiation, the only possible explanation for the removal of species A and B would be that they also photodecomposed when irradiated with the UV light. Indeed, the evolution of all four data sets presented in Figure 4-11 would be consistent with a sequential type of photodecomposition of Mo(CO)<sub>6</sub> to species A, species A to B and species B to C:  $Mo(CO)_6 \rightarrow A \rightarrow B \rightarrow C$ . No further photodecomposition of species C was observed, as indicated by its intensity value after 690 s. As discussed in Section 4.1.1., the first product of the one photon photolysis of Mo(CO)<sub>6</sub> is Mo(CO)<sub>5</sub>. Hence it would not be unreasonable to assume to assign species A to Mo(CO)<sub>5</sub>. Since a sequential process was observed, species B can be attributed to Mo(CO)<sub>4</sub> and species C to Mo(CO)<sub>6</sub>. Moreover for species C, XPS data collected during the photodecomposition process (presented in the following paragraph) and the position of the relevant FT-RAIRS band (at 2006 cm<sup>-1</sup>) are consistent with the assignment of photoproduct C to Mo(CO)<sub>3</sub>. Indeed bands situated around 2006 cm<sup>-1</sup> have previously been assigned to Mo(CO)<sub>3</sub> for studies conducted on planar Al<sub>2</sub>O<sub>3</sub><sup>185</sup> and on Si(111)-(7x7). 166 Finally, it should be noted that no absorption bands were observable at the final steps of the photolysis, indicating that the final photofragments, Mo(CO)<sub>3</sub>, adopted a geometry consistent with the alignment of their dipole moments perpendicular to the surface plane.

As mentioned earlier, the photodecomposition process was also followed by XPS. In the following Figures 4-12 and 4-13 three different properties of the  $Mo(3d_{5/2})$  and C(1s) peaks respectively are plotted against the time of UV exposure: area, FWHM

and position. All the spectra used to perform this analysis can be found in Appendix A. Figure 4-12 represents the above three plots for  $Mo(3d_{5/2})$ . The dependence of the  $Mo(3d_{5/2})$  peak area from the UV exposure can be observed in Figure 4-12a. Although the data exhibit a certain amount of scattering, a general trend can be observed according to which the amount of Mo on the surface remained constant. Consequently, the photolysis process did not induce any desorption of Mo from the surface, in accordance with previously studied behaviour of the molecule under UV illumination. In Figure 4-12b, the change of the Mo(3d<sub>5/2</sub>) peak FWHM value is plotted against UV irradiation time. As it can be observed, a small increase from ca 1.95 to 2.25 e V was obtained with prolonged irradiation, although for the last two stages of irradiation the values appeared to reach a plateau. This trend would be consistent with the observation made from FT-RAIRS, Figures 4-10 and 4-11, that during the intermediate stages of irradiation the photolysis process resulted in the formation of different species vi on the TiO<sub>2</sub>(110) surface. Figure 4-12c represents the variation of  $Mo(3d_{5/2})$  peak position as a function of UV irradiation time. During the first two steps of the photolysis process, a dramatic shift away from the 227.8 eV value of the Mo(CO)<sub>6</sub> molecule was observed. Further irradiation did not result in dramatic differences, with the values almost reaching a plateau. The change in trend after 270 s of irradiation agrees well with the data of Figure 4-11, where the intensity of the band attributed to Mo(CO)<sub>6</sub> exhibited a value near 0. Thus by combining FT-RAIRS and XPS results it would be safe to suggest that after 270 s of irradiation no Mo(CO)<sub>6</sub> was present on the surface. In addition, the plateau observed after 270 s would be in accordance with the fact that the population of photofragments on the surface was dominated by a single species. An indication for the nature of this species was provided in the previous paragraph by FT-RAIRS, where Mo(CO)<sub>3</sub> was identified. This assignment is in agreement with XPS data of Figure 12c, as explained henceforth.

It can be expected that the effective charge of Mo atom will change according to how many CO molecules are attached to the metal. It has been shown theoretically that the relation between the chemical shift of a core orbital i,  $\Delta E_i$ , and the charge,  $q_A$ , of its relevant atom A is linear, <sup>195</sup> according to the following equation:

\_

vi These contribute differently to the Mo(3d<sub>5/2</sub>) peak thus increasing the FWHM of the overall peak.

$$\Delta E_i = k_i q_A + \sum_{B \neq A} \frac{q_B}{R_{AB}} + l \tag{4-2}$$

where ki is a constant equal to the Coulomb repulsion integral between a core and a valence electron, I represents a constant determined by the energy reference level, and the summation term represents the effect from surrounding atomic charges, and is normally treated as a constant. 196 In addition, Lindberg et al. have experimentally confirmed the above for the case of sulphur compounds, where a linear relationship was observed between S(2p) binding energy and charge. 197 Based on the above, it would be within reason to assume that the change of Mo(3d<sub>5/2</sub>) binding energy depended linearly from the effective charge of Mo, which as mentioned before relates with the number of attached CO molecules. This linear relationship is represented schematically in Figure 4-13 where the  $Mo(3d_{5/2})$  binding energy is plotted against the number of CO molecules attached to Mo. The binding energy values of  $Mo(3d_{5/2})$  for  $Mo(CO)_x$  (x=1, 2, 3, 4 or 5) should lie along the line (blank dashed line) connecting metallic Mo at 227.8 eV <sup>73</sup> and Mo(CO)<sub>6</sub>, which from this set of data was measured at 228.77 eV. Three data points are also plotted in Figure 4-13, which correspond to an average binding energy value (calculated from the last three data points of figure 4-12c) for three different species: Mo(CO)<sub>2</sub> (red square), Mo(CO)<sub>3</sub> (green square) and Mo(CO)<sub>4</sub> (blue square). As it can be observed only the point corresponding to Mo(CO)<sub>3</sub> is close to the ideal line, while both other points deviate away from it. Hence another evidence is obtained of the Mo(CO)<sub>3</sub> nature of the final photoproduct, which is additionally supported by Figure 4-12d. Figure 4-12d represents the C to Mo relative area ratio, C<sub>rel.area</sub>/Mo<sub>rel.area</sub>, value as a function of UV irradiation time. Ideally, for the Mo(CO)<sub>6</sub> molecule this value should be at 6. From Figure 4-12d, for this set of data this value comes at 2.7 for Mo(CO)<sub>6</sub>, quite away from the ideal value. We believe that this is due to inconsistency in the values of relative sensitivity factors used during calculation. For the final three irradiation times, an average value of 1.68 is obtained. By normalising the first data point to 6, corresponding thus to Mo(CO)<sub>6</sub>, the value for the final photoproduct is calculated at  $3.73 \pm 0.7$ . Although this value is closer to Mo(CO)<sub>4</sub> than to Mo(CO)<sub>3</sub>, when placed in context with the previous presented XPS and FT-RAIRS data and taking into consideration the large amount of error present in the former calculation, the assignment of the final photoproduct to  $Mo(CO)_3$  appears more probable.

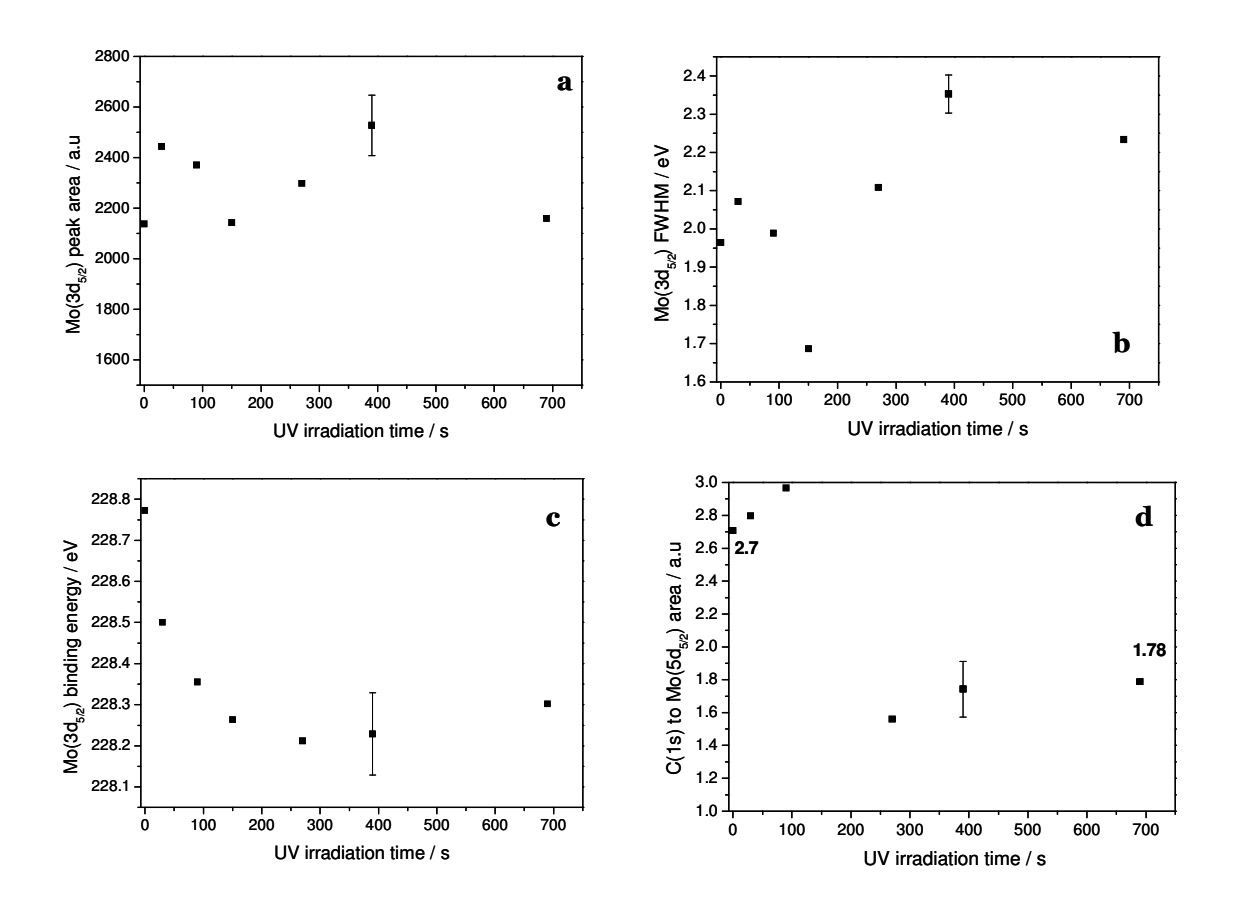


**Figure 4-12** (a) Mo(3d<sub>5/2</sub>) peak area as a function of irradiation time, (b) Mo(3d<sub>5/2</sub>) peak FWHM as a function of irradiation time, (c) Mo(3d<sub>5/2</sub>) peak position as a function of irradiation time (d) C(1s) to Mo(3d<sub>5/2</sub>) relative area as a function of irradiation time. The first point represents data collected immediately after deposition of the molecule.

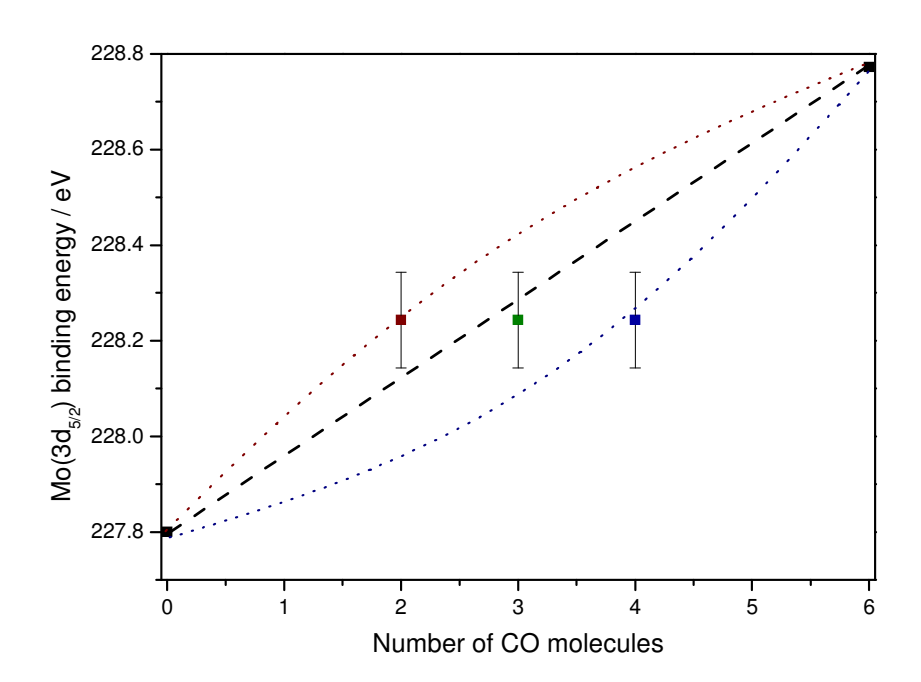


**Figure 4-13** Mo( $3d_{5/2}$ ) position plotted as a function of the number of CO molecules attached to the metal atom. The trend should follow the line (dashed) connecting metallic Mo and Mo(CO)<sub>6</sub>. As it can be observed only the point corresponding to Mo(CO)<sub>3</sub> (green square) lies close to the dashed line, whereas the other two for Mo(CO)<sub>2</sub>(red square) and Mo(CO)<sub>3</sub>(blue square) deviate away from it. The red and blue dotted lines are guides to the eye.

The area, intensity and position of C(1s) peak as a function of UV irradiation time are presented in Figure 4-14. The data collected for the area, Figure 4-14a, were very irregular. Within experimental error, the trend observed did not reveal any change over time. This is very peculiar because as shown before the photolysis process resulted in desorption of CO molecules from the surface. Initially we believed that this was due to an inability of the analysis software to correctly estimate the area under the C(1s) peak for low C coverages. To address this issue the spectra were analysed manually using a graph paper. Again though, the same irregular behaviour was observed. On the other hand the trend observed for the FWHM value of the peak, Figure 4-14b, was in accord with the photodecomposition process. Again as in the case of the Mo(3d<sub>5/2</sub>) peak an increase in value was observed as a function of irradiation time, consistent with the presence on the surface of more than one photodecomposed species for the intermediate stages of irradiation. The trend observed for the binding energy of C(1s), Figure 4-14c, resembled

that of an exponential like decay. After 270 s of irradiation, a plateau was reached in accordance with the presence of a single photoproduct, namely  $Mo(CO)_3$ . Figure 4-13d represents the change of O(1s) peak position as a function of irradiation time. By comparing the latter with the plot of Figure 4-13c a similar trend can be observed. This comparison reveals that the peak observed at 287.8 eV was indeed due to the CO ligands of the molecule and not due to graphitic carbon. In addition, according to the literature a photoelectron peak from the latter normally appears at  $284.5 \pm 0.5$  eV.  $^{198-200}$ 

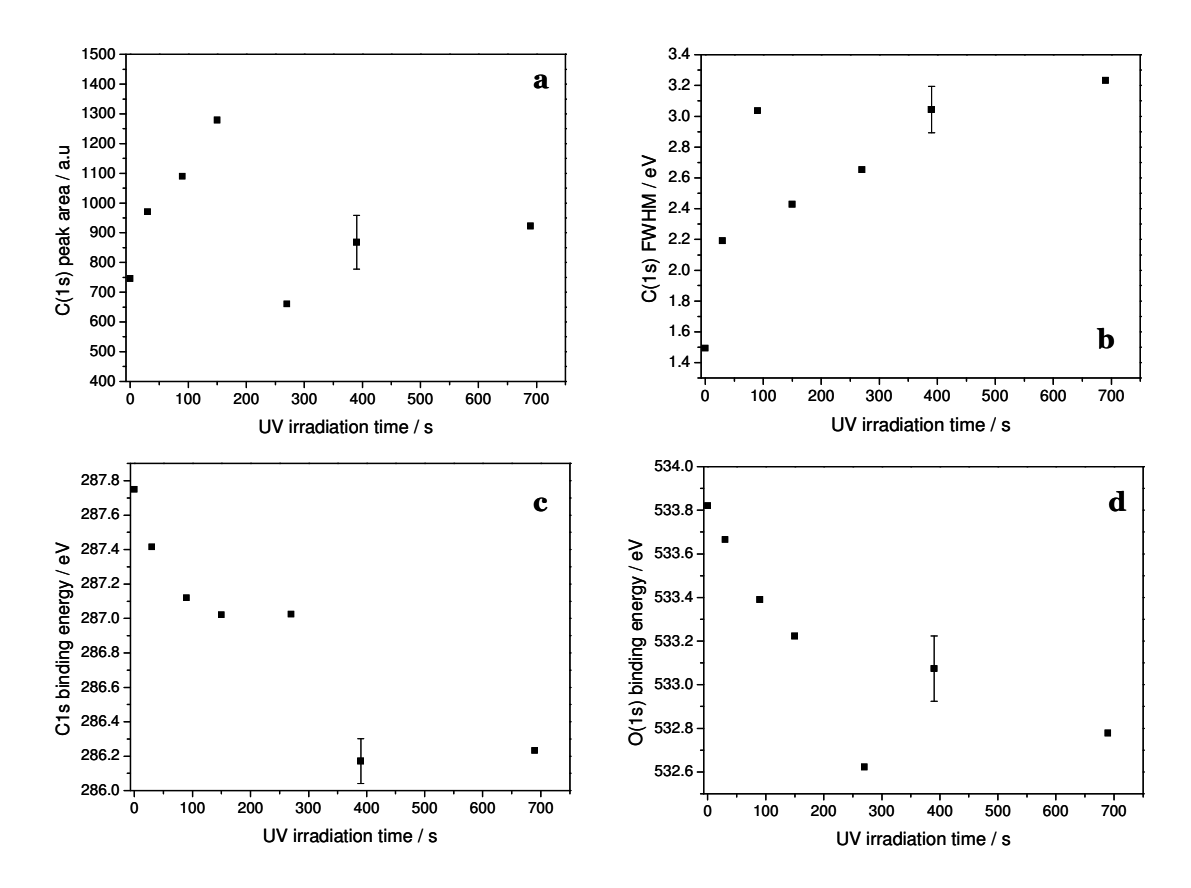


**Figure 4-14** (a) C(1s) peak area as a function of irradiation time (b) C(1s) peak FWHM as a function of irradiation time (c) C(1s) peak position as a function of irradiation time (d) O(1s) (from  $Mo(CO)_6$ ) peak intensity as a function of irradiation time. The first point on each plot represents data collected immediately after deposition of the molecule.

## 4.3.3 Photodecomposition of 2.73 L of Mo(CO)<sub>6</sub>

The photodecomposition of TiO<sub>2</sub>(110) supported Mo(CO)<sub>6</sub> was also investigated for higher coverage values of the latter, namely 0.7 ML. This specific overlayer was deposited by exposing the TiO<sub>2</sub>(110) surface to 2.73 L of Mo(CO)<sub>6</sub>. Figures 4-15 and 4-16 represent FT-RAIRS spectra collected following the photolysis process as a function of irradiation time. These data are presented in two separate figures to facilitate the presentation of these results. The first spectrum of Figure 4-15 was collected immediately after the deposition, whilst the first spectrum of Figure 4-16 is the same as the last one from Figure 4-15, collected after 450 s of UV exposure.

After 2.73 L of Mo(CO)<sub>6</sub> exposure two sharp infrared bands were observable, one transmission at 2041 cm<sup>-1</sup> and one absorption at 1951 cm<sup>-1</sup>. As mentioned earlier these belong to the triple degenerate  $T_{1u}$  mode of  $Mo(CO)_6$  and their positions are indicative of the presence of adsorbed multilayers. After a short UV exposure, 30 s, both bands decreased in intensity whereas a small shoulder (transmission band) started to grown around 2025 cm<sup>-1</sup>. Further 90 s of irradiation resulted in decrease of the intensity of both multilayer Mo(CO)<sub>6</sub> bands by almost half, whilst the shoulder at 2025 cm<sup>-1</sup> started to grow and shift into a peak at around 2020 cm<sup>-1</sup>. The same behaviour was observed for the following three UV exposures, and after 450 s the intensity of the bands due to the parent molecule was severely reduced while the shoulder had grown into a full peak situated at 2013 cm<sup>-1</sup>. By then the peak at 2041 cm<sup>-1</sup> had red shifted to 2038 cm<sup>-1</sup>. In addition a small absorption band was also observable at 1937 cm<sup>-1</sup>, which is more easily observed in the spectra of Figure 4-16. The intensity of both bands attributed to Mo(CO)<sub>6</sub> continued to drop as a function of exposure while at the same time the peak at 2013 cm<sup>-1</sup> red shifted. Its intensity was also reduced as was the case with the absorption peak at 1937 cm<sup>-1</sup>. At the end of irradiation, after a total of UV exposure of 1350 s, the spectrum had the following characteristics (inset of Figure 4-16). A broad transmission band was observed incorporating a variety of peaks with the ones at 2033 cm<sup>-1</sup> and 2004 cm<sup>-1</sup> best resolved. The absorption bands at 1951 cm<sup>-1</sup> and 1937 cm<sup>-1</sup> were barely observable.

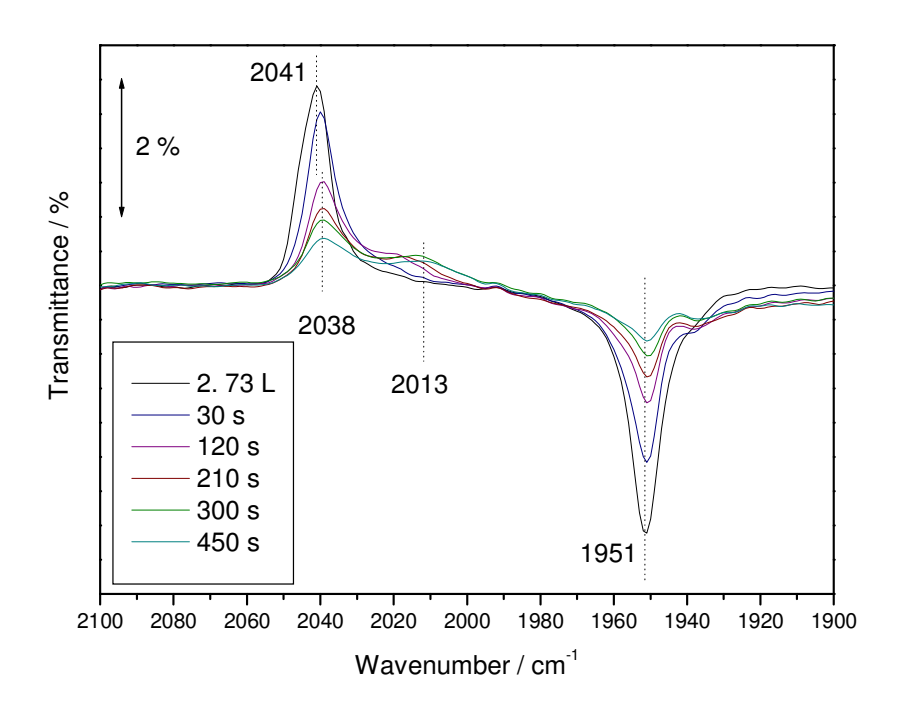


**Figure 4-15** FT-RAIRS spectra collected from the surface as a function of irradiation time. The first, black line, measured after 2.73 L of  $Mo(CO)_6$ .

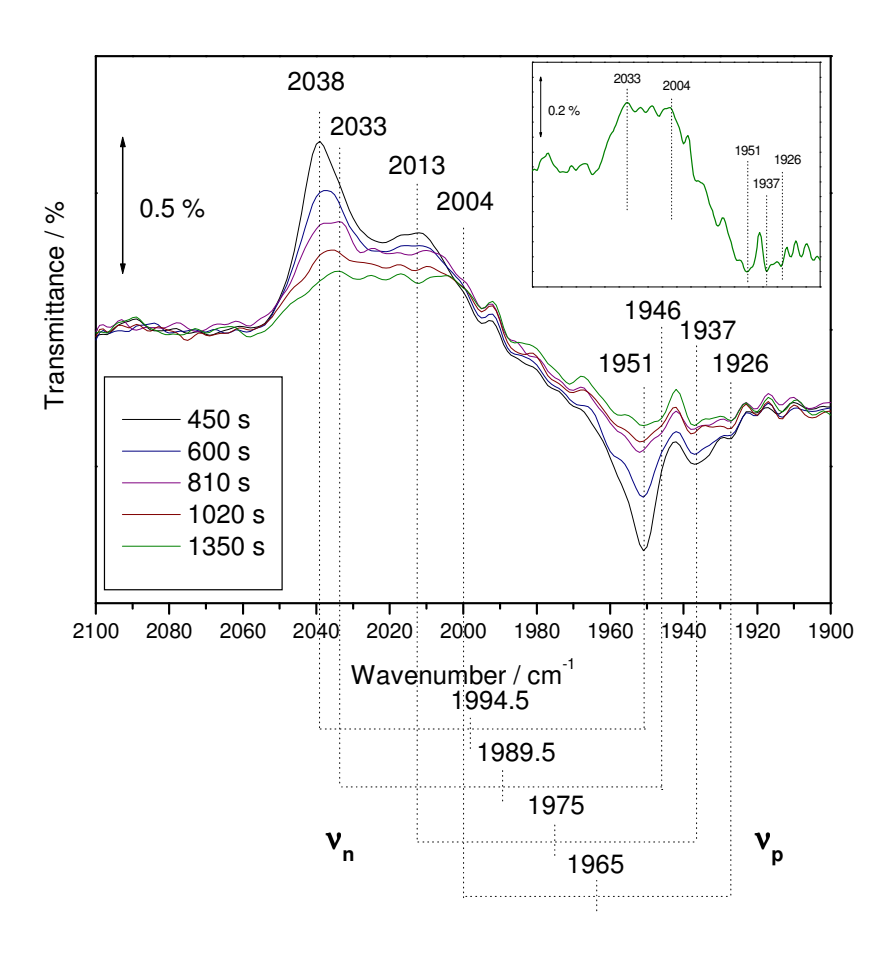


**Figure 4-16** FT-RAIRS spectra collected from the surface as a function of irradiation time. The first, black line, measured after 450 s irradiation. Inset: spectrum collected after the final 1350 s irradiation. Vertical dotted lines link

According to data presented above, evidence of photodecomposition was observable in FT-RAIRS spectra immediately after 30 s of irradiation. The reduction in intensity of both bands along with the appearance of a small shoulder around 2025 cm<sup>-1</sup> is indicative of the photolysis of Mo(CO)<sub>6</sub> to Mo(CO)<sub>x</sub>. This shoulder due to the unsaturated photofragments grew in intensity as a function of UV exposure, hinting that the population of the fragments increased with time. The red shift observed for the transmission band at 2041 cm<sup>-1</sup> complies well with the previous statement, as it is probably due to a change in the chemical environment of Mo(CO)<sub>6</sub>. In the previous section, Figure 4-10, bands around 2006 cm<sup>-1</sup> were attributed to Mo(CO)<sub>3</sub>. Similar bands appeared in the spectra of Figures 4-15 and 4-16 after 450 s of irradiation. Nevertheless several other bands were also

observable, for example at 2033, 2013 and 1937 cm<sup>-1</sup> respectively. An assignment of those bands can be made by taking into consideration the following two effects, present only when conducting FT-RAIRS on oxide single crystals. The first effect is the activation of infrared modes aligned both perpendicular  $(v_n)$  and parallel  $(v_n)$  to the surface. The second effect is the shifting of those modes away from the gas phase value due to dipole coupling. As mentioned in Section 4.3.1 coupling of dipoles aligned perpendicular to the surface results in a blue shift, whereas coupling of dipoles aligned parallel to the surface results in a red shift. For  $Mo(CO)_6$  the perpendicular  $(v_n)$  mode appeared at 2041 cm<sup>-1</sup> and the parallel  $(v_p)$  at 1951 cm<sup>-1</sup>, first spectrum of Figure 4-15 (black line). If we assume to a first approximation that both modes vii were shifted by equal amount away from the gas phase value, then the latter is calculated at 1996 cm<sup>-1</sup> which is very near the literature value of 2003 cm<sup>-1</sup>. 152 By applying the same approach to the other bands present in the spectra of Figure 4-16 an assignment can be made based on their gas phase value. For example by linking the 2033 cm<sup>-1</sup> transmission band with the 1946 cm<sup>-1</sup> absorption band, a gas phase value of 1989.5 cm<sup>-1</sup> is calculated, which according to Table 4-2 is very close to the gas phase value of the E v(C-O) mode of Mo(CO)<sub>5</sub>. Furthermore by associating the transmission band at 2013 cm<sup>-1</sup> with the absorption band at 1937 cm<sup>-1</sup> the calculated gas phase value is 1975 cm<sup>-1</sup>, which based on Table 4-2 can be correlated with the 1972 cm<sup>-1</sup> (or 1970 cm<sup>-1</sup>) gas phase value of the B<sub>1</sub> (or B<sub>2</sub>) or v(C-O) mode of Mo(CO)<sub>4</sub>. For the transmission band at 2004 cm<sup>-1</sup>, previously assigned to Mo(CO)<sub>3</sub>, an absorption counterpart could be assigned to the 1926 cm<sup>-1</sup> band, hence a gas phase value of 1965 cm<sup>-1</sup> can be found. The latter deviates from the literature value of 1990 cm<sup>-1</sup> by 25 cm<sup>-1</sup>, which is comparably higher than the previous three assignments. Nevertheless, as it can be observed in Table 4-2, Mo(CO)<sub>3</sub> exhibits also an E v(C-O) mode at 1891 cm<sup>-1</sup>. For this value the absorption band must be red shifted into a spectral region not accessible in this study due to the InSb detector limitations. The above calculations are presented schematically in Figure 4-16, while Table 4-4 contains all the numerical values. It should be noted that this analysis is consistent with the band assignment made in section 4.3.2,

\_

 $<sup>^{</sup>vii}$  To be more precise, Mo(CO)<sub>6</sub> has only one active infrared mode. The triple degenerate v(C-O) of  $T_{1u}$  symmetry.

photodecomposition of 1.53 L overlayer, highlighting the fact that two different analysis processes reached the same conclusion.

**Table 4-4**  $\nu_n$  and  $\nu_p$  modes for all carbonyls along with their calculated gas phase value. The observed literature values are also provided for comparison. All values in cm<sup>-1</sup>

	$\nu_{\rm n}$	$ u_{ m p}$	Calculated gas phase value	Literature gas phase value <sup>151, 152</sup>
Mo(CO) <sub>6</sub>	2041	1951	1996	2003
Mo(CO) <sub>5</sub>	2033	1946	1989.5	1990 / 1983
Mo(CO) <sub>4</sub>	2013	1937	1975	1972 / 1970
Mo(CO) <sub>3</sub>	2004	1926	1965	1990

Based on the previous analysis, at the end of photolysis the surface accommodated a plethora of photoproducts along of course with parent molecules which remained unaffected. The unsaturated carbonyls identified were Mo(CO)<sub>5</sub>, Mo(CO)<sub>4</sub> and Mo(CO)<sub>3</sub>, which highlighted the sequential nature of the photodecomposition. Furthermore it should be noted that the majority of the photoproducts adopted a geometry perpendicular to the surface, as indicated by the relevant intensities of transmission (normal,  $v_n$ ) and absorption (parallel,  $v_p$ ) bands. Apart from the aforementioned photofragments, the presence of polymer species should not be excluded. Indeed Richter et. al. have reported the formation of Mo<sub>x</sub>CO<sub>y</sub> carbonyls following the photolysis of multilayer Mo(CO)<sub>6</sub> on Si(111)<sup>170</sup>, whilst Perutz and Turner assigned infrared bands at 2000 cm<sup>-1</sup> and 2045 cm<sup>-1</sup> to polymer species of the hexacarbonyl. 164 Interestingly at no point during the photolysis of this overlayer did the bands attributed to Mo(CO)<sub>6</sub> disappear from the spectra, even though the irradiation time was almost double from the one used in Section 4.3.3. This observation asks the question of whether there is a factor hindering the decomposition for the multilayers or favours it for the low coverage overlayers. For example direct contact with the surface could favour the reaction due to excitation of surface electron holes, as with the case of high surface area  $TiO_2$  reported by Okamoto *et.* al. <sup>192</sup>

As with the 0.34 ML of Mo overlayer, the photodecomposition process was also followed by XPS. Figure 4-17 represents the  $Mo(3d_{5/2})$  peak area (a), peak intensity (b) and binding energy (c) as a function of irradiation time. The values collected for the area did not exhibit significant variation with time. Once more this indicated that no Mo was desorbed from the surface as part of the photodecomposition process. The change of FWHM as a function of irradiation time, Figure 4-17b, exhibited a trend similar to the one observed in Figure 4-12b for the low coverage overlayer. For intermediate irradiation times, an increase in the Mo(3d<sub>5/2</sub>) FWHM value was observed, indicative of the presence of various species on the TiO<sub>2</sub>(110) surface. Prolonged irradiation times, i.e. 1350 s, did not alter significantly the FWHM value, only by ca 0.04, in accordance with the final FT-RAIRS spectra of Figure 4-16 which hinted the presence of different species. Finally the change of binding energy as a function of time exhibited similar characteristics with the equivalent one in Figure 4-12c, although differences were also observable. To begin with a sharp decrease was evident in the first steps of the photolysis, indicating the decomposition of Mo(CO)<sub>6</sub>. On the other hand though the plateau observed in Figure 4-12c at 150 s was reached here after 450 s of irradiation, triple the time. As with FT-RAIRS spectra this could be considered as an indication for the dependence of the photoreaction from Mo(CO)<sub>6</sub> coverage. Nevertheless the energy difference between the 0 s exposure and the 1350 s one was calculated at 0.59 eV which is very close to the 0.47 eV value observed in Figure 4-12c. As a result the majority of photofragments should be Mo(CO)<sub>3</sub> although as observed in the FT-RAIRS spectra, Figure 4-16, other species were also adsorbed on the surface. The dominant presence of Mo(CO)<sub>3</sub> was also demonstrated by the values of C<sub>rel.area</sub>/Mo<sub>rel.area</sub> calculated before and at the end of the photodecomposition procedure. As it can be observed in Figure 4-17d, the value before exposing the sample to UV radiation was calculated at 2.67, whereas the value following the 1350 s irradiation was calculated at 1.61. As in the case of Figure 4-12d, these values are away from the ideal ones, but by assuming that 2.67 corresponds to Mo(CO)<sub>6</sub> hence 6 then 1.61 is estimated at 3.61. This value does deviate from the ideal 3 for Mo(CO)<sub>3</sub>, but it should be

taken into consideration first that the existence of other species on the surface would also affect the outcome of the calculation and second the amount of error relevant with this estimation.

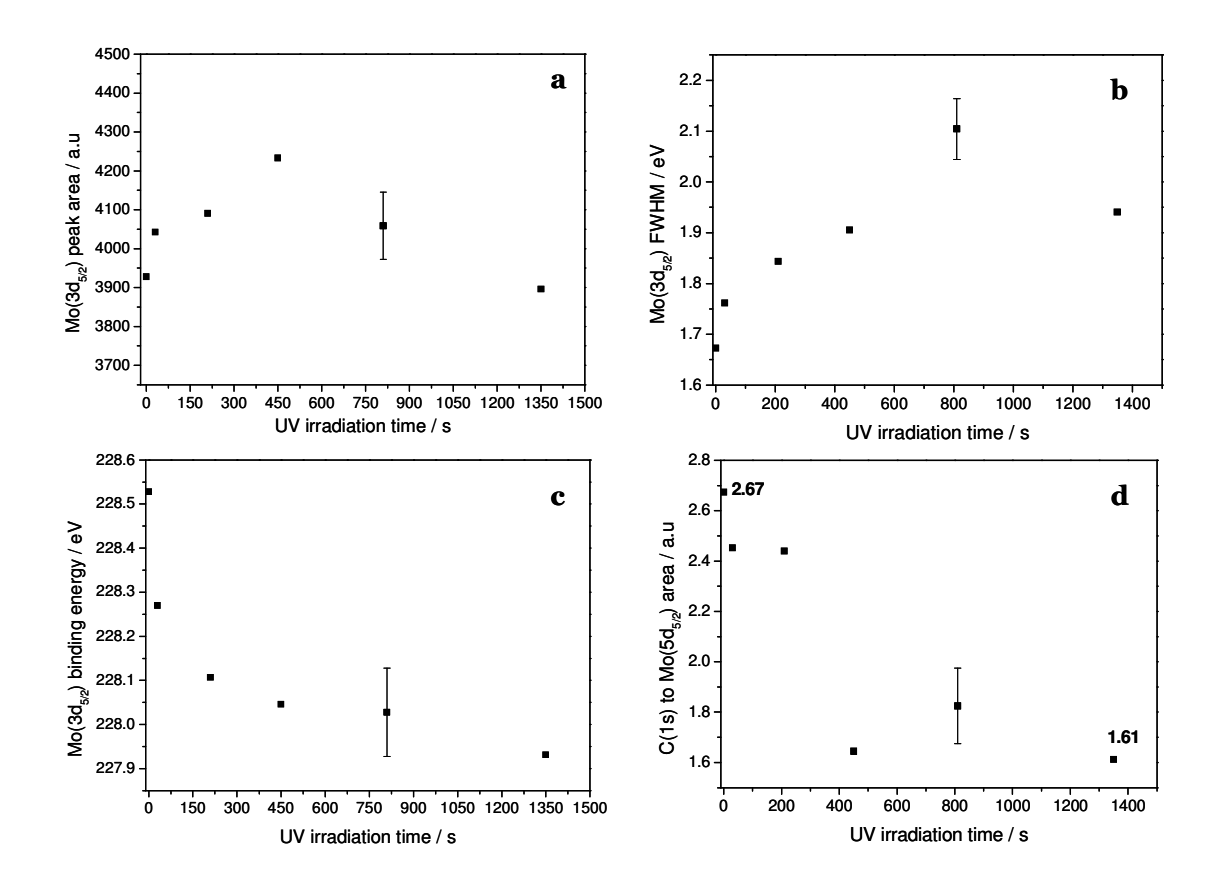


**Figure 4-17** (a) Mo(3d<sub>5/2</sub>) peak area as a function of irradiation time (b) Mo(3d<sub>5/2</sub>) peak intensity as a function of irradiation time (c) Mo(3d<sub>5/2</sub>) peak position as a function of irradiation time and (d) C(1s) to Mo(3d<sub>5/2</sub>) relative area as a function of irradiation time. The first point on each plot represents data collected immediately after deposition of the molecule.

Figure 4-18 represents the C(1s) peak area (a), peak intensity (b) and binding energy (c) as a function of irradiation time along with the binding energy of O(1s) due to  $Mo(CO)_6$  (d) to serve as a comparison. A linear decrease was observed for the C(1s) area as a function of irradiation time in accord with desorption from the surface of CO molecules. Contrary to Figure 4-14a this trend was in agreement with the photolysis process, indicating the difficulty of estimating the C(1s) area for very low coverages,

Figure 4-14a. The change of C(1s) FWHM value as a function of UV irradiation time is presented in Figure 4-17b. It can be observed that for intermediate UV exposures, up to 450 s, the C(1s) FWHM increased in size. As for the case of 0.34 ML of Mo, this increase hints at the existence of various species on the surface, produced by the photodecomposition of the parent molecule. On the other hand, the plateau observed for the last two exposures would indicate that the effect of prolonged UV irradiation was not as dramatic as for the initial times. An exponential like decay was also present in the data of Figures 4-18c and 4-18d. The comparable trends between C(1s) and O(1s) peaks and the position of the C(1s) peak, i.e. away from graphitic C which normally appears at 284.5  $\pm$  0.5 eV,  $^{198-200}$  indicated that the photofragments did indeed belong to carbonyls.

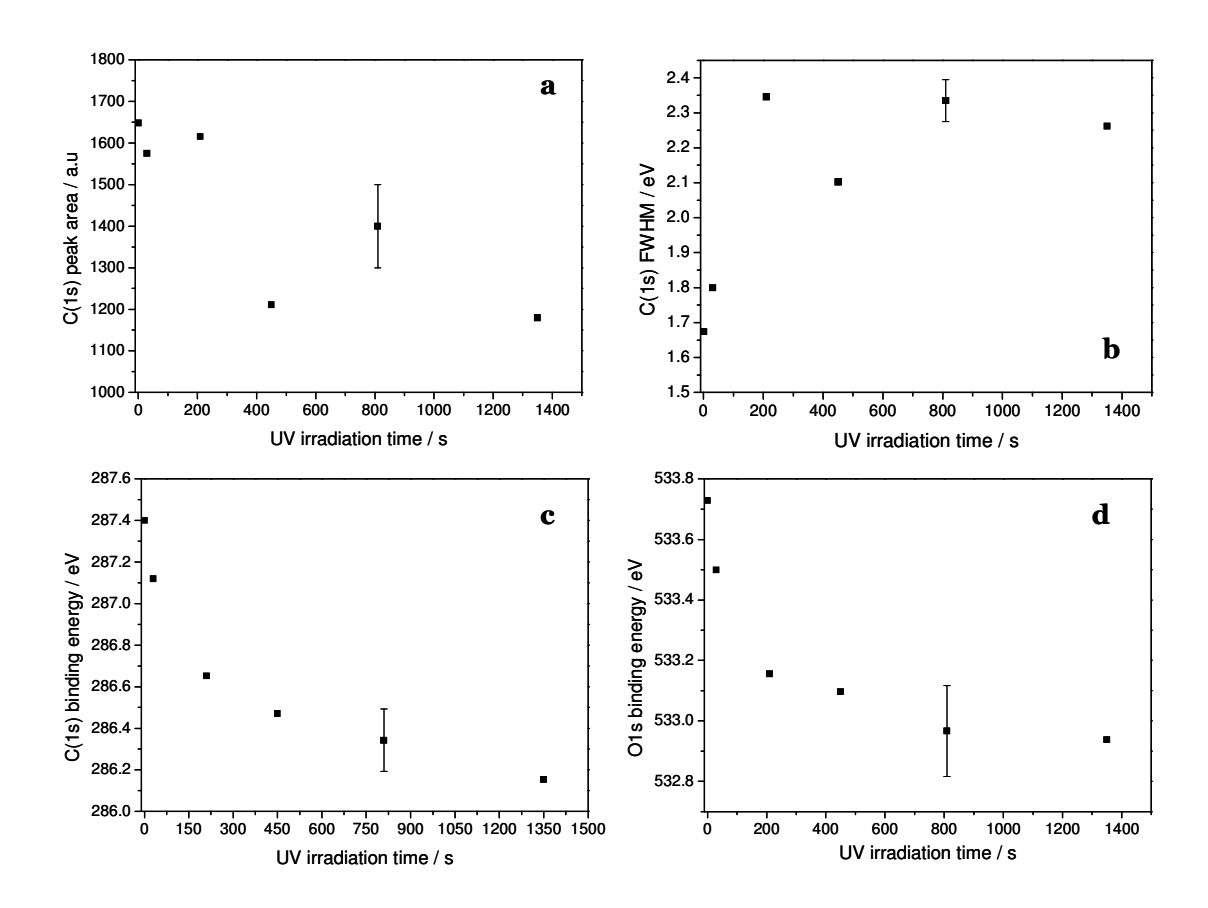


**Figure 4-18**(a) C(1s) peak area as a function of irradiation time (b) C(1s) peak intensity as a function of irradiation time (c) C(1s) peak position as a function of irradiation time (d) O(1s) (from Mo(CO)<sub>6</sub>) peak intensity as a function of irradiation time. The first point on each plot represents data collected immediately after deposition of the molecule.

# 4.3.4 Photodecomposition of 20.2 L of Mo(CO)<sub>6</sub>

The third overlayer examined with regards to its photolysis on the TiO<sub>2</sub>(110) surface, was the one produced after the deposition of 20.2 L of Mo(CO)<sub>6</sub>. This exposure value resulted in 14.95 MLE of Mo on the oxide surface. Figure 4-19 represents FT-RAIRS spectra collected during the photodecomposition process as a function of irradiation time. In contrast to the previous two overlayers (1.53 and 2.73 L of Mo(CO)<sub>6</sub>), exposing the sample to UV radiation did not induce significant changes to the collected spectra, even for long irradiation times. A steady decrease in intensity was observed for both bands attributed to the triple degenerate T<sub>10</sub> mode of Mo(CO)<sub>6</sub>, situated at 2040 cm<sup>-1</sup> and 1951 cm<sup>-1</sup>, whilst a broad shoulder became distinguishable after long irradiation times, ca 1170 s, near 2020 cm<sup>-1</sup>. It must also be mentioned that a small absorption band situated at 1937 cm<sup>-1</sup> was observable as well, which as explained in the previous Section, 4.3.3, is linked with the shoulder at 2020 cm<sup>-1</sup>. The reduction of bands at 2040 cm<sup>-1</sup> and 1951<sup>-1</sup> was consistent with the photodecomposition of the parent molecule. Based on the analysis performed in Sections 4.3.2 and 4.3.3, Mo(CO)<sub>5</sub> should be the product of the photolysis process. A distinguishable peak that could be attributed to Mo(CO)<sub>5</sub> was not observable, nevertheless the broadness exhibited by the 2040 cm<sup>-1</sup> peaks towards lower wavenumber values can be associated with the presence of Mo(CO)<sub>5</sub>. For longer irradiation times, evidence for the photodecomposition of Mo(CO)<sub>5</sub> into Mo(CO)<sub>4</sub> was observable. This was indicated by the transmission shoulder near 2015 cm<sup>-1</sup> which can be assigned to the B<sub>1</sub> or B<sub>2</sub> v(C-O) modes of Mo(CO)<sub>4</sub> aligned perpendicular to the surface and by the absorption band at 1937 cm<sup>-1</sup>, associated with the B<sub>1</sub> or B<sub>2</sub> v(C-O) modes of Mo(CO)<sub>4</sub> aligned parallel to the surface. Based on the intensity of the bands attributed to Mo(CO)<sub>6</sub>, Mo(CO)<sub>5</sub> and Mo(CO)<sub>4</sub>, the majority of species on the surface after 3870 s of irradiation comprised of the parent molecule. In addition the population of photoproducts was dominated by species belonging to Mo(CO)<sub>5</sub>. It is noticeable that no bands were observable due to the tricarbonyl even after prolonged irradiation. Thus it appears that the photolysis process stopped with the formation of the first two unsaturated carbonyls. Analogous behaviour was observed during the photolysis of Mo(CO)<sub>6</sub> in solution, where

the process stopped with the production of  $Mo(CO)_5$ , as the energy of the latter was quenched due to the formation of a bond with the solution.<sup>160</sup>

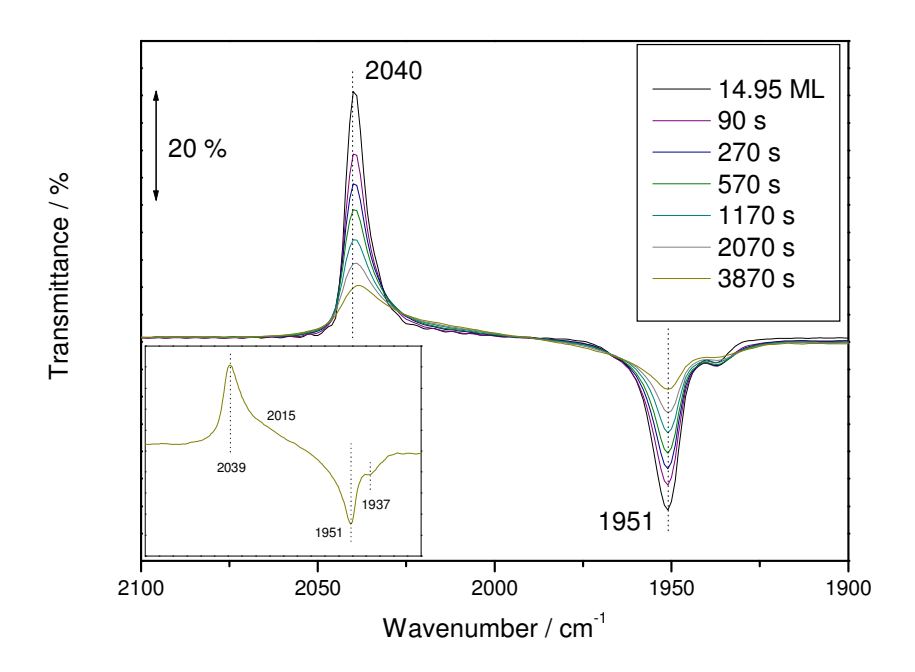


**Figure 4-19** FT-RAIRS spectra collected from the surface as a function of irradiation time. The first, black line, measured after 20.2 L of Mo(CO)<sub>6</sub>. Inset: spectrum collected after the final 3870 s irradiation.

The results collected following the photolysis process via XPS are presented in the next two figures. The Mo(3d<sub>5/2</sub>) peak area, FWHM and binding energy are plotted as a function of irradiation time in Figures 4-20a, 4-20b and 4-20c respectively. In the first two, similar trends were observed with the values increasing to begin with and after 570 s reaching a plateau. This small initial increase, approximately by 16 % for the data points of Figure 4-20a, could be associated with screening of the Mo atoms closest to the TiO<sub>2</sub>(110) surface by the top layers. As the latter were removed via photodecomposition, the former could contribute to the XPS Mo(3d<sub>5/2</sub>) signal. The presence of the plateau is consistent with the absence of any Mo desorption due to UV radiation. Contrary to the behaviour of the previous two overlayers, the binding energy change did not exhibit an exponential like decay. Initially, after 90s of irradiation, the Mo(3d<sub>5/2</sub>) value decreased by 0.23 eV but further irradiation did not appear to alter the peak position. Of course in can be observed that the next two data points were recorded at lower binding energies, but

based on the fact that the last three points had the same value  $\pm$  0.03 eV as 90 s one and the error involved, it would be safe to assume that the peak position did not change after the initial dose of radiation. The former observation would indicate that longer exposures did not induce further decomposition on the surface and consequently the photoreaction stopped with the production of  $Mo(CO)_5$  and  $Mo(CO)_4$ . Furthermore, the energy difference,  $\Delta E$ , of the  $Mo(3d_{5/2})$  peak before irradiation and after 3870 s is calculated at 0.28 eV, approximately 0.2 eV smaller than the one observed for the 0.34 ML overlayer,  $\Delta E$  at 0.47 eV, and for the 0.7 ML overlayer,  $\Delta E$  at 0.59 eV. This difference again offers an additional indication that the final products were quite different from the ones obtained at lower coverage overlayers. The data presented in Figure 4-20d, plot of  $C_{rel.area}/Mo_{rel.area}$  as a function of UV irradiation time, were in accordance with the previous statement. The first point, following the deposition of the multilayer, was calculated at 2.87. If the latter is normalised at 6 then the final point is calculated at 4.34 (originally at 2.08), value that deviates on average by 0.67 from the one obtained for the 0.34 ML overlayer,  $C_{rel.area}/Mo_{rel.area}$  at 3.73, and from the 0.7 ML,  $C_{rel.area}/Mo_{rel.area}$  at 3.61.

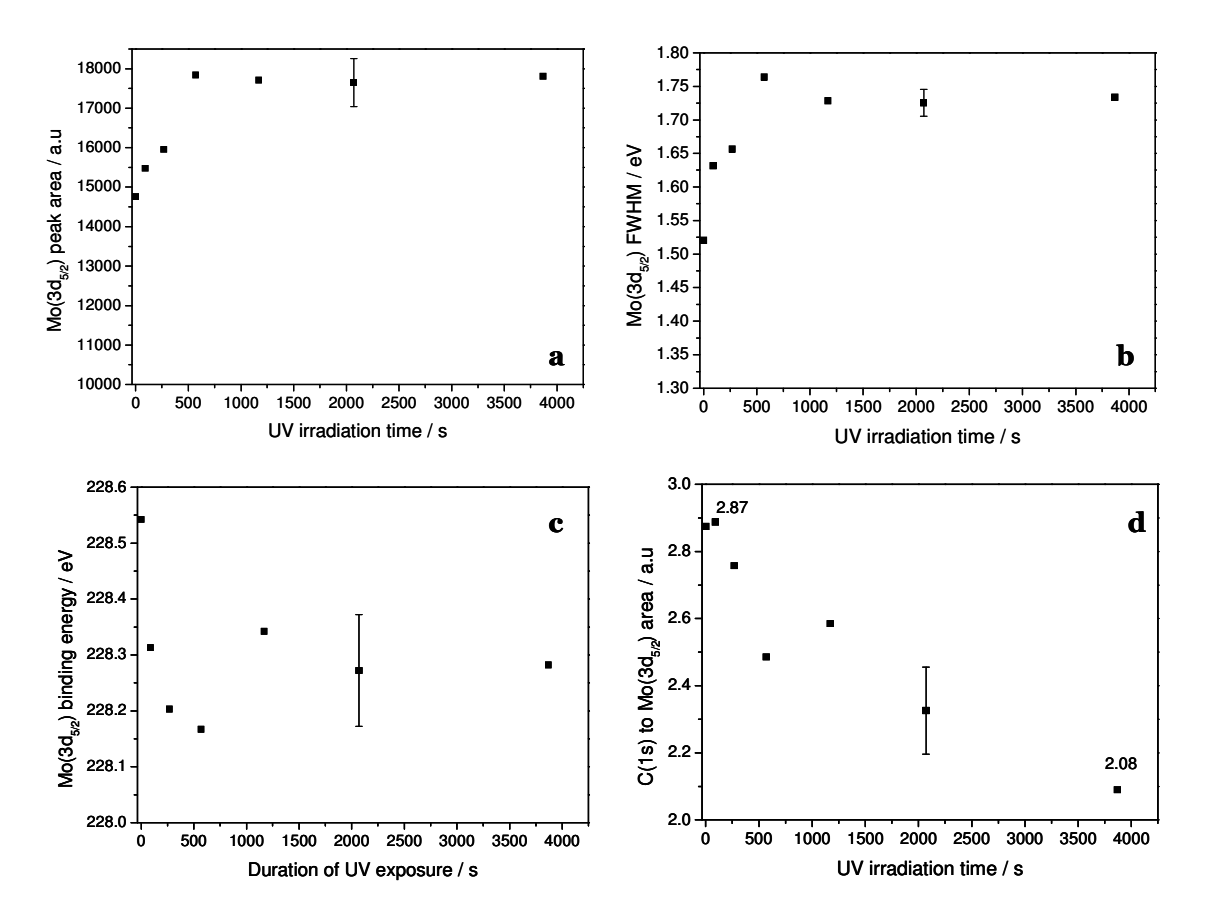


**Figure 4-20** (a)  $Mo(3d_{5/2})$  peak area as a function of irradiation time (b)  $Mo(3d_{5/2})$  peak intensity as a function of irradiation time (c)  $Mo(3d_{5/2})$  peak position as a function of irradiation time. The first point on each plot represents data collected immediately after deposition of the molecule.

Figure 4-21 represents the C(1s) peak area (a), FWHM (b) and binding energy (c) as a function of irradiation time along with the binding energy of O(1s) due to Mo(CO)<sub>6</sub> (d) to serve as a comparison. The first 4 exposures to radiation did not appear to alter dramatically the area under the C(1s) peak, probably due to the amount of CO remaining on the surface. Longer irradiation times though, resulted in a sharp decrease indicating CO desorption. The C1(s) FWHM values as a function of UV irradiation time are plotted in Figure 4-21b. During initial irradiation times, up to 1170 s, the values exhibited a steady increase, indicative of the formation of new species on the surface. On the other hand, no change was observed for the final two exposures, in accordance with the absence of formation of new products. Finally, the binding energy exhibited an exponential like decay with values reaching a plateau after 2070 s, hinting as well that no

Mo(CO)<sub>3</sub> species were produced by the photolysis process at the last stages of irradiation. The binding energy difference between initial and final state was 0.97 eV contrary to 1.52 eV for the 0.34 ML and 1.25 eV for the 0.7 ML, supporting the argument made before that the outcome of the photolysis of the multilayer was different to the one observed at lower coverages.

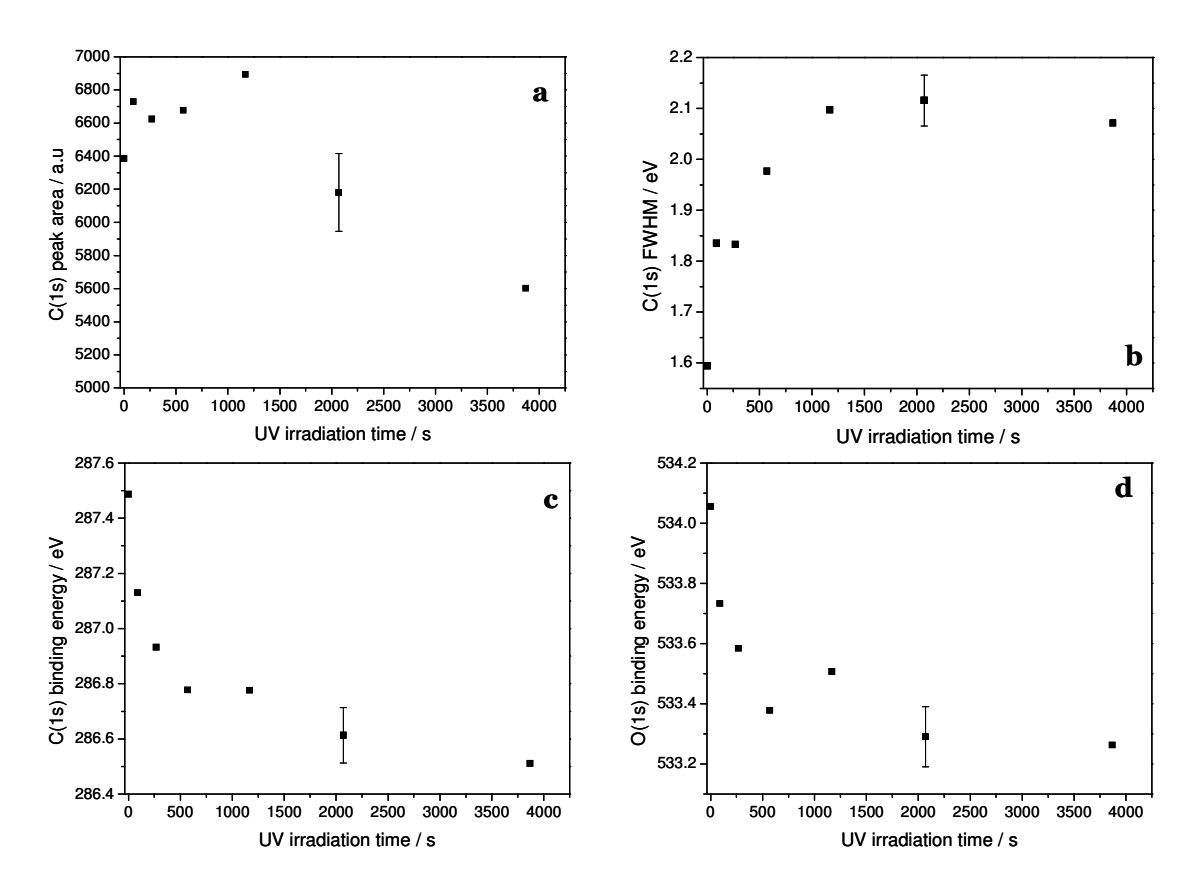


**Figure 4-21** (a) C(1s) peak area as a function of irradiation time (b) C(1s) peak intensity as a function of irradiation time (c) C(1s) peak position as a function of irradiation time (d) O(1s) (from Mo(CO)<sub>6</sub>) peak intensity as a function of irradiation time. The first point on each plot represents data collected immediately after deposition of the molecule.

# 4.3.5 Temperature Effects- Formation of Carbon Free Particles

The stability and thermal behaviour of the photofragments was also examined by performing annealing experiments after completion of the photolysis process. The goal for

these studies was to investigate whether is was possible to produce clean metallic Mo on the  $TiO_2(110)$  surface, similar to previous studies performed on the Au(111) substrate.<sup>201</sup> Consequently the effect of temperature was examined for overlayers produced by 1.53 L and 2.73 L  $Mo(CO)_6$  exposure. The thick overlayer was not investigated for two reasons. The first one was that we were mainly interested in producing nanoparticles, and the second one related with the presence of a substantial amount of  $Mo(CO)_6$  even after prolonged exposure. Based on previous studies annealing high coverages of  $Mo(CO)_6$  results in C contaminated  $Mo.^{202}$ 

Figure 4-22 represents FT-RAIRS spectra collected after terminating the photolysis of Mo(CO)<sub>6</sub> as a function of annealing temperature. The initial coverage of Mo was 0.34 ML, produced by exposing the surface to 1.53 L of Mo(CO)<sub>6</sub>, Section 4.3.2. The black line represents the spectrum collected after 690 s of UV exposure, while the following three lines represent spectra collected after flashing the sample to the relevant temperature. The final one was collected after annealing the surface at 400 K for 60 s. As it can be observed, the first two temperature rises did not result in any change, with the spectra retaining the same characteristics of one recorded after the photolysis. Further flashing to 300 K resulted in the disappearance of the broad transmission peak situated around 2000 cm<sup>-1</sup>. The final spectrum, collected after 60 s annealing at 400 K did not reveal any infrared bands. This is the reason why it is believed that the peaks at 1967 cm<sup>-1</sup> and 1943 cm<sup>-1</sup> were noise due to the spectrometer and not actual infrared bands. An interesting point to be made is the fact that the photofragments appeared to be more strongly bound on the surface than the parent molecule. Mo(CO)<sub>6</sub> has been found to desorb from the TiO<sub>2</sub>(110) surface at 200 K,<sup>62</sup> whilst here all the infrared bands assigned to the photofragments disappeared after annealing the surface above 245 K.

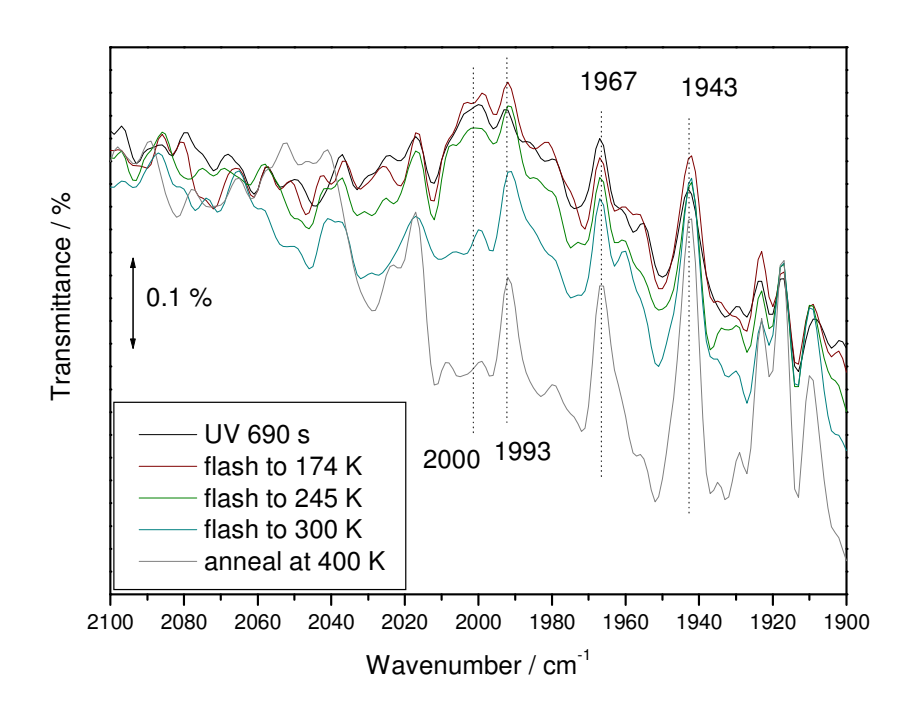


**Figure 4-22** FT-RAIRS spectra collected from the surface as a function of temperature. The first, black line, measured after the last irradiation, 960 s. The observation of noise in these spectra becomes facilitated by the low intensity values of the actual peaks. In other figures, the signal to noise ratio has large enough values that fluctuations due to noise cannot easily be distinguished.

Following desorption of all species after annealing at 400 K, the surface composition was examined with XPS. Figures 4-23, 4-24 and 4-25 represent the Mo(3d), C(1s) and O(1s) energy regions respectively. In each figure the spectra collected after adsorption of the parent molecule and after the end of the photolysis are given to work as a comparison. According to the spectrum of Figure 4-23, Mo was still present on the surface, its coverage calculated at 0.24 ML. The sizes of both Mo(3d) peaks were reduced compared with the two other spectra probably due to some coalescence of Mo into particles due to annealing. The position of the peak was very near the value of metallic Mo, at 228.7 eV. In addition the 0.4 eV difference from the UV exposed surface indicated that a change in the oxidation state of Mo had taken place as part of the annealing process. A barely distinguishable broad peak situated around 286.2 eV was present in C(1s) region, Figure 4-23, indicating that some C was still left on the surface, with its coverage calculated at 0.14 ML. On the other hand no O(1s) peak due to photodecomposed species

was observed in Figure 4-25, in accordance with the FT-RAIRS spectra of Figure 4-22. Overall annealing the photodecomposed species resulted in the formation of metallic Mo particles on the  $TiO_2(110)$  surface, but with some amount of C still present. It is worth mentioning that after performing these experiments the surface was cooled down to 130 K and exposed to 40 L of CO. There was no evidence of CO re-adsorption observed in FT-RAIRS possibly due to C contamination of the Mo particles.

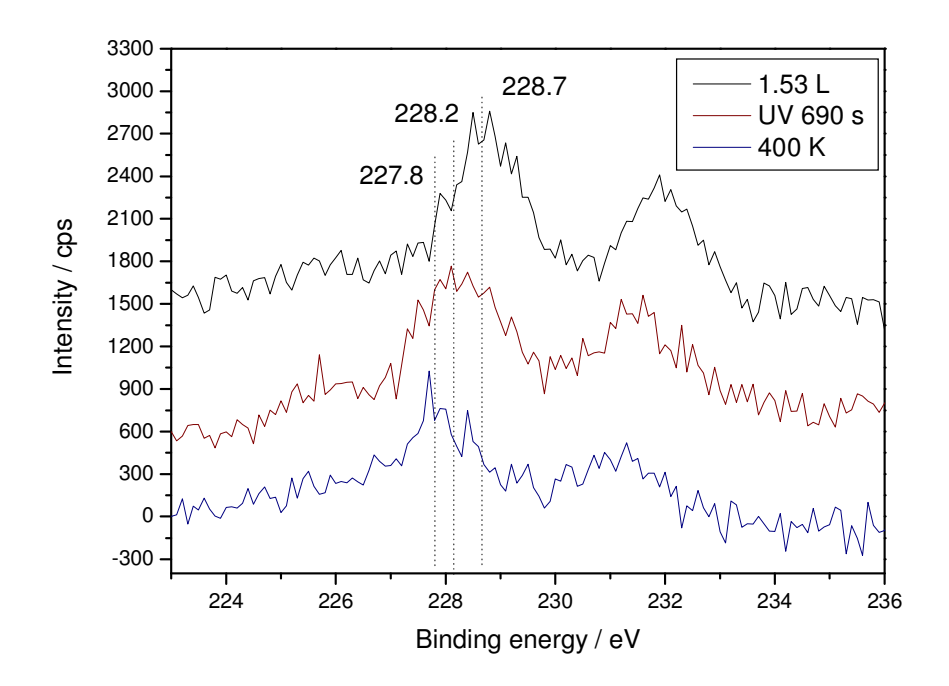


**Figure 4-23** XPS spectra of Mo(3d) region collected after 1.53 L deposition (black line), after 690 s of irradiation (dark red line) and following annual at 400 K (navy line). The spectra are separated in order to facilitate their observation.

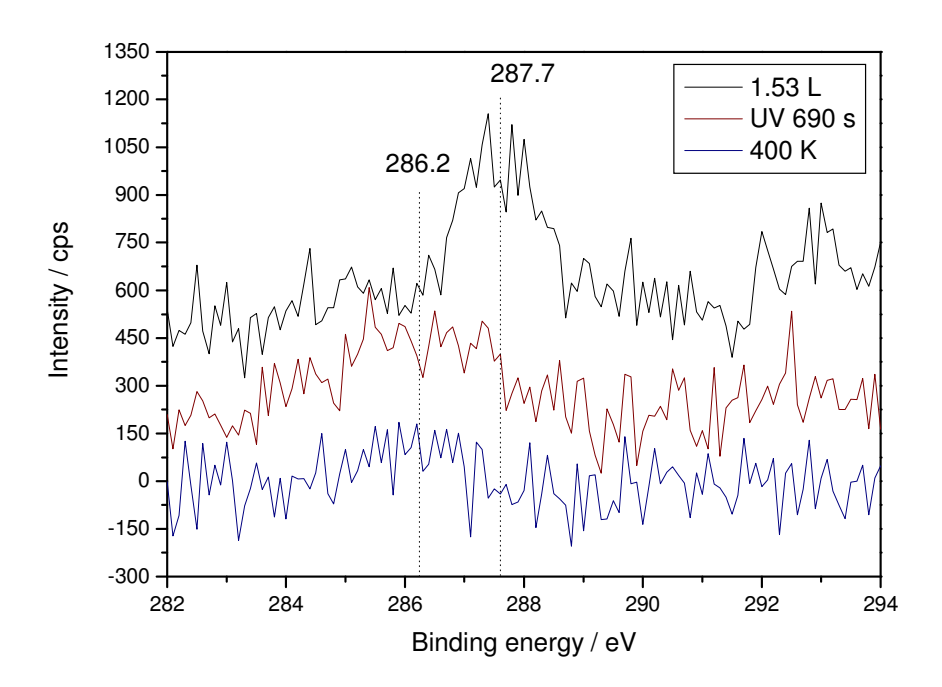


**Figure 4-24** XPS spectra of C(1s) region collected after 1.53 L deposition (black line), after 690 s of irradiation (dark red line) and following annual at 400 K (navy line). The spectra are separated in order to facilitate their observation.

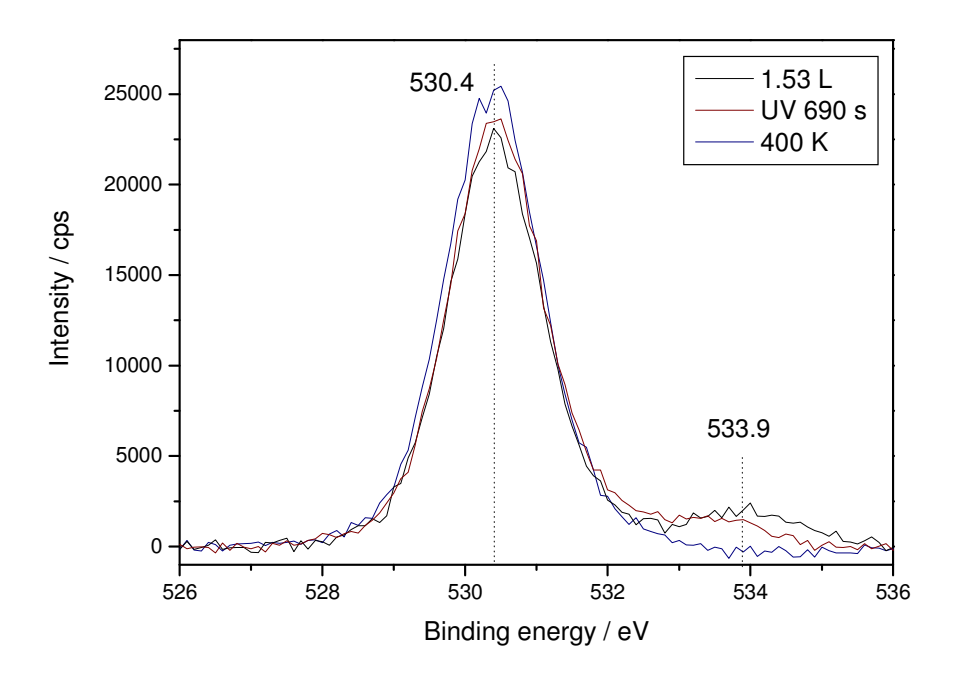


**Figure 4-25** XPS spectra of O(1s) region collected after 1.53 L deposition (black line), after 690 s of irradiation (dark red line) and following anneal at 400 K (navy line).

Analogous temperature dependence experiments were undertaken for the higher coverage overlayer, 0.7 ML, deposited from exposing the surface to 2.73 L of Mo(CO)<sub>6</sub>. Figure 4-26 represents FT-RAIRS spectra collected from the surface as a function of annealing time. Contrary to the ones of Figure 4-22 these were collected after annealing the surface for 60 s. After 300 K the appearance of the FT-RAIRS spectrum was almost identical to the one collected after 1350 s of UV exposure, with a broad transmission band that incorporated at least two smaller peaks at 2032 cm<sup>-1</sup> and 2009 cm<sup>-1</sup>. Further annealing at 368 K resulted in the complete transformation of the spectrum. The broad peak was replaced by a well defined one situated at 2062 cm<sup>-1</sup>, while a small shoulder was also evident around 2050 cm<sup>-1</sup>. Following the annealing at higher temperatures the intensity of the 2062 cm<sup>-1</sup> band was reduced in half and its position red shifted to 2058 cm<sup>-1</sup>. On the other hand the shoulder at 2044 cm<sup>-1</sup> became more distinct. Finally heating the surface to 495 K resulted in the disappearance of all the infrared features. In a similar way to Figure 4-11, the intensities of the four peaks present in the spectra of Figure 4-26 are plotted against annealing temperature in Figure 4-27.

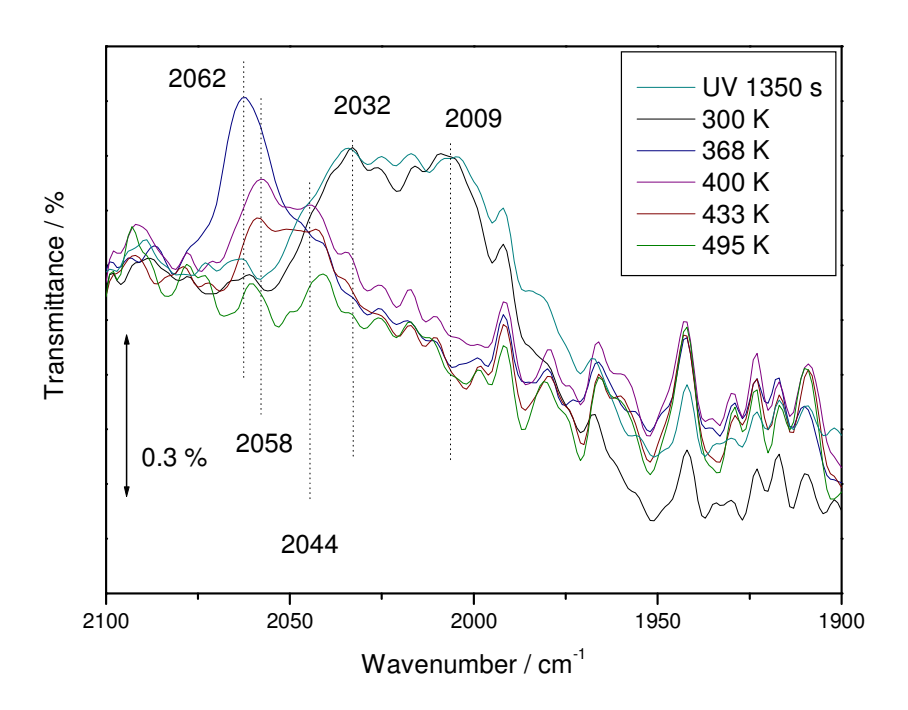


**Figure 4-26** FT-RAIRS spectra collected from the surface as a function of temperature. The first, cyan line, measured after the last irradiation, 960 s.

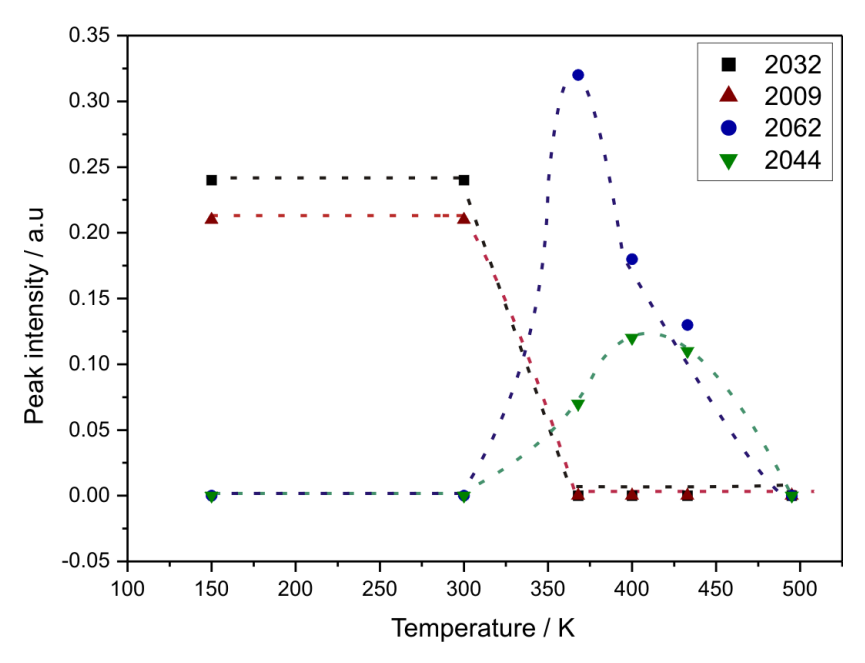


**Figure 4-27** Intensity of characteristic FT-RAIRS bands, Figure 4-26, as a function of annealing temperature. Black squares intensity of 2032 cm<sup>-1</sup> peak, red triangles intensity of 2009 cm<sup>-1</sup> peak, blue circles intensity of 2062 cm<sup>-1</sup> peak, green triangles intensity of 2044 cm<sup>-1</sup> peak. Lines are drawn as guide to the eye.

According to spectra of Figure 4-26 and intensity data presented in Figure 4-27, at 300 K the photodecomposed species (black squares and red triangles) were still adsorbed unperturbed on the surface. This indicates a surface bond stronger than the one formed by the parent molecule and by the species produced from the photolysis of the 0.34 ML overlayer. Annealing at 368 K resulted in the transformation of the majority of unsaturated carbonyls into a single adsorbate, as indicated by the peak at 2062 cm<sup>-1</sup> and its equivalent intensity, Figure 4-27. He *et. al.* while studying the adsorption on CO on an O covered Mo(110) surface, have reported an infrared band at the exact same position, 2062 cm<sup>-1</sup>. They attributed this band to an indirect interaction of O and CO, with O withdrawing electronic charge from the metal, and the latter causing a reduction in the backdonation from Mo to CO. A band due to direct interaction of O and CO was also reported at 1983 cm<sup>-1</sup>, which was not observed here. A similar band, at 2060 cm<sup>-1</sup>, has been reported following the simultaneous UV irradiation and CO exposure of a high surface area MoO<sub>3</sub>/SiO<sub>2</sub> catalyst. Thus it is extremely probable that the band observed

in Figure 4-26 was due to the v(C-O) mode of CO molecules adsorbed on oxidised Mo particles. A smaller band was also present in the spectrum collected after 368 K, in the form of a shoulder situated at 2044 cm<sup>-1</sup>. A possible assignment of this band could involve adsorbed CO on Mo particles of different oxidation state than the ones responsible for the peak at 2062 cm<sup>-1</sup>. In addition the band at 2044 cm<sup>-1</sup> appeared more resistant to annealing as its intensity value did not change even after annealing to 433 K. On the contrary, the intensity of the band at 2062 cm<sup>-1</sup> was reduced more that 50 % by the 433 K annealing. Finally both bands disappeared after 495 K, indicating the desorption of all species from the TiO<sub>2</sub>(110) surface at that temperature.

The XPS spectrum of the Mo(3d) region collected after annealing revealed the presence of oxidised Mo on the surface, Figure 4-28, in accordance with the FT-RAIRS data. The oxidation state was similar to the one observed after the photolysis process, while the amount of Mo appeared reduced probably due to some coalescence of the particles. As revealed by spectra of C(1s) and O(1s) regions no C or O due to carbonyls were present on the surface, Figures 4-29 and 4-30 respectively. Thus since no carbonyls were detected, the oxidation of Mo must have taken place due to an interaction with the support. Indeed the O(1s) spectrum collected after UV irradiation revealed a small shift of the peak due to TiO<sub>2</sub>. The shift though disappeared after annealing. Overall the thermal treatment of the surface resulted in the production of oxidised Mo particles which did not suffer from C contamination, Figure 4-29 navy line. It is quite possible that the CO species present at 368 K influenced this outcome, as they were not observed for the thinner overlayer. Finally it should be mentioned that following the thermal treatment, the surface was cooled to 130 K and exposed to 40 L of CO. No CO adsorption though was observed in FT-RAIRS spectra, despite the fact that the Mo particles were not contaminated with C.

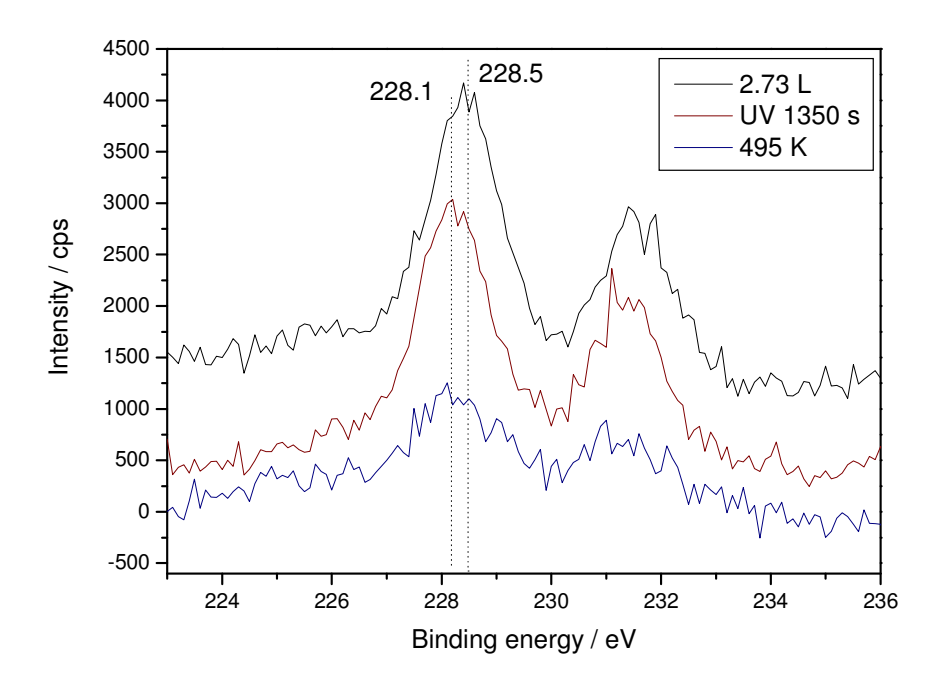


**Figure 4-28** XPS spectra of Mo(3d) region collected after 2.73 L deposition (black line), after 1350 s of irradiation (dark red line) and following annual at 495 K (navy line). The spectra are separated in order to facilitate their observation.

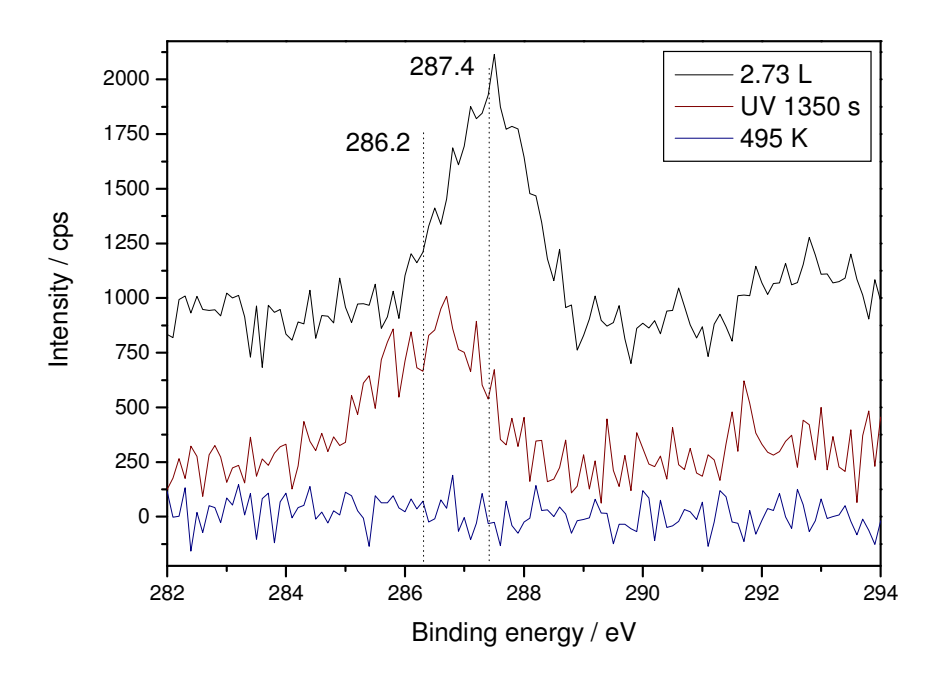


**Figure 4-29** XPS spectra of C(1s) region collected after 2.73 L deposition (black line), after 1350 s of irradiation (dark red line) and following anneal at 495 K (navy line). The spectra are separated in order to facilitate their observation.

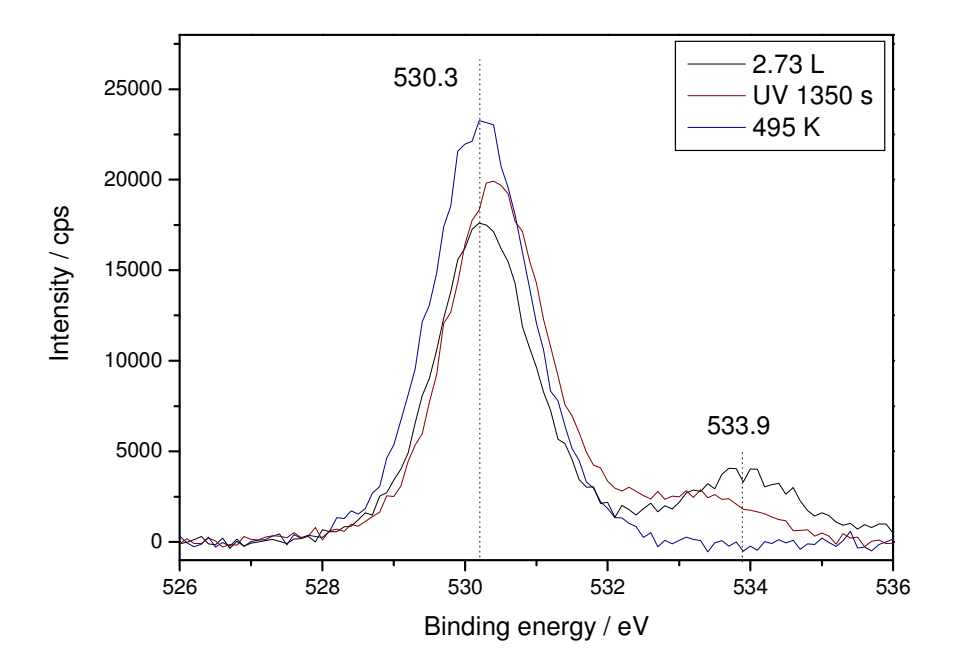


**Figure 4-30** XPS spectra of O(1s) region collected after 2.73 L deposition (black line), after 1350 s of irradiation (dark red line) and following anneal at 495 K (navy line).

## 4.3.6 Photodecomposition with Optical Filter

According to the results previously presented, the photolysis of Mo(CO)<sub>6</sub> on the TiO<sub>2</sub>(110) surface proceeded differently depending on the amount of adsorbed hexacarbonyl. A possible explanation for this phenomenon could involve the participation of the oxide surface in the photodecomposition reaction. Indeed there is evidence in the literature that such involvement is possible. For example as mentioned before Okamoto *et. al.* reported that the photooxidation of Mo(CO)<sub>6</sub> adsorbed on high surface area TiO<sub>2</sub> was induced by surface electron holes and not via direct UV excitation of the molecule. <sup>192</sup> In addition Ying and Ho observed that the yield of photodissociation of Mo(CO)<sub>6</sub> increased substantially when the molecule was adsorbed on a potassium (K) preadsorbed Cu(111) and Si(111)-(7x7) surface. <sup>172</sup> They attributed this increase due to a new photodissociation channel involving the adsorption of hot electrons from the support. The capturing of the photogenerated electrons by Mo(CO)<sub>6</sub> becomes possible due to a raise of the Fermi level by K. <sup>169</sup>

In an effort to observe similar effects, we repeated the photolysis of 0.34 ML of Mo, but using this time the light transmitted through a filter, the spectral characteristics of which can be found in the experimental Section, 4.2. TiO<sub>2</sub> has an indirect band gap of 3.0 eV, ~ 413 nm. Thus the light transmitted via the filter should be able to excite electrons from the surface. Figure 4-31 represents FT-RAIRS spectra collected during the photolysis process as a function of irradiation time. As it can be observed no change was observed in the spectra even after prolonged exposure to the light, 1590 s. Thus it would appear that no electrons from the support take part directly in the photodissociation process.

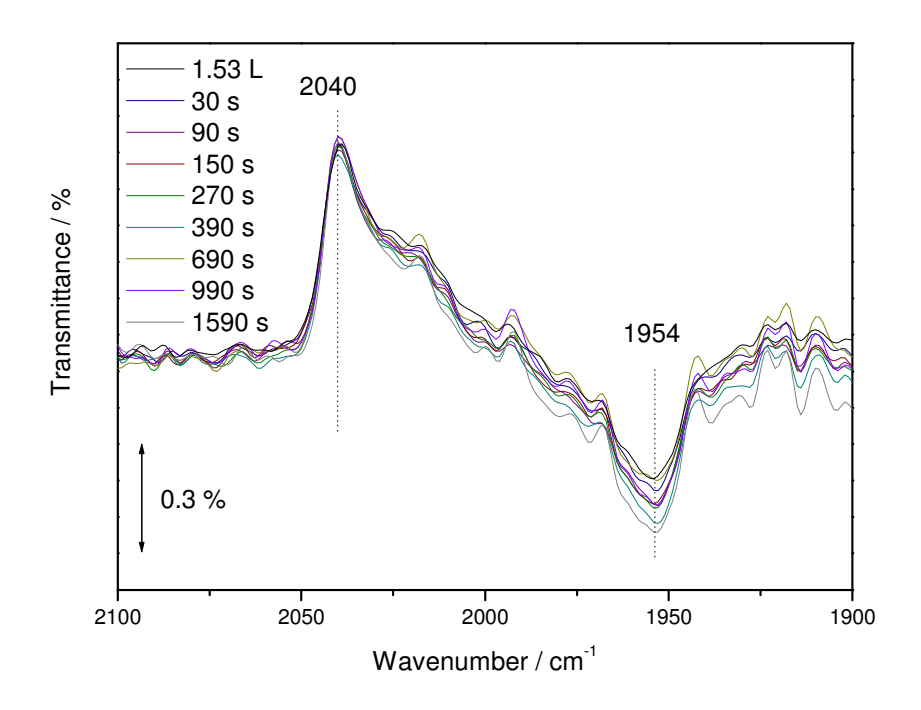


Figure 4-31 FT-RAIRS spectra collected from the surface as a function of irradiation time. The first, black line, measured after 1.53 L of  $Mo(CO)_6$ 

#### 4.4 Conclusions

The photolysis of Mo(CO)<sub>6</sub> supported on TiO<sub>2</sub>(110) was studied using a combination of FT-RAIRS and XPS as a function of overlayer coverage. It was observed that the final photofragments were different in every case. For the 1.53 L deposition, the majority of the species comprised of Mo(CO)<sub>3</sub> while no indication of the parent molecule was evident. For the 2.73 L deposition, several products were present on the surface after the end of irradiation. The FT-RAIRS spectra incorporated features attributed to Mo(CO)<sub>x</sub> (x=5,4, and 3) and also to the parent molecule, while the existence of polymer species was not excluded. XPS data though revealed that the oxidation state of Mo was similar in each case, indicating that the dominant photofragment was common for both. On the contrary the photolysis of multilayers, exposure 20.2 L, resulted in the formation of only Mo(CO)<sub>5</sub>, whilst the majority of adsorbates still comprised of Mo(CO)<sub>6</sub>. By comparing all of the above, a strong possibility emerges that the photolysis process is promoted in the low

coverage regime. Two were the variables in all cases studied: direct contact with the oxide support and the amount of adsorbed  $Mo(CO)_6$ . In multilayers the photolysis might be quenched in a similar way to the one observed in solution. On the other hand direct contact with the surface appeared to enhance the photodecomposition, as observed for the 1.53 L deposition. A possible scenario could involve the contribution to the process of photoexcited electrons from the support. Experiments were performed, section 4.3.6., upon which the sample was irradiated with energies that could invoke band gap excitations but not direct photodecomposition. Unfortunately there was no sign observed of photofragments being produced. Nevertheless this cannot be considered as clear evidence of the passive nature of the  $TiO_2(110)$  surface, as the latter could act as a catalyst for the photolysis process.

Finally the temperature dependence of the photofragments was investigated in an effort to produce clean metallic Mo particles. Annealing at 400K of the first Mo(CO)<sub>6</sub> overlayer, exposure 1.53 L, resulted in the formation of metallic particles, although C contaminants were also present on the surface. On the other hand, annealing the second Mo(CO)<sub>6</sub> overlayer, formed by exposure to 2.73 L, to 495 K resulted in the production of oxidised Mo particles while no C contamination was evident in XPS spectra. During this annealing process two new strongly bound species were observed, that contributed to an infrared band similar to the v(C-O) mode of CO adsorbed on oxidised Mo. It is plausible that the formation of this species was responsible for the complete removal of C from the surface. In both experiments no CO readsorption was detected via FT-RAIRS, possibly due to the presence of C in one case and due to oxidised particles in the other.

# Chapter 5

# The deposition of (CH<sub>3</sub>)<sub>2</sub>Au(acac) on TiO<sub>2</sub>(110)

#### 5.1 Introduction

Since the discovery by Haruta that oxide supported Au nanoparticles exhibit high catalytic activity towards many reactions,<sup>6</sup> a plethora of experimental and theoretical investigations have been performed exploring this phenomenon. In the following section a summary of these studies is going to be presented focusing mainly on model systems, particularly Au deposited on TiO<sub>2</sub>, and their involvement in the oxidation of CO to CO<sub>2</sub>, which is the simplest reaction.

### 5.1.1 Growth Mode of Au on TiO<sub>2</sub>(110) and TiO<sub>x</sub>

Following the discovery of the extraordinary catalytic properties of Au, when the latter is dispersed as nanoparticles on titania substrates, several studies have been performed to understand the growth mode and identify the adsorption sites of these particles on the oxide surface. Using a combination of LEIS and XPS Zhang *et al.* have shown that initially Au grows as 2D islands, or more precisely as quasi 2D islands for substrate temperatures between 160 and 300 K. <sup>129</sup> The growth continues in this fashion until a critical coverage,  $\theta_{cr}$ , was reached, upon which 3D islands started to form. The value of  $\theta_{cr}$  was estimated at 0.15 ML, and identified by a break in the plot of LEIS signal against average Au thickness. It should also be noted that no sign of oxidation or encapsulation of Au particles was observed. Similar results were obtained by Parker *et al.* where additionally, the value of  $\theta_{cr}$  was observed to decrease with increasing temperature. <sup>128</sup> In this study a kinetic model was proposed, according to which kinetic limitations result in the formation of two dimensional islands up to certain coverage. Further deposition is controlled thermodynamically, hence the formation of 3D structures. A schematic of the growth process can found in Figure 5-1.

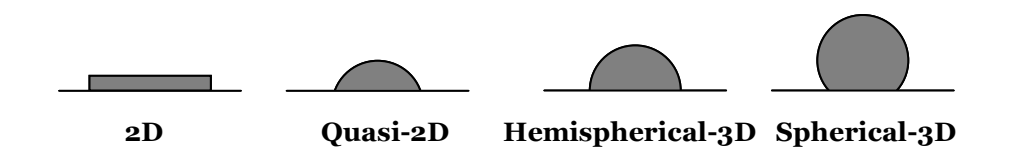


Figure 5-1 A schematic of the growth procedure established for Au islands on  $TiO_2(110)$ . The term quasi 2D was used as these particles were found to be more than 1 ML thick.<sup>205</sup>

The initial formation of two dimensional islands was also confirmed by STM-STS experiments, although the  $\theta_{cr}$  value was observed at coverages smaller than 0.1 ML.<sup>206</sup> At this value a transition was observed upon which the nature of Au particles changed from non-metallic to metallic. In addition these STM studies revealed that the quasi 2D Au islands were formed on defect sites. Only when the latter were filled did atoms nucleate on other sites. This observation is extremely important as it offers an insight on the preferable nucleation sites for Au on the surface. Indeed several theoretical studies have suggested that the most stable site for Au adsorption is an oxygen vacancy. 207-<sup>209</sup> Wang and Hwang have proposed the formation of a strong ionic bond between Au and Ti atoms on a reduced surface, <sup>207</sup> whereas Lopez *et al.* claimed that Au could not bind to a perfectly stoichiometric TiO<sub>2</sub> surface. <sup>209</sup> Furthermore Wahlstrom et al. observed experimentally using STM that the population of oxygen vacancies decreased almost linearly with increasing Au amount.<sup>208</sup> In addition their DFT calculations revealed that this adsorption site was the most stable amongst different sites on stoichiometric and reduced surfaces. Based on these findings a model was also proposed to account for the formation of 2D structures which has as follows. The existence of a strong bond between Au and vacancy prevents the creation of 3D particles, as Au-Au interactions are weak. Nevertheless each vacancy can only accommodate a certain number of Au atoms, thus when saturation is reached the Au island-vacancy system diffuses on the surface until it meets another vacancy. As the number of vacancies is limited, above a critical value 3D structures will appear. Changes in the photoemission spectra of Au and Ti induced as a function of Au coverage have also been attributed to interaction with defect sites.<sup>210</sup>

The pivotal role of oxygen vacancies both in the growth process and in the catalytic activity has been highlighted by some recent publications from the Goodman

group. <sup>211-214</sup> In their approach, Au atoms were deposited on a thin TiO<sub>x</sub> films, the surface of which has protruding Ti<sup>3+</sup> atoms. The oxidation state of these Ti atoms is similar to the one exhibited by Ti atoms situated below an oxygen vacancy on a TiO<sub>2</sub> crystal. When deposited on this substrate, Au completely wetted the surface forming (1x1) 2D domains. <sup>213</sup> After the completion of 1 ML, a second ordered structure was formed this time (1x3) with respect to the substrate. 3D Au islands were observed only after increasing the coverage value above 1.4 ML. The reason for this different growth mode originates in the strength of the Au-TiO<sub>x</sub> bond, which as observed with TPD was even stronger than the sublimation energy of Au. <sup>214</sup> Further increase in coverage resulted in 3D islands as the distance between atoms on the first two layers facilitated the formation of 3D structures. It is also remarkable that the highest catalytic activity was observed for the bilayer (1x3) structure. <sup>211, 212</sup>

## 5.1.2 Catalytically Active Au Nanoparticles

The origin of the catalytic activity of oxide supported Au nanoparticles has been the subject of many debates. Various factors appear to influence this activity such as quantum size effects, the particle's surface structure and electronic state, the presence of defect sites on the support and the support itself. As far as the CO oxidation reaction is concerned, open subjects involve the nature of the active site, the adsorption sites on the surface for CO and  $O_2$  and the reaction mechanisms. In the following paragraphs the above are going to be presented in detail.

One of the reasons proposed for the catalytic activity is the appearance of quantum size effects when the size of particles reaches a specific value.<sup>212, 215</sup> This conclusion was formed by the observation that Au particles of highest activity exhibited a non-metallic character, as indicated by the presence of band gap characteristics on STS measurments.<sup>139</sup> Contrary to the previous view, different researches have suggested that the crucial factor controlling the activity is the coordination number of the nanoparticles.<sup>216-218</sup> Indeed Lemire *et al.* using a combination of STM, FT-RAIRS and

TPD showed that the adsorption behaviour of CO on Au particles deposited on FeO(110) was similar to the one observed for thin Au films. 216 They argued that what separated the two systems was the presence of highly uncoordinated Au atoms for the nanoparticles. In addition, according to DFT calculations the bonding of CO and O increased by decreasing the coordination number. <sup>218</sup> The authors suggested that as activation barriers for surface reactions follow the adsorption energy trends, smaller particles (low coordination number) are more active towards CO oxidation. Nevertheless the electronic properties of Au nanoparticles should play a significant role in the reaction. Both experimental and theoretical results point towards the fact that Au particles with the highest activity are negatively charged. For example, Goodman and coworkers observed that the frequency of the v(CO) mode decreased with decreasing Au size, an effect attributed to the negatively charged smaller Au particles.<sup>215</sup> Similar shifts were observed for Au<sub>8</sub> clusters deposited on defect free and defect rich MgO surfaces.<sup>219</sup> Based on quantum ab initio calculations, the observed red-shift was explained due to enhanced back donation from Au clusters to the  $2\pi^*$  orbital of CO, whereas the formation of negatively charged particles was attributed to the interaction with surface defects. Electron transfer from the support has also been observed for high surface area Au/TiO2 catalysts by Boccuzzi et al. 220 The presence of anionic Au on a defect rich TiO<sub>2</sub> surface has been linked with redistribution of the electron density, accumulated on Ti 3d states due to the vacancy formation. <sup>221</sup> It is interesting that according to these calculations, SiO2 did not exhibit the same behaviour as the vacancy was 'compensated' by the formation of a Si-Si bond, and as a result Au particles on SiO<sub>2</sub> exhibited metallic character. This renders them less active towards CO oxidation as reaction activation barriers are higher than for anionic Au. Hence it can be postulated than the support can also influence the catalytic activity. Indeed experiments performed both with high surface area catalysts and have shown that different supports exhibit different activities towards CO oxidation. 218, 222, 223 The same effect was observed for the electrocatalytic activity towards CO oxidation of Au nanoparticles supported on C and TiO<sub>x</sub> thin films.<sup>224</sup>

The detailed role of the support on the catalytic activity has been widely studied. For example Liu *et al.* have postulated that the adsorption of  $O_2$  takes place at the interface

between TiO<sub>2</sub> support and Au particles.<sup>225</sup> According to their DFT calculations this resulted in the stretching of O-O bond, hence the adsorbed O<sub>2</sub> became highly activated. Similar bonding sites for O<sub>2</sub> have been reported by other authors as well, following DFT calculations. 51, 226, 227 Furthermore Mollina et al. proposed that at this bonding configuration, bridged between Ti and Au, O2 can react with CO with very low activation barriers.<sup>227</sup> Furthermore in the case of MgO they calculated that in the case of preadsorbed CO a reaction intermediate, namely CO+O<sub>2</sub>, can be formed at the interface. <sup>226</sup>In all the above cases an ionic type of bond has been proposed. Experimentally O<sub>2</sub> has been found to bind stronger on the 2D islands rather than the 3D ones. 228 As a result the activity exhibited by the 2D islands was attributed to their ability to dissociatively adsorb O<sub>2</sub>, although theoretically the activation barrier for dissociation is very high.<sup>229</sup> Enhanced bonding on 2D islands compared to 3D structures has also been reported by Meier and Goodman for the case of CO adsorption. <sup>230</sup> But contrary to O<sub>2</sub>, the adsorption sites for CO have been found to be located only on Au particles. This was confirmed both experimentally and using theoretical calculations. Experimentally, bands appearing on FT-RAIRS spectra have been attributed to CO adsorbed on top sites of Au. 217, 230 Boccuzzi et al. have also identified bands due to CO adsorbed on step sites near the perimeter of the particles and on top, for high surface area samples.<sup>231</sup> These results have been confirmed theoretically, as the most stable adsorption site has been found to be located on top of Au islands.<sup>51, 227</sup>

To conclude this section a remark has to be made regarding the mechanism of the CO oxidation reaction. Sanchez *et al.* have proposed two possible mechanisms for the low temperature oxidation.<sup>51</sup> The first, an Eley-Rideal type, involved the direct oxidation of gaseous CO with preadsorbed O<sub>2</sub>. The second one, a Langmuir-Hinshelwood type, involved the coadsorption of CO and O<sub>2</sub> and their subsequent reaction on an Au cluster. For the high temperature oxidation a Langmuir-Hinshelwood type was proposed that involved the reaction between CO adsorbed on Au clusters and O<sub>2</sub> bonded at the interface. The latter was also adopted by Boccuzzi *et al.* during their study of the reaction using high surface area catalysts.<sup>231</sup> A Langmuir-Hinshelwood type mechanism was also proposed by

Molina *et al.* based on the fact that for both reactants their calculated adsorption configurations were stable on the TiO<sub>2</sub> surface.<sup>227</sup>

### 5.1.3 Deposition of Au from (CH<sub>3</sub>)<sub>2</sub>Au(acac)

The use of Au organometallic complexes for the deposition of highly dispersed particles has been employed by different researches. For example Goodman et al. have reported the preparation of Au/TiO2 catalysts from Au organometallics such as  $[Au_2(dppm)_2](PF6)_2$ ,  $Au_3(Ph_2pz)_3$ ,  $[Au_4(dppm)_2(3,5-Ph_2pz)_2](NO_2)_2$ , and  $Au_4(form)_4$ . These high surface area catalysts exhibited high catalytic activity towards CO oxidation, with the maximum being observed for the catalysts prepared from the Au<sub>4</sub> compound. Active catalysts for CO oxidation have also been prepared from the deposition of (CH<sub>3</sub>)<sub>2</sub>Au(acac) compound on SiO<sub>2</sub><sup>233</sup> and TiO<sub>2</sub><sup>234</sup>. The method adopted in these studies comprised of adsorption at 33 °C followed by decomposition due to calcination in air at higher temperatures. In this way, metallic Au particles were produced, with sizes varying between 4 and 8 nm. (CH<sub>3</sub>)<sub>2</sub>Au(acac) was the compound used in this study for deposition of Au particles on the TiO<sub>2</sub>(110) surface. It was selected as it has been shown to produce good quality thin films via pyrolytic decomposition when deposited using the CVD method.<sup>235</sup> In addition Maeda et al. had recently reported the deposition of (CH<sub>3</sub>)<sub>2</sub>Au(acac) using OMCVD under UHV conditions on both TiO<sub>2</sub>(110) and Si(111) single crystals.<sup>236</sup> A molecular model of the (CH<sub>3</sub>)<sub>2</sub>Au(acac) molecule can be found in Figure 5.2, as reported by Shibata et al. 237

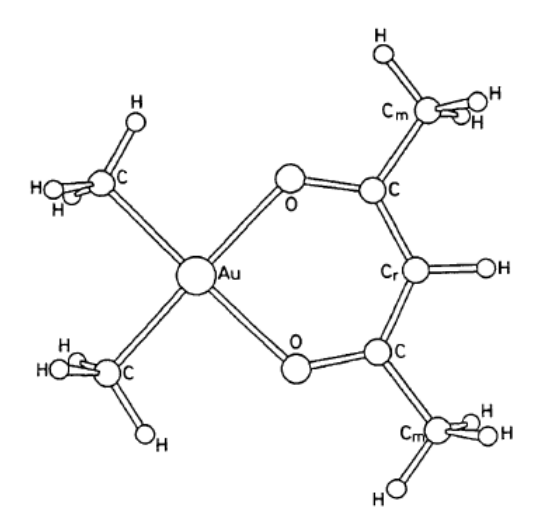


Figure 5-2 Molecular model of (CH<sub>3</sub>)<sub>2</sub>Au(acac) structure.<sup>237</sup>

It has been observed, by means of EXAFS and DRIFTS, that upon RT deposition of (CH<sub>3</sub>)<sub>2</sub>Au(acac) on partially dehydroxylated TiO<sub>2</sub>, the molecule reacted with the surface to form two kinds of bonds. The first comprised of (CH<sub>3</sub>)<sub>2</sub>Au species bonded on two oxygen atoms of the surface, and the second involved the formation of Ti(acac) groups. No Au-Au contributions were present in EXAFS spectra indicating the presence on the surface of mononuclear complexes, which retained their oxidation state namely Au<sup>3+</sup>. Upon heat treatment, all the organic ligands were removed from the surface, whilst Au aggregated into clusters of metallic character. Similar results were obtained for MgO<sup>239</sup> and  $\gamma$ -Al<sub>2</sub>O<sub>3</sub><sup>240</sup> supports, while the (CH<sub>3</sub>)<sub>2</sub>Au(acac) molecule appeared to physisorb on a zeolite NaY support.

## 5.2 Experimental

The experiments described in the following sections regarding the adsorption of  $(CH_3)_2Au(acac)$  on  $TiO_2(110)$ , were performed in the UHV chamber described in Section 2.1. The surface of the  $TiO_2(110)$  crystal was cleaned through repeated cycles of sputtering and annealing. Contrary to the treatment described in the previous two chapters, here the surface was annealed to 700 K without any further oxygen treatment. This was done in order to increase the population of defect sites, which as mentioned in Section 5-1 are the adsorption sites for Au on the  $TiO_2(110)$  surface.  $(CH_3)_2Au(acac)$  (Strem

Chemicals, powder, 98% pure) was placed inside a glass vial as acquired, i.e. without any further purification. The glass vial was attached to a leak valve already connected to the chamber. Subsequently repeated freeze-pump-thaw cycles were performed to purify the organometallic compound. The latter was introduced into the chamber through a thin stainless steel tube, the open end of which was situated approximately 15 mm from the sample.

All FT-RAIRS spectra were collected via the MCT detector and 1760-x Perkin Elmer spectrometer. Each spectrum was recorded using a p-polarised light, 200 scans and resolution of 4 cm<sup>-1</sup> in the spectral region from 2200 cm<sup>-1</sup> to 1200 cm<sup>-1</sup>. The XPS spectra were collected using the Mg anode (1253.6 eV), while for each scan the energy regions of C(1s), Ti(2p), O(1s) and Au(4f) were measured. The spectra for all areas were collected using a 0.1 eV step, duel time of 1 s and averaging over 3 scans. The analysis of the XPS data was performed using the WSPECTRA software. Prior to any analysis a Shirley background was subtracted from the raw data. The coverage and thickness values were estimated using equations 16 and 19, Section 2.4.2, respectively. As mentioned in that Section, an error of the order of 15-20 % can be expected from these calculations. For the substrate values, the peak area of  $Ti(2p_{3/2})$  was used, whilst for the adsorbate values the peak areas of  $Au(4f_{7/2})$  and C(1s).

For the low temperature (130 K) deposition experiments the following procedure was followed. First, the vial was degassed for 10 min,  $P_{ch}$  at  $1x10^{-7}$  mbar, with the crystal facing the opposite direction. Subsequently two cycles of sputtering and annealing were performed. An XPS measurement of the surface was then made, and if the latter was contaminated further cycles of cleaning were performed. If the surface was contaminant-free, the sample was cooled down to 130 K. At this temperature  $(CH_3)_2Au(acac)$  was dosed and FT-RAIRS spectra were collected after each exposure. At the end of the deposition an XPS measurement of the surface was performed. The same procedure was followed for the room temperature depositions.

For the high temperature (550 K) depositions the following experimental protocol was utilised. Initially the vial was degassed for 10 min, Pch at 1x10<sup>-7</sup> mbar, with the crystal facing the opposite direction. Subsequently two cycles of sputtering and annealing were performed. An XPS measurement of the surface was then made, and if the latter was contaminated further cycles of cleaning were performed. If the surface was contaminant-free, the sample's temperature was raised to 700 K, and with the crystal facing towards the opposite direction of the doser, the vial was again degassed briefly (approximately 2 to 5 min). Following this step, the sample's temperature was reduced to 550 K and (CH<sub>3</sub>)<sub>2</sub>Au(acac) was introduced in the chamber at P<sub>ch</sub>=1x10<sup>-7</sup> mbar. Molecular oxygen was then introduced at P<sub>ch</sub>=4x10<sup>-5</sup> mbar. Since the pressure inside the chamber was controlled by O<sub>2</sub>, the exposure values of (CH<sub>3</sub>)<sub>2</sub>Au(acac) reported in section 5.3.4 were calculated based on the initial pressure of  $1 \times 10^{-7}$  mbar. After the introduction of  $O_2$ , the sample was turned to face the dosing line, whilst the amount of (CH<sub>3</sub>)<sub>2</sub>Au(acac) deposited was controlled by varying the exposure time. At the end of the exposure the sample was allowed to cool down for three minutes in O2 atmosphere. Finally an XPS spectrum was collected.

### 5.3 Results and discussion

The main objective of experiments presented in following sections was to investigate whether (CH<sub>3</sub>)<sub>2</sub>Au(acac) could be utilised as an organometallic precursor for the OMCVD of highly dispersed Au particles on TiO<sub>2</sub>(110), which as stated in Section 5.1 exhibit unusual catalytic activity. Hence the adsorption behaviour of (CH<sub>3</sub>)<sub>2</sub>Au(acac) on TiO<sub>2</sub>(110) was examined using XPS at three different temperatures: 130, 300 and 550 K. In addition, in order to gain some insight into the adsorption geometry of (CH<sub>3</sub>)<sub>2</sub>Au(acac) and possible interaction with the TiO<sub>2</sub>(110) surface, FT-RAIRS data collected during the 130 K adsorption are also presented in Section 5.3.4.

### 5.3.1 Adsorption of (CH<sub>3</sub>)<sub>2</sub>Au(acac) on the TiO<sub>2</sub>(110) Surface at 130 K

Figures 5-3 to 5-5 represent XPS spectra recorded immediately after exposure of 32.45 L of (CH<sub>3</sub>)<sub>2</sub>Au(acac) on the TiO<sub>2</sub>(110) surface, for Au(4f), C(1s) and O(1s) regions. As it can be observed in Figure 5-3, two peaks were recorded in the Au(4f) region at 87.6 and 91.2 eV which can be assigned to  $Au(4f_{7/2})$  and  $Au(4f_{5/2})$  respectively. 122 For metallic Au, the two peaks appear at 84 (Au(4 $f_{7/2}$ )) and 87.7 eV (Au(4 $f_{5/2}$ )), <sup>122</sup> hence the positive shift observed here would indicate that the Au species present on the surface were in an oxidised state. Au $(4f_{7/2})$  binding energies near 87.7 + 0.6 eV have been previously been assigned to Au<sup>3+</sup> state. 242-244 Hence since in the parent molecule Au is in an Au<sup>3+</sup> state, it would be reasonable to assume that Au retained its oxidation state upon adsorption on the surface. In the C(1s) region, Figure 5-4, one main peak was observable at 286 eV while a small shoulder was also distinguishable around 287.3 eV. These features would indicate the presence of two different carbon species on the surface, as for example C-H and C-O. Indeed peaks observed at 287.3 ± 0.8 eV have been attributed to C-O and C=O bonds. 198, <sup>245</sup> In the O(1s) region, Figure 5-5, only a single peak at 533 eV was observed attributed to the adsorbates. No contribution from the oxygen support was recorded indicating the complete coverage of the surface by adsorbates. This was also verified by the lack of peaks in the Ti(2p) region, inset of Figure 5-5.

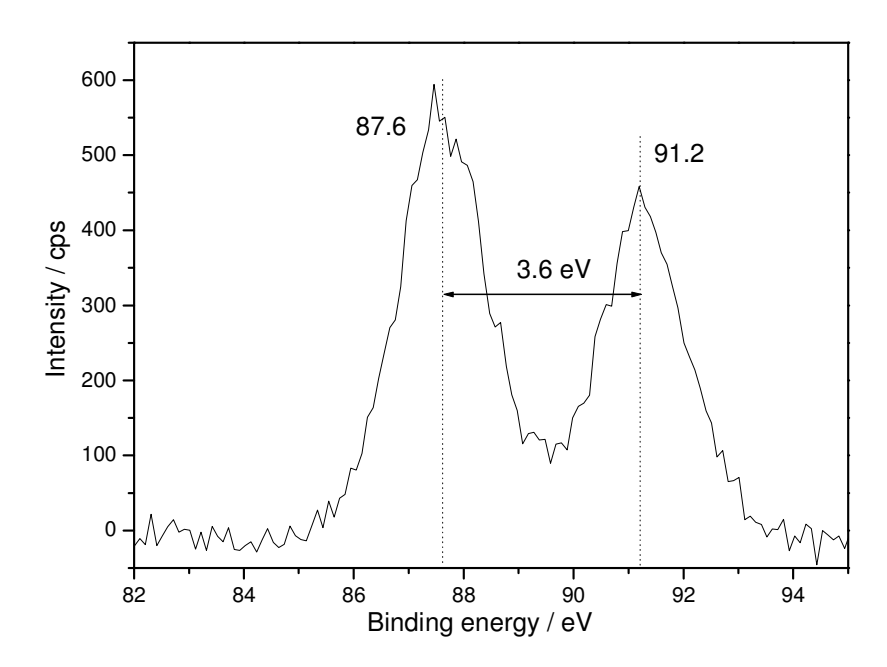


**Figure 5-3** XPS spectra of Au(4f) region collected after exposing the  $TiO_2(110)$  surface to 32.45 L of  $(CH_3)_2Au(acac)$  at 130 K.

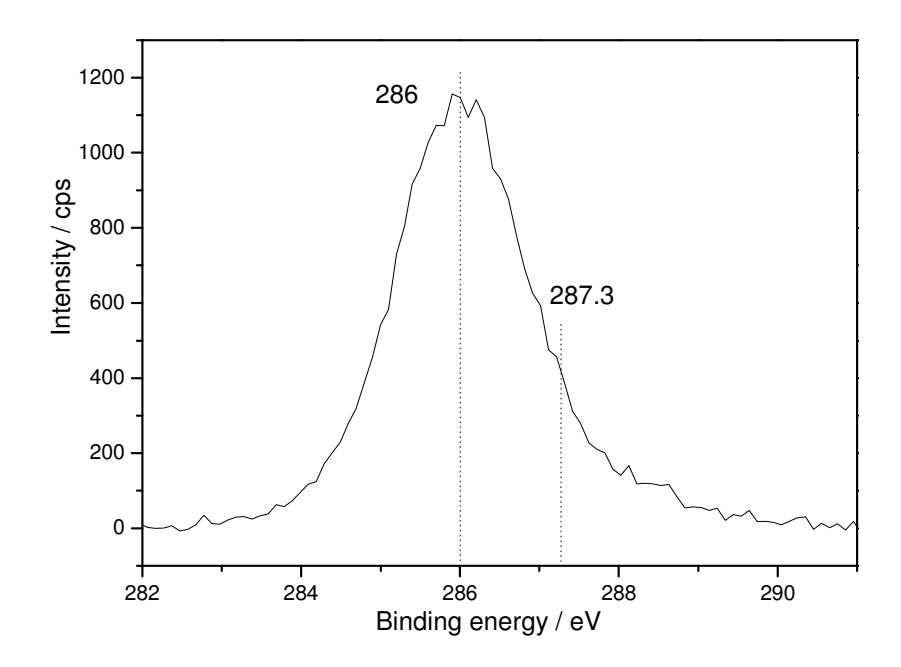


**Figure 5-4** XPS spectra of C(1s) region collected after exposing the  $TiO_2(110)$  surface to 32.45 L of  $(CH_3)_2Au(acac)$  at 130 K. One peak can be observed at 286 eV along with a shoulder situated at 287.3 eV.

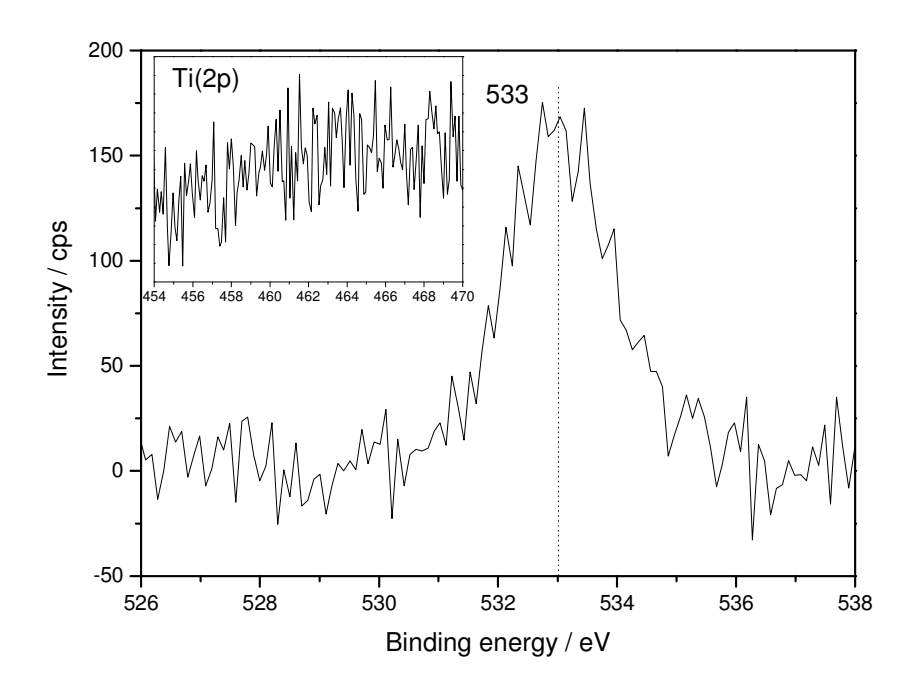


**Figure 5-5** XPS spectra of O(1s) region collected after exposing the  $TiO_2(110)$  surface to 32.45 L of  $(CH_3)_2Au(acac)$  at 130 K. No oxygen due to the oxide is observed, indicating the coverage of the surface by the molecule. This is also confirmed by the absence of any peaks in the Ti region (inset).

### 5.3.2 Annealing Behaviour of Adsorbed (CH<sub>3</sub>)<sub>2</sub>Au(acac)

The behaviour of adsorbed (CH<sub>3</sub>)<sub>2</sub>Au(acac) upon annealing the sample to high temperature was investigated using XPS. Figure 5-6 represents the Au(4f) energy region (black line) recorded after adsorption at 130 K of 70 L (CH<sub>3</sub>)<sub>2</sub>Au(acac) and after thermally annealing this overlayer to 728 K for 10 min (red line). The first spectrum contained two sharp peaks at 87.7 and 91.3 eV which as mentioned before can be attributed to  $Au(4f_{7/2})$ and Au(4f<sub>5/2</sub>), with Au in a 3+ oxidation state. Their intensity was increased compared with the spectrum of Figure 5-5 due to the higher exposure. Upon annealing these two peaks shifted in lower binding energies whilst their intensity was also reduced. At 84.1 eV,  $Au(4f_{7/2})$  peak was very close to the value normally observed for metallic Au, <sup>122</sup> indicating the reduction of Au due to annealing. This effect is probably associated with desorption of organic ligands attached to Au during the 130 K adsorption, as indicated also by XPS spectra of C(1s) and O(1s) regions discussed in the following paragraph. The reduction in intensity can be attributed to either screening effects due to the formation of larger Au clusters or to encapsulation of Au into the support or due to Au desorption. The latter is highly improbable as the desorption temperature of Au from the titania surface is above 1200 K.<sup>211</sup> In addition, encapsulation has not been observed for this system.<sup>129</sup> On the other hand physically deposited Au particles have been found to form larger clusters upon annealing above 700 K, exposing more of the support. 246 This was also the case here, as after annealing the characteristic Ti(2p) peaks of the support were observed in the XPS spectrum, Figure 5-7. Thus the reduction of the Au signal must be due to screening of Au atoms located at the core of large particles. Goodman et al. 206 and Zhang et al. 246 have reported the reconstruction of Au particles into hexagonal shaped structures upon annealing above 700 K. As a result the surface was probed with LEED following annealing, but no hexagonal pattern was observed. A possible explanation would involve that these Au clusters were not large enough to give coherent scattering and hence produce a pattern. From our experience with Cu (Chapter 3, Figure 3-16), in order to obtain a new pattern the overlayer has to be very thick, and the calculated thickness of Au particles produced upon annealing was approximately 0.22 nm, as calculated by the XPS signals of

Figure 5-6. Of course this value is not exact due to the screening effect but it provides an estimate for the thickness of Au overlayer.

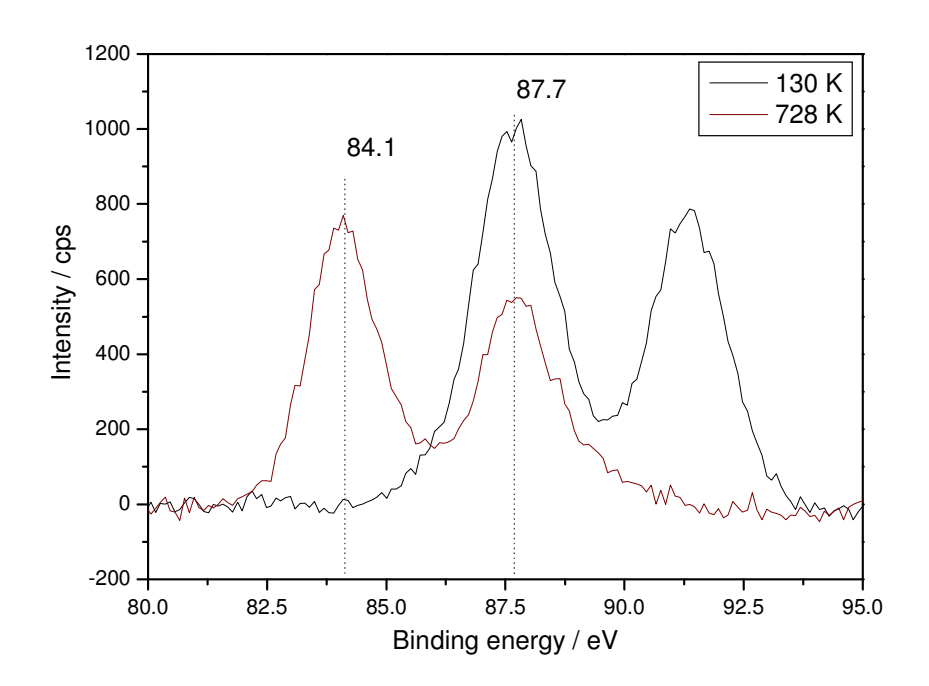


**Figure 5-6** XPS spectra of Au(4f) region collected after 70 L of  $(CH_3)_2Au(acac)$  exposure 130 K (black line) and subsequent anneal to 728 K (red line).

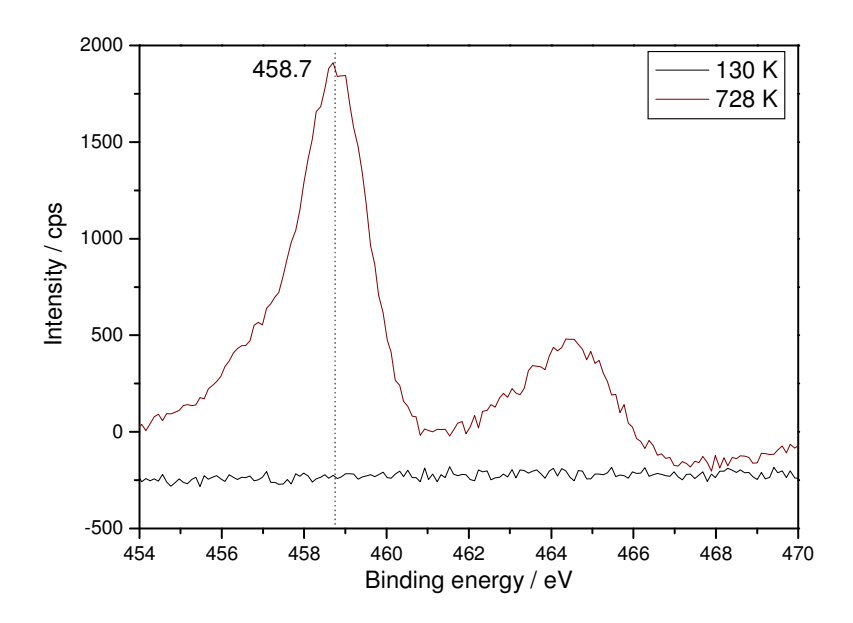


**Figure 5-7** XPS spectra of Ti(2p) region collected after 70 L of  $(CH_3)_2Au(acac)$  exposure at 130 K (black line) and subsequent anneal to 728 K (red line). Notice the shoulder on the left of  $Ti(2p_{3/2})$  peak indicative of surface defects.<sup>5</sup>

Figures 5-8 and 5-9 represent XPS spectra collected from C(1s) and O(1s) regions respectively, after 130 K deposition (black line) and after annealing at 728 K (red line). The spectrum of C(1s) following the 70 L (CH<sub>3</sub>)<sub>2</sub>Au(acac) exposure exhibited similar characteristics with the one presented in Figure 5-4, although the two features were more pronounced. The main peak at 286 eV increased in intensity while the shoulder associated with CO species increased in intensity and appeared shifted towards higher binding energies by about 0.3 eV. These changes can be accounted by taking into consideration the increased exposure. After the thermal annealing, these features disappeared from the spectrum whilst a new peak emerged at 284.5 eV. Its spectral position would be consistent with the presence on the surface of graphitic C, since a photoelectron peak from the latter normally appears at 284.5 + 0.5 eV. 198-200 There is no indication of carbidic carbon in the spectrum, usually situated at lower binding energies, <sup>247</sup> as for example for WC at 283.1 eV  $^{248}$  or for TiC at 281.8 eV.  $^{249}$  The broadness of the peak observed here is an artefact due to the scale of the plot. On the inset it can be observed that the peak is well defined, centred at 284.5 eV. The presence of graphitic carbon along with the dramatic reduction of carbon species is an indication that organic ligands adsorbed on the surface during the 130 K deposition were removed upon annealing. This is also in accordance with the complete disappearance from the O(1s) region of the peak attributed to the organic ligands, Figure 5-9. The process of decomposition is difficult to understand. For Rh(acac)(CO)<sub>2</sub> adsorbed on TiO<sub>2</sub>(110) it has been proposed that the acac ligand decomposed into CH3, CH, CO with C present on the surface.<sup>250</sup> The latter was then removed into CO via oxidation with lattice oxygen. At the end the surface exhibited no sign of C contamination. Maeda et al. proposed the same decomposition process for (CH<sub>3</sub>)<sub>2</sub>Au(acac) on TiO<sub>2</sub>(110), based on the fact that metallic Au particles were observed following annealing at 770 K. Nevertheless this cannot constitute strong evidence since metallic Au particles were also produced in our studies, Figure 5-6, but a significant amount of carbon was still left on the surface.

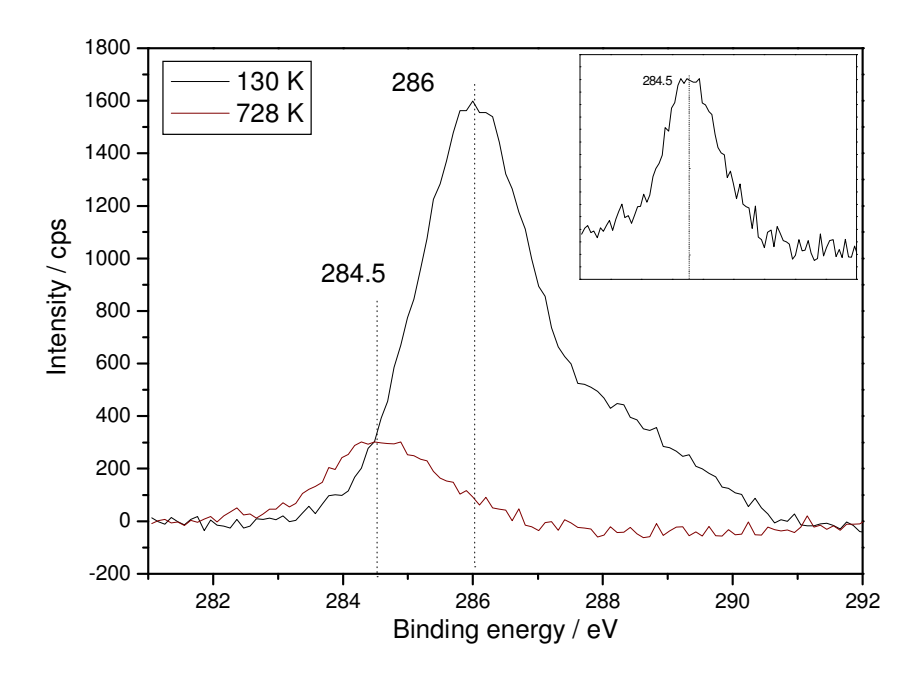


**Figure 5-8** XPS spectra of C(1s) region collected after 70 L of  $(CH_3)_2Au(acac)$  exposure at 130 K (black line) and subsequent anneal to 728 K (red line). Inset: spectrum after anneal.

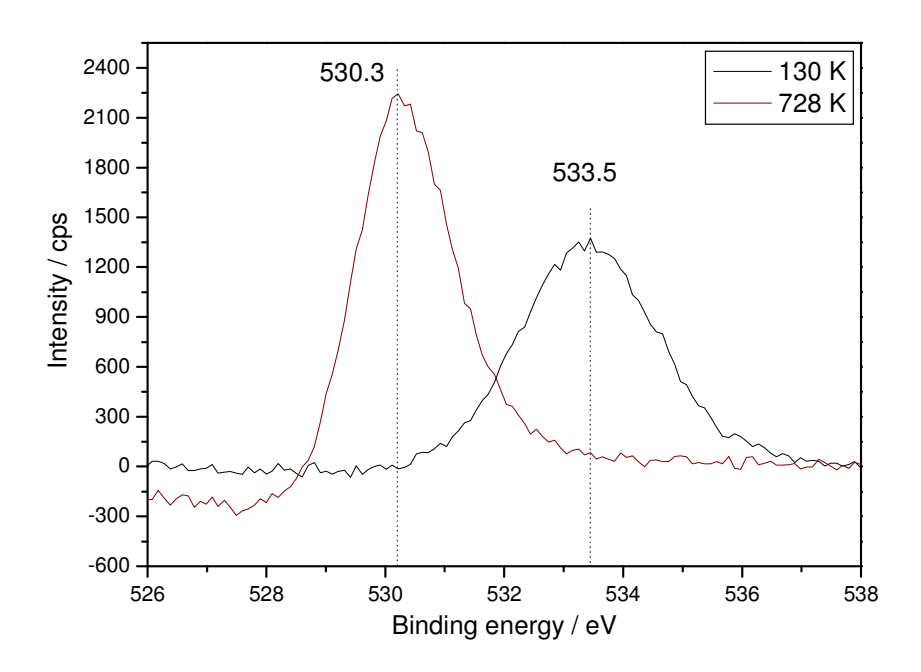
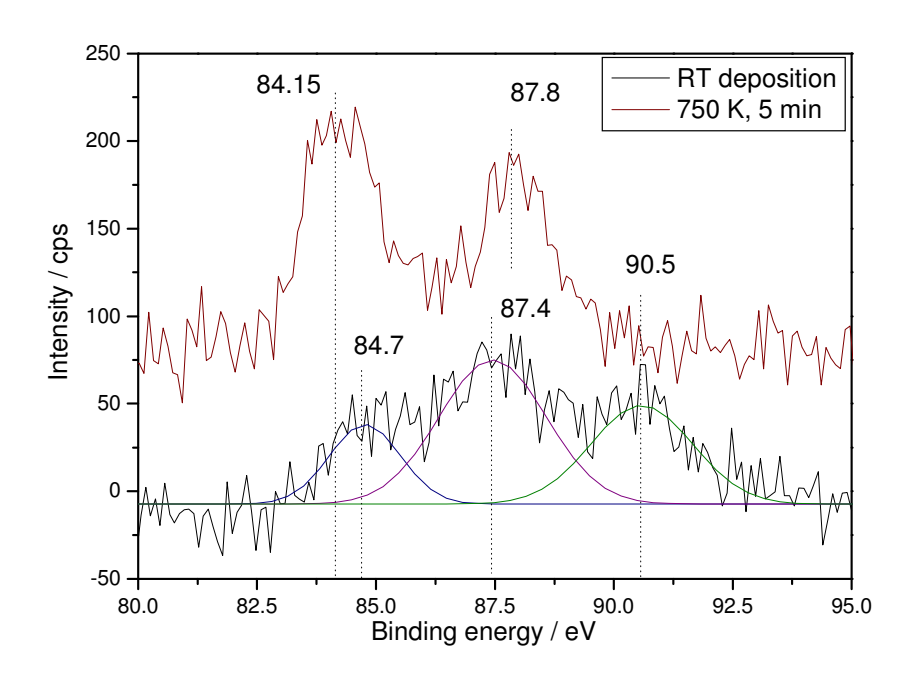
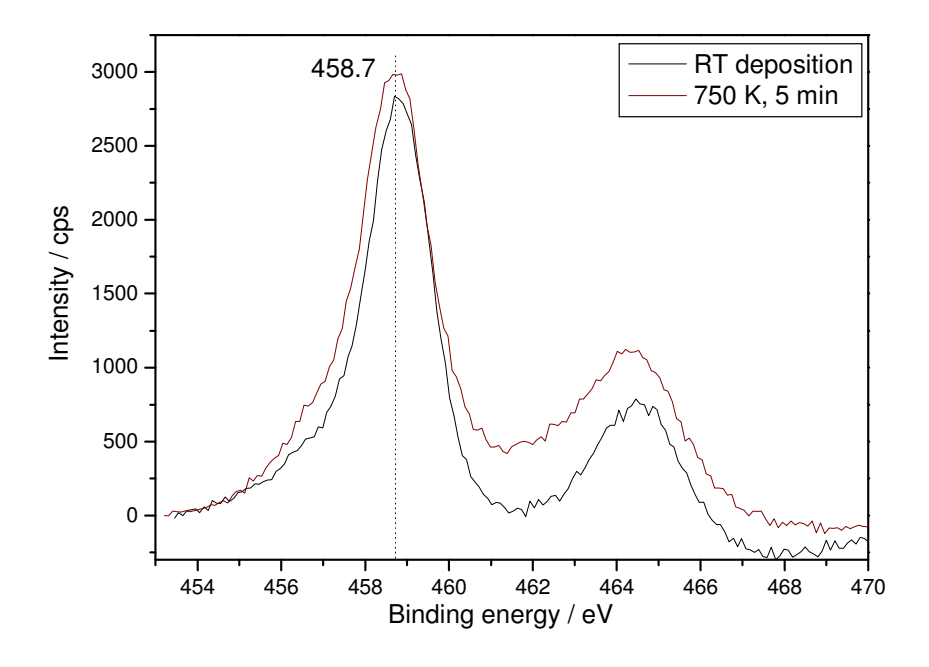


Figure 5-9 XPS spectra of O(1s) region collected after 70 L of  $(CH_3)_2Au(acac)$  exposure at 130 K (black line) and subsequent anneal to 728 K (red line).

The adsorption of (CH<sub>3</sub>)<sub>2</sub>Au(acac) on the TiO<sub>2</sub>(110) surface was also investigated at room temperature. During the deposition no infrared bands were observable in FT-RAIRS spectra hinting that upon adsorption the molecule underwent severe decomposition. Nevertheless, adsorbates were to be found on the surface as indicated by XPS. Figure 5-10 represents XPS spectra collected firstly from the Au(4f) energy region following the room temperature exposure of 456 L of (CH<sub>3</sub>)<sub>2</sub>Au(acac) (black line) and secondly after subsequent annealing to 750 K for 5 min (red line). The first spectrum comprised of three not well resolved peaks situated at 84.7, 87.4 and 90.5 eV respectively. The existence of these features suggested that Au was present on the surface following the deposition, but in different oxidation states. As observed previously, the energy splitting between  $Au(4f_{7/2})$  and  $Au(4f_{5/2})$  is 3.6 eV. The energy difference between each two peaks of Figure 5-10 is smaller, as between first and second is 2.7 eV and between second and third 3.1 eV. Hence none of them could form the Au(4f) pair. On the other hand if peak two, at 87.4 eV, was comprised of two peaks one at 88.3 eV and one at 86.9 eV, then we could get two Au(4f) pairs. The first would consist of 84.7 eV  $(Au(4f_{7/2}))$  and 88.3 eV  $(Au(4f_{5/2}))$  whilst the second of 86.9 eV  $(Au(4f_{7/2}))$  and 90.5 eV  $(Au(4f_{5/2}))$ . Based on this analysis, two different Au species were present on the surface. One closer to metallic state and one closer to the 3<sup>+</sup> state (at 87.7 eV), hinting the presence of organic ligands attached to Au. Thus, could be associated with an intermediate decomposition product of the precursor. Upon annealing two clear peaks were recorded in the spectrum, at 84.15 and 87.8 eV respectively. Their values were near the ones of Au<sup>o</sup>, hence it can be postulated that upon annealing all ligands attached to Au were decomposed leaving the latter in metallic state. Some clustering must have also occurred since the Ti(2p) peaks increased faintly in intensity, Figure 5-11.



**Figure 5-10** XPS spectra of Au(4f) region collected after 456 L of (CH<sub>3</sub>)<sub>2</sub>Au(acac) exposure at RT (black line) and subsequent anneal to 750 K (red line).



**Figure 5-11** XPS spectra of Ti(2p) region collected after 456 L of (CH<sub>3</sub>)<sub>2</sub>Au(acac) exposure at RT (black line) and subsequent anneal to 750 K (red line).

The presence of organic ligands on the surface of TiO<sub>2</sub>(110) was also indicated by the XPS spectrum collected from C(1s) region. Figure 5-12 represents the spectra collected from C(1s) region after adsorption at RT (black line) and following subsequent annealing at 750 K (red line). The first spectrum comprised of a broad peak centred around 285.6 eV. Its position hints that organic ligands were adsorbed on the surface, while a small shoulder near 284.7 eV indicates that some graphitic carbon was also present. Upon annealing the spectrum was transformed into a small peak situated at 284.7 eV, attributed to graphitic C. This observation, along with the presence of metallic Au, is in accordance with the removal of organic ligands from the surface. The O(1s) spectrum, Figure 5-13, did not exhibit any significant changes due to the annealing process, only a small increase which can be assigned to clustering of Au particles.

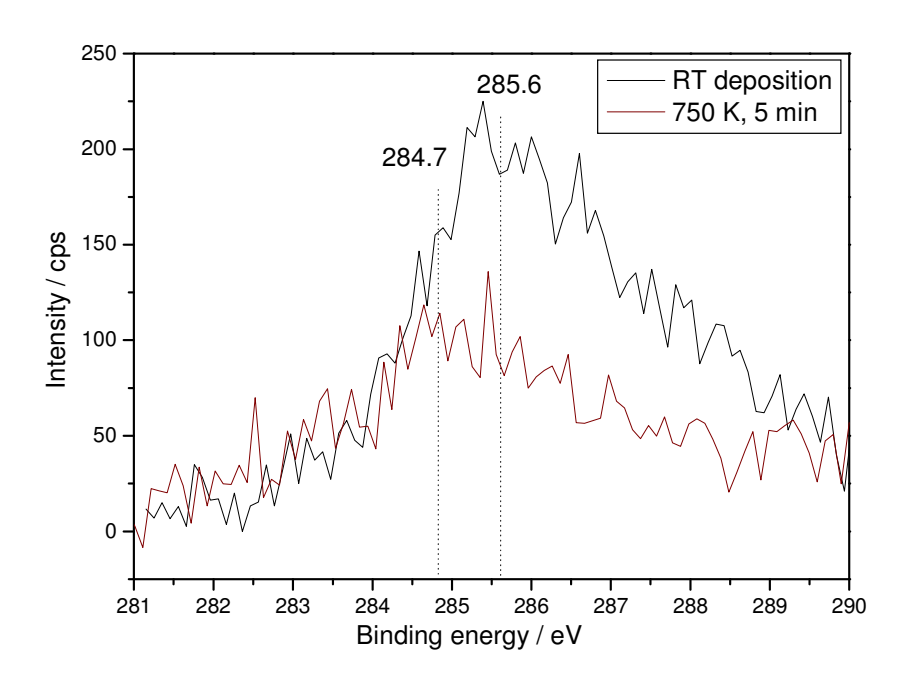


Figure 5-12 XPS spectra of C(1s) region collected after 456 L of  $(CH_3)_2Au(acac)$  exposure at RT (black line) and subsequent anneal to 750 K (red line).

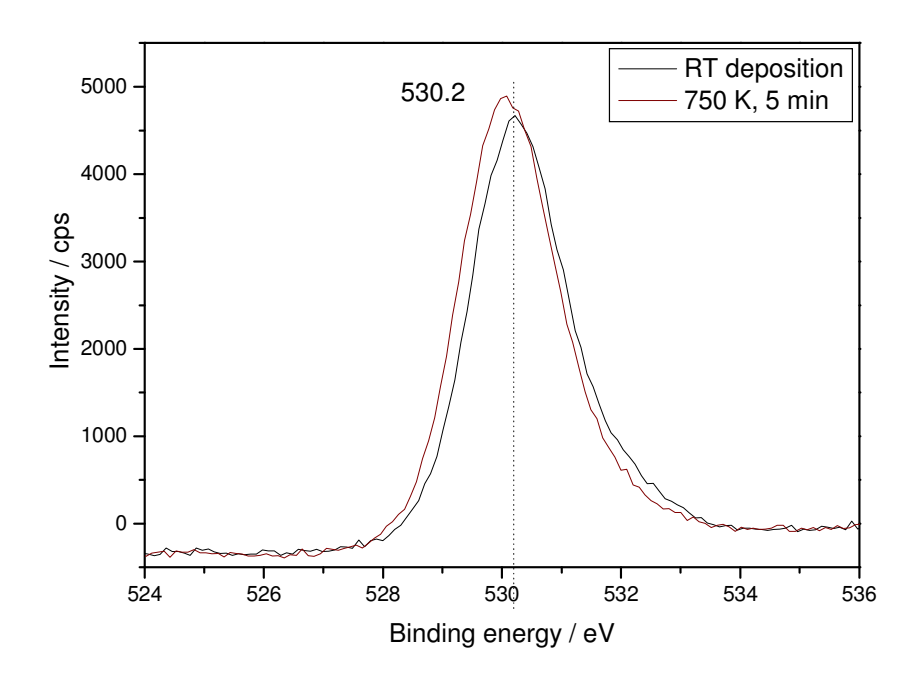


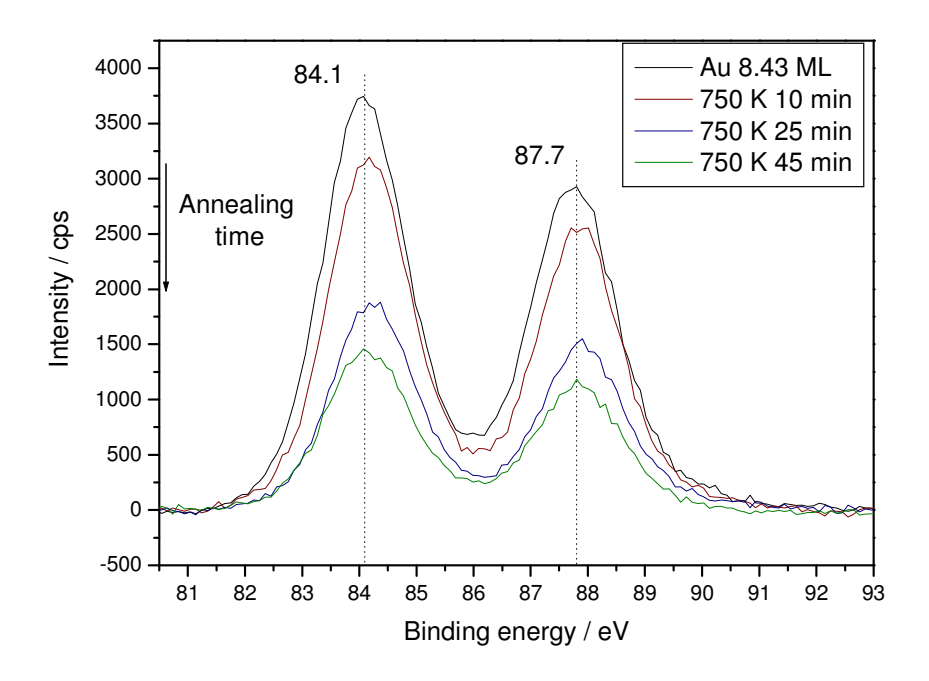
Figure 5-13 XPS spectra of O(1s) region collected after 456 L of  $(CH_3)_2Au(acac)$  exposure at RT (black line) and subsequent anneal to 750 K (red line).

### 5.3.4 Deposition of (CH<sub>3</sub>)<sub>2</sub>Au(acac) at 550 K

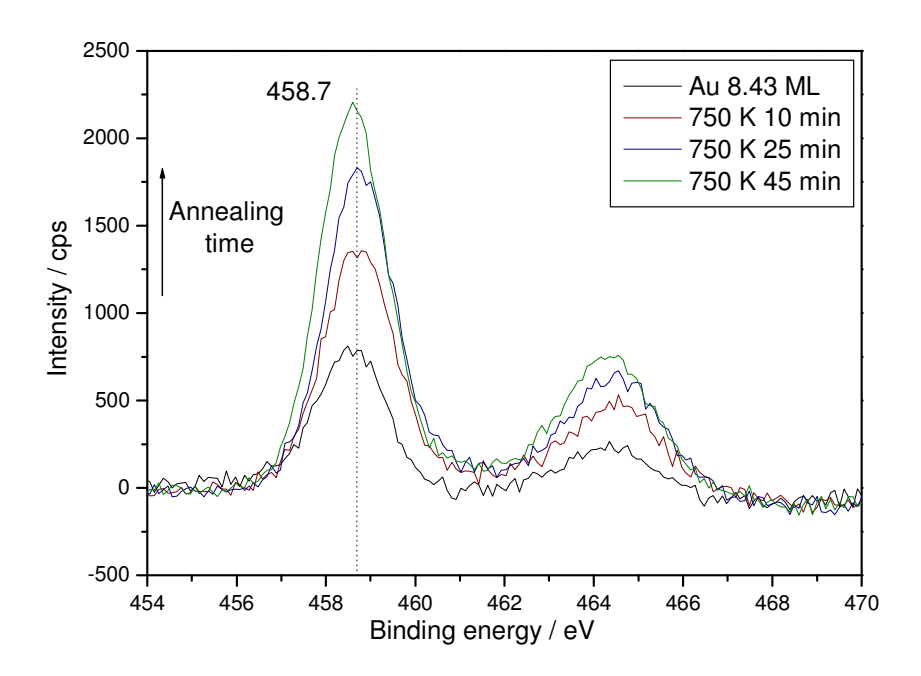
As mentioned in Section 5.1.3, (CH<sub>3</sub>)<sub>2</sub>Au(acac) has been used in CVD for the deposition of Au thin films via pyrolytic decomposition. Consequently, we performed OMCVD experiments during which the sample's temperature was kept at 550 K. Since annealing the sample removed all the organic ligands leaving only graphitic C on the surface, it was within reason to assume that after deposition at 550 K carbon contamination would be minimal. In an effort to eliminate the graphitic C as well, these depositions were performed in an oxygen atmosphere of 4x10<sup>-5</sup> mbar, as some of the C could potentially react with oxygen to produce CO, desorbing in this form from the surface.

Figure 5-14 represents XPS spectra collected from the Au(4f) region following the deposition of 500 L of  $(CH_3)_2Au(acac)$  at 550 K (black line), along with spectra collected after annealing the surface at 750 K for different durations. After deposition two

sharp peaks emerged situated at 84.1 and 87.7 eV respectively. As before, these can be attributed to  $Au(4f_{7/2})$  and  $Au(4f_{5/2})$  and since they appeared very close to the literature value for  $Au^0$ , it would be safe to assume that the Au overlayer was metallic in nature. Using the area under the  $Au(4f_{7/2})$  peak, Au coverage was calculated at 8.43 ML. Upon annealing in an oxygen atmosphere of  $4x10^{-5}$  mbar, the intensity of both peaks reduced as a function of annealing time, while their position remained the same. As argued previously, this decrease in intensity is not related either with desorption of Au from the surface or with encapsulation. Instead, it relates to screening of photoelectrons originating from core atoms of Au particles. As the latter grow in size due to annealing, more photoelectrons are screened. Another consequence of the coalescence of smaller particles into larger ones, is the increase in the surface area of the support. As evident from the XPS spectra of Figure 5-15, the intensity of both  $Ti(2p_{3/2})$  and  $Ti(2p_{1/2})$  increased as a function of annealing time.



**Figure 5-14** XPS spectra of Au(4f) region collected after 500 L of (CH<sub>3</sub>)<sub>2</sub>Au(acac) exposure at 550 K (black line) and following annealing at 750 K for different duration. The accumulated annealing time along with the allocation of each spectrum can be found in the legend.



**Figure 5-15** XPS spectra of Ti(2p) region collected after 500 L of (CH<sub>3</sub>)<sub>2</sub>Au(acac) exposure at 550 K (black line) and following annealing at 750 K for different duration. The accumulated annealing time along with the allocation of each spectrum can be found in the legend.

As observed previously, depositing (CH<sub>3</sub>)<sub>2</sub>Au(acac) at 550 K resulted in the formation of metallic Au particles on the surface of TiO<sub>2</sub>(110). Unfortunately though, the surface suffered from C contamination as evident in the XPS spectrum of C(1s) region, Figure 5-16. A single peak was observed situated at 284.5 eV, indicating the presence of graphitic carbon. But upon annealing in O<sub>2</sub> atmosphere of 4x10<sup>-5</sup> mbar, this peak was dramatically reduced and at the end of the annealing process no C was detectable with XPS. Two explanations could account for this result. The first could involve desorption of C from the surface, but this is improbable as according to our previous results annealing the sample above 700 K did not result in the removal of graphitic C. The second relates to the presence of O<sub>2</sub>. It would be possible that above 700 K a reaction took place between C and O<sub>2</sub> to produce CO<sub>2</sub> or CO, with the latter reacted away from the surface. A similar type of reaction was proposed by Evans *et al.* to account for the removal of residual C.<sup>250</sup> Although in their case C reacted above 500 K with lattice oxygen to produce CO. After the end of this process we probed the surface with LEED in an attempt to observe the

hexagonal pattern previously reported.<sup>206</sup> Unfortunately, no pattern due to the overlayer was observable. The spectra collected from the O(1s) region, Figure 5-17, exhibited the same characteristics with the ones from Ti(2p) region, Figure 5-15, indicating the coalescence of Au into larger particles.

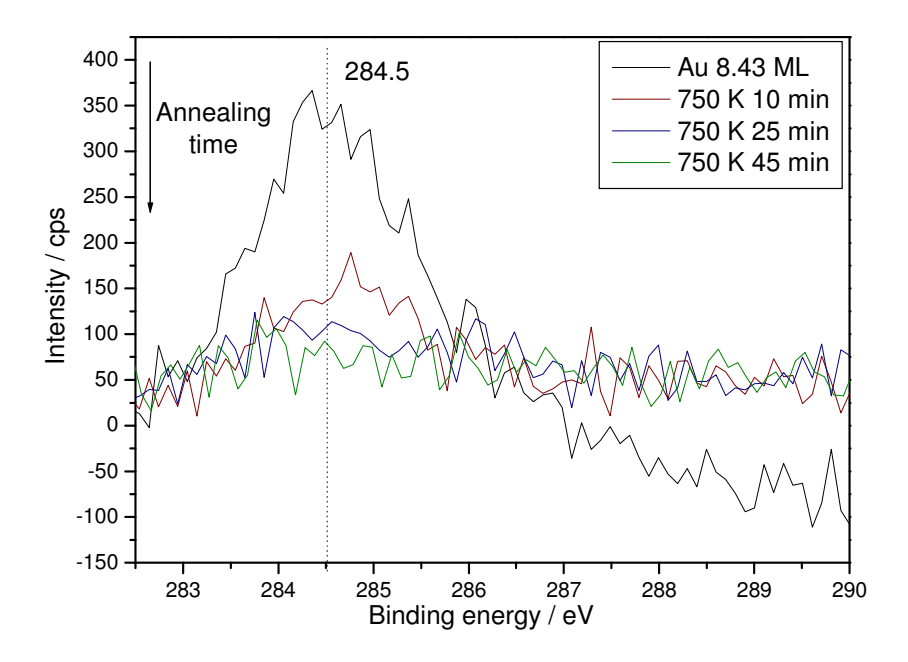


**Figure 5-16** XPS spectra of C(1s) region collected after 500 L of  $(CH_3)_2Au(acac)$  exposure at 550 K (black line) and following annealing at 750 K for different duration. The accumulated annealing time along with the allocation of each spectrum can be found in the legend.

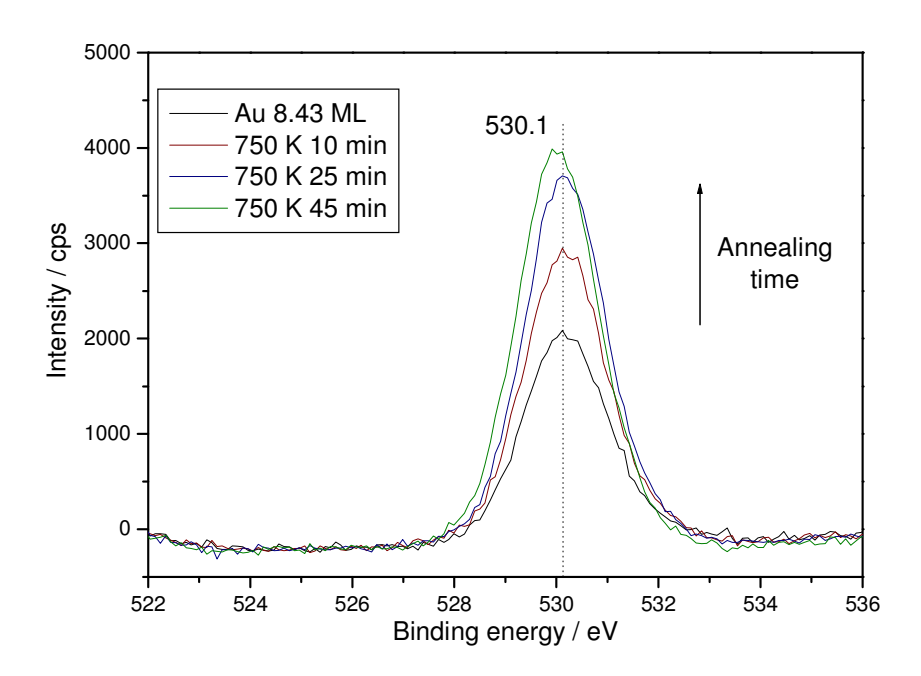


**Figure 5-17** XPS spectra of O(1s) region collected after 500 L of (CH<sub>3</sub>)<sub>2</sub>Au(acac) exposure at 550 K (black line) and following annealing at 750 K for different duration. The accumulated annealing time along with the allocation of each spectrum can be found in the legend.

Despite the fact that C residue was still present on the surface following the 550 K deposition, its quantity was small compared to low temperature depositions, with the C relative area ratio amounting to 1.13. Hence we decided to explore in detail the deposition of (CH<sub>3</sub>)<sub>2</sub>Au(acac) at 550 K. It should be noted that although annealing at 750 K appeared to remove all excess C, deposition at this temperature was avoided since it would result in large particles which do not exhibit catalytic activity. Figure 5-18 represents the Au coverage in MLE as a function of (CH<sub>3</sub>)<sub>2</sub>Au(acac) exposure (L). As it can be observed, Au coverage increased linearly with exposure. According to the literature, a linear dependence of overlayer coverage from exposure is an indication of Volmer-Weber type of growth.<sup>87</sup> The other two types of growth are identified by a break in the plot, indicative of the completion of the first monolayer. For a Volmer-Weber type of growth the linear increase of overlayer coverage is also accompanied by a linear decrease in substrate area. This was also the case here as observed in figure 5-19, where the area of Ti(2p<sub>3/2</sub>) peak is plotted against (CH<sub>3</sub>)<sub>2</sub>Au(acac) exposure. These results are in agreement with the behaviour of physically deposited Au on TiO<sub>2</sub>(110) at 475 K.<sup>129</sup>

According to these authors, at this deposition temperature Au adopted a Volmer-Weber type of growth from the beginning of the deposition. In a separate communication they also reported that based on HRSEM pictures, Au clusters exhibited ordered structures of hexagonal shape, indicative of epitaxial growth. Although we probed the surface with LEED we could not observe any pattern due to Au overlayer. Again a possible explanation could involve the size of these particles. In our case the maximum thickness was calculated at 1.9 nm, whilst in Zhang *et al.* study thicknesses of 5 and 12 nm were measured. The reason for the different growth at higher temperatures has been attributed to lifting of energy barriers which limit the mobility of Au atoms during room temperature deposition. 128

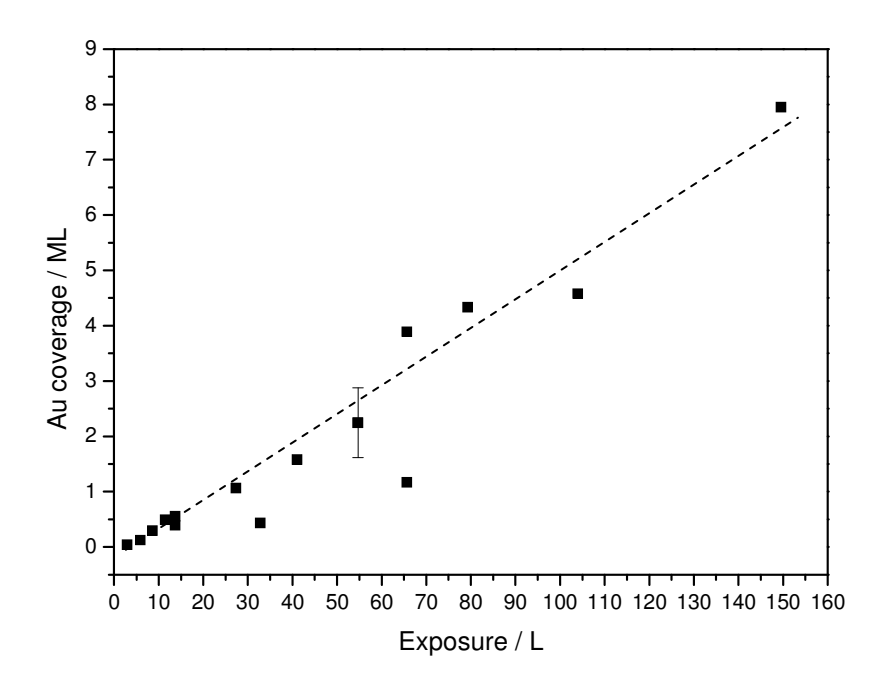


**Figure 5-18** Au coverage as a function of  $(CH_3)_2Au(acac)$  exposure, deposition at 550 K in  $O_2$  atmosphere. Line is drawn to guide the eye.

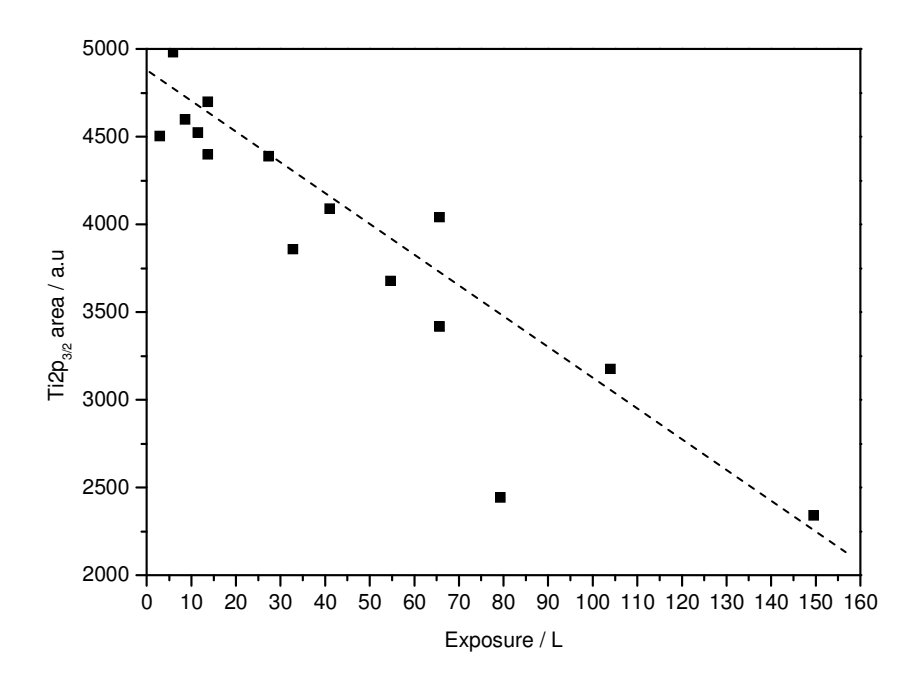


**Figure 5-19** Ti $(2p_{3/2})$  as a function of  $(CH_3)_2$ Au(acac) exposure, deposition at 550 K in  $O_2$  atmosphere. Line is drawn to guide the eye.

Since an important aspect of this investigation was to obtain Au/TiO<sub>2</sub> systems with minimum C contamination, the amount of the latter present on the surface following the deposition, was also monitored. Figure 5-20 represents the dependence of C coverage as a function of (CH<sub>3</sub>)<sub>2</sub>Au(acac) exposure. It can be observed that the trend followed by C coverage was that of a linear increase as a function of exposure. Contrary though to Au coverage, the first point on the plot of Figure 5-20 is at 2.4 ML, indicating a significant amount of C contamination being present at the initial stages of deposition. This was also confirmed by plotting the C relative area to Au relative area ratio as a function of (CH<sub>3</sub>)<sub>2</sub>Au(acac) exposure, Figure 5-21. An exponential like decay was observed, with the values decreasing rapidly at the first 10 L of exposure and a plateau being observed after ca. 40 L. Hence although during early stages of deposition the surface was dominated by C residue, larger Au overlayers did not suffer to the same extent from C contamination, with the C relative area to Au relative area reaching values of 1. The most probable source of C contamination must have been decomposed (CH<sub>3</sub>)<sub>2</sub>Au(acac) species reaching the surface either from the doser or from the vial.

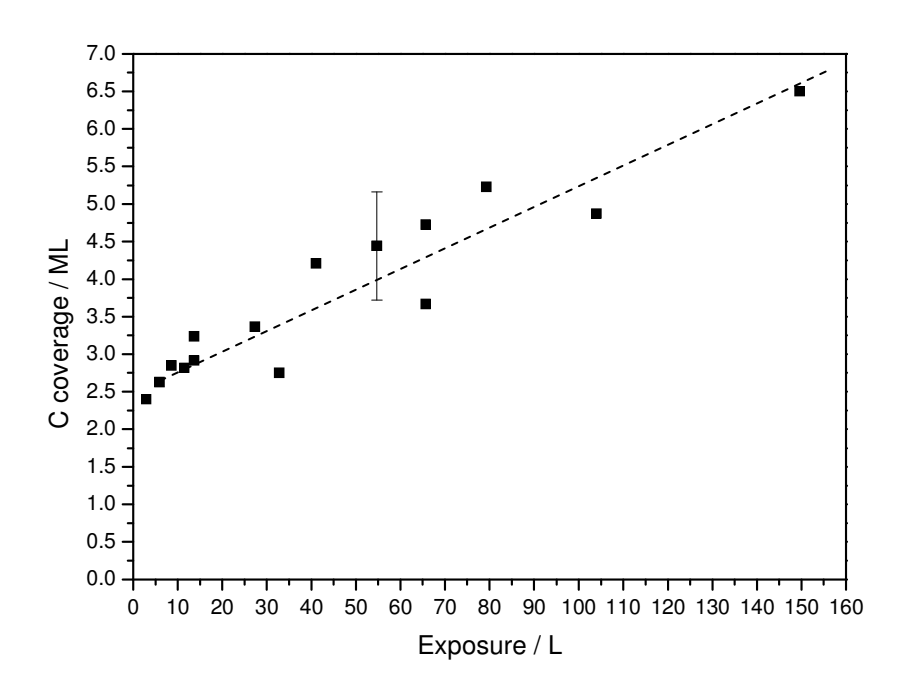


**Figure 5-20** C coverage as a function of  $(CH_3)_2Au(acac)$  exposure, deposition at 550 K in  $O_2$  atmosphere. Line is drawn to guide the eye.

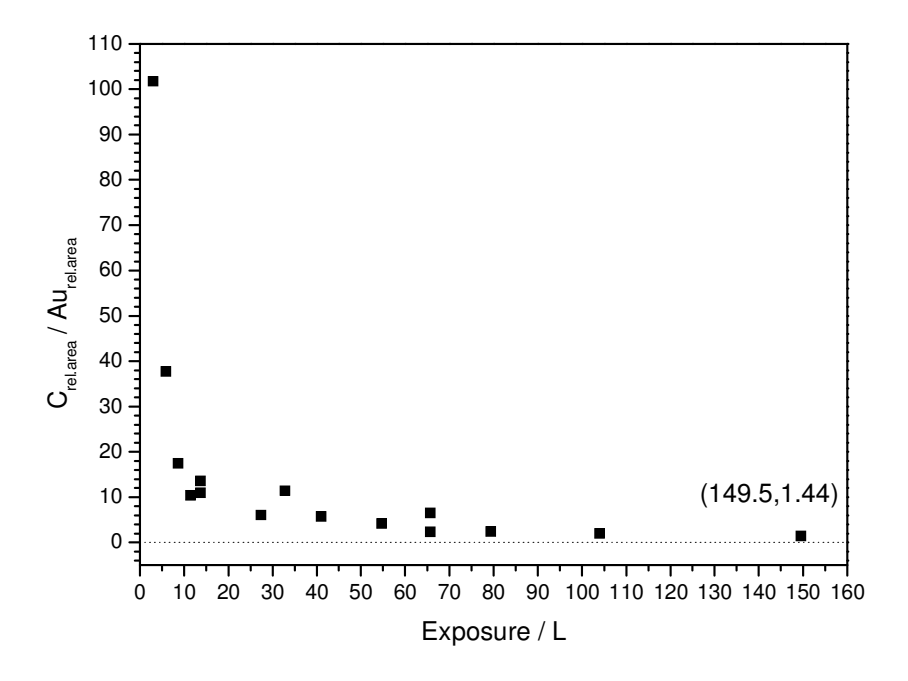


**Figure 5-21**  $C_{rel.area}/Au_{rel.area}$  ratio as a function of  $(CH_3)_2Au(acac)$  exposure, deposition at 550 K in  $O_2$  atmosphere.

Finally it should be noted that following the deposition at 550 K an effort was made to adsorb CO at 130 K and monitor its behaviour using FT-RAIRS. No indication of CO adsorption was observed for all coverages studied, probably due to the presence of C contamination.

# 5.3.5 FT-RAIRS Investigation of (CH<sub>3</sub>)<sub>2</sub>Au(acac) Adsorption at 130 K

The adsorption of (CH<sub>3</sub>)<sub>2</sub>Au(acac) at 130 K on TiO<sub>2</sub>(110) was additionally studied using FT-RAIRS, with the relevant spectra divided between Figures 5-22 and 5-23, in order to facilitate their presentation. Figure 5-22 represents FT-RAIRS spectra collected during the initial stages of (CH<sub>3</sub>)<sub>2</sub>Au(acac) adsorption on the TiO<sub>2</sub>(110) surface as a function of (CH<sub>3</sub>)<sub>2</sub>Au(acac) exposure. No distinguishable bands were observed following the initial exposure of 1.66L, but upon further exposure, 6.22 L, two absorption peaks started to emerge, situated at 1521 and 1650 cm<sup>-1</sup> respectively. Exposing the surface further to 18.76 L and 27.88 L increased the intensity of the previous two peaks, without though any detectable frequency changes. After 31.30 L the recorded spectrum changed, with the absorption band at 1650 cm<sup>-1</sup> being transformed into a transmission one, exhibiting a blue shift in frequency value by 6 cm<sup>-1</sup>. In addition a new transmission band emerged at 2009 cm<sup>-1</sup>, while the peak at 1521 cm<sup>-1</sup> remained unchanged. Finally a small transmission peak was detectable situated on the left of the 1521 cm<sup>-1</sup> one, which would later grew into the main band of the spectra, as observed in the following plot, Figure 5-23.

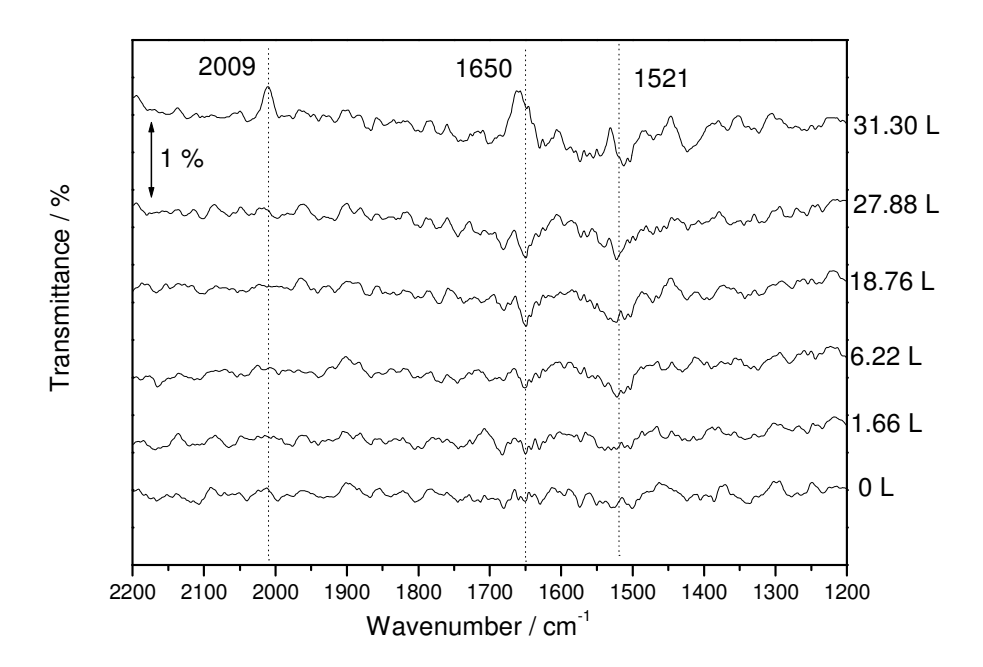


**Figure 5-22** FT-RAIRS spectra collected during the adsorption of  $(CH_3)_2Au(acac)$  at 130 K on  $TiO_2(110)$ , as a function of exposure (L). Note that these spectra were smoothed from the original ones. This was undertaken as the latter exhibited a certain amount of noise, which combined with the low intensity values did not help identifying the bands.

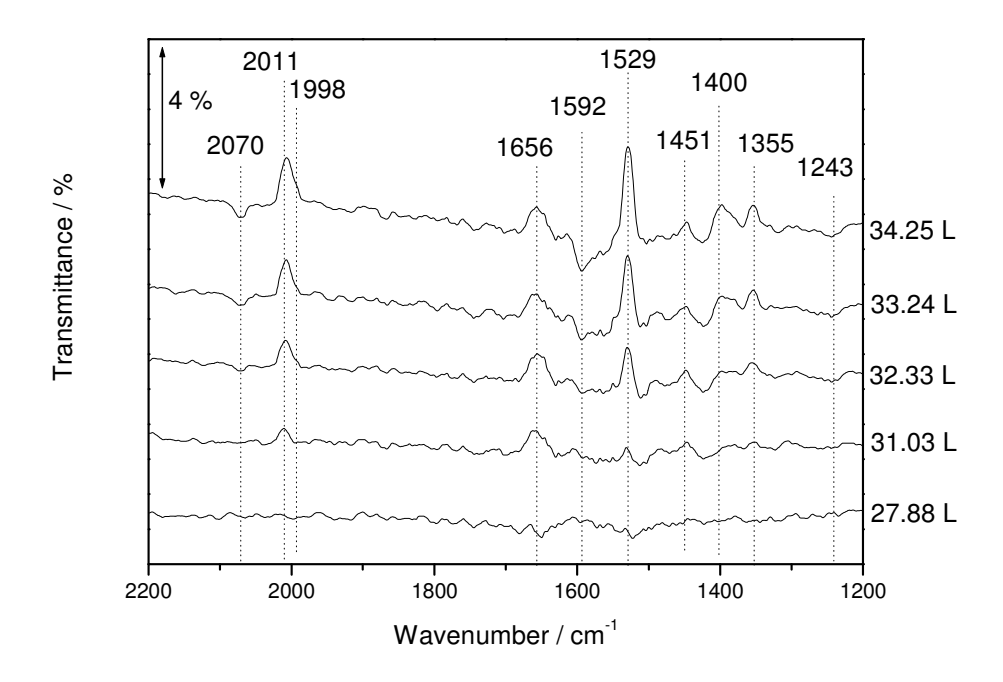


**Figure 5-23** FT-RAIRS spectra collected during the adsorption of  $(CH_3)_2Au(acac)$  at 130 K on  $TiO_2(110)$ , as a function of exposure (L). Note that these spectra were smoothed from the original ones.

Figure 5-23 represents FT-RAIRS spectra collected during the later stages of (CH<sub>3</sub>)<sub>2</sub>Au(acac) adsorption, as a function of (CH<sub>3</sub>)<sub>2</sub>Au(acac) exposure. The first two spectra are the same as the ones presented in figure 5-4. After 32.33 L of (CH<sub>3</sub>)<sub>2</sub>Au(acac) exposure the band at 2009 cm<sup>-1</sup> blue shifted to 2011 cm<sup>-1</sup> while it also grew in intensity. In this frequency region, two new features also appeared, the first one in the form of a small transmission shoulder situated at 1998 cm<sup>-1</sup>, whilst the second one in the form of absorption band at 2070 cm<sup>-1</sup>. In the lower frequency region, the band at 1656 cm<sup>-1</sup> remained unchanged while the one at 1529 cm<sup>-1</sup> grew significantly in intensity. Furthermore several new features started to emerge, both as transmission and absorption bands. In detail two absorption peaks were observed at 1592 and 1243 cm<sup>-1</sup>, while three new transmission bands emerged at 1451, 1400, and 1355 cm<sup>-1</sup> respectively. All these five features along with the one at 1656 cm<sup>-1</sup> did not change significantly upon further (CH<sub>3</sub>)<sub>2</sub>Au(acac) exposures of 33.24 and 34.25 L. On the contrary the 1529 cm<sup>-1</sup> band grew further in intensity and became the dominant feature of the spectra. On the higher wavenumber region, increasing the exposure of the molecule resulted in the increase of the

three features, with the shoulder and the absorption band becoming more distinct, and the main band at 2011 cm<sup>-1</sup> growing in height. At the end of this process, the surface was covered completely with the adsorbate as it will become evident from XPS spectra presented in forthcoming pages. These spectra were collected immediately after ending the 34.24 L exposure. An analysis of the FT-RAIRS bands observed in figures 5-22 and 5-23 is going to be presented in the following paragraphs.

The spectra of Figures 5-22 and 5-23 can be divided into two regions, a high frequency one between 2200 and 1800 cm<sup>-1</sup> and a low frequency between 1800 and 1200 cm<sup>-1</sup>. The latter is also known as the fingerprint region<sup>240</sup> of (CH<sub>3</sub>)<sub>2</sub>Au(acac) as the majority of its active infrared modes appear in this region. At initial exposures, up to 27.88 L, only two absorption bands were observable at 1521 and 1650 cm<sup>-1</sup> respectively. An assignment of these bands can be made by comparing them with infrared bands collected from solid (CH<sub>3</sub>)<sub>2</sub>Au(acac) by Miles et al. <sup>251</sup> This comparison can be found in Table 5-1, where the first band at 1521 cm<sup>-1</sup> is correlated with the v(C-O) stretch and the second one at 1650 cm<sup>-1</sup> with the v(C-C) stretch. Another important observation relates with the direction of both bands. As indicated in Chapter 4, stretching modes aligned parallel to the surface will result in absorption bands on an FT-RAIRS spectrum. Based on the above observation, the dipole moment vector of both v(C-O) and v(C-C) should lie parallel to the surface. Hence since the (CH<sub>3</sub>)<sub>2</sub>Au(acac) molecule exhibits a planar geometry between Au and the (acac) ring, <sup>237</sup> it would be reasonable to assume that at the initial stages of adsorption the molecule adopted a geometry parallel to the TiO<sub>2</sub>(110) surface. No other infrared bands due to the parent molecule were observable, but this could have been due to the inability of the instrument to detect them. Both v(C-O) and v(C-C) were detectable as they give the strongest peaks<sup>251</sup>. Upon further exposure though, above 31.03 L, new peaks emerging at 1243, 1355, 1400, 1451 and 1592 resembled more the vibrations of molecule. Indeed Miles et al. observed bands close to the above at 1236, 1335, 1392, 1400 and 1421 cm<sup>-1</sup> which they assigned to  $\delta_s(CH_3)(Au-CH_3)$ ,  $\delta_s(CH_3)acac$ ,  $\delta_d(CH_3)acac$ ,  $\delta_a(CH_3)(Au-CH_3)$ CH<sub>3</sub>) and  $v(C-O) + \delta(C-H)(B_2)$  respectively. This comparison is summarised in Table 5-2. Based on direction of the bands of Figure 5-23, it would appear that the adsorption geometry of the (CH<sub>3</sub>)<sub>2</sub>Au(acac) molecule changed for higher exposure values, or

adsorption of multilayers. Indeed as observed in Table 5-2, the majority of bands were expressed as transmission peaks, indicating alignment perpendicular to the  $TiO_2(110)$  surface.

**Table 5-1** FT-RAIRS bands observed during the first stages of  $(CH_3)_2Au(acac)$  adsorption on  $TiO_2(110)$  at 130 K. Table also includes similar bands recorded for solid  $(CH_3)_2Au(acac)$  and their assignment. Wavenumber values in cm<sup>-1</sup>. (Abs) denotes absorption band.

Observed bands this study	(CH <sub>3</sub> ) <sub>2</sub> Au(acac) <sup>251</sup>	Assignment <sup>251</sup>
1521 (Abs)	1520	ν(C-O) (A <sub>1</sub> )
1650 (Abs)	1590	ν(C-C) (B <sub>2</sub> )

**Table 5-2.** FT-RAIRS bands recorded after the complete coverage of  $TiO_2(110)$  surface by  $(CH_3)_2Au(acac)$  at 130 K. Table also includes similar bands recorded for solid  $(CH_3)_2Au(acac)$  and their assignment. Wavenumber values in cm<sup>-1</sup>. Symbols:  $\delta_s$  for symmetric in-plane bending,  $\delta_d$  for degenerate in-plane bending,  $\delta_a$  for asymmetric in-plane bending and  $\nu$  for stretching. (Abs) denotes absorption and (Trans) transmission band respectively.

Observed bands this study	(CH <sub>3</sub> ) <sub>2</sub> Au(acac) <sup>251</sup>	Assignment <sup>251</sup>
1243 (Abs)	1236	$\delta_s(CH_3)(Au-CH_3)$
1355 (Trans)	1335	δ <sub>s</sub> (CH <sub>3</sub> )acac
1400 (Trans)	1392	$\delta_d$ (CH <sub>3</sub> )acac
-	1400	$\delta_a(CH_3)(Au\text{-}CH_3)$
1451 (Trans)	1421	$\nu$ (C-O)+ $\delta$ (C-H)(B <sub>2</sub> )
1529 (Trans) or 1592 (Abs)	1520	ν(C-O) (A <sub>1</sub> )
1656 (Trans)	1590	ν(C-C) (B <sub>2</sub> )

Vibrations observed at the high frequency region are complex to understand as the parent molecule does not exhibit infrared modes in this area. It should be noted that these bands emerged at exposure values higher than 31.03 L, where also a change in the orientation of the molecule was observed. Since the bands cannot be attributed to the parent molecule, their appearance must be associated with species other than the (CH<sub>3</sub>)<sub>2</sub>Au(acac) molecule. One possible explanation involves the adsorption on the surface of decomposed species originating from either the glass vial or the stainless steel tube. Another interpretation could be consistent with an interaction between these decomposed species and the already adsorbed parent molecule. Fierro-Gonzalez et al. observed the appearance of infrared bands at 2070, 2032 and 2000 cm<sup>-1</sup> during the interaction of CO with high surface area (CH<sub>3</sub>)<sub>2</sub>Au(acac)/NaY samples.<sup>241</sup> In our case, the decomposed species could contain CO molecules resulting from the fragmentation of diketone. For a complete understanding of the adsorption process at 130 K, these FT-RAIRS results should have been complemented with XPS data. This would have given us the opportunity to screen the chemical state of all the species during adsorption and to extract valuable information regarding the interaction of the molecule with the surface. Such experiments were not performed though, and future work on this system should include such a study.

The above discussion assumed the associate adsorption of the molecule on the surface. Indeed, this would be consistent with STM observations by Maeda *et al.* proposing the associative adsorption of the molecule on  $TiO_2(110)$  at  $RT.^{236}$  Furthermore other organometallic complexes containing (acac) ligands, such as  $Rh(acac)(CO)_2$  have been found to adsorb intact on the single crystal surface. On the other hand though, dissociative adsorption could also have taken place, with both bands attributed to adsorbed fragments. This would be in accordance with the findings on high surface catalysts at RT, where two separate bonds were formed,  $(CH_3)_2Au$  with lattice oxygen and (acac) with Ti, with the V(C-C) and V(C-O) vibrations of the latter occurring near the observed values.

#### 5.4 Conclusions

In this Chapter, the adsorption of (CH<sub>3</sub>)<sub>2</sub>Au(acac) on TiO<sub>2</sub>(110) was examined at three different temperatures in order to explore the possibility of using this organometallic molecule as a precursor for the deposition of highly dispersed Au particles on the titania single crystal. At 130 K, XPS spectra indicated the presence of Au<sup>3+</sup> on the surface along with two different kinds of C, probably C-H and C-O. Upon annealing, Au was reduced to metallic while larger Au particles were formed. Decomposition of all organic ligands was also observed indicated first by the reduction of Au and second by the disappearance of XPS peaks in the C(1s) and O(1s) regions attributed to organic ligands. Nevertheless graphitic C remained on the surface. Deposition at RT resulted in the formation of two states of Au, one metallic and one oxidised. Although no infrared bands were observable with FT-RAIRS, some organic ligands were present on the surface as indicated by XPS. Upon annealing these decomposed leaving only graphitic C on the surface, whilst Au was reduced to metallic. Deposition at 550 K resulted in the formation of metallic Au and graphitic C. Upon annealing to 750 K in oxygen atmosphere, larger Au particles were formed while all C contamination was removed from the surface, probably via reaction with oxygen. Finally the growth mode of Au overlayers at 550 K was examined. A Volmer-Weber type of growth mode was observed similar to the results obtained after the PVD of Au at 475 K. 129 For all exposure values, the surface was found to suffer from C contamination, although this reduced as a function of Au coverage. Finally FT-RAIRS spectra were also collected during the 130 K adsorption. According to these results, the orientation of the adsorbed (CH<sub>3</sub>)<sub>2</sub>Au(acac) molecule changed as a function of exposure, with molecules aligning parallel to the surface at the initial stages of adsorption, and perpendicular to the surface at higher (CH<sub>3</sub>)<sub>2</sub>Au(acac) exposure values.

# **General Conclusions**

6.1 TiO<sub>2</sub>(110) Supported Cu Particles and Films

Cu particles and thin films were deposited on the TiO<sub>2</sub>(110) surface via PVD at 295 K. Using CO as a probe molecule, the structural properties of these overlayers as a function of size were investigated by means of FT-RAIRS. It was found that islands with size up to ca. 3.5 nm, accommodated high Miller Index structures, such as (211), (311) and (755). On the other hand, the surface of larger islands, up to ca. 5 nm, was characterised by (110), (100) and (111) formations. The latter structures were also observed for thin Cu films. Based on the appearance of the v(C-O) bands, i.e. transmission or absorption, another important observation was made. Spectra collected from high Miller Index overlayers were characterised by transmission bands, consistent with the inability of the latter to transform the character of the local dielectric field into metallic. On the contrary, absorption bands were present on FT-RAIRS spectra collected from larger structures, indicating metallic response. A threshold coverage value at 4.48 MLE, or  $4.2 \pm$ 0.6 nm, was identified upon which the local dielectric field was in transition, exhibiting both metallic and non metallic characteristics. By comparison to previously literature values, this coverage was found common within experimental error to TiO<sub>2</sub>(110) supported Rh and Pd. Additionally, XPS results revealed a change in the binding energy of Cu(2p<sub>3/2</sub>) as a function of coverage. This dependence was explained as ineffective screening of holes created during the photoelectron process, effect commonly observed for small metal clusters. Annealing these Cu overlayers resulted in the transformation of their structures into the most thermodynamically favoured. For small islands this was indicated by a red shift of v(C-O) bands, whereas for larger islands and films by the dominant presence of v(C-O) bands attributed to CO adsorbed on Cu(111) sites. Furthermore, for thin Cu films a hexagonal LEED pattern was detected, indicative of Cu(111). The LEED pattern collected from the annealed 8.95 MLE surface also revealed an epitaxial relation between Cu and TiO<sub>2</sub>(110). Evidence of coalescence was observed with XPS, although

FT-RAIRS results were consistent with the formation of highly dispersed Cu particles due to the annealing process. In order to reconcile the difference, a complex growth mode was proposed that resembled a combination of Volmer-Weber and Stranski-Krastanov types. Finally the interaction of  $O_2$  with preadsorbed CO at 130 K appeared to be more pronounced for the high Miller Index structures.

### 6.2 The Photolysis of MoCO<sub>6</sub> on TiO<sub>2</sub>(110)

The photolysis of various layers of physisorbed Mo(CO)<sub>6</sub> on the TiO<sub>2</sub>(110) surface at 130 K was studied as part of an alternative method to common thermal evaporation. According to FT-RAIRS spectra collected during irradiation of the molecule with UV light, the photodecomposition of 1.53 L of exposed Mo(CO)<sub>6</sub> proceeded in a sequential fashion, until the production of Mo(CO)<sub>3</sub>. The tricarbonyl adopted a geometry perpendicular to the surface, as indicated by the appearance of only transmission bands in FT-RAIRS spectra. This final product was also confirmed via XPS (collected as well during irradiation) first by measuring the dependence of the  $Mo(3d_{5/2})$  binding energy as a function of irradiation time, and second by calculating the Mo/C relative ratio. Annealing the surface revealed that Mo(CO)<sub>3</sub> was stronger bound to the surface than the parent molecule. The former desorbed after annealing to 400 K, resulting in metallic Mo particles which suffered from C contamination. Upon increasing the exposure of photolysed Mo(CO)<sub>6</sub> to 2.73 L, FT-RAIRS indicated that various unsaturated carbonyls were present on the surface at the end of photolysis, which were identified as Mo(CO)<sub>5</sub>, Mo(CO)<sub>4</sub> and Mo(CO)<sub>3</sub>. This was performed by taking into consideration the blue and red shift away from the gas phase value, observed for modes aligned perpendicular and parallel to the surface due to dipole coupling. Additionally, XPS revealed Mo(CO)<sub>3</sub> as the major photoproduct. Similar to the lowest exposure overlayer, these photoproducts were stronger bound to the surface than Mo(CO)<sub>6</sub> as indicated by FT-RAIRS spectra collected during annealing. These spectra also revealed the formation of two new species upon annealing to 368 K, which desorbed after 495 K. The latter resulted in C free oxidised Mo particles as verified by XPS. Photolysis of adsorbed multilayers resulted in minimum change of FT-

RAIRS spectra, while the main photoproduct was identified as Mo(CO)<sub>5</sub>. Contrary to the previous two overlayers, no indication of Mo(CO)<sub>3</sub> was observed. This observed dependence between Mo(CO)<sub>6</sub> coverage and photoproducts, could be related with a promotion of the photolysis process due to direct contact with the oxide support.

### 6.3 The Deposition of (CH<sub>3</sub>)<sub>2</sub>Au(acac) on TiO<sub>2</sub>(110)

The deposition of (CH<sub>3</sub>)<sub>2</sub>Au(acac) on the TiO<sub>2</sub>(110) surface was studied in order to assess the potential application of this molecule as a precursor for the OMCVD of highly dispersed Au nanoparticles. Consequently depositions took place at three different substrate temperatures: 130 K, 295 K and 550 K. In all cases the effect of annealing above 700 K was also investigated. At 130 K, XPS revealed the formation of oxidised Au overlayers and in particular Au<sup>3+</sup>, which is the oxidation state of Au in the organometallic precursor. The presence of organic ligands on the surface was also identified by distinct C(1s) peaks which did not belong neither to graphitic or carbidic carbon, and by the appearance of an additional peak at the O(1s) region. Upon annealing to 728 K, Au was converted to metallic, whilst all organic ligands desorbed resulting in C contamination of the surface. Deposition at 130 K was also examined via FT-RAIRS. Preliminary results indicated that at the first stages of exposure, the molecule adopted geometry parallel to the surface. Upon the formation of multilayers, this alignment changed as indicated by the presence of both absorption and transmission bands on the infrared spectra. Following deposition at RT, XPS indicated the presence of both metallic and oxidised Au, while some organic ligands were also detected. This overlayer could be associated with an intermediate decomposition product of the precursor. Again upon annealing to 750 K, Au was transformed to metallic suffering from C contamination. At 550 K, only metallic Au was detected on the TiO<sub>2</sub>(110) surface. In order to remove any C contamination, the surface was annealed in O2 at 750 K. Indeed this procedure resulted in the complete removal of any C residue, although evidence of Au coalescence was also observed. By plotting the Au coverage as a function of exposure, it was established that at 550 K, Au followed a Volmer-Weber type of growth. Based on these results it would be extremely

difficult to utilise  $(CH_3)_2Au(acac)$  as a precursor of C free highly dispersed Au nanoparticles, at least using the conditions described in this thesis.

# Appendix A

In Appendix A the raw XPS data collected during the photolysis of the three different  $Mo(CO)_6$  overlayers are presented. These spectra were analysed by WSPECTRA software and information regarding the area, FWHM and position of each peak were extracted.

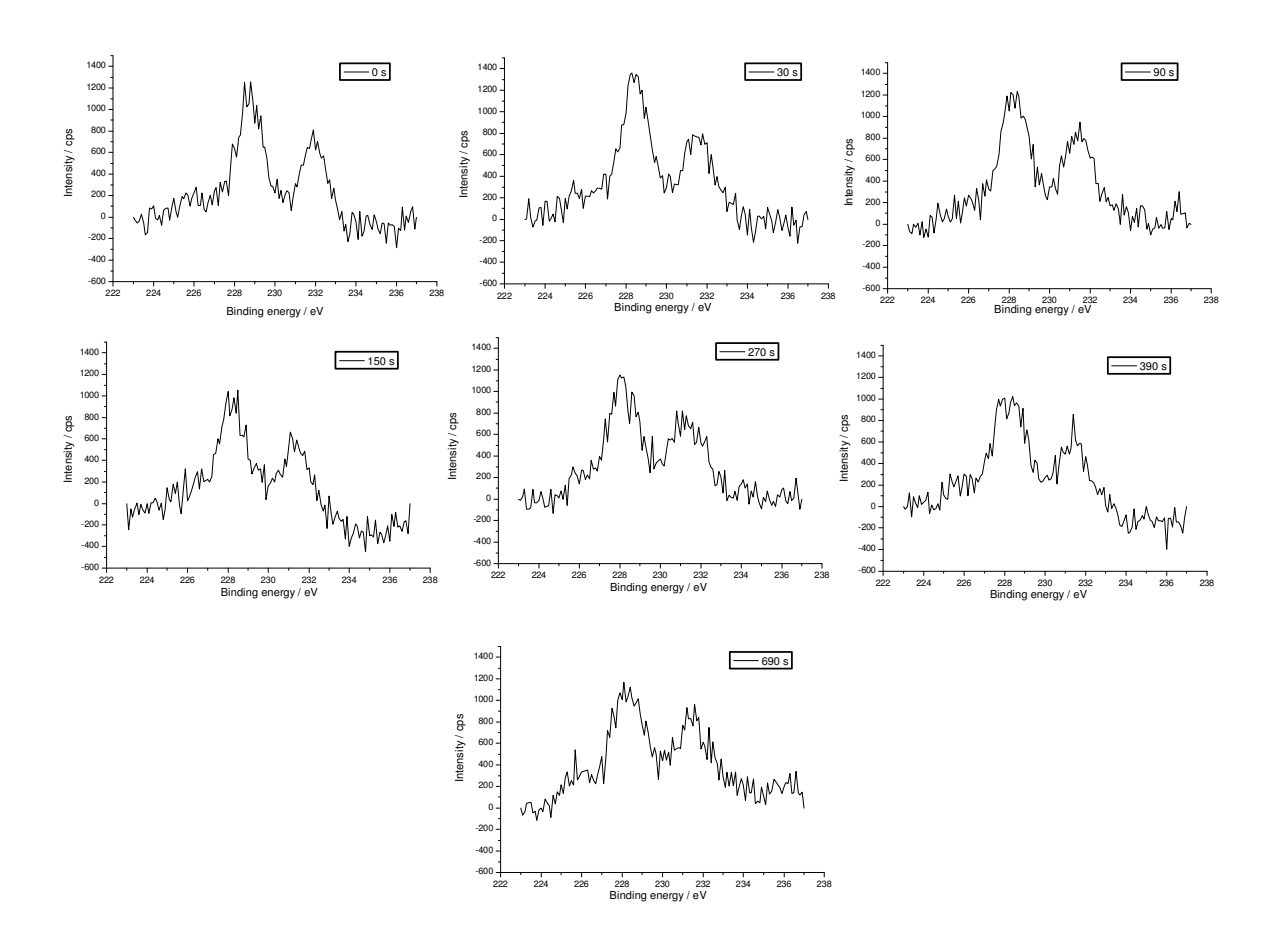


Figure A-1 Mo(3d) energy region for 1.53 L Mo(CO)<sub>6</sub> and its photodecomposition on  $TiO_2(110)$ . The label on each plot represents the irradiation time in seconds.

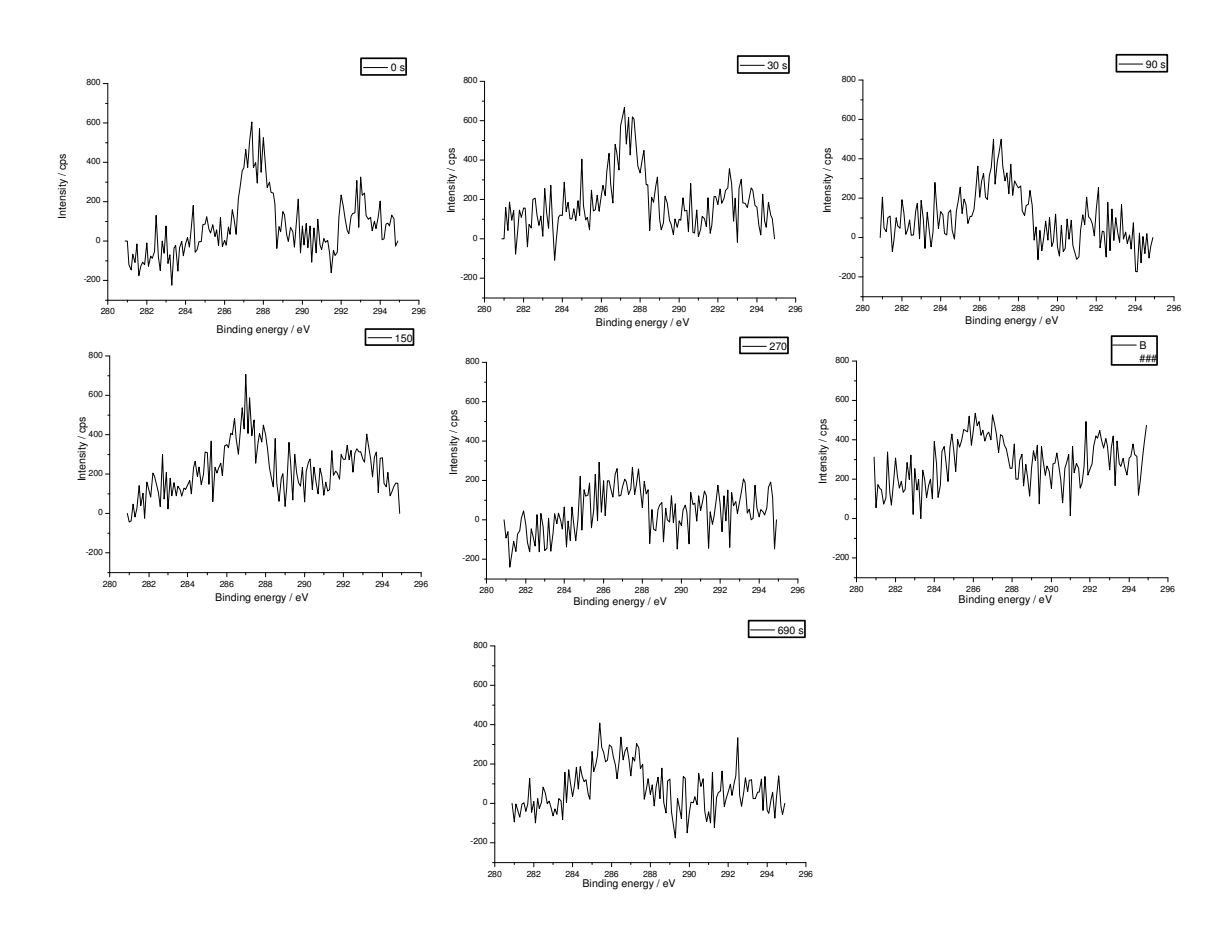
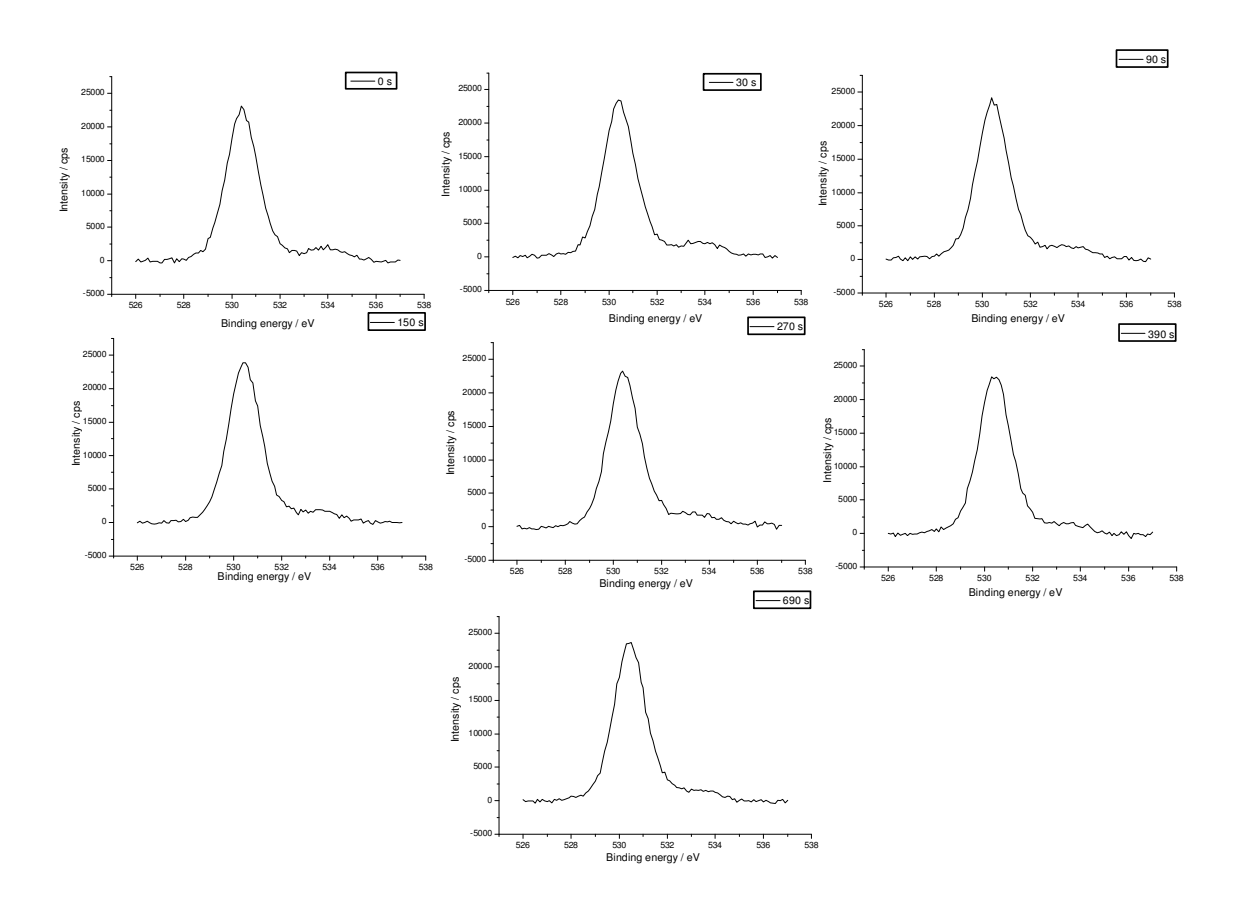


Figure A-2 C(1s) energy region for 1.53 L Mo(CO)<sub>6</sub> and its photodecomposition on  $TiO_2(110)$ . The label on each plot represents the irradiation time in seconds.



**Figure A-3** O(1s) energy region for 1.53 L Mo(CO)<sub>6</sub> and its photodecomposition on  $TiO_2(110)$ . The label on each plot represents the irradiation time in seconds.

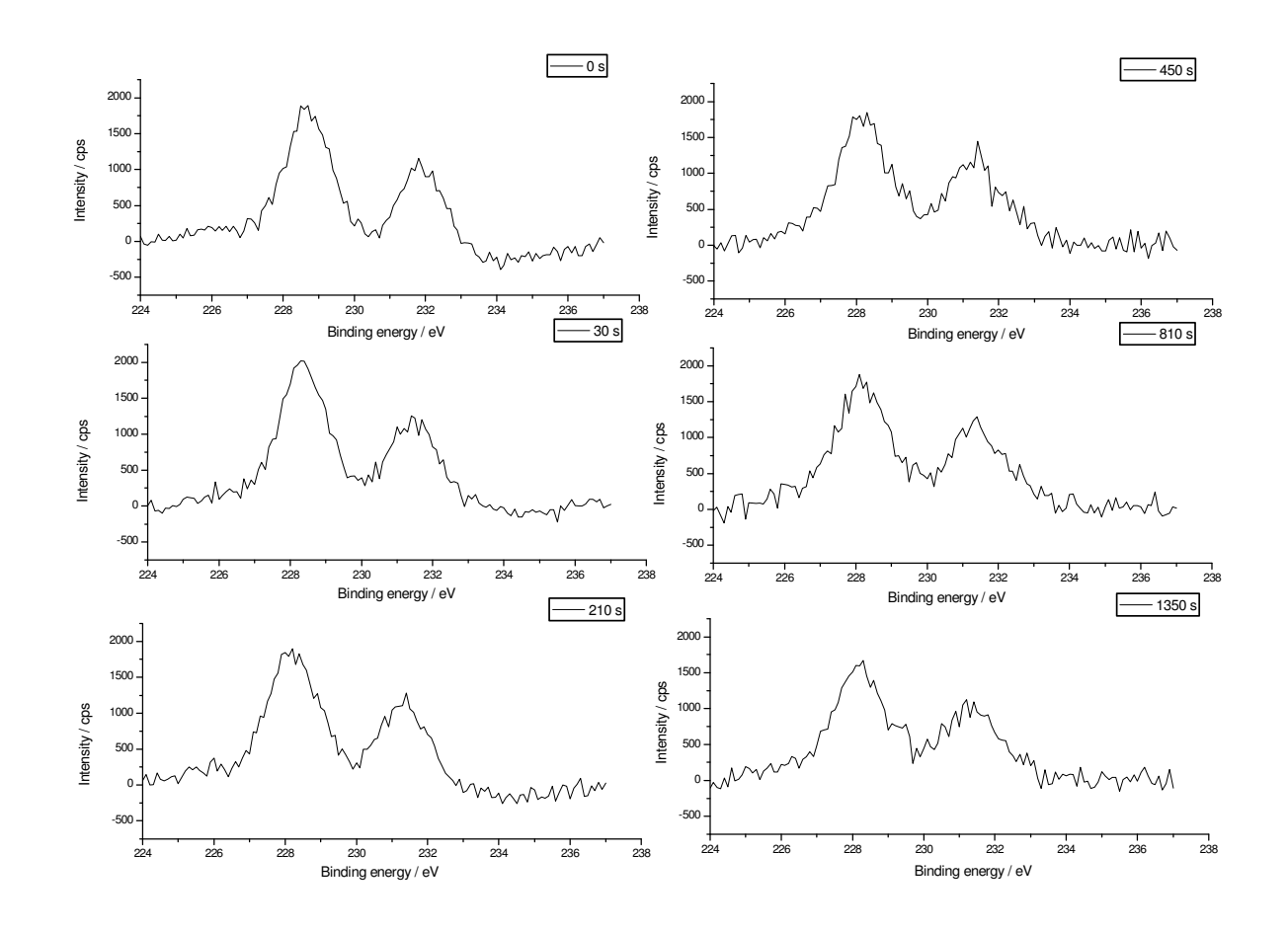
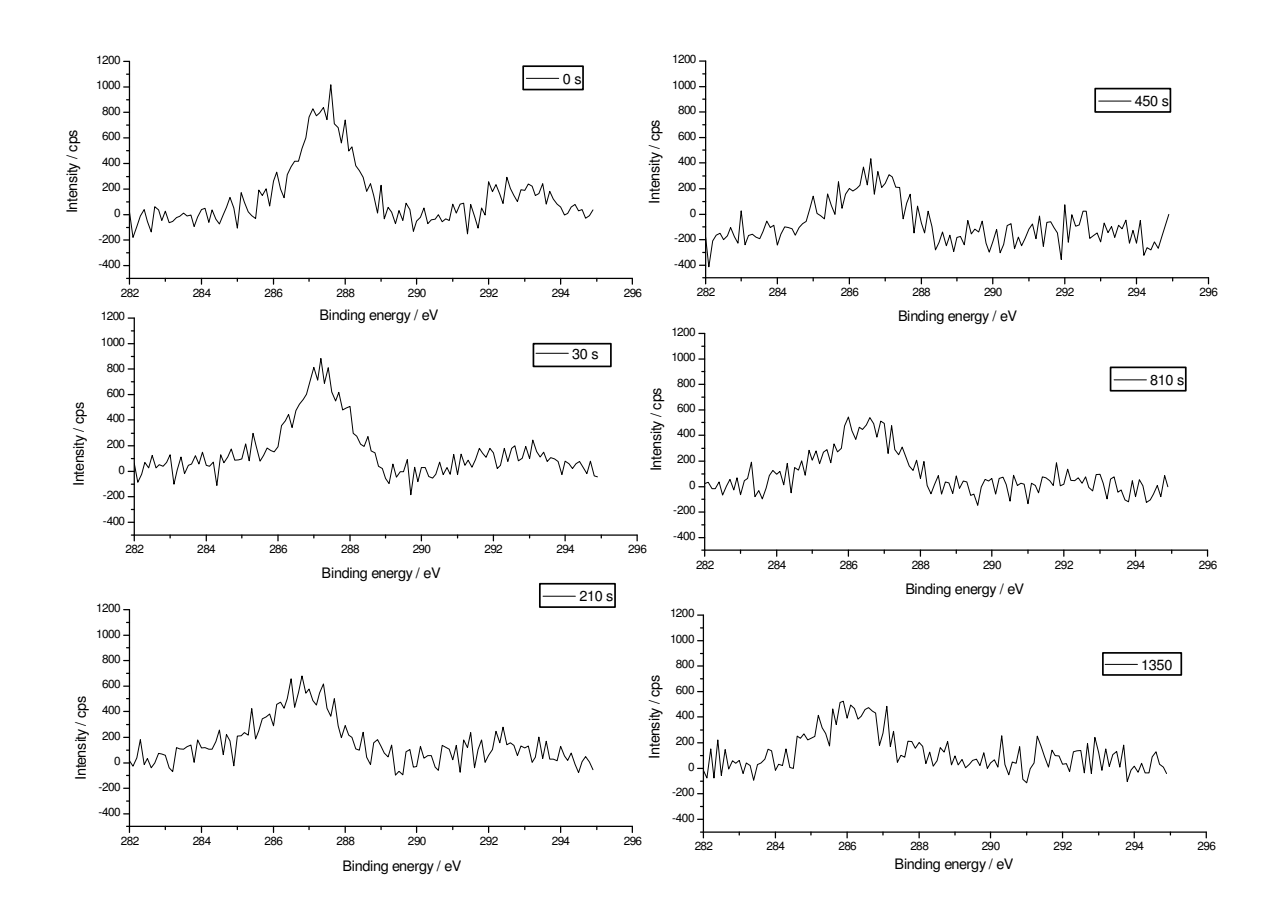
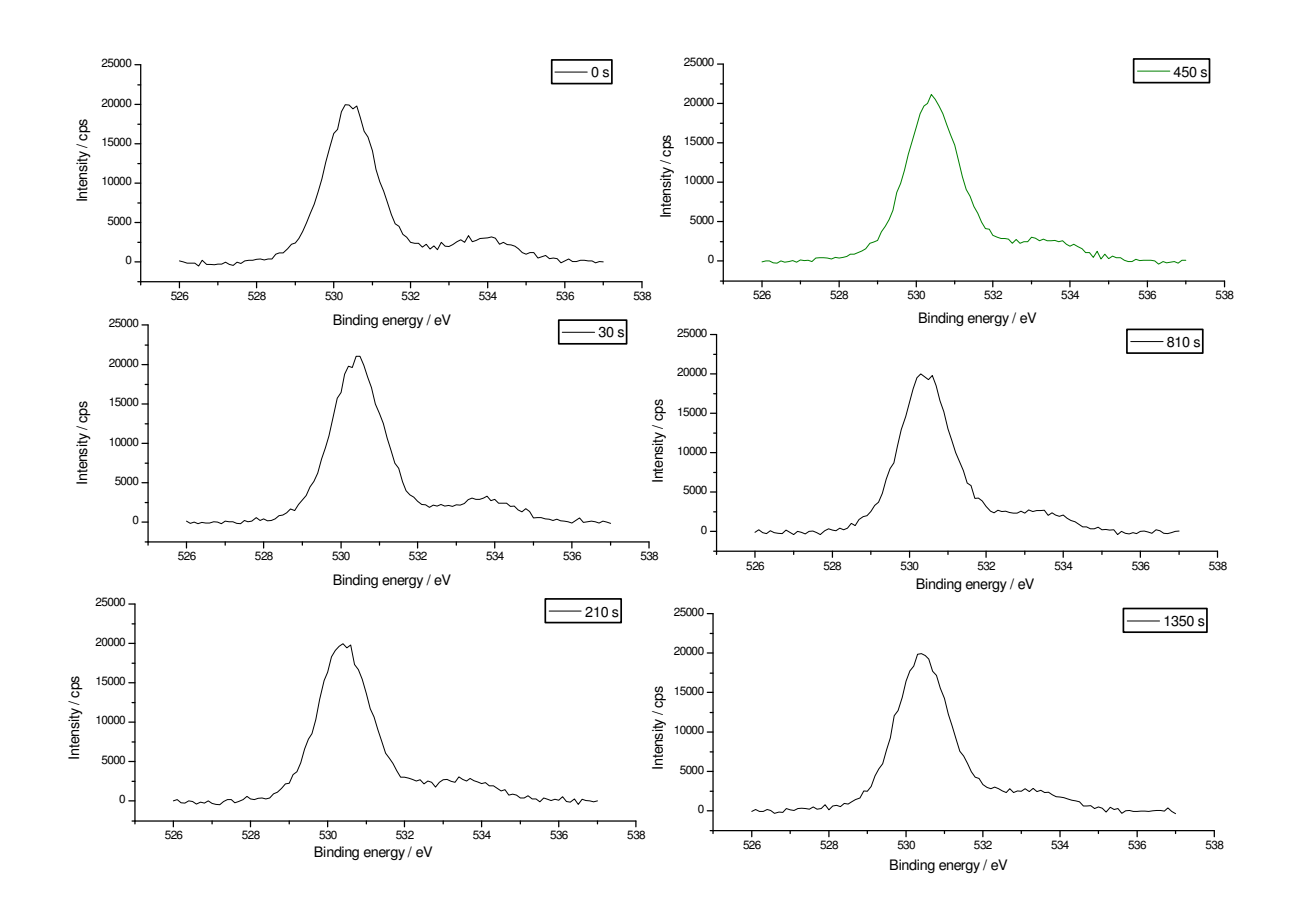


Figure A-4 Mo(3d) energy region for  $2.73 \text{ L Mo(CO)}_6$  and its photodecomposition on  $\text{TiO}_2(110)$ . The label on each plot represents the irradiation time in seconds.



**Figure A-5** C(1s) energy region for 2.73 L Mo(CO)<sub>6</sub> and its photodecomposition on TiO<sub>2</sub>(110). The label on each plot represents the irradiation time in seconds.



**Figure A-6** O(1s) energy region for  $2.73 \text{ L Mo(CO)}_6$  and its photodecomposition on  $\text{TiO}_2(110)$ . The label on each plot represents the irradiation time in seconds.

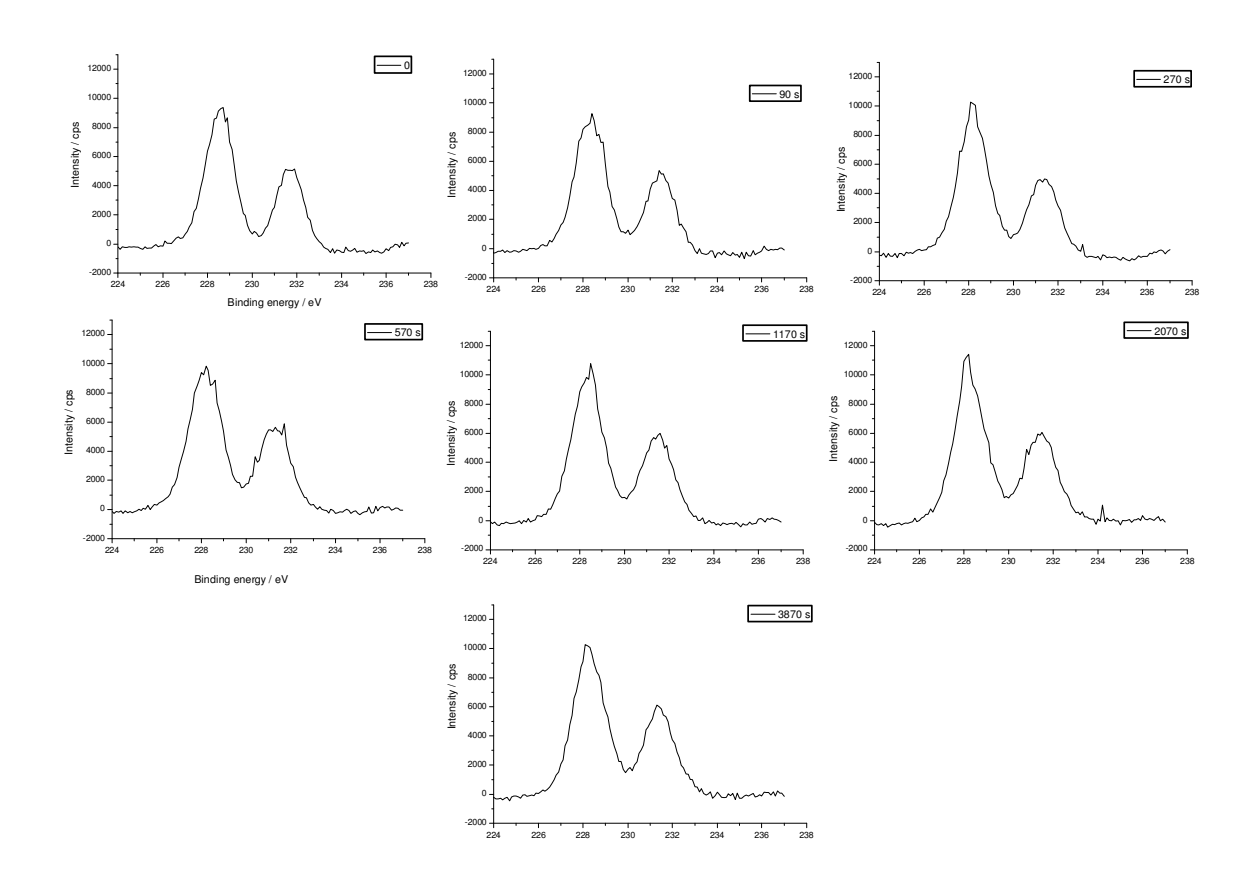


**Figure A-7** Mo(3d) energy region for 20.2 L Mo(CO)<sub>6</sub> and its photodecomposition on  $TiO_2(110)$ . The label on each plot represents the irradiation time in seconds.

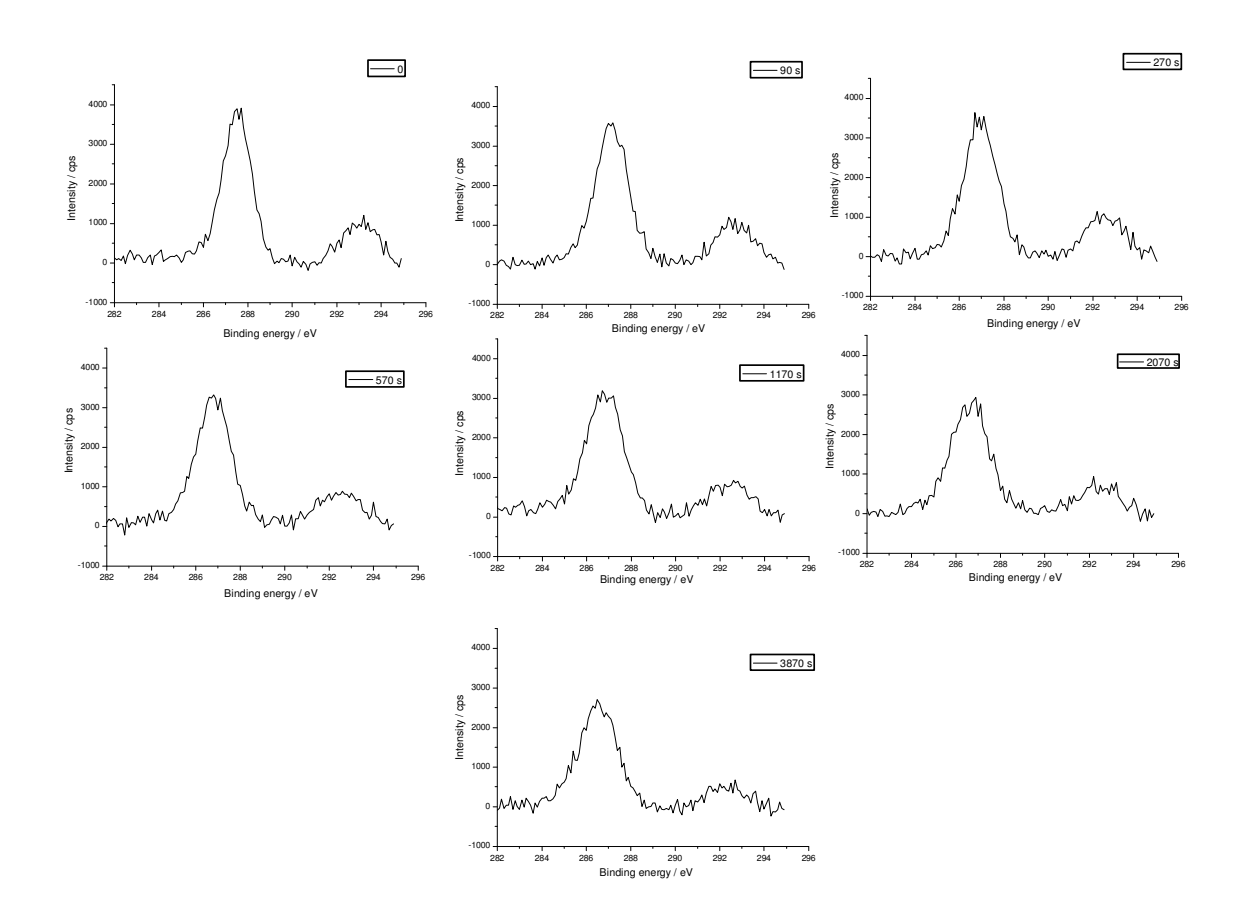


**Figure A-8** C(1s) energy region for  $20.2 \text{ L Mo(CO)}_6$  and its photodecomposition on  $\text{TiO}_2(110)$ . The label on each plot represents the irradiation time in seconds.

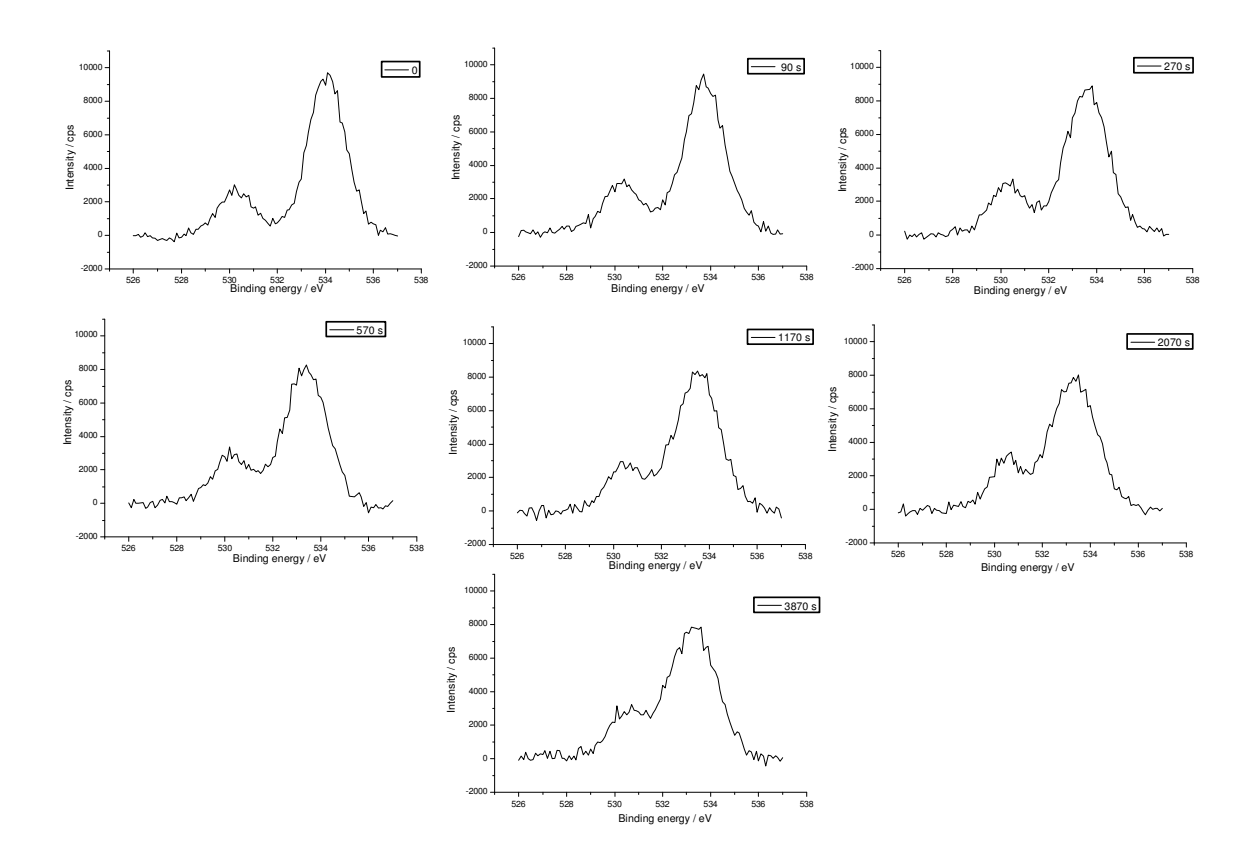


**Figure A-9** O(1s) energy region for 20.2 L Mo(CO)<sub>6</sub> and its photodecomposition on  $TiO_2(110)$ . The label on each plot represents the irradiation time in seconds.

## References

- H. J. Freund. Clusters and islands on oxides: from catalysis via electronics and magnetism to optics. Surface Science 500, 271 (2002).
- M. Baumer and H. J. Freund. *Metal deposits on well-ordered oxide films*. Progress in Surface Science 61, 127 (1999).
- W. T. Wallace, B. K. Min, and D. W. Goodman. *The nucleation, growth, and stability of oxide-supported metal clusters*. Topics in Catalysis 34, 17 (2005).
- Q. Fu and T. Wagner. *Interaction of nanostructured metal overlayers with oxide surfaces*. Surface Science Reports 62, 431 (2007).
- U. Diebold. *The surface science of titanium dioxide*. Surface Science Reports 48, 53 (2003).
- M. Haruta. Size- and support-dependency in the catalysis of gold. Catalysis Today 36, 153 (1997).
- M. Chen and D. W. Goodman, in *The Chemical Physics of Solids Surfaces* Vol. 12. (Elsevier, 2007).
- 8 C. T. Campbell. *Ultrathin metal films and particles on oxide surfaces: Structural, electronic and chemisorptive properties.* Surface Science Reports 27, 1 (1997).
- J. Marien, T. Wagner, G. Duscher, A. Koch, and M. Ruhle. *Nb on (110) TiO2 (rutile): growth, structure, and chemical composition of the interface.* Surface Science 446, 219 (2000).
- G. Blanco, J. J. Calvino, M. A. Cauqui, P. Corchado, C. Lopez-Cartes, C. Colliex, J. A. Perez-Omil, and O. Stephan. *Nanostructural evolution under reducing conditions of a Pt/CeTbOx catalyst: A new alternative system as a TWC component*. Chemistry of Materials 11, 3610 (1999).
- S. Bernal, J. J. Calvino, M. A. Cauqui, J. M. Gatica, C. L. Cartes, J. A. P. Omil, and J. M. Pintado. *Some contributions of electron microscopy to the characterisation of the strong metal-support interaction effect*. Catalysis Today 77, 385 (2003).
- M. Ramamoorthy, D. Vanderbilt, and R. D. Kingsmith. *1st-Principles Calculations of the Energetics of Stoichiometric Tio2 Surfaces*. Physical Review B 49, 16721 (1994).
- D. A. Bonnell and J. Garra. Scanning probe microscopy of oxide surfaces: atomic structure and properties. Reports on Progress in Physics 71 (2008).
- <sup>14</sup> K. Fukui, H. Onishi, and Y. Iwasawa. *Atom-resolved image of the TiO2(110)* surface by noncontact atomic force microscopy. Physical Review Letters 79, 4202 (1997).
- J. V. Lauritsen, A. S. Foster, G. H. Olesen, M. C. Christensen, A. Kuhnle, S. Helveg, J. R. Rostrup-Nielsen, B. S. Clausen, M. Reichling, and F. Besenbacher. *Chemical identification of point defects and adsorbates on a metal oxide surface by atomic force microscopy*. Nanotechnology 17, 3436 (2006).

- G. Charlton, P. B. Howes, C. L. Nicklin, P. Steadman, J. S. G. Taylor, C. A. Muryn, S. P. Harte, J. Mercer, R. McGrath, D. Norman, T. S. Turner, and G. Thornton. *Relaxation of TiO2(110)-(1x1) using surface X-ray diffraction*. Physical Review Letters 78, 495 (1997).
- 17 R. Lindsay, A. Wander, A. Ernst, B. Montanari, G. Thornton, and N. M. Harrison. *Revisiting the surface structure of TiO2(110): A quantitative low-energy electron diffraction study*. Physical Review Letters 94, 246102 (2005).
- S. J. Thompson and S. P. Lewis. *Revisiting the (110) surface structure of TiO2: A theoretical analysis.* Physical Review B 73, 073403 (2006).
- R. Schaub, E. Wahlstrom, A. Ronnau, E. Laegsgaard, I. Stensgaard, and F. Besenbacher. *Oxygen-mediated diffusion of oxygen vacancies on the TiO2(110) surface*. Science 299, 377 (2003).
- U. Diebold, J. Lehman, T. Mahmoud, M. Kuhn, G. Leonardelli, W. Hebenstreit, M. Schmid, and P. Varga. *Intrinsic defects on a TiO2(110)(1x1) surface and their reaction with oxygen: a scanning tunneling microscopy study*. Surface Science 411, 137 (1998).
- M. Li, W. Hebenstreit, and U. Diebold. *Oxygen-induced restructuring of the rutile TiO2(110)(1x1) surface*. Surface Science 414, L951 (1998).
- E. Wahlstrom, E. K. Vestergaard, R. Schaub, A. Ronnau, M. Vestergaard, E. Laegsgaard, I. Stensgaard, and F. Besenbacher. *Electron transfer-induced dynamics of oxygen molecules on the TiO2(110) surface*. Science 303, 511 (2004).
- Y. G. Du, Z. Dohnalek, and I. Lyubinetsky. *Transient mobility of oxygen adatoms upon O-2 dissociation on reduced TiO2(110)*. Journal of Physical Chemistry C 112, 2649 (2008).
- S. Wendt, P. T. Sprunger, E. Lira, G. K. H. Madsen, Z. S. Li, J. O. Hansen, J. Matthiesen, A. Blekinge-Rasmussen, E. Laegsgaard, B. Hammer, and F. Besenbacher. *The role of interstitial sites in the Ti3d defect state in the band gap of Titania*. Science 320, 1755 (2008).
- R. Schaub, R. Thostrup, N. Lopez, E. Laegsgaard, I. Stensgaard, J. K. Norskov, and F. Besenbacher. *Oxygen vacancies as active sites for water dissociation on rutile TiO2(110)*. Physical Review Letters 87, 266104 (2001).
- Z. Zhang, O. Bondarchuk, B. D. Kay, J. M. White, and Z. Dohnalek. *Imaging water dissociation on TiO2(110): Evidence for inequivalent geminate OH groups*. Journal of Physical Chemistry B 110, 21840 (2006).
- O. Bikondoa, C. L. Pang, R. Ithnin, C. A. Muryn, H. Onishi, and G. Thornton. *Direct visualization of defect-mediated dissociation of water on TiO2(110)*. Nature Materials 5, 189 (2006).
- S. Wendt, J. Matthiesen, R. Schaub, E. K. Vestergaard, E. Laegsgaard, F. Besenbacher, and B. Hammer. *Formation and splitting of paired hydroxyl groups on reduced TiO2(110)*. Physical Review Letters 96, 066107 (2006).
- S. Suzuki, K. Fukui, H. Onishi, and Y. Iwasawa. *Hydrogen adatoms on TiO2(110)-(1 x 1) characterized by scanning tunneling microscopy and electron stimulated desorption*. Physical Review Letters 84, 2156 (2000).
- M. A. Henderson. Surface perspective on self-diffusion in rutile TiO2. Surface Science 419, 174 (1999).

- H. Iddir, S. Ogut, P. Zapol, and N. D. Browning. *Diffusion mechanisms of native point defects in rutile TiO2: Ab initio total-energy calculations*. Physical Review B 75, 073203 (2007).
- M. Li, W. Hebenstreit, L. Gross, U. Diebold, M. A. Henderson, D. R. Jennison, P. A. Schultz, and M. P. Sears. *Oxygen-induced restructuring of the TiO2(110) surface: a comprehensive study*. Surface Science 437, 173 (1999).
- K. T. Park, M. H. Pan, V. Meunier, and E. W. Plummer. *Surface Reconstructions of TiO[sub 2](110) Driven by Suboxides*. Physical Review Letters 96, 226105 (2006).
- R. A. Bennett, P. Stone, N. J. Price, and M. Bowker. Two (1 x 2) reconstructions of TiO2(110): Surface rearrangement and reactivity studied using elevated temperature scanning tunneling microscopy. Physical Review Letters 82, 3831 (1999).
- C. L. Pang, S. A. Haycock, H. Raza, P. W. Murray, G. Thornton, O. Gulseren, R. James, and D. W. Bullett. *Added row model of TiO2(110)1x2*. Physical Review B 58, 1586 (1998).
- H. Onishi and Y. Iwasawa. *Dynamic visualization of a metal-oxide-surface/gas-phase reaction: Time-resolved observation by scanning tunneling microscopy at 800 K.* Physical Review Letters 76, 791 (1996).
- A. W. Grant and C. T. Campbell. *Cesium adsorption on TiO2(110)*. Physical Review B 55, 1844 (1997).
- <sup>38</sup> Z. S. Li, J. H. Jorgensen, P. J. Moller, M. Sambi, and G. Granozzi. *A photoemission and resonant photoemission study of Ba deposition at the TiO2* (110) surface. Applied Surface Science 142, 135 (1999).
- U. Martinez, L. Giordano, and G. Pacchioni. *Tuning the work function of ultrathin oxide films on metals by adsorption of alkali atoms*. Journal of Chemical Physics 128 (2008).
- O. Bikondoa, C. L. Pang, C. A. Muryn, B. G. Daniels, S. Ferrero, E. Michelangeli, and G. Thornton. *Ordered overlayers of Ca on TiO2(110)-1x1*. Journal of Physical Chemistry B 108, 16768 (2004).
- A. K. See and R. A. Bartynski. *Electronic properties of ultrathin Cu and Fe films on TiO2(110) studied by photoemission and inverse photoemission.* Physical Review B: Condensed Matter 50, 12064 (1994).
- A. Berko, J. Szoko, and F. Solymosi. *High temperature postgrowing of Pt-nanocrystallites supported and encapsulated on TiO2(110) surface*. Surface Science 532, 390 (2003).
- A. Berko, I. Ulrych, and K. C. Prince. *Encapsulation of Rh nanoparticles supported on TiO2(110)-(1x1) surface: XPS and STM studies*. Journal of Physical Chemistry B 102, 3379 (1998).
- Q. Fu, T. Wagner, S. Olliges, and H. D. Carstanjen. *Metal-oxide interfacial reactions: Encapsulation of Pd on TiO2 (110)*. Journal of Physical Chemistry B 109, 944 (2005).
- J. A. Nieminen and K. Kaski. *Rate-equation study of nucleation and growth of thin films. I. Growth of one monolayer.* Physical Review A 40, 2088 (1989).
- J. A. Venables, *Introduction to Surface and Thin Film Processes* (Cambrdge University Press, 2000).

- J. A. Venables, G. D. T. Spiller, and M. Hanbucken. *Nucleation and Growth of Thin-Films*. Reports on Progress in Physics 47, 399 (1984).
- P. Atkins and J. d. Paula, *Atkins' Physical Chemistry* (Oxford University Press, 2002).
- <sup>49</sup> A. Zangwill, *Physics at Surfaces* (Cambridge University Press, 1988).
- G. Attard and C. Barnes, *Surfaces* (Oxford University Press, 1998).
- A. Sanchez, S. Abbet, U. Heiz, W. D. Schneider, H. Hakkinen, R. N. Barnett, and U. Landman. *When gold is not noble: Nanoscale gold catalysts*. Journal of Physical Chemistry A 103, 9573 (1999).
- J. T. Mayer, U. Diebold, T. E. Madey, and E. Garfunkel. *Titanium and Reduced Titania Overlayers on Titanium Dioxide*(110). Journal of Electron Spectroscopy and Related Phenomena 73, 1 (1995).
- P. J. Moeller and M. C. Wu. Surface geometrical structure and incommensurate growth: ultrathin copper films on titania(110). Surface Science 224, 265 (1989).
- F. M. Hoffmann. *Infrared reflection-absorption spectroscopy of adsorbed molecules*. Surface Science Reports 3, 107 (1983).
- P. Hollins, K. J. Davies, and J. Pritchard. *Infrared spectra of carbon monoxide chemisorbed on a surface vicinal to copper(110): the influence of defect sites.* Surface Science 138, 75 (1984).
- P. Hollins. *The influence of surface defects on the infrared spectra of adsorbed species*. Surface Science Reports 16, 51 (1992).
- C. N. Banwell and E. M. McCash, Fundamentals of Molecular spectroscopy (McGraw-Hill, London, 1994).
- J. D. E. McIntyre and D. E. Aspnes. *Differential reflection spectroscopy of very thin surface films*. Surface Science 24, 417 (1971).
- Y. J. Chabal. Surface infrared spectroscopy. Surface Science Reports 8, 211 (1988).
- B. E. Hayden, in *The Chemical Physics of Solid Surfaces: Oxide Surfaces*, edited by D. P. Woodruff (Elsevier, Amsterdam-London-New York, 2001), Vol. 9, p. 514.
- J. Evans, B. E. Hayden, F. Mosselmans, and A. Murray. *The chemistry of rhodium on TiO2(110) deposited by MOCVD of [Rh(CO)2Cl2] and MVD.* Surface Science 301, 61 (1994).
- J. Evans, B. E. Hayden, and G. Lu. *Adsorption and thermal decomposition of Mo(CO)6 on TiO2(110)*. Journal of the Chemical Society, Faraday Transactions 92, 4733 (1996).
- B. E. Hayden, in *NATO ASI Series E: Applied Sciences*, edited by R. M. Lambert and P. G. (Academic Publishers, 1997), Vol. 331, p. 215.
- J. A. Mielczarski and R. H. Yoon. Fourier-Transform Infrared External Reflection Study of Molecular-Orientation in Spontaneously Adsorbed Layers on Low-Absorption Substrates. Journal of Physical Chemistry 93, 2034 (1989).
- M. D. Porter, T. B. Bright, D. L. Allara, and T. Kuwana. *Quantitative Aspects of Infrared External Reflection Spectroscopy Polymer Glassy-Carbon Interface*. Analytical Chemistry 58, 2461 (1986).

- R. G. Musket, W. McLean, C. A. Colmenares, D. M. Makowiecki, and W. J. Siekhaus. *Preparation of Atomically Clean Surfaces of Selected Elements a Review*. Applied Surface Science 10, 143 (1982).
- J. Pritchard, T. Catterick, and R. K. Gupta. *Infrared spectroscopy of chemisorbed carbon monoxide on copper*. Surface Science 53, 1 (1975).
- W. W. Crew and R. J. Madix. CO adsorption and oxidation on oxygen precovered Cu(110) at 150 K: Reactivity of two types of adsorbed atomic oxygen determined by scanning tunneling microscopy. Surface Science 356, 1 (1996).
- D. P. Woodruff and T. A. Delchar, *Modern Techniques of Surface Science* (Cambridge University Press, 1994).
- J. M. Hollas, *Modern Spectroscopy* (John Wiley & Sons, 1987).
- J. C. Riviere, *Surface Analytical Techniques* (Oxford University Press, 1990).
- M. P. Seah and W. A. Dench. Quantitative electron spectroscopy of surfaces: a standard data base for electron inelastic mean free paths in solids. Surface and Interface Analysis 1, 2 (1979).
- M. P. Seah, in *Practical Surface Analysis*, edited by D. Briggs and M. P. Seah (John Wiley & Sons, 1983).
- W. M. Riggs, L. E. Davis, J. F. Moulder, and G. E. Muilenberg, *Handbook of X-ray Photoelectron Spectroscopy* (Perkin-Elmer Corporation, 1979).
- C. Davisson and L. H. Germer. *Diffraction of Electrons by a Crystal of Nickel*. Physical Review 30, 705 (1927).
- G. A. Somorjai, *Chemistry in two dimensions: Surfaces* (Cornell University Press, 1981).
- N. W. Ashcroft and N. D. Mermin, *Solid State Physics* (Brooks Cole, 1976).
- G. Ertl and J.Kuppers, *Low Energy Electrons and Surface Chemistry* (Verlag Chemie, 1974).
- D. M. Mattox, *Handbook of Physical Vapor Deposition (PVD) Processing* (Noyes Publications, 1998).
- J. E. Mahan, *Physical Vapor Deposition of Thin Films* (Wiley-Interscience, 2000).
- M. L. Hitchman, in *Chemical Vapor Deposition*, edited by M. L. Hitchman and K. F. Jensen (Academic Press.
- K. L. Choy. *Chemical vapour deposition of coatings*. Progress in Materials Science 48, 57 (2003).
- K.-H. Dahmen, in *Encyclopedia of Physical Science and Technology* (Academic Press, New York, 2001), p. 787.
- R. D. Dupuis, in *Encyclopedia of Physical Science and Technology* (Academic Press, New York, 2001), p. 495.
- P. Serp, J.-C. Hierso, and P. Kalck, in *Precursor Chemistry of Advanced Materials: CVD*, *ALD and Nanoparticles*, edited by R. A. Fischer (Springer, 2005).
- N. Nakajima, H. Kato, T. Okazaki, and Y. Sakisaka. *Photoemission study of the modification of the electronic structure of transition-metal overlayers on TiO2 surfaces III. Ni on TiO2(0 0 1) and Cu on TiO2(1 1 0).* Surface Science 561, 93 (2004).
- U. Diebold, J. M. Pan, and T. E. Madey. *Growth mode of ultrathin copper overlayers on titania* (110). Physical Review B: Condensed Matter and Materials Physics 47, 3868 (1993).

- P. Lu and F. Cosandey. *Epitaxial growth defects and interfacial structures of Cu deposited on TiO2*. Interface Science 2, 169 (1994).
- D. A. Chen, M. C. Bartelt, R. Q. Hwang, and K. F. McCarty. *Self-limiting growth of copper islands on TiO2(110)-(1x1)*. Surface Science 450, 78 (2000).
- U. Diebold, J. M. Pan, and T. E. Madey. *Ultrathin Metal-Films on Tio2(110) Metal Overlayer Spreading and Surface Reactivity*. Surface Science 287, 896 (1993).
- J. M. Pan, U. Diebold, L. Z. Zhang, and T. E. Madey. *Ultrathin Reactive Metal-Films on Tio2(110) Growth, Interfacial Interaction and Electronic-Structure of Chromium Films*. Surface Science 295, 411 (1993).
- T. Wagner, J. Marien, and G. Duscher. *Cu, Nb and V on (110) TiO2 (rutile). Epitaxy and chemical reactions.* Thin Solid Films 398-399, 419 (2001).
- G. Charlton, P. B. Howes, C. A. Muryn, H. Raza, N. Jones, J. S. G. Taylor, C. Norris, R. McGrath, D. Norman, T. S. Turner, and G. Thornton. *Copper interface induced relaxation of TiO2(110)-1\*1*. Physical Review B: Condensed Matter and Materials Physics 61, 16117 (2000).
- <sup>94</sup> K. Ding, J. Li, and Y. Zhang. *Cu and NO coadsorption on TiO2(110) surface. A density functional theory study.* Theochem 728, 123 (2005).
- D. Pillay, Y. Wang, and G. S. Hwang. Nucleation and growth of 1B metal clusters on rutile TiO2(110): Atomic level understanding from first principles studies. Catalysis Today 105, 78 (2005).
- M. C. Wu and P. J. Moeller. Studies of the electronic structure of ultrathin copper films on a titania(110) surface. Surface Science 224, 250 (1989).
- P. L. Wincott, J. S. G. Irwin, G. Jones, P. J. Hardman, G. Thornton, S. Weichel, P. J. Moller, and V. R. Dhanak. *Angle-resolved photoemission studies of the (Gamma)over-bar Shockley surface state on ordered Cu(111) overlayers on TiO2(110)*. Surface Science 377, 242 (1997).
- <sup>98</sup> Z. Chang, S. Haq, and G. Thornton. *Morphology of Cu overlayers on TiO2(110)*. Surface Science 467, L841 (2000).
- J.-M. Pan, B. L. Maschhoff, U. Diebold, and T. E. Madey. *Structural study of ultrathin metal films on TiO2 using LEED, ARXPS and MEED.* Surface Science 291, 381 (1993).
- M. Wagner, O. Kienzle, D. A. Bonnell, and M. Ruhle. *Nonstoichiometry on TiO2(110) and Cu-TiO2 interfaces*. Journal of Vacuum Science & Technology, A: Vacuum, Surfaces, and Films 16, 1078 (1998).
- D. L. Carroll, M. Wagner, M. Ruhle, and D. A. Bonnell. *The thermal stability of thin copper films deposited on TiO2(110) studied by scanning tunneling microscopy*. Journal of Materials Research 12, 975 (1997).
- J. Zhou, Y. C. Kang, and D. A. Chen. Oxygen-Induced Dissociation of Cu Islands Supported on TiO2(110). Journal of Physical Chemistry B 107, 6664 (2003).
- J. Zhou, Y. C. Kang, S. Ma, and D. A. Chen. Adsorbate-induced dissociation of metal clusters: TiO2 (110)-supported Cu and Ni clusters exposed to oxygen gas. Surface Science 562, 113 (2004).
- K. H. Ernst, A. Ludviksson, R. Zhang, J. Yoshihara, and C. T. Campbell. *Growth model for metal films on oxide surfaces: copper on zinc oxide*(0001)-oxygen. Physical Review B: Condensed Matter and Materials Physics 47, 13782 (1993).

- R. Zhang, A. Ludviksson, and C. T. Campbell. *The Chemisorption of H2o and O-2 on Cu Films on Zno(0001)-O*. Surface Science 289, 1 (1993).
- A. Ludviksson, K. H. Ernst, R. Zhang, and C. T. Campbell. *The chemisorption of carbon monoxide on copper films on oxygen-terminated zinc oxide* (0001). Journal of Catalysis 141, 380 (1993).
- S. V. Didziulis, K. D. Butcher, S. L. Cohen, and E. I. Solomon. *Chemistry of copper overlayers on zinc oxide single-crystal surfaces: model active sites for copper/zinc oxide methanol synthesis catalysts*. Journal of the American Chemical Society 111, 7110 (1989).
- X. Xu and D. W. Goodman. Structural and chemisorptive properties of model catalysts: copper supported on silica thin films. Journal of Physical Chemistry 97, 683 (1993).
- X. P. Xu, J. W. He, and D. W. Goodman. A Surface Spectroscopic Study of Metal Support Interactions Model Studies of Copper on Thin Sio2-Films. Surface Science 284, 103 (1993).
- Q. L. Guo and P. J. Moller. On the Thermal-Stability of Copper-Deposits on a (0001) Sapphire Surface. Surface Science 244, 228 (1991).
- T. T. Magkoev, K. Christmann, A. M. C. Moutinho, and Y. Murata. *Alumina vapour condensation on Mo(110) surface and adsorption of copper and gold atoms on the formed oxide layer*. Surface Science 515, 538 (2002).
- D. R. Rainer, C. Xu, P. M. Holmblad, and D. W. Goodman. *Pd, Cu, and Au particles on Al2O3 thin films: an infrared reflection absorption spectroscopy study of monometallic and bimetallic planar model supported catalysts.* Journal of Vacuum Science & Technology, A: Vacuum, Surfaces, and Films 15, 1653 (1997).
- M.-C. Wu and D. W. Goodman. *Particulate Cu on Ordered Al2O3: Reactions with Nitric Oxide and Carbon Monoxide*. Journal of Physical Chemistry 98, 9874 (1994).
- K. Varazo, F. W. Parsons, S. Ma, and D. A. Chen. *Methanol chemistry on Cu and oxygen-covered Cu nanoclusters supported on TiO2(110)*. Journal of Physical Chemistry B 108, 18274 (2004).
- S. Ma, J. Zhou, Y. C. Kang, J. E. Reddic, and D. A. Chen. *Dimethyl methylphosphonate decomposition on Cu surfaces: Supported Cu nanoclusters and films on TiO2(110)*. Langmuir 20, 9686 (2004).
- F. Boccuzzi and A. Chiorino. FTIR study of carbon monoxide oxidation and scrambling at room temperature over copper supported on ZnO and TiO2 .1. Journal of Physical Chemistry 100, 3617 (1996).
- H. W. Chen, J. M. White, and J. G. Ekerdt. *Electronic Effect of Supports on Copper-Catalysts*. Journal of Catalysis 99, 293 (1986).
- K. K. Bando, K. Sayama, H. Kusama, K. Okabe, and H. Arakawa. *In-situ FT-IR study on CO2 hydrogenation over Cu catalysts supported on SiO2, Al2O3, and TiO2*. Applied Catalysis a-General 165, 391 (1997).
- F. Boccuzzi, A. Chiorino, M. Manzoli, D. Andreeva, T. Tabakova, L. Ilieva, and V. Iadakiev. *Gold, silver and copper catalysts supported on TiO2 for pure hydrogen production*. Catalysis Today 75, 169 (2002).

- J. N. Nian, S. A. Chen, C. C. Tsai, and H. S. Teng. *Structural feature and catalytic performance of Cu species distributed over TiO2 nanotubes*. Journal of Physical Chemistry B 110, 25817 (2006).
- C. Evangelisti, G. Vitulli, E. Schiavi, M. Vitulli, S. Bertozzi, P. Salvadori, L. Bertinetti, and G. Martra. *Nanoscale Cu supported catalysts in the partial oxidation of cyclohexane with molecular oxygen*. Catalysis Letters 116, 57 (2007).
- D. Briggs and M. P. Seah, *Practical Surface Analysis* (John Wiley & Sons, 1983).
- D. Q. Yang, M. Meunier, and E. Sacher. *The estimation of the average dimensions of deposited clusters from XPS emission intensity ratios*. Applied Surface Science 173, 134 (2001).
- X. Xu, S. M. Vesecky, and D. W. Goodman. *Infrared reflection-absorption spectroscopy and STM studies of model silica-supported copper catalysts*. Science 258, 788 (1992).
- J. Evans, B. E. Hayden, and G. Lu. *The adsorption of carbon monoxide on TiO2(110) supported palladium*. Surface Science 360, 61 (1996).
- J. Evans, B. E. Hayden, J. F. W. Mosselmans, and A. J. Murray, in *Elementary Reaction Steps in Heterogeneous Catalysis*, edited by R. W. Joyner and R. A. VanSanten, 1993), Vol. 398, p. 179.
- J. Evans, B. E. Hayden, and G. Lu. *The Adsorption of CO on TiO2(110) supported Pd.* Surface Science 360, 61 (1996).
- S. C. Parker, A. W. Grant, V. A. Bondzie, and C. T. Campbell. *Island growth kinetics during the vapor deposition of gold onto TiO2(110)*. Surface Science 441, 10 (1999).
- L. Zhang, R. Persaud, and T. E. Madey. *Ultrathin metal films on a metal oxide surface: Growth of Au on TiO2 (110)*. Physical Review B 56, 10549 (1997).
- E. Huger and K. Osuch. *Ferromagnetism in body centred cubic Rh*. Solid State Communications 131, 175 (2004).
- J. Wang, W. M. Lau, and Q. Li. Effects of particle size and spacing on the optical properties of gold nanocrystals in alumina. Journal of Applied Physics 97 (2005).
- J. Y. Bigot, V. Halte, J. C. Merle, and A. Daunois. *Electron dynamics in metallic nanoparticles*. Chemical Physics 251, 181 (2000).
- W. F. Egelhoff, Jr. Core-level binding-energy shifts at surfaces and in solids. Surface Science Reports 6, 253 (1986).
- M. G. Mason. *Electronic structure of supported small metal clusters*. Physical Review B: Condensed Matter and Materials Physics 27, 748 (1983).
- G. K. Wertheim. *Core-Electron Binding-Energies in Free and Supported Metal-Clusters*. Zeitschrift Fur Physik B-Condensed Matter 66, 53 (1987).
- C. Kuhrt and M. Harsdorff. *Photoemission and Electron-Microscopy of Small Supported Palladium Clusters*. Surface Science 245, 173 (1991).
- G. K. Wertheim, S. B. Dicenzo, and S. E. Youngquist. *Unit Charge on Supported Gold Clusters in Photoemission Final-State*. Physical Review Letters 51, 2310 (1983).
- C. H. F. Peden, K. B. Kidd, and N. D. Shinn. *Metal/metal-oxide interfaces: a surface science approach to the study of adhesion*. Journal of Vacuum Science & Technology, A: Vacuum, Surfaces, and Films 9, 1518 (1991).

- M. Valden, X. Lai, and D. W. Goodman. *Onset of catalytic activity of gold clusters on titania with the appearance of nonmetallic properties*. Science 281, 1647 (1998).
- R. Meyer, C. Lemire, S. K. Shaikhutdinov, and H. Freund. *Surface chemistry of catalysis by gold*. Gold Bulletin 37, 72 (2004).
- S. S. Fu and G. A. Somorjai. *Interactions of O2, Co, Co2, and D2 with the Stepped Cu(311) Crystal-Face Comparison to Cu(110)*. Surface Science 262, 68 (1992).
- T. Sueyoshi, T. Sasaki, and Y. Iwasawa. Reactive oxygen species on reconstructed Cu(110); Catalytic CO oxidation by reactive oxygen species at Low temperatures. Surface Science 358, 764 (1996).
- G. L. Geoffroy and M. S. Wrighton, *Organometallic Photochemistry* (Academic Press, 1980).
- H. B. Gray and N. A. Beach. *The Electronic Structures of Octahedral Metal Complexes*. *I. Metal Hexacarbonyls and Hexacyanides*. Journal of the American Chemical Society 85, 2922 (1963).
- J. A. Welch, K. S. Peters, and V. Vaida. *Medium Effects on the Photo-Dissociation of Cr(Co)6*. Journal of Physical Chemistry 86, 1941 (1982).
- G. W. Tyndall and R. L. Jackson. *Single-Photon and Multiphoton Dissociation of Molybdenum Hexacarbonyl at 248 Nm*. Journal of Physical Chemistry 95, 687 (1991).
- B. Venkataraman, H. Q. Hou, Z. G. Zhang, S. H. Chen, G. Bandukwalla, and M. Vernon. *A Molecular-Beam Study of the 1-Photon, 2-Photon, and 3-Photon Photodissociation Mechanism of the Group-Vib (Cr, Mo, W) Hexacarbonyls at 248nm.* Journal of Chemical Physics 92, 5338 (1990).
- Y. J. Chen, C. L. Liao, and C. Y. Ng. A molecular beam photoionization mass spectrometric study of Cr(CO)(6), Mo(CO)(6), and W(CO)(6). Journal of Chemical Physics 107, 4527 (1997).
- Y. E. Belyayev, A. V. Demyanenko, and A. A. Puretzky. Formation and Luminescence of Molybdenum Atoms after Uv Multiphoton Excitation of Gas-Phase Mo(Co)6. Laser Chemistry 12, 223 (1992).
- D. M. Rayner, Y. Ishikawa, C. E. Brown, and P. A. Hackett. *Branching Ratios and Bond-Dissociation Energies from the Excimer Laser Photolysis of Group-6 Metal-Carbonyls*. Journal of Chemical Physics 94, 5471 (1991).
- J. A. Ganske and R. N. Rosenfeld. *Photochemistry of Mo(Co)6 in the Gas-Phase*. Journal of Physical Chemistry 93, 1959 (1989).
- Y. Ishikawa, C. E. Brown, P. A. Hackett, and D. M. Rayner. *Excimer Laser Photolysis of Group-6 Metal-Carbonyls in the Gas-Phase*. Journal of Physical Chemistry 94, 2404 (1990).
- J. A. Ganske and R. N. Rosenfeld. *Molybdenum-Carbon Bond-Dissociation Energies in Mo(Co)6*. Journal of Physical Chemistry 94, 4315 (1990).
- Y. I. Ishikawa and K. Kawakami. Structure and infrared Spectroscopy of group 6 transition-metal carbonyls in the gas phase: DFT studies on M(CO)(n) (M = Cr, Mo, and W; n = 6, 5, 4, and 3). Journal of Physical Chemistry A 111, 9940 (2007).
- S. A. Buntin, R. R. Cavanagh, L. J. Richter, and D. S. King. *Photodissociation Dynamics of Mo(Co)6 at 266-Nm and 355-Nm Co Photofragment Kinetic-Energy and Internal-State Distributions*. Journal of Chemical Physics 94, 7937 (1991).

- F. Qi, S. H. Yang, L. S. Sheng, W. Q. Ye, H. Gao, Y. W. Zhang, and S. Q. Yu. *Dissociative photoionization of Mo(CO)(6) in the photon energy range of 8-40 eV*. Journal of Physical Chemistry A 101, 7194 (1997).
- R. N. Perutz and J. J. Turner. *Photochemistry of Group-6 Hexacarbonyls in Low-Temperature Matrices*. *3. Interaction of Pentacarbonyls with Noble-Gases and Other Matrices*. Journal of the American Chemical Society 97, 4791 (1975).
- X. Z. Sun, M. W. George, S. G. Kazarian, S. M. Nikiforov, and M. Poliakoff. Can organometallic noble gas compounds be observed in solution at room temperature? A time-resolved infrared (TRIR) and UV spectroscopic study of the photochemistry of M(CO)(6) (M=Cr, Mo, and W) in supercritical noble gas and CO2 solution. Journal of the American Chemical Society 118, 10525 (1996).
- J. R. Wells and E. Weitz. Rare-Gas Metal-Carbonyl-Complexes Bonding of Rare-Gas Atoms to the Group-Vi Pentacarbonyls. Journal of the American Chemical Society 114, 2783 (1992).
- C. Kayran, M. Richards, and P. C. Ford. *Activation parameters in flash photolysis studies of Mo(CO)6*. Inorganica Chimica Acta 357, 143 (2004).
- H. Hermann, F. W. Grevels, A. Henne, and K. Schaffner. *Flash-Photolysis with Infrared Detection the Photochemistry and Secondary Thermal-Reactions of Cr(Co)6,Mo(Co)6,W(Co)6*. Journal of Physical Chemistry 86, 5151 (1982).
- J. C. King, J. Z. Zhang, B. J. Schwartz, and C. B. Harris. *Vibrational-Relaxation of M(Co)6 (M=Cr, Mo, W) Effect of Metal Mass on Vibrational Cooling Dynamics and Non-Boltzmann Internal Energy-Distributions*. Journal of Chemical Physics 99, 7595 (1993).
- T. Q. Lian, S. E. Bromberg, M. C. Asplund, H. Yang, and C. B. Harris. Femtosecond infrared studies of the dissociation and dynamics of transition metal carbonyls in solution. Journal of Physical Chemistry 100, 11994 (1996).
- R. N. Perutz and J. J. Turner. *Photochemistry of Group-6 Hexacarbonyls in Low- Temperature Matrices .4. Tetracarbonylmolybdenum and Tricarbonylmolybdenum.* Journal of the American Chemical Society 97, 4800 (1975).
- J. R. Creighton. *Photodecomposition of Mo(Co)6 Adsorbed on Si(100)*. Journal of Applied Physics 59, 410 (1986).
- N. S. Gluck, G. J. Wolga, C. E. Bartosch, W. Ho, and Z. Ying. *Mechanisms of Carbon and Oxygen Incorporation into Thin Metal-Films Grown by Laser Photolysis of Carbonyls*. Journal of Applied Physics 61, 998 (1987).
- N. S. Gluck, Z. Ying, C. E. Bartosch, and W. Ho. *Mechanisms of Laser Interaction with Metal-Carbonyls Adsorbed on Si(111)7x7 Thermal Vs Photoelectronic Effects*. Journal of Chemical Physics 86, 4957 (1987).
- C. C. Cho and S. L. Bernasek. *Molybdenum Deposition from the Decomposition of Molybdenum Hexacarbonyl*. Journal of Applied Physics 65, 3035 (1989).
- Z. C. Ying and W. Ho. Photodissociation of Adsorbed Mo(Co)6 Induced by Direct Photoexcitation and Hot-Electron Attachment .2. Physical-Mechanisms. Journal of Chemical Physics 94, 5701 (1991).
- L. J. Richter, S. A. Buntin, P. M. Chu, and R. R. Cavanagh. Adsorption and Photodecomposition of Mo(Co)(6) on Si(111) 7x7 an Infrared Reflection-Absorption Spectroscopy Study. Journal of Chemical Physics 100, 3187 (1994).

- P. M. Chu, S. A. Buntin, L. J. Richter, and R. R. Cavanagh. *Photodecomposition of Mo(Co)(6)/Si(111) 7x7 Co State-Resolved Evidence for Excited-State Relaxation and Quenching*. Journal of Chemical Physics 101, 2929 (1994).
- <sup>172</sup> Z. C. Ying and W. Ho. *Photodissociation of Adsorbed Mo(Co)6 Induced by Direct Photoexcitation and Hot-Electron Attachment .1. Surface-Chemistry*. Journal of Chemical Physics 93, 9077 (1990).
- S. K. So and W. Ho. Resonant Photodissociation of Mo(Co)6 Adsorbed on Graphite and Ag(111). Journal of Chemical Physics 95, 656 (1991).
- C. C. Yeh, Y. H. Lai, W. Y. Chu, C. T. Yeh, and W. H. Hung. *Photon-induced chemical vapor deposition of molybdenum on Pt(111)*. Surface Science 565, 81 (2004).
- H. H. Huang, C. S. Sreekanth, C. S. Seet, X. Jiang, and G. Q. Xu. *Thermal and photoinduced chemistry of Mo(CO)6 on clean and chemically modified Ru(001)*. Surface Science 365, 769 (1996).
- T. A. Germer and W. Ho. *Energy-Transfer and Photochemistry on a Metal-Surface Mo(Co)6 on Rh(100)*. Journal of Vacuum Science & Technology a-Vacuum Surfaces and Films 7, 1878 (1989).
- <sup>177</sup> Z. Song, T. H. Cai, J. A. Rodriguez, J. Hrbek, A. S. Y. Chan, and C. M. Friend. *A novel growth mode of Mo on Au (111) from a Mo(CO)(6) precursor: An STM study*. Journal of Physical Chemistry B 107, 1036 (2003).
- J. A. Rodriguez, J. Dvorak, T. Jirsak, and J. Hrbek. Formation of Mo and MoSx nanoparticles on Au(1 1 1) from Mo(CO)6 and S2 precursors. Electronic and chemical properties. Surface Science 490, 315 (2001).
- Y. Wang, F. Gao, and W. T. Tysoe. *Interaction of molybdenum hexacarbonyl with metallic aluminum high temperatures: Carbide and alloy formation*. Journal of Molecular Catalysis a-Chemical 236, 18 (2005).
- T. E. Jones, T. C. Q. Noakes, P. Bailey, and C. J. Baddeley. Structural and compositional analysis of two ordered near-surface alloys produced by adsorption and thermal decomposition of Mo(CO)6 on Ni{1 1 1}. Surface Science 523, 12 (2003).
- A. Zecchina, E. E. Platero, and C. O. Arean. *Infrared Characterization of Group-Vi* (61) *Metal-Carbonyls Absorbed onto Gamma-Alumina*. Inorganic Chemistry 27, 102 (1988).
- K. P. Reddy and T. L. Brown. *Kinetics of Surface Processes for Mo(Co)(6) on Partially Dehydroxylated Alumina and Hydroxylated Alumina Observation of Mo(Co)(5)(Ads)*. Journal of the American Chemical Society 117, 2845 (1995).
- M. Kaltchev and W. T. Tysoe. Surface Chemistry and Decarbonylation of Molybdenum Hexacarbonyl on Thin Alumina Films. Journal of Catalysis 193, 29 (2000).
- M. Kaltchev and W. T. Tysoe. *The Decomposition of Molybdenum Hexacarbonyl on Thin Alumina Films at High Temperatures: Formation and Reduction of Carbides*. Journal of Catalysis 196, 40 (2000).
- Y. Wang, F. Gao, M. Kaltchev, and W. T. Tysoe. *The effect of electron beam irradiation on the chemistry of molybdenum hexacarbonyl on thin alumina films in ultrahigh vacuum*. Journal of Molecular Catalysis A: Chemical 209, 135 (2004).

- Y. Wang, F. Gao, and W. T. Tysoe. *Interaction of molybdenum hexacarbonyl with hydroxylated alumina thin films at high temperatures: Formation and removal of surface carbides*. Journal of Molecular Catalysis A: Chemical 248, 32 (2006).
- M. Kaltchev and W. T. Tysoe. *Preparation and characterization of alumina-supported metal-carbonyl-derived model catalytic systems in UHV conditions*. Topics in Catalysis 13, 121 (2000).
- Y. Wang, F. Gao, M. Kaltchev, D. Stacchiola, and W. T. Tysoe. *An investigation of the chemistry of molybdenum hexacarbonyl on thin dehydroxylated alumina films in ultrahigh vacuum*. Catalysis Letters 91, 83 (2003).
- Z. Jiang, W. Huang, Z. Zhang, H. Zhao, D. Tan, and X. Bao. *Thermal decomposition of Mo(CO)6 on thin Al2O3 film: A combinatorial investigation by XPS and UPS*. Surface Science 601, 844 (2007).
- J. Prunier, B. Domenichini, Z. Li, P. J. Moller, and S. Bourgeois. *A photoemission study of molybdenum hexacarbonyl adsorption and decomposition on TiO2 (110) surface*. Surface Science 601, 1144 (2007).
- G. A. Rizzi, A. E. Reeder, S. Agnoli, and G. Granozzi. *Epitaxial MoOx nanostructures on TiO2(110) obtained using thermal decomposition of Mo(CO)6*. Surface Science 600, 3345 (2006).
- Y. Okamoto, Y. Kobayashi, Y. Teraoka, S. Shobu, and S. Kagawa. *Photooxidation of M(CO)6 (M = Mo, W) adsorbed on TiO2*. Journal of the Chemical Society, Faraday Transactions 93, 2561 (1997).
- L. H. Jones, R. S. McDowell, and M. Goldblatt. Force constants of the hexacarbonyls of chromium, molybdenum, and tungsten from the vibrational spectra of isotopic species. Inorganic Chemistry 8, 2349 (1969).
- E. W. Plummer, W. R. Salaneck, and J. S. Miller. *Photoelectron spectra of transition-metal carbonyl complexes: comparison with the spectra of adsorbed CO*. Physical Review B 18, 1673 (1978).
- U. Gelius. *Binding-Energies and Chemical-Shifts in Esca*. Physica Scripta 9, 133 (1974).
- J. Blomquist. On Some Relationships between Energy, Charge and Electrostatic Potential at the Nucleus and the Interpretation of Chemical-Shifts in Xps. Journal of Electron Spectroscopy and Related Phenomena 36, 69 (1985).
- B. J. Lindberg, K. Hamrin, G. Johansson, U. Gelius, A. Fahlman, C. Nordling, and K. Siegbahn. *Molecular spectroscopy by means of ESCA. III. Sulfur compounds correlation of electron binding energy with structure.* Physica Scripta 1, 286 (1970).
- Y. Taki and O. Takai. XPS structural characterization of hydrogenated amorphous carbon thin films prepared by shielded arc ion plating. Thin Solid Films 316, 45 (1998).
- E. Riedo, F. Comin, J. Chevrier, F. Schmithusen, S. Decossas, and M. Sancrotti. Structural properties and surface morphology of laser-deposited amorphous carbon and carbon nitride films. Surface & Coatings Technology 125, 124 (2000).
- T. W. Scharf, R. D. Ott, D. Yang, and J. A. Barnard. Structural and tribological characterization of protective amorphous diamond-like carbon and amorphous CNx overcoats for next generation hard disks. Journal of Applied Physics 85, 3142 (1999).

- D. V. Potapenko, J. M. Horn, R. J. Beuhler, Z. Song, and M. G. White. *Reactivity studies with gold-supported molybdenum nanoparticles*. Surface Science 574, 244 (2005).
- G. Lu, PhD in *Chemistry* (Southampton, 1995).
- J. W. He, W. K. Kuhn, and D. W. Goodman. *Co Adsorption on Clean and C-Covered, O-Covered and H-Covered Mo(110) Surfaces an Iras Study.* Surface Science 262, 351 (1992).
- A. Ogata, A. Kazusaka, M. Enyo, and I. Toyoshima. *Active-Sites on the Moo3/Sio2 Catalyst Photoreduced with Co for Co2 Reduction to Co*. Chemical Physics Letters 127, 283 (1986).
- F. Cosandey and T. E. Madey. *Growth, morphology, interfacial effects and catalytic properties of Au on TiO2*. Surface Review and Letters 8, 73 (2001).
- X. Lai, T. P. St Clair, M. Valden, and D. W. Goodman. Scanning tunneling microscopy studies of metal clusters supported on TiO2 (110): Morphology and electronic structure. Progress in Surface Science 59, 25 (1998).
- Y. Wang and G. S. Hwang. Adsorption of Au atoms on stoichiometric and reduced TiO2(110) rutile surfaces: a first principles study. Surface Science 542, 72 (2003).
- E. Wahlstrom, N. Lopez, R. Schaub, P. Thostrup, A. Ronnau, C. Africh, E. Laegsgaard, J. K. Norskov, and F. Besenbacher. *Bonding of gold nanoclusters to oxygen vacancies on rutile TiO2(110)*. Physical Review Letters 90, 026101 (2003).
- N. Lopez, J. K. Norskov, T. V. W. Janssens, A. Carlsson, A. Puig-Molina, B. S. Clausen, and J. D. Grunwaldt. *The adhesion and shape of nanosized Au particles in a Au/TiO2 catalyst*. Journal of Catalysis 225, 86 (2004).
- A. Howard, D. N. S. Clark, C. E. J. Mitchell, R. G. Egdell, and V. R. Dhanak. *Initial and final state effects in photoemission from Au nanoclusters on TiO2(110)*. Surface Science 518, 210 (2002).
- M. S. Chen and D. W. Goodman. *The structure of catalytically active gold on titania*. Science 306, 252 (2004).
- M. S. Chen and D. W. Goodman. *Catalytically active gold: From nanoparticles to ultrathin films*. Accounts of Chemical Research 39, 739 (2006).
- M. S. Chen and D. W. Goodman. *Interaction of Au with titania: the role of reduced Ti*. Topics in Catalysis 44, 41 (2007).
- M. S. Chen, K. Luo, D. Kumar, W. T. Wallace, C. W. Yi, K. K. Gath, and D. W. Goodman. *The structure of ordered Au films on TiOx*. Surface Science 601, 632 (2007).
- M. Chen, Y. Cai, Z. Yan, and D. W. Goodman. *On the origin of the unique properties of supported Au nanoparticles*. Journal of the American Chemical Society 128, 6341 (2006).
- C. Lemire, R. Meyer, S. Shaikhutdinov, and H. J. Freund. *Do quantum size effects control CO adsorption on gold nanoparticles?* Angewandte Chemie-International Edition 43, 118 (2004).
- C. Lemire, R. Meyer, S. K. Shaikhutdinov, and H. J. Freund. *CO adsorption on oxide supported gold: from small clusters to monolayer islands and three-dimensional nanoparticles.* Surface Science 552, 27 (2004).

- N. Lopez, T. V. W. Janssens, B. S. Clausen, Y. Xu, M. Mavrikakis, T. Bligaard, and J. K. Norskov. *On the origin of the catalytic activity of gold nanoparticles for low-temperature CO oxidation*. Journal of Catalysis 223, 232 (2004).
- B. Yoon, H. Hakkinen, U. Landman, A. S. Worz, J. M. Antonietti, S. Abbet, K. Judai, and U. Heiz. *Charging effects on bonding and catalyzed oxidation of CO on Au-8 clusters on MgO*. Science 307, 403 (2005).
- F. Boccuzzi, A. Chiorino, and M. Manzoli. *FTIR study of the electronic effects of CO adsorbed on gold nanoparticles supported on titania*. Surface Science 454, 942 (2000).
- S. Laursen and S. Linic. Oxidation catalysis by oxide-supported Au nanostructures: The role of supports and the effect of external conditions. Physical Review Letters 97, 026101 (2006).
- M. M. Schubert, S. Hackenberg, A. C. van Veen, M. Muhler, V. Plzak, and R. J. Behm. *CO oxidation over supported gold catalysts-"inert" and "active" support materials and their role for the oxygen supply during reaction*. Journal of Catalysis 197, 113 (2001).
- M. Comotti, W. C. Li, B. Spliethoff, and F. Schuth. Support effect in high activity gold catalysts for CO oxidation. Journal of the American Chemical Society 128, 917 (2006).
- B. E. Hayden, D. Pletcher, M. E. Rendall, and J. P. Suchsland. *CO oxidation on gold in acidic environments: Particle size and substrate effects*. Journal of Physical Chemistry C 111, 17044 (2007).
- Z. P. Liu, X. Q. Gong, J. Kohanoff, C. Sanchez, and P. Hu. *Catalytic role of metal oxides in gold-based catalysts: A first principles study of CO oxidation on TiO2 supported Au.* Physical Review Letters 91 (2003).
- L. M. Molina and B. Hammer. *Active role of oxide support during CO oxidation at Au/MgO*. Physical Review Letters 90 (2003).
- L. M. Molina, M. D. Rasmussen, and B. Hammer. *Adsorption of O-2 and oxidation of CO at Au nanoparticles supported by TiO2(110) (vol 120, pg 7673 2004)*. Journal of Chemical Physics 123 (2005).
- V. A. Bondzie, S. C. Parker, and C. T. Campbell. *Oxygen adsorption on well-defined gold particles on TiO2(110)*. Journal of Vacuum Science & Technology a-Vacuum Surfaces and Films 17, 1717 (1999).
- <sup>229</sup> Z. P. Liu, P. Hu, and A. Alavi. *Catalytic role of gold in gold-based catalysts: A density functional theory study on the CO oxidation on gold.* Journal of the American Chemical Society 124, 14770 (2002).
- D. C. Meier and D. W. Goodman. *The influence of metal cluster size on adsorption energies: CO adsorbed on Au clusters supported on TiO2*. Journal of the American Chemical Society 126, 1892 (2004).
- F. Boccuzzi, A. Chiorino, M. Manzoli, P. Lu, T. Akita, S. Ichikawa, and M. Haruta. *Au/TiO2 nanosized samples: A catalytic, TEM, and FTIR study of the effect of calcination temperature on the CO oxidation.* Journal of Catalysis 202, 256 (2001).
- Z. Yan, S. Chinta, A. A. Mohamed, J. P. Fackler, and D. W. Goodman. *CO oxidation over Au/TiO2 prepared from metal-organic gold complexes*. Catalysis Letters 111, 15 (2006).

- M. Okumura, S. Tsubota, and M. Haruta. *Preparation of supported gold catalysts by gas-phase grafting of gold acethylacetonate for low-temperature oxidation of CO and of H-2*. Journal of Molecular Catalysis a-Chemical 199, 73 (2003).
- M. Okumura, K. Tanaka, A. Ueda, and M. Haruta. *The reactivities of dimethylgold(III)beta-diketone on the surface of TiO2 A novel preparation method for Au catalysts*. Solid State Ionics 95, 143 (1997).
- C. E. Larson, T. H. Baum, and R. L. Jackson. *Chemical Vapor-Deposition of Gold.* Journal of the Electrochemical Society 134, 266 (1987).
- Y. Maeda, M. Okumura, M. Date, S. Tsubota, and M. Haruta. *STM observations of organometallic complexes on the TiO2(110) and Si(111) surfaces*. Surface Science 514, 267 (2002).
- S. Shibata, K. Iijima, and T. H. Baum. *Molecular-Structure of Dimethyl*(2,4-*Pentanedionato*)*Gold*(*Iii*). Journal of the Chemical Society-Dalton Transactions, 1519 (1990).
- J. C. Fierro-Gonzalez and B. C. Gates. Genesis of gold clusters from mononuclear gold complexes on TiO2: Reduction and aggregation of gold characterized by time-resolved X-ray absorption spectroscopy. Journal of Physical Chemistry B 109, 7275 (2005).
- J. Guzman, B. G. Anderson, C. P. Vinod, K. Ramesh, J. W. Niemantsverdriet, and B. C. Gates. *Synthesis and reactivity of dimethyl gold complexes supported on MgO: Characterization by infrared and x-ray absorption spectroscopies*. Langmuir 21, 3675 (2005).
- J. Guzman and B. C. Gates. Reactions of Au(CH3)(2)(acac) on gamma-Al2O3: Characterization of the surface organic, organometallic, metal oxide, and metallic species. Langmuir 19, 3897 (2003).
- J. C. Fierro-Gonzalez, B. G. Anderson, K. Ramesh, C. P. Vinod, J. W. Niemantsverdriet, and B. C. Gates. *Zeolite NaY-supported gold complexes prepared from Au(CH3)(2)(C5H7O2): reactivity with carbon monoxide*. Catalysis Letters 101, 265 (2005).
- <sup>242</sup> X. Zhang, H. Shi, and B. Q. Xu. *Comparative study of Au/ZrO2 catalysts in CO oxidation and 1,3-butadiene hydrogenation*. Catalysis Today 122, 330 (2007).
- I. Tuzovskaya, N. Bogdanchikova, A. Simakov, V. Gurin, A. Pestryakov, M. Avalos, and M. H. Farias. *Structure and electronic states of gold species in mordenites*. Chemical Physics 338, 23 (2007).
- W. S. Epling, G. B. Hoflund, J. F. Weaver, S. Tsubota, and M. Haruta. *Surface characterization study of Au/alpha-Fe2O3 and Au/Co3O4 low-temperature CO oxidation catalysts*. Journal of Physical Chemistry 100, 9929 (1996).
- X. B. Yan, T. Xu, G. Chen, S. R. Yang, and H. W. Liu. Study of structure, tribological properties and growth mechanism of DLC and nitrogen-doped DLC films deposited by electrochemical technique. Applied Surface Science 236, 328 (2004).
- L. Zhang, F. Cosandey, R. Persaud, and T. E. Madey. *Initial growth and morphology of thin Au films on TiO2(110)*. Surface Science 439, 73 (1999).
- X. N. Li, Y. Zhang, and K. J. Smith. *Metal-support interaction effects on the growth of filamentous carbon over CO/SiO2 catalysts*. Applied Catalysis a-General 264, 81 (2004).

- J. Luthin and C. Linsmeier. *Carbon films and carbide formation on tungsten*. Surface Science 454, 78 (2000).
- K. U. Klages, A. Wiltner, J. Luthin, and C. Linsmeier. *Deuterium bombardment of carbon and carbon layers on titanium*. Journal of Nuclear Materials 313, 56 (2003).
- J. Evans, B. E. Hayden, and M. A. Newton. A comparison of the chemistry of Rh-I(acac)(CO)(2) and Rh-I(CO)(2)Cl adsorbed on TiO2[110]: development of particulate Rh and oxidative disruption by CO. Surface Science 462, 169 (2000).
- M. G. Miles, G. E. Glass, and R. S. Tobias. Structure of Dimethylgold(III) Compounds. Spectroscopic Studies on the Aquo Ion and Several Coordination Compounds. Journal of the American Chemical Society 88, 5738 (1966).